COMPUTATIONAL INVESTIGATIONS OF TURBULENT RECTANGULAR JETS IN A NARROW CHANNEL CROSSFLOW

BY
MANABENDRA PATHAK

DEPARTMENT OF MECHANICAL ENGINEERING
INDIAN INSTITUTE OF TECHNOLOGY GUWAHATI
GUWAHATI

MAY 2007

COMPUTATIONAL INVESTIGATIONS OF TURBULENT RECTANGULAR JETS IN A NARROW CHANNEL CROSSFLOW

A thesis
submitted in partial fulfilment of the
requirements for the Degree of
Doctor of Philosophy
in
Engineering

by
Manabendra Pathak
(*Roll No 01610306*)

under the guidance of
Prof. Anupam Dewan
and
Prof. Anoop Kumar Dass

DEPARTMENT OF MECHANICAL ENGINEERING
INDIAN INSTITUTE OF TECHNOLOGY GUWAHATI
GUWAHATI

MAY 2007

CERTIFICATE

It is certified that the work contained in this thesis entitled **Computational Investigations of Turbulent Rectangular Jets in a Narrow Channel Crossflow**, by **Manabendra Pathak**, a student of the Department of Mechanical Engineering, Indian Institute of Technology, Guwahati, India, for the award of the degree of Doctor of Philosophy has been carried out under our supervision and that this work has not been submitted elsewhere for a degree.

Dr. Anupam Dewan
Professor
Department of Mechanical Engineering
Indian Institute of Technology
Guwahati

Dr. Anoop Kumar Dass
Professor
Department of Mechanical Engineering
Indian Institute of Technology
Guwahati

Dedicated
To my father Late Banamali Pathak

Acknowledgements

I am very grateful to my supervisor Prof. Anupam Dewan, for providing invaluable support and advice throughout this research work and for his never-ending patience and care in advising me. He has not only given me continuous guidance but also spurred my interest in various aspects of the physics of turbulence.

I would also like to express my gratitude to my other supervisor Prof. Anoop Kumar Dass, whose wisdom and sagacity always touched me in a profound way, not only in academic pursuits, but in life in general. My special gratefulness is extended to him for his great input and insight into my research especially in the area of computational techniques.

.

I sincerely appreciate the role played by all of my doctoral committee members Dr. M.K. Das, Dr. M. Pandey and Dr. P. Mahanta for their valuable advice and encouragement at different stages of the Ph.D. work. I am grateful to Prof. S.C. Mishra, Dean of Academic affair and Prof U.S. Dixit, Head of the Mechanical Engineering Department for their support and personal encouragement throughout my Ph.D. work. I would also like to extend my thanks to all the faculty members of the Mechanical Engineering Department for their encouragement. My sincere acknowledgement goes to Dr. J. Kalita, Department of Mathematics for his valuable advice during the numerical code development.

I am very grateful to Professor A. Roshko, California Institute of Technology, for his permission to reproduce the sketch of different vortices from his article in my thesis (Fig. 1.2).

I am thankful to all the people with whom I worked throughout this journey of doctoral program, especially to Dr. P. Talukdar, Dr. P. R. Kanan, Dr. K. Kalita, Mr. D.K. Sarma, Mr. E.V. Rao, Mr. G. V. D. Prasad, Mr. M. Sivasankar and many more.

I am also thankful to all the staff members of the Mechanical Engineering Department for their support and cooperation especially to Mr. A. Kalita, Mr. D.J. Bordoloi, Mr. R. Saikia and Mr. R. Patowary.

My special thanks go to my friend Mr. A. Borsaikia for his endless support and encouragement. I am extremely thankful to all the members of my family for their constant encouragement, especially to my wife Juthika (Majoni) and my daughter Michiky for their uncomplaining support, love and understanding despite going through a difficult time when I had to keep long hours away from home.

"Om Krishnaya Namaha"

Manabendra Pathak
I.I.T. Guwahati

May 2007.

List of Publications from the present work

International Journals

1. M. Pathak, A. Dewan and A. K. Dass, 2005 *"An assessment of Streamline Curvature Effects on the Mixing Region of a Turbulent Plane Jet in Crossflow",* Applied Mathematical Modeling, Vol. 29, No. 8, pp. 711-725.
2. M. Pathak, A. Dewan and A. K. Dass, 2006, *"Computational prediction of a slightly heated turbulent rectangular jet discharged in to a narrow channel crossflow using two different turbulence models",* International Journal of Heat and Mass Transfer, Vol 21-22, No.49, pp. 39214-3928.
3. M. Pathak, A. Dewan and A. K. Dass, 2007, "*Effect of Streamline Curvature on Flow Field of a Turbulent Plane Jet in Crossflow",* Mechanics Research, Communication, Vol. 34, No. 3, pp. 241-248.
4. M. Pathak, A.K. Dass, and A. Dewan, 2007, "*An Investigation of Turbulent Rectangular Jet Discharged into a Narrow Channel Weak Crossflow"*, J. Hydrodynamics, (In press).

Refereed Conferences

1. M. Pathak, A. Dewan and A. K. Dass, 2004, "*A Review of Effect of Streamline Curvature on Turbulence and a Case Study of Turbulent Plane Jet in Crossflow,"* Proc. 7th annual CFD Symposium, of Aeronautical Society of India, Bangalore.
2. M. Pathak, A. Dewan and A.K. Dass, 2005, "*A Computational Study of Three-Dimensional Turbulent Flow Due to Interaction of a Slot Jet and Crossflow Using Reynolds-Stress Transport Model"*, Proc. 8th Annual Computational Fluid Dynamics Symposium of Aeronautical Society of India, Bangalore.
3. M. Pathak, A. Dewan and A.K. Dass, 2006, "*Computational Fluid Dynamics of Flow Field of a Heated Turbulent Plane Jet in Crossflow using Reynolds-stress Transport Model"*, Proc. 18th National and 7th ISHMT-ASME Heat and Mass Transfer Conference, Guwahati, India (Paper No. HMT-2006-C125).
4. A. Dewan, M. Pathak and A.K. Dass, 2006, *Heated Turbulent Rectangular Jet Discharged Into a Narrow Channel Cross flow*, Proc. International Conference on Recent Advances in Heat Transfer, Coimbatore, India, pp. 73-83.

Abstract

The present work deals with the computational investigation of a practically important and theoretically interesting flow field of turbulent isothermal and heated rectangular jets in a narrow channel crossflow for high velocity ratios. The main objective of the work is to provide a more detailed information about the flow characteristics of this important flow configuration compared with available literature. The other objective is to assess the performance of different turbulence models in predicting the behaviour of this flow configuration. The investigation is carried out first for the 2D flow field and subsequently for the 3D flow field. In the 2D investigation, the computations are carried out using the standard k-ε model and the streamline curvature modification to the k-ε model. The physical effects of the streamline curvature on the flow field are studied and the improvement over the standard k-ε model is discussed. In the 3D investigation of the flow field, the standard k-ε model and the Reynolds stress transport (RST) model are used. Computational tools in the form of two FORTRAN 77 computer codes based on the SIMPLE algorithm, finite volume formulation and staggered grid arrangement are developed. The first code tackles the 2D problem using the standard k-ε model and its streamline curvature modification. The other code tackles the 3D problem through the standard k-ε model. In addition a commercial code FLUENT 6.2 is used to compute the 3D heated jets in crossflow using the RST model. About the 2D computation it can be said that in those situations where smaller computational time gets priority over flow details and accuracy, a 2D investigation has its merit in that the results obtained for the jet central plane are physically realistic though not very accurate. Streamline curvature modification to the k-ε model is observed to produce somewhat improved results, especially in the inner part of the jet. 3D computations with both standard k-ε and RST models demonstrate that the central vertical plane is a plane of symmetry and it is possible to carry out the computation in half the flow field with a symmetry boundary condition. The standard k-ε model performs well and reproduces many physical features that are similar to those reported in the literature, besides producing reasonably good quantitative agreement with experiments. The results demonstrate that the velocity ratio affects flow features such as the trajectory and the lateral spread of the jet, and the low velocity region

downstream of the jet. A higher value of the velocity ratio is associated with a reduced size of the wake vortices and the reverse flow region downstream of the jet slot. The RST model shows some improvement in the predictions compared with the standard k-ε model especially in the reverse flow region. It also captures two secondary vortices at the bottom corners far downstream, whereas the k-ε model fails to do so. However, it does not show significant improvement over the standard k-ε model. The mean temperature field in the case of heated jet appears to be controlled by different vortices formed in the flow field and observed temperature distribution is consistent with similar results reported in the literature. Also it is interesting to note that the flow in the jet duct itself gets affected as a result of the interaction between the jet and the cross-stream and the origin of the counter rotating vortex pair (CRVP) can be traced back to well within the jet duct. The present work also establishes the three-dimensionality of the flow field highlighting the insufficiency of the only two experimental works dealing with the problem that have come to our notice. The 3D investigation produces results not only in the jet central plane but in various other regions in the flow field. Thus these results bring to light not only the various features in the jet shear layer but also some interesting aspects of the flow in the neighbourhood including two hitherto unreported secondary vortices. Besides closely reproducing existing experimental results, the present work also gives a deeper insight into various features of the complex flow field under investigation, thus providing new information and opening up possibilities for further experimental and numerical investigation.

Contents

List of Figures

List of Tables

Nomenclature

b_{ij} *Reynolds stress anisotropy term*

C *model constant*

C_1, C_2, C_3, C_4 *model constant*

C_3^* *model constant*

C_{ij} *convection term of Reynolds stress*

C_μ *model constant*

$C_{\varepsilon 1}$ *model constant*

$C_{\varepsilon 2}$ *model constant*

D *width of the jet slot*

D_{ij}^T *turbulence diffusion term of Reynolds stress*

g *acceleration due to gravity*

H *height of the jet plenum*

i *spatial index of grids in x- direction*

J *momentum flux ratio*

k *turbulence kinetic energy, spatial index of grids in z- direction*

L *length of the jet plenum*

n *coordinate perpendicular to the jet trajectory*

p *mean pressure*

p' *fluctuating pressure*

Pr *Prandtl number*

P_{ij} *production of Reynolds stress*

P_k *production of turbulence kinetic energy*

q *square root turbulence kinetic energy*

R *jet to crossflow velocity ratio* (v_j / u_a)

Re *Reynolds number*

R_{bj} *exit Richardson number*

R_f *flux Richardson number*

Sc *Schmidt number*

s *distance along the jet trajectory from the centre of the jet slot*

T *mean temperature of the flow field*

T_a *mean temperature of the crossflow*

T_j *mean temperature of the jet*

ΔT T-T_a

ΔT_j $T_j - T_a$

u *mean velocity along the crossflow direction (along the x- direction)*

$\overline{u'^2}$ *Reynolds normal stress*

$\overline{u'v'}$ *Reynolds shear stress*

$\overline{u'w'}$ *Reynolds shear stress*

$\overline{u'_s v'_n}$ *Reynolds stress in s-n coordinate*

u_a *crossflow velocity*

u_s *component of mean velocity along s direction*

v *mean velocity along the jet discharge direction (y- direction)*

$\overline{v'^2}$ *Reynolds normal stress*

$\overline{v'w'}$ *Reynolds shear stress*

v_j *jet velocity*

v_n *component of mean velocity along n direction*

w *mean velocity along spanwise (z direction)*

$\overline{w'^2}$ *Reynolds normal stress*

x *coordinate along the crossflow direction*

Δx *length of the control volume in x-direction*

y *coordinates along the direction of jet discharge*

Δy *length of the control volume in y-direction*

y_p^+ *normalised distance of first grid point from the wall*

z *coordinates along spanwise*

Δz *length of the control volume in z-direction*

Greek alphabet

δ_{ij} *Kronecker delta*

ε *rate of dissipation of turbulence kinetic energy k*

ε_{ij} *dissipation term of Reynolds stress*

ϕ *model constant*

ϕ_{ij} *pressure strain term of Reynolds stress*

λ *clustering parameter of grids*

μ *molecular viscosity*

μ_t *eddy viscosity*

ρ *density*

σ_k *model constant*

σ_t *turbulence Prandtl number*

σ_ε *model constant*

υ *molecular viscosity*

υ_t *eddy viscosity*

ω *specific rate of the turbulence dissipation*

ψ *instantaneous value of any fluid property*

$\overline{\psi}$ *averaged value of any fluid property*

ψ' *fluctuating part of any fluid property*

Subscript

a *crossflow condition*

j *jet condition at the discharge*

i, j, k *tensor notations*

max *maximum value*

Abbreviation

CPU *central processing unit*

DNS *direct numerical simulation*

LES *large eddy simulation*

PIV *particle image velocimetry*

PLIF *planar laser-induced fluorescence*

RAM *random access memory*

RANS *Reynolds-averaged Navier-Stokes*

RST *Reynolds stress transport*

Chapter 1

Introduction

1.1 Turbulent Flow

Most fluid flows encountered in engineering applications are turbulent. Turbulent flows are characterized by the following properties:

(i) Unsteadiness: The behaviour of the turbulent flow variables appears to be random if monitored as a function of time at a fixed point and also if monitored as a function of space at an instant of time.

(ii) Vorticity and three-dimensionality: Turbulent flows exhibit high level of fluctuating vorticity. The alteration of the direction and magnitude of the vorticity takes place by rotation and stretching. The vortex-stretching is an important factor in increasing the intensity of turbulence. Even in flows, where the mean velocities and pressure vary in only one or two space dimensions, turbulence fluctuations always have a three-dimensional spatial character.

(iii) Dissipation: Turbulent flows are highly dissipative. Viscous forces dissipate kinetic energy into thermal energy. To make up for these losses, the kinetic energy needs to be generated, otherwise turbulent flow will die. To maintain the flow, turbulent flows depend on its environment.

(iv) Broad spectrum: The turbulent flows fluctuate on a broad range of length and time scales. The length scale of the largest eddies is of the order of the size of the flow geometry and the smallest scale is of the order of the viscous size, termed as the Kolmogorov length scale. The time scales also behave in similar fashion.

(v) High mixing: Turbulent flows mix much stronger than laminar flows. This is due to the vigorous motion of the fluid which enhances friction, heat and scalar transfers.

1.2 Computational Predictions of Turbulent Flows

In the early stages of fluid flow analysis, the primary approach to study turbulent flow was experimental. Later on with the emergence of computer and different computational techniques, the computational fluid dynamics (CFD) became an

important tool for analyzing turbulent flows. In CFD techniques, the governing equations that are derived from the conservation laws of mass, momentum and energy are set over a physical domain along with the boundary conditions describing the fluid flow. These equations are then solved numerically to generate the pressure and velocity fields in the flow domain. The Navier-Stokes equations which are derived from the conservation of momentum consist of the nonlinear partial differential equations with an intricate dependency on velocity components within the system of equations. Apart from some specific cases, these partial differential equations are not solvable using analytical methods. There are only a very small number of flows that permits simplification of the governing equations in such a way that it is possible to obtain an analytical solution. Consequently for most cases, one is required to solve the Navier-Stokes equations numerically. The highest level of reliability in numerical simulation is given by Direct Numerical Simulations (DNS) and Large Eddy Simulations (LES). Numerical simulations performed using Reynolds-Averaged Navier-Stokes (RANS) solvers are, apart from being numerical approximations, also affected by physical approximations in the models due to averaging of different length scales in the turbulence field. We will discuss these methods briefly in the following sections.

1.2.1 DNS

The most accurate approach to turbulence simulations is to solve the Navier-Stokes equations without averaging or approximation other than numerical discretisation whose errors can be estimated and controlled. But the limitations of the computational resources (storage capacity and speed) restrict the use of direct numerical simulation (DNS) in many practical flow problems. For DNS, the grid to be used must be fine enough to resolve the smallest eddies whose sizes are of the order of Kolmogorov length scale, $(\nu^3/\varepsilon)^{1/4}$, where ν is the kinematic viscosity and ε the rate of dissipation of turbulence kinetic energy. Therefore the number of grid points required in DNS is very high and this number increases with the Reynolds number. The limitations and scope of the DNS were discussed by Kim et al. (1997) considering the flow in a channel. They observed that to simulate the problem with a Reynolds number of 3300 (a value considerably less than that relevant to the practical

applications) based on the centerline mean velocity and channel half width, one needs to use two million grid points in the computational domain. The large number of grid points lead to complexity in the data handling and storage while performing DNS. It is believed that unless a higher speed and more storage capacity computer than the existing ones are not developed, the DNS for flow configurations and Reynolds number of practical problems will not be feasible in the near future.

1.2.2 LES

In large-eddy simulations (LES), the large-scale motions are resolved and the small scales, termed as the subgrid scales are modeled. This approach is based on the idea that the large-scale motions are highly dependent on the boundary conditions whereas the small scale motions are relatively universal everywhere. The equations are filtered in space and the division into the large and small-scale motions is dependant on the length of the filter. The numbers of grid points needed in LES is much less than that in DNS. The accuracy of LES largely depends upon the modeling of the subgrid scales, resulting from filtering the time-dependent Navier-Stokes equations which are based on the assumption of isotropy of the smallest scales. LES is comparatively more expensive than the RANS modeling. The RANS modeling and LES can be combined and this approach is called hybrid RANS/LES or detached eddy simulation (DES). In this approach RANS is used to model the flow in the near-wall region, which requires less resolution as compared to resolving the boundary layer vortices with LES. Further away the LES is used to resolve the turbulence (Dahlstrom, 2003).

1.2.3 RANS Models

For engineering applications, it is unaffordable to treat the time-dependant Navier-Stokes equations directly as excessively demanding computational resources are needed for DNS. This is true to some extent even for LES. Thus a suitable approximation of the time dependant Navier-Stokes equation has to be taken. Reynolds (1895) proposed that the quantities (ψ) in the Navier-Stokes equation could be divided into a mean ($\overline{\psi}$) and a fluctuating part (ψ'):

$$\psi = \overline{\psi} + \psi'$$

where the mean part is the time-average of a parameter over a certain time. The averaging time needs to be longer than the small turbulence fluctuations, however shorter than any mean flow oscillating period. If Reynolds decomposition is applied to the Navier-Stokes equation the result is an equivalent set of equations, termed as the Reynolds-averaged Navier-Stokes (RANS) equations. The time averaging procedure however produces additional terms, the Reynolds stresses ($\overline{u_i' u_j'}$), which are unknown and need to be modeled using a suitable turbulence model. This is referred as the closure problem with the Reynolds averaging. There are two distinct approaches to model the Reynolds stresses, either the eddy-viscosity models (EVM), or the Reynolds stress transport (RST) models. In the latter case the actual stresses are solved, while in the former the Boussinesq eddy-viscosity hypothesis (Hinze, 1975) is employed to estimate the Reynolds stresses. The eddy viscosity hypothesis of Boussinesq results in a first-order closure of the system of the governing equations. A suitable turbulence model is used to provide the eddy viscosity to the RANS equations. The RANS equations represent transport equations for the mean flow quantities only, with all the scales of the turbulence being modeled. The approach of permitting a solution for the mean flow variables greatly reduces the computational effort compared to DNS or LES.

In the past, several kinds of first-order closure turbulence models have been devised. The class of zero-equation or algebraic models are those proposed by Baldwin and Lomax (1978), Cebeci and Smith (1974). The turbulence models are categorized by the number of transport equations employed in addition to the momentum equations. The most widely used one-equation turbulence model has been developed by Spalart and Allmaras (1992), which is a relatively simple model that solves a modeled transport equation for the eddy viscosity. Two-equation turbulence models in general are built mostly from the transport equation for the turbulence kinetic energy and a suitable second transport equation. The k-ε model is the one most commonly used and this is one of the simplest two-equation models in which the solution of two separate transport equations allows the turbulence velocity and length scales to be independently determined. The velocity and the length scales are determined from the transport equation of turbulence kinetic energy and the dissipation rate of the turbulence kinetic energy. The model has become the workhorse of practical engineering flow calculations since the time it was proposed

by Launder and Spalding (1972). Robustness, economy, and reasonable accuracy for a wide range of turbulent flows explain its popularity in industrial flow and heat transfer investigations. Another important two-equation model is the $k-\omega$ model developed by Wilcox (1998). In this model the length scale is determined from the specific rate of the turbulence dissipation rate (ω). Both the models use the assumption of the isotropic turbulence viscosity, even though this is not strictly consistent with the anisotropic nature of the turbulence structure of the flow field. Still, as far as the prediction of the global parameters such as the pressure drops is concerned, the two equation models have proven to be adequately accurate. If further details of the flow field are desired, these models could still be used with some modifications.

In Reynolds stress transport (RST) models, the eddy viscosity approach is not used and the closure of the Reynolds-averaged Navier-Stokes equations is obtained by solving transport equations for the Reynolds stresses, together with an equation for the dissipation rate (2^{nd}-order accurate). This means that five additional transport equations are required in case of two-dimensional (2D) flows and seven additional transport equations must be solved in case of the three-dimensional (3D) flows. Since the RST model accounts for the effects of streamline curvature, swirl, rotation, and rapid changes in the strain rate, in a more rigorous manner than one-equation and two-equation models, it has good potential to provide accurate predictions for complex flows. However, the reliability of RST model predictions is still limited by the closure assumptions employed to model various terms in the exact transport equations for the Reynolds stresses. The modeling of the pressure-strain and dissipation-rate terms is particularly challenging, and often considered to be responsible for compromising the accuracy of RST model predictions. The RST model might not always yield results that are clearly superior to the simpler models in all classes of flows to warrant the additional computational expense. However, the use of the RST model is recommended when the flow features of interest are the result of anisotropy in the Reynolds stresses. Among the examples are cyclone flows, highly swirling flows in combustors, rotating flow passages, and the stress-induced secondary flows in ducts.

1.3 Turbulent Jets in Crossflow

A jet is formed when a fluid is ejected from a nozzle. The instability of a jet occurs at a low Reynolds number (Kaplan, 1964), which may become turbulent. When the geometry of the discharge nozzle is rectangular the jet formed is three-dimensional and when it is a slit (two-dimensional), the jet formed is plane. Depending upon the condition of the surrounding fluid, jets may be termed as jet in quiescent surroundings, coflowing jet (jet stream and surrounding fluid move parallel to each other) and jet in crossflow (surrounding fluid moves normal to the discharge direction of the jet stream).

The problem of turbulent jets in crossflow is important both from the application point of view as well as fundamental research point of view. The problem is encountered in numerous engineering applications, where jets are found in both confined and unconfined environments. Some examples of confined jets in crossflow are the internal cooling of turbine blades by air jets, vertical and short take-off and landing (VSTOL) aircraft, dilution by air jets in combustion chambers of gas-turbine engine, several industrial processes such as mixing of product streams, drying of product streams, etc.

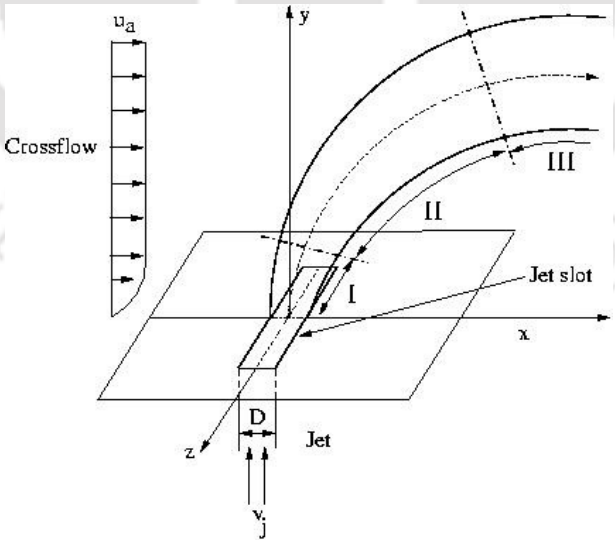

Fig. 1.1: Configuration of a jet in crossflow.

Jets in unconfined or semi-infinite crossflow are found in more numerous practical problems, which include flow fields resulting from the action of cross winds on

chimney stacks or flames from petrochemical plants, discharge of sewage or waste heat into rivers or oceans, film cooling of turbine blades, thermal plumes rising into cross winds in the atmosphere, exhaust gas discharged to atmosphere from automobile engine, thermal plumes generated near ground level by volcanoes, thunderstorms, or forest fires that can often rise to heights in the atmosphere where significant crossflow exists, etc.

The problem is also important from the fundamental research point of view, as many complex fluid dynamics phenomena such as vortices, flow reversal, entrainment and mixings are involved with it. The problem represents both free-shear flows (jet) and boundary-layer flows (crossflow). After interactions of both the flows, the flow field becomes complex. It is also characterized by the streamline curvature and different types of vortices are formed due to interactions of the jet and crossflow.

The configuration of a rectangular jet in crossflow is shown in Fig. 1.1. The axis of the jet is usually defined as the locus of the maximum velocity or total pressure. The main parameter which characterizes jet in crossflow is the jet-to-crossflow velocity ratio, $R\ (= v_j/u_a)$ or the momentum flux ratio $J\ (=\frac{\rho_j}{\rho_a}R^2)$. The low velocity ratio ($R <$ 0.5) is seen in the case of turbine blade cooling whereas $1< R < 10$ is found in the case of jet stabilisation in the combustion chamber. The jet with $R > 10$ is characterised with free jet characteristics. In confined jets, the normalized wall distance may also be an important factor, if the distance is not too large. In the multiple jets the normalized distance between two jets is an additional parameter. As shown in Fig. 1.1, the whole flow field of a jet in crossflow can be classified in three distinct regions (Demuren, 1986, Sherif and Pletcher, 1990 and Said et al., 2005). In the first region (I), the initially uniform jet flow interacts with the ambient crossflow causing a shear layer to develop at the jet boundaries. Upstream of this region, the crossflow is decelerated and a positive pressure region is formed. The length of the initial region depends on the jet cross-section, velocity ratio and jet discharge Reynolds number. The second region (II) is the main region or the established flow region, where the jet experiences large deflection. Two mechanisms have been claimed in the literature to explain this deflection: (a) the pressure gradient between the upstream (high) and downstream (low) flow over the bottom wall at the jet exit; and (b) the entrainment between the jet flow and the crossflow stream. The second region is complex, being characterized by

the development of turbulence mixing layer around the jet boundaries and the flow becomes fully turbulent. Due to the shearing action of the crossflow, the jet sides experience strong lateral spread. The third region (III) is the far-field region, where the jet axis approaches the crossflow direction asymptotically and the flow field becomes nearly self-similar. In this region, the magnitude and direction of the jet velocity are close to those of the crossflowing stream and it becomes difficult to distinguish between crossflow and jet fluids.

Vortical flow evolution around a jet in crossflow has been of considerable interest for some time and the subject of several investigations. This is mainly due to its wide application in the vast array of engineering problems and the complex mechanisms of interaction between the jet and the cross-stream. The structurally interesting phenomena observed in jet in a crossflow are the formation of (i) roll-up in the jet-shear layer vortices; (ii) formation of the counter-rotating vortex pair; (iii) a horse-shoe vortex system in the crossflow boundary layer upstream from the jet exit; and (iv) the creation of wake vortices (Fric and Roshko, 1994 and Kelso et al., 1996). Fig.1.2 (reproduced from Fric and Roshko, 1994) shows a schematic of these major vortex systems for a typical round jet in a crossflow. Some of these vortical structures have been found to be responsible for a significant entrainment of the crossflow fluid by the jet as the latter penetrates into the former.

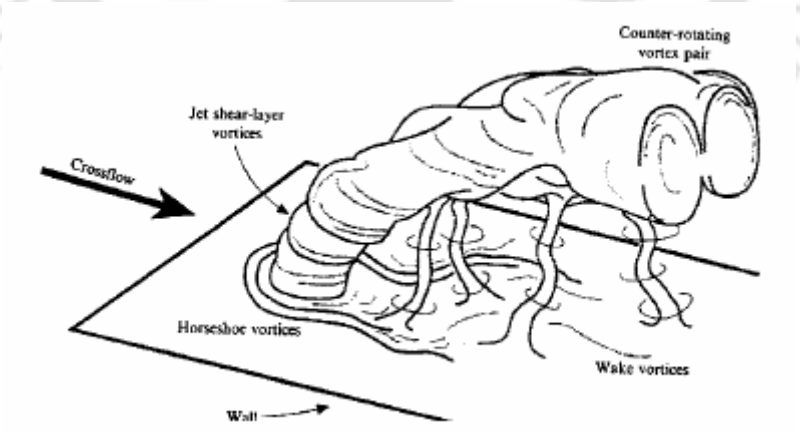

Fig. 1.2: Different vortices associated in the flow field of jet in crossflow (reproduced with permission from Fric and Roshko, 1994).

The shear layer vortices form near the initial region of the jet due to the interaction of the uniform jet velocity and the crossflow. These form on the leeward and

windward edges of the jet and have been attributed to Kelvin-Helmholtz type instabilities (Kelso et al., 1996 and Andreoplous and Rodi, 1984). Due to the adverse pressure gradient upstream of the jet, a horseshoe vortex system is formed which wraps around the base of the jet and travels downstream. The wake vortices form in the second region and at the inner part of the jet. The wake vortices are initiated by the entrainment of the crossflow boundary-layer into the wake and the upward re-orientation of the entrained flow into the wake structures. Lim et al. (1992) observed that the size of the wake region depends upon the velocity ratio (R). For high velocity ratios ($R > 2$), the jet penetrates significantly into the crossflow and it bends over far enough downstream of the injection hole. Therefore for these types of jets, there is little influence of the wall on its development. Moreover there is a little effect of the crossflow boundary layer characteristics on the flow for high values of R as the jet is able to penetrate through a relatively thin boundary layer. On the other hand for low velocity ratios ($R < 1$) the jet bends over into the wall at a small downstream distance and then it spreads over the wall. There is a lack of the wake region downstream of the jet injection hole and the jet behaves like a wall jet. In this type of situation, the jet flow is unable to cross the crossflow boundary layer thus producing less complex flow behaviour in the near-field of the jet compared to that with a high value of R. The counter-rotating vortex pair (CRVP) forms at the vertical plane just after the jet hole and it becomes dominant structures in the downstream of the flow field. These are formed due to both the shearing between the jet and the crossflow and the vorticity issuing from the jet-hole exit (Andreoplous and Rodi, 1984). In fact, this feature appears even in the steady and laminar numerical calculations of the flow, and it seems to be qualitatively independent of the velocity ratio, Reynolds number, and the shape of the nozzle. Besides these four structures, some authors (Kelso et al., 1996, Peterson and Plesniak, 2002, Haven and Kurosaka, 1997, Kuzo, 1995 and Hale et al., 2000) have reported the presence of secondary vortices in the flow field. They have found an additional pair of counter-rotating vortex located between the jet and wall, thus bifurcating the traditional CRVP.

In most practical situations, jets and plumes are either discharged vertically or at an angle to a crossflow. In such flow conditions the jet and crossflow interaction and thermal spread are extremely important flow properties. Accordingly when the temperature field is strongly affected by the velocity field, temperature can be regarded as a passive scalar, it is necessary to understand the mean and fluctuating

characteristics of the thermal spread and mixing in such jets in crossflow. The flow behaviour and heat transfer analysis of a heated jet in crossflow are reported by several researchers (for example by Wark and Foss, 1998, Chen and Hwang, 1991, Sherif and Pletcher, 1991, Nishiyama et al., 1993, Sarkar and Bose, 1995, Hwang and Chiang, 1995, Shi et al., 2003 and Said et al., 2003).

Even though extensive studies have been carried out in the past few decades to investigate the problem of jets in crossflow, some aspects of the flow requires a more detailed investigation. These aspects are in terms of resolving the flow physics, the effects of the geometry of nozzle and dimensions of the flow field etc. One of these aspects is the jet in a narrow channel crossflow and this is the subject of the present investigation.

1.4 Motivation

We have already discussed that, the flow field of high velocity ratio jet in crossflow is observed in combustion chamber of the gas turbine engine and the discharge of sewage or waste into rivers or ocean. Not many papers reporting the investigation of the flow field of rectangular jets in weak crossflows have been found in the literature. Though Ramaprian and Haniu (1983) and Haniu and Ramaprian (1989) have performed experimental study of this flow configuration, they have reported the results only in the jet central plane ($z/D = 0$). They have not provided any information about the spanwise variation of the flow properties. They have also not reported the near wall flow behaviour which is an important phenomenon in turbulent flows. Further in their study there is no detailed information about the complex pattern of vortices that form in the flow field. It is felt that there are important voids that need filling and that is what has provided the initial motivation for the current investigation.

1.5 The Scope of the Present Work

In the present work, a 3D computational investigation of the turbulent isothermal and heated rectangular jet discharged into a narrow channel crossflow for high velocity

ratios is performed. This flow configuration corresponds to the experimental work of Ramaprian and Haniu (1983) and Haniu and Ramaprian (1989). The present topic is unique due to several reasons. Firstly the jet discharge slot spans more than 55% of the crossflow duct width, rather than issuing into a semi-infinite crossflow. Thus the jet is confined in the spanwise direction. Secondly the velocity ratio is quite high (R = 6 and 9). Thirdly the flow configuration of a slightly heated jet (a temperature difference of about 6^0C between the jet and crossflow) is investigated. Also, the effect of streamline curvature is studied by using the standard k-ε model and its curvature modification for a preliminary 2D investigation. Besides k-ε model, Reynolds stress transport model is also used to investigate the 3D flow field of rectangular jets in crossflow, which is not reported in the literature. This type of flow configuration is encountered in a variety of different industrial processes, used to mix two product streams.

To obtain results in a simple and economical way, an investigation of the 2D flow field is done as a first step. The 2D investigation corresponds to the flow field at the central plane of the jet slot (z/D = 0, Fig. 1.1). The flow field obviously contains streamline curvature and therefore a modification to the standard k-ε model to account for the effects of the streamline curvature proposed by Cheng and Farokhi (1992) is considered. This model is relatively simple and computationally economical compared to the more advanced ways to treat turbulence, such as the use of a Reynolds stress transport (RST) model, LES or DNS. As mentioned earlier the standard k-ε model is also employed to study the turbulence characteristics of the 2D flow field. A computer code is developed in FORTRAN 77 to solve the governing 2D Reynolds-Averaged Navier-Stokes (RANS) equations numerically, using the finite volume method and SIMPLE (Patnakar, 1980) algorithm. From the investigation of 2D flow field, several important details of reasonable accuracy of the flow field in the central plane of the jet are obtained for two values of the velocity ratio (R = 6 and 9). To extract information of the flow field in the spanwise direction a 3D investigation is necessary. A finite volume computer code is developed in FORTRAN 77 on a non-uniform staggered grid arrangement using the SIMPLE algorithm (Patankar, 1980) to investigate the 3D flow field. This code not only can give those details that a 2D code cannot give, but also is expected to give more physically realistic results in the central plane itself. The standard k-ε model is used to treat fluid turbulence in this code.

In the final phase, an investigation of a slightly heated jet in a cold crossflow is performed. The effect of buoyancy is neglected as the heating is small and the temperature is assumed to be playing the role of a passive scalar only. This computation is carried out with the commercial code FLUENT 6.2. A Reynolds stress transport (RST) model is employed to resolve the turbulence of the flow field. The different terms of the Reynolds stress transport equations that require modelling are modelled by carefully studying different proposals in the literature and selecting the ones that are thought to be the most suitable for the present flow configuration.

To put it more succinctly - the present work is concerned with the development of computational tools i.e. computer codes for 2D and 3D turbulent flows on one side and use of different turbulence models in predicting the flow field of rectangular jets in crossflow to assess their relative strengths and weaknesses on the other. Also studied are effects of streamline curvature on different flow parameters and characteristics. Influence of the relative strength of the jet discharge to that of the crossflow (R = 6 and 9) on the flow characteristics is another area that is investigated. Overall a detailed qualitative and quantitative description of the flow field is provided with exhaustive illustrations. In the study of the slightly heated jet, the temperature variation in the flow field is investigated.

The dispersion of the temperature in all three directions is studied. The structurally interesting phenomena of the formation of different types of vortices in the flow field and their characteristics are studied. Their effects on the velocity and temperature fields are also discussed. The ability of the turbulence models in capturing those different types of vortices is discussed. The distinct flow features due to the relatively narrow passage between the sidewalls are also described by discussing the qualitative differences of the present observations from those of jets in semi-confined or unconfined crossflow reported in the literature. Also the drawbacks of the 2D predictions are reported by making a comparison of 2D and 3D predictions with the experimental data. Wherever possible, the predictions are validated by careful comparison with established results.

1.6 Layout of the Thesis

The thesis is organized in six chapters. Chapter 1 describes the present work and its objectives. In chapter 2, the pertinent literature is reviewed to present an overview of the problem. Chapter 3 is concerned with the investigation of the 2D flow field with two different turbulence models (the standard k-ε model and k-ε model with streamline curvature modification). Chapter 4 describes the 3D investigations of the problem with the standard k-ε model. A comparison of 2D and 3D predictions is also made in this chapter. The investigations of heated jet in crossflow using the Reynolds stress transport model are discussed in chapter 5. Chapter 6 provides the conclusions of the thesis. The scope for future works is also presented in this chapter.

भारतीय प्रौद्योगिकी संस्थान गुवाहाटी
Indian Institute of Technology Guwahati

Chapter 2

Literature Review

2.1 Introduction

In this chapter, the pertinent literature on various aspects of the present flow configuration is reviewed. Because of its enormous applications and complex fluid flow phenomenon involved, the problem of a jet in a crossflow has been studied extensively both experimentally and computationally during the last many decades. The early investigation of the problem started in 1930s (Schlichting and Andew 1933). There are several review papers on this topic including those by Margason (1993), Holdeman (1993), Sherif and Pletcher (1990) and Acharya et al. (2001). The problem has been studied extensively under different perspectives by different groups of researchers. An attempt has been made to categorise these perspectives in the present chapter. A historical perspective of the research reported in the literature on jets in crossflow is described in Section 2.2. The coherent structures are the integral part of the flow field of jets in crossflow. In Section 2.3 the different vortical structures are reviewed. The present investigation concerns the rectangular jets in crossflow and therefore the difference of flow structures between circular and non-circular jets in crossflow are discussed in Section 2.4. A discussion of some specific studies concerning the significance of different parameters such as the physical dimensions of the slot, multiple jets, angular jets, impinged jets in crossflow, etc, is presented in Section 2.5. A review of investigations on the heat transfer characteristics and scalar mixing in case of jets in crossflow is presented in Section 2.6. In Section 2.7 the important numerical studies of jets in crossflow are discussed and finally the conclusions of the literature survey are presented in Section 2.8.

2.2 Historical Perspective of Studies

The earliest studies of jet in crossflow were concerning the gross flow behaviour, such as, the jet trajectory, jet penetration, jet spreading, mean velocity fields, and effect of the cross-sectional shapes of the nozzle using the empirical methods (Keffer and

Baines, 1963, Pratte and Baines, 1967, Abramovich, 1963). Little was known then about the non-stationary phenomena and the coherent structures of the jet, which are related to the mixing and entrainment. Some early studies of jets in a crossflow were reported by Ruggeri and Callaghan in a series of publications (Callaghan and Ruggeri 1948, 1951, Ruggeri et al., 1950, Ruggeri, 1952). In these studies the effects of changing the shape of the orifice and of heating the jet on a 2D flow were reported. Jordinson (1956) was the first to determine experimentally the trajectory of the jet, which is defined as the axis of the line joining the points of the maximum velocity and demonstrated that the cross-section of an initially cylindrical jet is distorted by the shear flow into a horseshoe shape. Gordier (1969) used the photographic techniques to geometrically determine the trajectories of jets of air-water mixtures discharging into a water channel. Keffer and Baines (1963) used oil-vapour and nitrogen aerosol for the qualitative visual investigations of an air jet injected in a low velocity wind tunnel. From the experimental observations, Pratte and Baines (1967) established the equation of jet trajectory in terms of the flow variable.

$$\frac{y}{RD} = A(x/RD)^B \tag{2.1}$$

Where D is the diameter of jet and A = 2.05, B = 0.28. Fan (1967) introduced the effect of a stratified atmosphere and suggested a mathematical model based on the resistance caused by the smoke jet in the flow. Abramovich (1967) established the expression for circular jets discharged at oblique angles into the crossflow using the empirical method. Platten and Keffer (1968) suggested a model taking into consideration of the two entrainment effects occurring in a deflected jet.

There have been numerous investigations on the jet in crossflow leading to the perception that the flow fields of jet in crossflow possess some difficulties in contrast to other flows like free jets and mixing layers. One main difficulty is that the flow field cannot be described in terms of its self similarity and Reynolds number dependence, due to the strong nonlinear effects. The systematic analysis of the jet in crossflow started in 1970s with the discovery and acceptance of coherent structures that are able to explain various nonlinear effects in the flow field of jet in crossflow. The majority of the studies reported in the 1970s and 1980s were motivated by V/STOL related applications and several flow visualization and experimental studies (Mcmahon et al., 1971, Kamotani and Greber, 1971, 1972, Moussa et al., 1977, Fearn and Weston, 1978, Schetz, 1980, Rajaratnam and Gangadhariah, 1981, Foss, 1980,

Crabb et al., 1981, Andreopoulos and Rodi, 1984, Andreopoulos 1985, Sykes et al., 1986, Coelho and Hunt, 1989) were conducted to understand the characteristics of the jet-crossflow interactions. These studies exemplified the transverse jet dynamic effects by providing detailed experimental data on the mean and statistical characteristics of the flow field. Their measurement of axial velocity decay and the distribution of the turbulence intensity along the jet axis showed that the fluid entrainment and mixing process is more intensive for this flow field compared to that occurring in a free jet. The studies by Rajaratnam and Gangadhariah (1981) gave emphasis to the volume flux and entrainment characteristics of the deflected jets. The augmentation of entrainment was reflected by the larger entrainment velocity obtained in their investigation. A more complete survey was conducted by Crabb et al. (1981), who measured the mean and fluctuating velocity magnitudes with a Laser-Doppler anemometer near the jet exit and hot wires further downstream. The most referred work on jets in crossflow is that by Andreopouios and Rodi (1984), who reported a series of hot-wire measurements in the flow generated by a jet issuing from a circular outlet in a wall into a cross-stream along the wall and analyzed these in terms of the mean and turbulent flow characteristics. They commented on the extremely complicated nature of the flow in deflected jets, which they characterized by the ratio of the mean velocity in the jet orifice to a representative velocity of the crossflow. Andreopoulos and Rodi (1984) identified two pairs of trailing contra-rotating vortices with opposite senses of rotation, a dominant primary pair bound within the deflected jet and a weaker secondary pair close to the wall in the wake of the jet, the bound pair having upflow through the centre of the jet and the wall pair having central downflow. This topographical description of the deflected jets was valuable, but Andreopoulos and Rodi (1984) were unable to provide any satisfactory explanation of the flow structure.

After 1990s, the attention of researchers has shifted towards the characterization of the organized large-eddy motions (coherent structures) of this flow by means of flow visualization, numerical simulation, and pattern recognition analysis of hot-wire data. Specific studies such as area-wise (near- and far-fields) investigations are made. Several experimental studies have been reported in the literature dealing with the flow near the jet exit region and the effects of different parameters on the penetration of the jet (Licinsky, et al., 1996, Haven and Kurosaka, 1997, Zaman and Foss, 1997). The flow visualization studies include the visualization of the wake (Fric and Roshko,

1994) and of the counter-rotating vortex pair (Morton and Ibbetson, 1996, Blanchard et al., 1999). Along with accurate experimental techniques, advanced turbulence models such as direct numerical simulation (DNS) and large eddy simulation (LES) are also used to investigate the flow configuration. Rudman (1996) performed the first direct numerical simulation to predict the time-dependent behavior of a weakly compressible axisymmetric jet exiting normally into a crossflow. Yuan et al. (1999) used LES to study turbulent flow conditions. Eiff et al. (1995) and Eiff and Keffer (1997) used the pattern recognition to study the coherent structures in a jet in crossflow issuing from an elevated exhaust stack. They observed that the wake behind the stack synchronizes with the pseudo-wake of the jet and that some sort of structural connection exists in the far-field between the pseudo-wake and the jet core.

In the present decade (from the year 2000 till date) the number of reported investigations of this flow configuration is quite encouraging. The number of investigations reported in the literature using the advanced experimental techniques such as particle image velocimtery (PIV) and advanced turbulence models such as DNS and LES is continuously increasing with time. Most of the studies deal with the advanced analysis of unsteady flow field, vortex evolution, mixing enhancement and scalar distribution in the flow field. Some important works are reported by Hale et al. (2000), Hoda and Acharya (2000), Kassimatis et al. (2000), Walter and Leylek (2000), Zhang (2000), Cortelezzi and Karagozian (2001), Keimasi and Rahni (2001), Lim et al. (2001), Rivero et al. (2001), Kalita et al. (2002), Peterson and Plesniak (2002), Johnston et al. (2002), New et al. (2003), Kolar et al. (2003), Naraynan et al. (2003), Said et al. (2003), Shi et al. (2003), New et al. (2004), Su and Mungal (2004), Sau et al. (2004), Peterson and Plesniak (2004), Wegner et al. (2004), Pathak et al. (2005), Said et al. (2005), Plesniak and Cusano (2005), Yang and Wang (2005), Mupidi and Maheshan (2005), Guo et al. (2006), Shan and Dimotakis (2006), Jovanovic et al. (2006), Majander and Siikonen (2006), Pathak et al. (2006), Muppidi and Mahesh (2007) and Pathak et al. (2007).

2.3 Studies of Vortical Structures in the Flow Field

Vortical flow evolution in the flow field of a jet in crossflow has been of considerable interest for a long time and the subject of several investigations. We have already

mentioned in Chapter 1 (Fig. 1.2) that four types of vertical structures are formed in the flow field of jets in crossflow. These four structures can be classified broadly into two categories as:

(1) Class 1 structures

(2) Class 2 structures

The class 1 structures are formed by the interaction of the jet with the crossflow and the wall and are not observed in free jets. Among structures of this kind, the following three types of vortices are included.

(i) Horseshoe vortices

(ii) Wake vortices

(iii) Counter-rotating vortex pair (CRVP)

The class 2 structures are observed in free jets also, but in the flow field of jets in crossflow, their vorticity content, evolution and destabilization are in some way influenced by the presence of the crossflow. Jet-shear-layer vortices are structures of this kind.

2.3.1 Horseshoe Vortices

The formation of a horseshoe-type vortex, around surface mounted obstacles in a uniform stream was reported by several investigators (Baker, 1979, Thomas, 1987, Seal et al., 1995, Sau et al. 2003). The presence of similar horseshoe-type vortices upstream of transverse jets, resulting from the interaction between the jet and the upstream crossflow boundary-layer was experimentally observed by Andreopoulos (1985), Shang et al. (1989), Krothapalli et al. (1990), Fric and Roshko (1994), Kelso and Smits (1995), Morton and Ibbeston (1996), Kelso et al. (1996) and numerically by Kim and Benson (1993), Chiu et al. (1993) and Rudman (1996). All the above investigations were for round jets in crossflow. It was observed that the approaching crossflow wall boundary layer, while encountering an adverse pressure gradient ahead of the jet, separates to form the horseshoe vortices. These vortices wrap around the base of the jet and travel downstream. Kelso et al. (1996) visualized the roll-up mechanism on the upstream side and the vortex breakdown on the downstream side of the horseshoe vortex. Krothapalli et al. (1990), Kelso and Smits (1995), and Rudman (1996) studied how these vortices relate to the shear layer roll-up and the shedding of vortices in the wake of the jet. The horseshoe vortex system can be very complex,

with the number of upstream separation points depending on Reynolds number and the relative magnitudes of the crossflow and jet velocities. The observations made by Kelso and Smits (1995) further reveal that the behaviour of a horseshoe system, can be steady, oscillating, and coalescing, depending on a combination of values of the important flow parameters, such as the Reynolds number and the jet to crossflow velocity ratio. Their results also suggest a strong connection between the unsteadiness in the horseshoe vortex system.

2.3.2 Wake Vortices

The wake vortices are initiated by the entrainment of the crossflow boundary-layer into the wake and the upward re-orientation of the entrained flow into the wake structures. The wake system is the least understood system in the jet in crossflow and has received special attention in many studies. A false or pseudo-wake, with an almost null deficit of the momentum develops downstream of the jet. Experiments and DNS/LES studies of jets in crossflow (McMahon et al., 1971, Fric and Roshko, 1994, Rudman, 1996, Kelso et al., 1996, Morton and Ibbetson 1996, Yuan et al. 1999) have shown that alternate vortices are shed for Reynolds numbers in the range $500 \leq Re = vu_a/D \leq 1000$ and jet-to-crossflow velocity ratio R = 3-4, in a way similar to the Karman vortex street formed behind cylinders or solid bluff bodies.

Fric and Roshko (1994) used the smoke-wire technique to visualize the flow field of a round jet in crossflow in a wind tunnel and showed that fluid coming from the wall boundary layer, and shed regularly from the leeward side of the jet, can be detected in the wake as ascending vortices. They found no evidence that the fluid coming from the jet was shed into the wake. Eiff et al. (1995) studied a thermally contaminated round jet issuing from a stack using hot-wire anemometry. The spectral analysis of the temperature signals in the wake showed that the hot fluid was present in the wake with an almost periodic organization. Some contradiction seems to exist between these results and those of Fric and Roshko (1994). Nevertheless, it should be noted that in air the diffusion of smoke ($Sc > 1$) is smaller than the diffusion of heat, which closely follows the diffusion of vorticity ($Pr \approx 1$). The studies of Kelso and Smits (1995) reveal that the origin and formation of the vortices in the wake are fundamentally different from the well-known phenomenon of vortex shedding from

solid bluff bodies. Instead, the wake vortices have their origins in the laminar boundary layer of the wall from which the jet issues.

2.3.3 Counter-Rotating Vortex Pair (CRVP)

The far-field structures of the jet in crossflow that have received most of the attention of researchers are the counter-rotating vortex pair (CRVP). The CRVP are an important feature of the flow, which begin to take form in the near-field of the jet and become dominant in the far-field, where they appear synonymous with the jet. The CRVP is undoubtedly the most studied structure, due to its robustness and distinct appearance in the flow field. All studies seem to indicate that, irrespective of the velocity ratio, the Reynolds number or other parameters (shape of the nozzle, laminar or turbulence boundary-layer, thickness of the boundary-layer, etc.), the counter-rotating pair of vortex is present thus indicating an essential feature of the flow. However, the instantaneous photographs or numerical simulations of the flow by Smith et al. (1993), Smith and Mungal (1998) and Yuan et al. (1999) show that the symmetrical CRVP is an artefact of the averaging process since the instantaneous velocity field does not contain a symmetrical vortex pair. In addition, Zaman and Foss (1997) and Smith and Mungal (1998) have found that, despite the accurate control of the experimental conditions, sometimes it is difficult to obtain a symmetrical mean velocity field in the far region.

The creation of the counter-rotating vortex pair is still disputed and many hypotheses exist upon the formation of the counter-rotating vortex pair. Notably, a number of experimental and numerical investigations have been carried out to identify the origin of inception of the CRVP. Andreopoulos and Rodi (1984) stated that for velocity ratios ($R < 0.5$) the CRVP is generated by the interfacial shear between the jet and the crossflow. Fric and Roshko (1994) reported that the CRVP is formed by the shear layer vorticity in the flow field. Kamotani and Greber (1972) suggested that the vortex pair is created in the wake behind the jet, while Crabb et al. (1981) claimed that the CRVP can be visualized upstream of the injection hole and that the pressure gradient in the near hole region is responsible for the formation of CRVP. Broadwell and Breidenthal (1984) compared the formation of the CRVP to the vortex formed by a wing in the air and concluded that a lift force is imparted on the boundary-layer by the penetrating jet forming the CRVP.

Morton and Ibbetson (1996) presented a detailed description of the CRVP production mechanism, suggesting that the puncturing of the wall boundary-layer by the jet creates the CRVP, whose azimuthal vorticity reorients, forming the two vortices. Yuan et al. (1999) proposed that the CRVP originates from the quasi-steady vortices on each lateral edge of the jet. These vortices encounter an adverse pressure gradient as they approach the lee side of the jet and break down into the CRVP. Walters and Leylek (1997), in a computational study of the streamwise injected jets, concluded that the two mechanisms that produce the CRVP are the interaction of the jet with the cross-stream and in-hole vorticity. They further concluded that the in-hole vorticity was the more significant of the two production mechanisms. Kelso et al. (1996) suggested that the roll-up of the jet-shear-layer is the mechanism that creates the CRVP, while Hale et al. (2000) hypothesized that the CRVP is formed by the roll-up of the boundary-layer fluid outboard of the jet and is intensified in the near jet region by the jet momentum.

Leylek and Zerkle (1994) while simulating the experiments of Pietrzyk et al. (1988) computed in-hole counter-rotating vortices of the same rotational sense as the primary CRVP in addition to the standard downstream vortex pair. Kohli and Thole (1998) performed calculations of a jet supplied by a plenum and were able to produce in-hole velocity fields containing either a pair of vortices or a single vortex. In both cases, the CRVP developed downstream of the injection, implying that the CRVP is not simply an in-hole vortices advected into the free stream. Furthermore, Lemmon et al. (1999) determined from an Euler inviscid computation that a CRVP forms downstream of an injection hole without any in-hole vorticity supplied and slip along the surface, i.e., no boundary-layer vorticity. The genesis and development of a counter-rotating vortex pair was very well explained by Lim et al. (2001). Their experimental findings indicate that as soon as the developed cylindrical vortex sheet emerges out of the jet pipe, in the presence of the crossflow, it immediately gets folded up on both lateral edges to form the CRVP. Rivero et al. (2001) observed that the CRVP is not a steady feature of the jet in a crossflow, rather the intensity of the two counter-rotating vortices fluctuates strongly with time.

2.3.4 Jet-shear-Layer Vortices

The jet-shear layer vortices are the near-field features of the developed flow field of a jet in a crossflow. The growth of instability-induced leading edge shear layer vortices along the jet/crossflow interface is a very noticeable flow structure, as it continues to dominate the initial portion of the jet. The studies conducted by Fric and Roshko (1994), Kelso et al. (1996), and Lim et al. (2001) for a round jet in crossflow confirm the existence and growth of such shear layer vortices on the initial portion of the jet. These large-scale structures are either similar to those formed in the shear layer of a round free jet under the Kelvin Helmholtz instability or to the horseshoe vortices formed at a cylinder wall junction. The roll-up process of the shear layer in the jet in crossflow occurs both along the upstream and downstream sides. These vortices are generated due to the Kelvin-Helmholtz like instability of the annular shear layer emanating from the jet orifice (Yuan et al., 1999). On the upstream side the evolution of the shear layer vortices is more evident, clearer and occurs over a larger time scale than that on the downstream side. This is so because in the latter these vortices break down and the mixing processes are very fast, and the roll-up takes place within a couple of diameters.

2.4 Non-circular Jets in Crossflow

Much of the previous studies on jets in crossflow have been carried out using a circular jet, and the number of investigations on non-circular jet is small. This may be due to the relative ease of making an experimental facility with circular jets than that for non-circular jet. While most studies on jets in crossflow concentrated their efforts on the circular jet geometry, it is believed that jets of other geometries can also be of immense potential, especially in the area of passive mixing. Previous studies have shown that even in the free jet configuration, non-circular geometries (i.e., square, rectangular and elliptic) exhibit higher mixing rates than that in a circular geometry (Grinstein et al., 1995). Unlike circular jets, non-circular jets usually possess a large variation in the momentum thickness of the boundary-layer along the jet exit perimeter, often resulting in highly 3D flows even in a simple free-jet configuration. This is especially true for jets with corners such as square and rectangular jets, where resolving the highly complex 3D resultant flows remains a continuing effort of

researchers. The early studies of non-circular jets in crossflow are reported by Ruggeri et al. (1950), Weston and Thames (1979), Wu et al. (1988) and Kavsaoglu et al. (1989) where the information of deflected jet trajectories, pressure distribution and the qualitative information about the associated vortices are found. Weston and Thames (1979) compared the pressure field around rectangular and circular jets. They found that a streamwise-oriented slot generates a pressure profile similar to that of a round jet.

Several researchers have observed that the structure of the flow field of square jets in crossflow is nearly identical to that of a round jet in crossflow. Humber et al. (1993) experimentally investigated the flow field of a sharp-edged rectangular jet with an aspect ratio (the ratio of length and width of the jet slot) of 10 and velocity ratios of 2.0 and 3.4. They observed that the jet trajectory exhibits the initial high penetration region similar to a round jet, followed by a region further downstream, where the trajectory is proportional to the streamwise distance. According to them

$$y\alpha\left(\frac{s}{RD}\right)^{0.17} \tag{2.2}$$

Where s is the distance along the streamwise direction. They found the initial jet penetration height similar to that in the case of the round jet. They also observed high levels of entrainment indicated by the mean decay and scalar concentration. Liscinsky et al. (1996) observed the similarity of the flow field between the square jet and round jet in crossflow in terms of the mixing effectiveness. Findlay et al. (1996) studied experimentally the flow behaviour of a row of inclined 30^0 square jets at low velocity ratios (R = 0.5, 1.0 and 2.0). They found that the outward spread of the jet is not affected as greatly by velocity ratio as for vertical jets. Haven and Kurosaka (1996) pointed out that higher-aspect ratio jets have lower trajectories, owing partly to the decreased degree of interaction between the counter-rotating vortex-pairs. Kavsaoglu et al. (1989) also observed this phenomenon.

Sivadas et al. (1997) studied the exit geometry effect on the growth of the cross sectional area of the transverse jets for a range of the velocity ratios. They observed that the initial mixing of the transverse jet can be enhanced by increasing the jets bluntness with respect to the crossflow. Jets having a large frontal area with respect to a crossflow are devoid of horse shoe flow pattern and the wake vortex system in its cross section. This is in contrast to the behaviour of a deflected circular jet.

The different vortical structures, present in the flow field of round jet in crossflow are also reported in the flow field of square jet in crossflow (Sau et al., 2004, Findlay et al., 1996, Ajersch et al., 1997, Hoda and Acharya, 2000, Keimasi and Rahni, 2001). Haven and Kurosaka (1997) conducted a series of experiments to investigate the effects of jet geometry on film cooling, and one of the cases they considered was an elliptic jet in crossflow. While they have uncovered certain flow differences between the elliptic and circular jet geometries, their findings are restricted to very low velocity ratio only, with maximum velocity ratio of 2, since they were primarily interested in the situation where the deflected jets stay close to the cooling surface. They also observed that for rectangular jets the amplitude of the CRVP depends on the aspect ratio of the jet section. The investigation of elliptic jets in crossflow by New et al. (2003) have shown that with the major axis of the ellipse aligned with the crossflow, the flow field does not deviate significantly from that of circular jet in crossflow as long as $R < 3$. Moreover for flow conditions with $R < 3$, the vortex-pairing phenomenon of the leading-edge vortices was found to dominate the near-field. They also investigated quantitatively through a series of PIV measurements the leading-edge vortex-pairing phenomenon exhibited by the streamwise elliptic jet in the crossflow when the $R \geq 3$.

Recently Plesniak and Cusano (2005) studied the scalar mixing in a confined rectangular jet in a crossflow. They observed that the flow is more complex than a canonical unconfined round jet in crossflow. They also observed that the large scale CRVP structures dominate the scalar mixing of the jet stream and crossflow stream. They made another important observation that the flow field is asymmetric.

2.5 Specific Studies on Different Parameters

In this section we review some literatures that study the effects of different parameters such as the velocity ratio, injection angle, plenum geometry, etc., on the flow structures.

2.5.1 Effect of Velocity Ratio on the Flow Field

We have already discussed in Chapter 1 that the velocity ratio (R) is an important parameter for this flow configuration. Indeed the flow regime can change, depending on value of R. The jet often exhibits several behavioural zones as the trajectory varies from the minimum to maximum due to the variation of the velocity ratio from small to large values. Sherif and Pletcher (1990, 1991) have pointed out that the velocity ratio of 2 should be a borderline case between high and low velocity ratio jet behaviour.

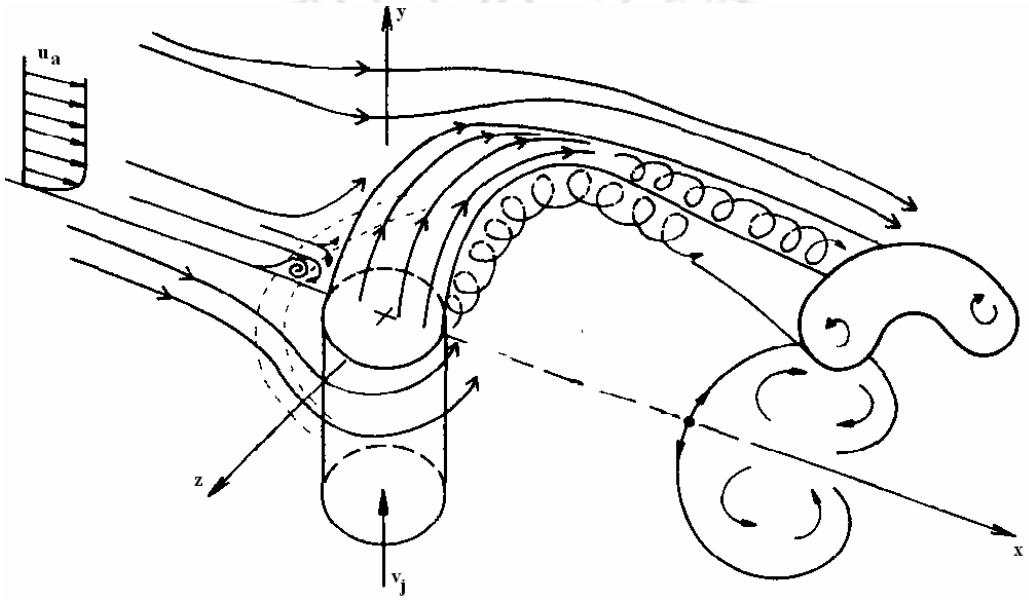

Fig. 2.1: Flow development and streamlines of jet in crossflow with a high velocity ratio ($R > 2$).

Lim et al. (1992) observed that the changing velocity ratio from 1 to 5.5 produced two distinctly different flow structures. At a high velocity ratio $R > 2$, the jet penetrates significantly into the crossflow and it bends over far enough downstream of the injection hole. Therefore for these types of jets, there is little influence of the wall on its development. Moreover there is a little effect of the crossflow boundary layer characteristics on the flow for high values of R as the jet is able to penetrate through a relatively thin boundary-layer. The flow development and associated streamlines of jet and crossflow for a high velocity ratio are shown in Fig. 2.1. On the other hand for low velocity ratios, i.e., $R < 1$, the jet bends over into the wall at a small downstream distance and then it spreads over the wall. There is a lack of the wake region downstream of the jet injection hole and the jet behaves like a wall jet. In this type of

situation, the jet flow is unable to cross the crossflow boundary-layer thus producing less complex flow behaviour in the near-field of the jet compared to that with a high value of *R*. The flow development and associated streamlines of jet in crossflow for a low velocity ratio are shown in Fig. 2.2. For $1 \leq R \leq 2$, the jet seems to be in an intermediate regime, in which the jet can reattach to the injection wall.

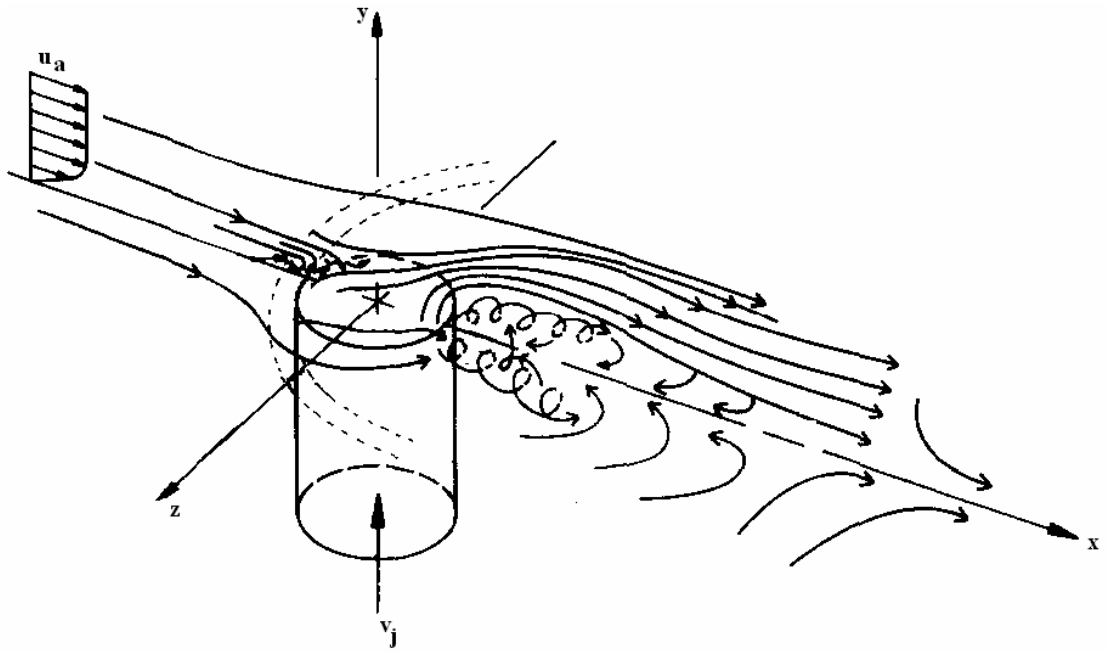

Fig. 2.2: Flow development and streamlines of jet in crossflow with a low velocity ratio ($R < 1$).

Most of the studies of jets in crossflow are for the velocity ratio in the range of 0.5 to 2. The numerical investigations by Brittingham and Leylek (2000), Hyams and Leylek (2000), McGovern and Leylek (2000), Walters and Leylek (2000) are based on velocity ratios of $R = 1.25$ and $R = 1.88$. Hardly any detailed study dealing with small velocity ratios, i.e., ratios in the range of $R < 0.5$ has been reported in the literature. Recently Guo et al. (2006) investigated the flow field for a very low velocity ratio $R = 0.1$ and 0.48 using LES. They also studied the effects of the jet inclination angle and the velocity ratio *R* on the flow structures. The increase of the jet velocity enables the jet to penetrate deeply into the crossflow, resulting in a more upstream located and stronger CRVP. Downstream of the jet exit the recirculation zone is so large that the jet fluid and partially also the crossflow fluid are entrained into the reverse flow region.

Andreopoulos and Rodi (1984) observed that at relatively low velocity ratios in the range of $R \geq 0.5$ the cooling jet did not cover the complete exit hole. The impact of

the jet hole arrangement, the velocity ratio, and the density ratio was investigated by Baldauf et al. (1999). Their findings conclude that the best cooling efficiency occurs at $0.85 \leq R \leq 1.0$. The recent experimental investigation of Peterson and Plesniak (2005) deals with jets into crossflow at velocity ratio $R \geq 0.5$. However, their main objective is the impact of short holes and channel feed orientation, unlike the subject of the present work.

To understand the vortex structure in the vicinity of the jet hole, Kelso et al. (1996) performed hot-wire measurements for the velocity ratio $R =$ 2 to 6. They observed that the velocity ratio may not yield a global view of the jet flow field, since the resultant flow is more wake-like than jet-like because of the dominance of the crossflow. The velocity ratios higher then 10 have different features as they behave more and more like free jets with increasing velocity ratios.

2.5.2 Rectangular Skewed Jets in Crossflow

Among most of the reported works of the rectangular jet in crossflow, the jet slot is placed perpendicular to the crossflow, i.e., the length of the jet slot is perpendicular to the crossflow direction (90^0 skew angle). A jet positioned skewed to the crossflow direction can be used as a vortex generator. Zhang (2000) performed an experiment with rectangular inclined jet positioned with different skew angles in a flat plate boundary-layer flow as the crossflow. He used a pitch angle (angle made by the jet plenum with crossflow) of 30^0 and used different skew angles ranging from 0^0 to 135^0 at intervals of 15^0. The velocity ratio used was one for each case. He investigated the effect of the skew angle and streamwise development of vortices and compared the streamwise development vortices with that in a round jet. He observed that for skew angle of 90^0 (general configuration) the rectangular jet produces streamwise vortex of higher strength than that of a round jet while keeping the same size and shape as that of a round jet in crossflow. An increase of 63% in the maximum vorticity was observed. The 45^0 skew angle was identified as the optimal skew angle for the vortex production.

2.5.3 Angular Jets in Crossflow

In many practical applications the jet is injected at an inclination to the vertical direction such as in turbine blade cooling processes and combustion chambers. Burd et al. (1996) reported hydrodynamic measurements of a 35° streamwise injection jet for the injection hole length to diameter ratios (*L/D*) of 7.0 and 2.3. They found significant differences in the penetration of the jet into the crossflow and the region of influence downstream of the jet. This study was extended by Burd and Simon (1998) to investigate the effect of the jet flow in plenum. They used the same *L/D* (*L* denotes the length of the plenum and *D* the diameter of nozzle) ratios as in previous work. They investigated, the experiment with a plenum height of 2*D* for coolant flow co-current to the crossflow (the direction of the coolant flow in the plenum is same with the crossflow direction) and counter-current to the crossflow (direction of the coolant flow in the plenum is opposite to the crossflow direction). Significant differences in the surface film cooling effectiveness values in the near hole region were found as the plenum flow direction was opposite. These results contradicted the numerical results of Berhe and Patankar (1996), which indicated the effect of the plenum flow direction to be negligible for *H/D* = 2 (*H* denotes the height of the plenum). In a continuation of this effort, Burd and Simon (1998) reported discharge coefficients and turbulence spectra and length scale data for the same cases. Recently Yang and Wang (2005) performed a 3D numerical simulation of the fluid flow and heat transfer characteristics for an inclined jet with crossflow impinging on a heated plate. They studied the effect of the inlet temperature of the crossflow, the velocity ratio (values in the range 3–7) and the injected angle. They observed that the heat transfer enhancement can be found over a wider spanwise region as the velocity ratio is increased. The peak value of the Nusselt number was located around a spanwise location at z/*D* = 4 and it was caused by the upwash region supplying fresh fluid to the near region of the target plate surface. The generation of a pair of counter-rotating longitudinal vortices was clearly observed from the computations. They observed that the heat transfer enhancement can be attained over wider spanwise region as the velocity ratio value was increased. The analysis provided a fundamental insight into the complex heat transfer characteristics for an inclined jet in a crossflow.

2.5.4 Opposite Jets in Crossflow

In most of the work of jets in crossflow, the jet is discharged normally into the crossflow from one direction, generally from the bottom side of the crossflow. Atkinson et al. (1982) experimentally studied the flow field of two opposite jets discharged normally into a crossflow from both bottom and top sides of the crossflow. Holdeman and Srinivasan (1984) predicted non-isothermal mixing in a confined crossflow, where a single row and opposed rows of jets were injected. Chen and Hwang (1991) investigated the mixing of heated jets injected normally from the two sides into a cold crossflow, in which detailed velocity measurements were made. They observed that the flow structure is more complex in the case of two jets compared to the single jet in crossflow. Chang and Chen (1994) investigated experimentally the effect of the jet incident angle on the mixing of opposing heated line jets with a confined crossflow. The same work was performed numerically by Chang and Chen (1995) using the standard k-ε model. From both the studies they observed that as compared to the case of one-sided line jet, the opposing jets result in a higher turbulence kinetic energy and better thermal mixing effects. That is, a more uniform temperature profile can be achieved in a shorter distance by the opposing jets, especially at higher velocity ratio and incident angle. This is important, for example, in the design of dilution zone length in the gas-turbine combustors, in which the size and the cost of the combustion chamber can be reduced. It is believed that even better mixing can be achieved if opposing jets are set at different streamwise locations.

2.5.5 Multiple Jets in Crossflow

While majority of literatures have studied single jet in crossflow in detail, the literature on the multiple jets in crossflow is relatively scarce (Holdmann and Walker, 1977, Makihata and Miyai, 1979, Gregoric et al. 1982, Isaac and Jakubowski, 1985, Karagozian et al., 1986, Savory and Toy, 1991, Barata et al., 1991). These papers bring useful information predominantly on the global characteristics such as the jet path or vortex trajectory, on multiple or confined multiple jets in crossflow by varying the number of jets in a row, or considering specific geometrical configurations of nozzles. Some of the works reviewed here for multiple jets in crossflow have included the effect of the impingement which we will discuss in Section 2.5.7. Barata et al.

(1991) examined the characteristics of vortex and upwash flows generated by twin jets in a crossflow. Karagozian et al. (1986) considered the motion of a vortex pair issuing from the jet orifice and discharged into the crossflow. From their analytical study they derived the trajectory of the jet in terms of the velocity ratio and some constants. According to them trajectory is given as

$$\frac{y}{D} = \alpha R^{\beta} (x/D)^{\gamma} \tag{2.3}$$

Where $\alpha = 0.527, \beta = 1.178$ and $\gamma = 0.314$. Chuang et al. (1992) used 2D numerical model to determine the flow characteristics associated with an unsteady, compressible impinging twin slot jets between two plates coupled with the crossflow. Kim and Benson (1993) employed a turbulence model to simulate the 3D impingement of multiple jets with crossflow. Their results presented that the row of jets in the crossflow is characterized by a highly complex flow field that includes a horseshoe vortex and two helical vortices whose secondary velocity components are co-rotating in space.

Kolar et al. (2003) experimentally studied the dominant vortical structure and the associated turbulence vorticity transports of twin jets in crossflow using the standard crossed hot-wire anemometry technique. They measured the mean flow velocity vector and associated turbulence statistics using two geometrically symmetric twin jets in the crossflow arrangements, namely, tandem and side-by-side (both with a nozzle centre-to-centre separation of 5*D*). They observed that the two arrangements under consideration have their own specific features in terms of the formation and decay of these dominant vortical structures. They showed how the tandem and side-by-side twin jets in crossflow differ in terms of the properties of the resulting mean-flow CRVP, namely vorticity distribution, vortex strength (circulation), transverse penetration ability (inferred from the trajectory of the peak vorticity region), and intensity of vorticity transport and of the associated circulation decay rate.

2.5.6 Geometry of Jet Plenum

We have already reviewed some studies reporting different shapes of the nozzle geometry and their effects on the flow field. Several papers report the effects of the jet plenum geometry on the flow field of jets in crossflow. The first study to address a narrow flow plenum was conducted by Wittig et al. (1996) who presented preliminary

results for an experimental and numerical study of a single jet in crossflow fed by a narrow plenum (H/D = 2, where H denotes the height of the plenum and D the diameter of the nozzle). The work was extended by Thole et al. (1997), Gritsch et al. (1997), and Kohli and Thole (1998). In this series of studies, the authors investigated the difference of the flow structures due to channels feeding the film cooling holes and the narrow plenum introduced by Berhe and Patankar (1996). The implications of these studies are well summarized by Kohli and Thole (1998). Pietrzyk et al. (1989), Sinha et al. (1991), Sen et al. (1994) and Kohli and Bogard (1995) investigated different aspects of the film cooling performance for short injection holes ($L/D \leq 4$, where L denotes the length of the plenum). The holes were supplied by a large, low-speed reservoir, or plenum, which fed normal to the film cooling hole. Various short hole numerical studies by Walters and Leylek (1997), Berhe and Patankar (1996) have used the above experimental measurements as the benchmark for their numerical results. Peterson and Plesniak (2002, 2004) examined the influence of the supply plenum configuration. Averaged results of the flow field in all the three planes were presented. They found that the plenum feed direction has an influence on the flow field.

Johnston et al. (2002) observed that the inlet geometry changes significantly near-field and does not have a large influence on the far-field. Recently Jovanovic et al. (2006) experimentally investigated the influence of a small hole geometry variation on the jet crossflow interaction using the particle image velocimetry (PIV) and liquid crystal thermography. The experiments were conducted without and with the hole imperfection at three different velocity ratios. If the imperfection was absent, the flow field was stable and the clockwise vortices were detected downstream. The imperfection blocked the hole, accelerated the jet and changed the formation of large vortical structures. It produced the additional windward vortices, which influenced the flow field and enhanced the inflow of the crossflow towards the cooled surface. The imperfection reduced the film cooling effectiveness.

2.5.7 Impinging Jet in Crossflow

Several researches have studied the effect of the crossflow on the heat transfer characteristics of impinging turbulent jets (Metzger and Korstad, 1972, Bouchez and Goldstein, 1975, Sparrow et al., 1975, Saad et al., 1980, Goldstein and Behbahani,

1982, Al-Sanea, 1992, Barata, 1996). The numerical result of Al-Sanea (1992) on single jet combined with crossflow showed that a crossflow degrades the favourable characteristics of impinging jet. The impingement of confined single and twin turbulent jets through a crossflow was studied experimentally and numerically by Barata et al. (1996) to examine the characteristics of vortex and complex flows generated by the multiple jets in a crossflow. Nakabe et al. (1998) studied various aspects of the jet impingement heat transfer under the influence of the crossflow and observed that the Nusselt number distribution became a plateau-like pattern, which means that the enhanced region of heat transfer expanded more than the case of impinging jets without crossflow.

San and Lai (2001) investigated experimentally the configuration of five confined circular air jets in staggered arrays vertically impinging on a flat plate. An optimum ratio of jet-to-jet spacing was obtained. Heat transfer from a discrete heat source to multiple, normally impinging and confined air jet was experimentally investigated by Garimella and Schroeder (2001). They performed numerical simulations to gain insight into the fluid flow and heat transfer characteristics of inclined jet with crossflow impinging on a heated plate. The effect of the jet to crossflow velocity ratio on the flow and thermal fields were investigated.

2.6 Studies of Heat Transfer and Scalar Distribution

In most practical situations, jets and plumes are either discharged vertically or at an angle to a crossflow. In such flow conditions the jet and crossflow interaction and thermal spread are extremely important factors. The flow behaviour and heat transfer analysis of a heated jet in crossflow are reported by several researchers (Kamotani and Greber, 1972, Holdman and Walker, 1977, Andreopoulos, 1982, Wark and Foss, 1988, Chen and Hwang, 1991, Sherif and Pletcher, 1991, Nishiyama et al., 1993, Sarkar and Bose, 1995, Hwang and Chiang, 1995, Sherif and Pletcher, 1998, Shi et al., 2003 and Said et al., 2003). Most of these studies provided detailed correlations for predicting the temperature distributions and the relevant parametric variations downstream of the jets discharged normally from one side into the confined crossflow. Holdman and Walker (1977) predicted the temperature distribution downstream of a row of jets injected normally into a confined crossflow of hot fluid.

Chen and Hwang (1991) experimentally studied a 2D heated plane jet in a crossflow, where the jet was confined in a channel. In this flow configuration, the jet injected from a narrow slot developed between the two sidewalls of the channel, without any clearance between the jet and walls. They reported about the two-dimensionality of the flow field, especially at the centre of the slot.

Sherif and Pletcher (1991) made an experimental investigation of a round heated jet in crossflow for different velocity ratios of 1, 2, 4 and 7. They analysed the jet wake thermal characteristics for those velocity ratios. They found the difference of the flow behaviour for small velocity ratios ($R < 2$) and large velocity ratios ($R > 2$). They observed the existence of a double vortex structure in the flow field for both the velocity ratios, but weaker in strength in small velocity ratio. Based on their results, they suggested that the velocity ratio $R = 2$ should be a borderline between the high and low velocity ratios. Nishiyama et al. (1993) reported the characteristics of temperature fluctuations in a slightly heated 2D jet issuing through a slot normally into a crossflow for different velocity ratios and they studied the effects of the velocity ratio on the mean and fluctuating temperature fields. They observed that the low velocity ratio jets behave like a wall jet and the high velocity ratio jets are lift-off jets with a recirculation region. They also derived a relation of the decay characteristics of the maximum temperature. The decay characteristics are represented in a following equation, where m means the slope of the decay.

$$\frac{T_{\max} - T_{\alpha}}{T_j - T_{\alpha}} = (s.D/R^2 - s_D.D/R^2)^{-m} \tag{2.4}$$

Where $T_{\max}$ is the maximum temperature, T_j is the jet temperature at the centre line and T_{α} is the crossflow temperature. The distance along streamline is s and s_D is the distance of the jet along streamline. Said et al. (2003) performed numerical investigation of a round heated jet in crossflow using different turbulence models. They reported the distribution of the velocity and temperature fields and mass fraction of different constituents of the jet. They observed that the velocity field fully controls the dilution of temperature and concentration of the jet. They also found a better performance of the Reynolds stress transport model compared to the two-equation models.

Like heated jets in crossflow some authors have also investigated the flow field of a cold jets in a warmer crossflowing ambient. The cold jets in hot crossflow may have

sinking trajectories when the buoyancy forces are dominant. Sherif and Pletcher (1998) performed the experimental investigation of cooled jets discharged into heated crossflowing ambient in a water channel. They presented the results in the region of jet and wake thermal regions in terms of the mean and root-mean-square temperature fluctuations profiles. They also compared the results with the heated jets discharged into cold crossflow. They observed similar temperature profiles in the region of jet discharge as in the case of heated jet in cold crossflow and farther downstream of jet discharge, the agreement between the two was poor.

The investigation of the scalar field of transverse jets has received somewhat less attention than the velocity and vorticity fields. Mean scalar fields were experimentally measured by Andreopoulos and Rodi (1984) and Niederhaus et al. (1997). Niederhaus et al. (1997) applied planar laser-induced fluorescence (PLIF) to obtain the scalar concentration fields in the cross-sections of the crossflowing jets in water, with velocity ratio R = 4.9 to 11.1. While applying PLIF in air-into-air crossflowing jets, Smith and Mungal (1998) mapped the concentration field in cross-sectional planes, the symmetry plane, and in planes parallel to the jet exit plane, for the velocity ratios ranging from 5 to 20. They also measured the vortex interaction region, mean trajectories and concentration decay, and overall structural features of mixing of a round jet in a crossflow. Su and Mungal (2004) provided a comprehensive view of the scalar and velocity fields in the developing region of the crossflowing turbulent jet in the gas phase, using planar imaging techniques. Simultaneous planar measurements of scalar mixing and 2D velocity fields permitted the detailed study of the developing region of turbulent crossflowing jets with velocity ratio R = 5.7. The results show that the intensity of the mixing, as quantified by the scalar variance and the magnitude of the turbulence scalar fluxes, is initially higher on the jet windward side, but eventually becomes higher on the wake side. Plesniak and Cusano (2005) performed an experimental investigation of a confined rectangular jet in crossflow to investigate the scalar mixing. They performed the systematic variation of three pertinent parameters, i.e., the momentum ratio, injection angle and development length. They observed the three regimes (wall jet, fully lifted jet and reattached jet) for the jet crossflow interaction and the resulting concentration field. The combined scalar concentration and velocity field data provided an understanding of the large-scale mixing and the role of coherent structures and their evolution. Recently Shan and Dimotakis (2006) investigated the Reynolds number dependence of the scalar mixing by examining the

probability distribution of the jet fluid in strong liquid-phase transverse jets at a fixed far-downstream location. In their study, the high-Schmidt-number mixing was compared between transverse jets and ordinary jets to investigate possible differences in the mixing for the fully developed (but finite Reynolds number) turbulent flows.

2.7 Numerical Studies

Since the present work uses a numerical technique to investigate the flow field of rectangular jets in crossflow, important numerical works reported in the literature are discussed in this section.

2.7.1 Integral Models

The first elaborate calculation procedures applied to predict the behaviour of jets in crossflow were the integral models in which the integral equations were derived either by considering a balance of forces acting over an elementary control volume of the jet or by integrating in two spatial dimensions, the three-dimensional partial-differential equations governing the flow. Abramovich (1963) developed such a model for predicting the trajectory of a jet in a crossflow by assuming that the momentum of the jet in the direction normal to the crossflow was preserved and that the pressure difference across the jet was balanced by the centrifugal force due to its curvature. Fan (1967) developed an integral model incorporating the effects of the drag forces and entrainment for buoyant jets in crossflow and obtained fairly good agreement with his experimental data. Chien and Schetz (1975) proposed a more elaborate model, which took into consideration the effects of the drag forces, entrainment, buoyancy, axial pressure gradient, turbulence shear stress between the jet and crossflow fluid, and heat transfer due to the forced convection from jet to crossflow fluid. Model predictions showed relatively good agreement with the experimental data.

2.7.2 RANS Models

In the 1980s, with the rapid advances in computational resources and with the development of better and faster algorithms, finite difference methods began to replace integral methods for investigating fluid flow problems. Most numerical investigations of jet in crossflow after 1975 involved the solution of the Reynolds-averaged Navier-Stokes (RANS) equations and the energy equation on a finite difference grid, with closure for turbulence quantities obtained through a turbulence model.

The majority of the RANS simulations for jet in a crossflow have employed a variant of the standard k-ε model (originally proposed by Launder and Spalding, 1974) to obtain the distribution of the eddy viscosity. Patankar et al. (1977) were among the early researchers to use this model to perform a detailed study of the jet in a crossflow, and even with a relatively coarse grid (15×15×10), observed reasonable agreement with the experimental data for the jet trajectory and streamwise velocity. Demuren (1983) investigated the grid resolution requirements for a row of jets in a crossflow. Results on a 37×70×14 grid (37 in the streamwise, 70 in the vertical and 14 in the spanwise directions) were shown to be grid independent and captured experimental trends fairly well. Claus and Vanka (1990) used a refined grid (256×96×96) and the k-ε model and found that they could not capture the horseshoe vortex. Kim and Benson (1993) employed a multiple-time-scale turbulence model to perform a detailed analysis of the flow field of a row of jets in a confined crossflow. The horseshoe structure was predicted correctly using a non-uniform 165×59×80 grid and the good agreement was attributed partly to the multiple-time-scale model used in their study.

In a series of investigations, Garg and co-workers systematically studied the effects of turbulence models (Garg, 1999) and the hole physics (Garg and Gaugler, 1997a, 1997b, Garg and Rigby, 1999). Garg (1999) numerically predicted the behaviour of a film-cooled, rotating turbine blade. His computational domain included the blade on a rotor with five rows containing 93 film cooling holes. He used three different turbulence models (Wilcox's k-ω, Coakley's q-ω, where q is the square root of turbulence kinetic energy and the Baldwin-Lomax model) in the numerical investigations and compared his results with the experimental data of Abhari (1991). Overall, the k-ω model appeared to provide the best agreement with the

measurements, particularly on the pressure side of turbine blades. Garg and Rigby (1999) used the Wilcox's k-ω turbulence model, and found that the coolant velocity and temperature profiles at the hole exit did not conform to the commonly used parabolic or $1/7^{th}$ power law distribution. Leylek and Zerkle (1994) were the first to model the flow within the coolant supply plenum and film hole in addition to the crossflow. They found that the flow upstream of the jet exit plane was quite complex with a considerable influence on the coolant jet exit conditions. The jet exit conditions influenced the subsequent downstream behaviour and overall film-cooling performance.

Ajersch et al. (1997) performed detailed measurements of multiple square jets injected normally into a crossflow and carried out an accompanying numerical simulation using a multi-grid, segmented, CFD code using standard k-ε model. Their predictions and measurements did not compare well for the velocities and stresses on the jet centerline, while values off the centerline matched those of the experiments much more closely. A numerical study of the discrete-hole film cooling was conducted by Berhe and Patankar (1996) on a 3D film cooling geometry that included the main flow, injection hole and the plenum. Walters and Leylek (1997) presented a systematic computational methodology for investigating the flow field of a jet in crossflow, in which each critical aspect of simulation was addressed. They performed systematic investigation of the key numerical issues, including accurate computational modeling of the physical problem, exact geometry and high-quality grid generation techniques, higher-order numerical discretization, and accurate evaluation of turbulence model performance.

Walters and Leylek (2000) in a computational study of streamwise injected jets, concluded that the two mechanisms that produce the CRVP are the interaction of the jet with the freestream and in-hole vorticity. They discussed in the detail the effect of various variables like velocity ratio, density ratio, hole length, plenum height, plenum flow direction and turbulence level at the inlet. Berhe and Patankar (1999a, 1999b) extended their flat plate studies and included the effect of the curvature using a Richardson type correction and a two-equation model. The standard k-ε and the two-layer k-ε turbulence models were used by Lakehal et al. (1998) for investigating the film cooling effectiveness of a flat plate by a row of laterally injected jets. Hoda and Acharya (2000) compared seven different turbulence models for film cooling flows

and concluded that the Lam-Bremhorst (1981) formulation provided the best comparison with the measurements.

There are few literatures reporting the use of RST model for the investigation of the flow field of jet in crossflow. Inze and Leschziner (1990, 1993) carried out an investigation using a high-Re Reynolds stress transport (RST) model employing wall functions in order to avoid solving the Reynolds stresses all the way to the wall. Demuren (1993) also reported predictions with a high-Re RST model using a multigrid method and obtained fairly good prediction of the mean flow trends. Alvarez et al. (1993) compared the k-ε model predictions with the RST model predictions for velocity ratios of 2.35 and 5. They concluded that both models result in a similar level of agreement. Jansson and Davidson (1996) applied the near-wall corrections to the basic linear model and solved a low-Re RST model to predict effusion cooling in a double-row discrete-hole configuration and reported better predictions than those by a two-layer k-ε model. Hoda et al. (2000) used two different formulations of the RST model and did not find any significant improvements in the predictions using the RST model. Hale et al. (2000) used commercial flow solver FLUENT to study the surface heat transfer associated with a row of short-hole jets in a crossflow. They used a RST model with the non-equilibrium wall functions and a two-layer zonal approach and found a better performance by two-layer zonal method than that by the RST model. The investigation performed by Hale et al. (2000) was for the multiple round jets in a crossflow. However, no work on the study of plane jet in crossflow using RST model has been reported in the literature.

2.7.3 DNS and LES

The simulation of a transverse jet constitutes a challenge for any numerical technique as the nature of the flow field is in general 3D and unsteady. Therefore either direct numerical simulation (DNS) or large eddy simulation (LES) can capture the flow field in an accurate way.

Jones and Willie (1996) presented the results of LES of plane jets in crossflow on a 87×30×30 mesh. The Reynolds number based on the jet velocity and the nozzle width was 5815 and the velocity ratio was 7.34. LES was performed by Wille (1997) for the experimental conditions of Crabb et al. (1981). He used both a coarse mesh and a fine mesh, which included 88440 and 997920 elements, respectively. Considering the

Reynolds number of 46700 based on the jet bulk velocity and the jet exit diameter, both grids are quite coarse even if the near-wall boundary layers are modelled. Wille (1997) did not explicitly state whether the value of the Reynolds number was the same as in the experiments of Crabb et al. (1981).

Yuan and Street (1998) examined the trajectory and entrainment characteristics of a round jet in a crossflow using LES at Reynolds numbers of 1,050 and 2,100 based on the jet diameter and freestream velocity. The simulations were performed for jet to crossflow velocity ratios of 2.0 and 3.3 on grids using 1.34×10^{6} elements (also Yuan et al., 1999). Yuan et al. (1999) performed LES at two jet-to-crossflow velocity ratios, 2.0 and 3.3, and two Reynolds numbers, 1050 and 2100, based on the crossflow velocity and the jet diameter. They discretized the computational area into a total of 1.34×10^{6} control volumes. Schluter and Schonfeld (2000) compared the results of LES with experimental velocity profiles of Andreopoulos and Rodi (1984) and scalar fields of Smith and Mungal (1998) and obtained reasonable agreement. They observed that the LES reproduced the large-scale coherent structures observed experimentally and their results suggested that the wake vortices seen in the wake of the jet are related to the horseshoe vortices upstream of the jet.

Wegner et al. (2004) studied turbulence mixing using LES. They varied the angle between the jet and the crossflow and observed that the mixing was enhanced as the angle was increased, i.e., as the jet was directed against the crossflow. The baseline flow in their simulation was that measured by Andreopoulos and Rodi (1984). Recently Guo et al. (2006) and Majander and Siikonen (2006) investigated the flow field of jets in crossflow using LES. Guo et al. (2006) investigated the flow field for very low velocity ratios R = 0.1 and 0.48. They also studied the effects of the jet inclination angle and the velocity ratio R on the flow structures. They observed that an increase of the jet velocity enabled the jet to penetrate deeply into the crossflow, resulting in an upstream located and stronger CRVP. Downstream of the jet exit the recirculation zone was so large that the jet fluid and partially also the crossflow were entrained into the reverse flow region. Majander and Siikonen (2006) performed the study for a round jet in crossflow for the velocity ratio of 2.3 at a Reynolds number of 46,700, based on the jet bulk velocity and the jet diameter. They performed the LES using both the steady and unsteady boundary conditions. They observed that the LES with the unsteady condition possesses a stronger back-flow in the lee side of the jet

and increases the mixing of the passive scalar compared to that using the steady boundary conditions. The LES reproduced many phenomena present in the flow, such as the shear layer vortices and the counter-rotating vortex pair. They observed a reasonable agreement with the experimental measurements of Crabb et al. (1981).

Rudman (1996) performed the first direct numerical simulation (DNS) to predict the time dependent behavior of a weakly compressible axisymmetric jet exiting normally into a crossflow. He captured the jet-shear layer vortices in the simulation formed due to the Kelvin-Helmholtz instabilities. However the horseshoe vortex system was not captured in the simulation due to an insufficient grid resolution. He captured the formation of wake vortices for the first time in a numerical simulation of jets in crossflow and observed that that the vorticity in the wake system originates in the crossflow boundary layer upstream of the jet exit. His numerical observations were consistent with the experimental observations of Fric and Roshko (1994). Hahn and Choi (1997) presented unsteady simulations of circular jets in crossflow using second order spatial schemes with 14.6×10^{6} grid points at a Reynolds number of 1750 (based on the jet velocity and the duct width) for a momentum ratio of 0.5. Sharma and Acharya (1998) presented the results from direct numerical simulation of a rectangular coolant jet injected normally into a periodic crossflow using a high order spatial discretization on a 128×64×64 grid for a channel Reynolds number of 5600 and momentum ratio of 0.25.

Sau et al. (2004) performed the DNS to predict the 3D, unsteady flow interactions in the near-field of a square jet issuing normal to a crossflow. The simulated flow features reveal the formation of an upstream horseshoe vortex system, which was the result of an interaction between the oncoming channel floor shear layer and the transverse jet. They observed the growth of a unsteady sequence of Kelvin-Helmholtz instability-induced vortical rollers in the mixing layer between the jet and the crossflow, which wrap around the front side of the jet to form the jet-shear layer vortices. They could also observe the inception process of the counter-rotating vortex pair (CRVP), which is initiated through the folding of the lateral jet-shear layers. It has been observed that for a square jet in a crossflow, the developed Kelvin-Helmholtz instability induced shear layer rollers do not form closed circumferential vortex rings. Along the downstream side of the jet, the extended tails of such rollers gradually join the locally evolving CRVP.

Recently Muppidi and Mahesh (2005) carried out DNS calculations of round jets in crossflow on an unstructured mesh. The simulations were performed at two velocity ratios 1.5 and 5.7. By varying the crossflow boundary-layer thickness and the jet velocity profile, they showed that the trajectory depends on both these parameters. A jet with a higher centreline velocity issuing into a crossflow with a thicker boundary layer penetrates deeper compared to other jets at the same jet-to-crossflow velocity ratio. The jet trajectory was shown to be determined by the near-field of the jet exit.

More recently Muppidi and Mahesh (2007) used direct numerical simulation to study a round turbulent jet in a laminar crossflow for the velocity ratio of 5.7 using the experimental conditions of Su and Mungal (2004). They observed the 3D nature of the flow field, involving with a wide range of scales of motion. They observed the phenomena of deformation of the jet, from a circular cross section to a kidney shape which is due to the flattening of the trailing edge of the jet close to the jet discharge. From an examination of turbulence kinetic energy budget they showed that the flow was not in turbulence equilibrium. The near-field was characterized by higher productions of kinetic energy than the dissipation rate along the jet edges and the reverse values along the jet centre. Jet and crossflow fluid interaction in the near-field caused peak production of the turbulence kinetic energy on the leading edge of the jet.

2.7.4 Vortex Method

Some authors have used vortex methods to investigate the 3D evolution of the vortex in the flow field of a jet in crossflow (Coelho and Hunt, 1989, Cortelezzi and Karagozian, 2001). Vortex methods are particularly useful in simulating unbounded, incompressible, unsteady flows where the fluid containing vorticity occupies only a small fraction of the total fluid volume. Vortex methods permit accurate, gridless simulation of the evolution of the vorticity field. An inviscid 3D vortex sheet model was used to study the near-field flow in the vicinity of the orifice of a transverse jet by Coelho and Hunt (1989). The vortex sheet model included a distribution of sinks as well as vortices, used to simulate the complex distortion of the vorticity field as well as the entrainment just above the injection wall. Cortelezzi and Karagozian (2001) performed transient numerical simulations of the flow field of jet in crssflow using 3D vortex elements. They observed the vortex ring rollup, interactions, tilting, and folding of the vortices in the near-field, which were consistent with the experimental

observations of Kelso et al. (1996). They also observed that the jet penetration as well as the periodicity is associated with the rollup, folding, and interaction with prior and new vortex ring structures which are seen to be dependent on the specific flow conditions, including the jet velocity, crossflow velocity, and upstream boundary-layer thickness.

2.8 Conclusions

In this chapter an extensive review of important works pertaining to the investigations of the flow field of jet in crossflow is presented. From the comprehensive literature review, the following conclusions can be drawn:

(i) Numerous studies, both experimental and numerical, investigating the flow fields of jets in crossflow have been reported in the literature.

(ii) Most of the studies are concerning single jet in crossflow and a few studies are concerning multiple jets in crossflow.

(iii) Most of the studies are for low velocity ratio (less than 2).

(iv) Most earliest studies of jet in crossflow were concerning the gross flow behaviour, such as, jet trajectory, jet penetration, jet spreading, etc.

(v) With the advancement of technology in both experimental and numerical fields, several new features of the flow field were analyzed in the literature such as the effects of the velocity or momentum ratio, jet injection angle, skew angle, multiple jets, jet spacing, jet geometry, jet Reynolds number, impingements and scalar mixing, etc. These studies extended the analysis of the flow field from the basic flow properties to the formation of different vortices, turbulence mixing and concentration studies.

(vi) Though a variety of different geometries have been studied during the past few decades, a relatively few studies on the rectangular jet in crossflow have been reported in the literature and even fewer on the jet in a narrow crossflow channel have been reported. Furthermore, to the best knowledge of the present author, no numerical or analytical work has been carried out for the problem of jets in a narrow channel crossflow for high velocity ratio. The present work intends to fill this gap through the current investigation.

भारतीय प्रौद्योगिकी संस्थान गुवाहाटी
Indian Institute of Technology Guwahati

Chapter 3

Two-Dimensional Jets in Crossflow

3.1 Introduction

In this chapter, the results of the numerical investigations of 2D flow field of jets in crossflow are presented. The governing equations, the turbulence models and numerical methods used for the investigation of 2D flow field are also discussed in this chapter.

As discussed in Chapter 1, the flow field of a turbulent jet in crossflow is basically 3D owing to the presence of large coherent structures, strong pressure gradients across the jet, and the effects of sidewalls. However, a 2D investigation of certain areas of the flow field can give useful information of the flow structures. Generally 2D investigations are performed in the central vertical plane of the jet slot, considering that there are no variations of flow properties normal to this plane. Such a jet is termed as a plane jet and the flow field is called a plane jet in crossflow. The 2D flow fields are reported by Ramaprian and Haniu (1983), Haniu and Ramaprian (1989), Chen and Hwang (1991), Jones and Wille (1996), Hahn and Choi (1997) and Kassimatis et al. (2000). Ramaprian and Haniu (1983) and Haniu and Ramaprian (1989) observed that the two-dimensionality of the velocity field is maintained within 12% of the jet slot around the central spanwise region. They observed less than 5% variation of the velocity in the spanwise direction in the flow field, ranging from the jet discharge point up to forty times the jet slot width along the streamline direction. However, further downstream the flow tends to loose its two-dimensionality due to the effects of the sidewalls. Chen and Hwang (1991) also observed that the temperature and velocity fields exhibit good two-dimensionality in the spanwise direction away from the sidewalls. Thus when the channel is not narrow, a study of the 2D flow field can represent sufficient characteristics of the flow field. Moreover as stated by Hahn and Choi (1997), it is reasonable to explore the flow structures of the flow field by investigating a rather simple and less time consuming situation, such as a 2D flow field.

The flow field of turbulent jet in crossflow is characterized by streamline curvature, which occurs not due to the geometry of the flow field, but due to the interaction of the jet with the crossflow. The effect of the streamline curvature on turbulence is a well established phenomenon and numerous literatures (Bradshaw, 1969, Moser et al., 1986, Holloway and Tavoularis, 1992) are available describing the effect of streamline curvature on turbulence for the wall bounded flows. Experimental studies reviewed by Bradshaw (1969) show that the magnitude of the turbulence shear stress and the degree of anisotropy between the normal stresses are sensitive to the streamline curvature. Curvature strongly influences the production as well as the transport in shear layers. Due to the streamline curvature, there evolves an extra rate of strain in the flow field besides the main strain rate. Another important aspect of the flow field, which may have significant influence on turbulence, is the presence of the moving stream external to the jet. For numerical predictions of such complex flow fields, direct numerical simulation (DNS), large eddy simulation model (LES) or the use of Reynolds stress transport (RST) model and anisotropy-resolving non-linear eddy-viscosity model can provide a satisfactory flow field. However, being relatively simpler and computationally more efficient, two equation models (k–ε, k–ω) have been extensively used for the prediction of such flow fields with varying degrees of success (Sarkar and Bose, 1995, Hoda and Acharya, 2000, Keimasi and Rahni, 2001, and Kalita et al., 2002). Kalita et al. (2002) used the standard k–ε model to investigate the 2D flow field and compared their predictions with the experimental work of Ramaprian and Haniu (1983) and Haniu and Ramaprian (1989) at the central vertical plane of the jet slot and reported a moderate success and this was one of the motivations of the present work. An effort is made in the present work to improve the numerical predictions of the flow field by considering the effect of streamline curvature on the flow field.

Numerous modifications have been proposed in the literature to account for the effect of streamline curvature in the formulation of the standard k–ε model. The streamline curvature modification made to the standard k–ε model, originally proposed by Leschziner and Rodi (1981) for axisymmetrical flow configuration was used by Kassimatis et al. (2000) to investigate the aerodynamics of the near-slot film cooling which represents the flow field of jet in crossflow. Kassimatis et al. (2000) reported a slight improvement in the predictions in the recirculation region of the

flow. Since the geometry of the present work is rectangular and the flow field of the jet in crossflow is characterized by the local curvature effect, the streamline curvature modification to the standard $k-\varepsilon$ model proposed by Cheng and Farokhi (1992) has been used. In this modification, the algebraic formulation of the eddy viscosity ν_t is done by extracting the extra strain rate and the main strain rate for the flow field with streamline curvature. This correction leads to a significant reduction in the eddy viscosity around the separation streamline, i.e., in the curved shear layer bordering the recirculation region. Moreover, the model is simpler and computationally more efficient than the RST model or non-linear eddy-viscosity model.

Cheng and Farokhi (1992) used the model to study the backward-facing step flow and observed significant improvement in the results compared to those using the standard $k-\varepsilon$ model. In the present work both the standard $k-\varepsilon$ model and streamline curvature modification to the $k-\varepsilon$ model proposed by Cheng and Farokhi (1992) are employed to predict the flow field of plane jet in crossflow for the values of R = 6 and 9 and the predictions are compared with the experimental measurements of Ramaprian and Haniu (1983) and Haniu and Ramaprian (1989). Section 3.2 describes the problem formulation and Section 3.3 describes the numerical procedures. The predictions of the mean and turbulence quantities and their comparisons with the measurements have been reported in Section 3.4, followed by conclusions in Section 3.5.

3.2 Problem Formulation

In this section the descriptions of computational domain, governing equations, turbulence models and boundary conditions used for the numerical investigation of the 2D flow field of jets in crossflow are discussed. The general practice of making use of 2D investigation is that it should be a fair representation of the conditions along the central plane of the configuration. This can be considered when the spanwise distance is very large. In the present work, the 2D investigation may be considered as referring to the central vertical plane of the flow field, where the experimental data is available.

3.2.1 Computational Domain

A schematic of the computational domain for the present work for R = 6 is shown in Fig. 3.1. The left boundary from which the crossflow enters the domain is positioned sufficiently away upstream from the jet discharge slot as suggested by Amer et al. (1992) and the right boundary is placed sufficiently away downstream from the jet source, such that the zero gradient condition for all the variables can be applied there (Sykes et al., 1986). The bottom boundary is the wall from which the jet emanates and the top boundary is placed sufficiently away from the bottom so that the free stream conditions can be applied there (Hwang and Chiang, 1995). In the crossflow direction, the computational domain extends from 10D (D is the width of the slot) upstream of the centre of the jet to 40D downstream. The appropriate size of the computational domain depends upon the value of the jet to crossflow velocity ratio (R). Clearly the separation between the top and bottom boundaries should increase with the value of R. This distance is selected in such a way as to make the aforementioned boundary conditions are applicable in the top boundaries. For example, for R = 6, a separation of 30D between the top and the bottom walls is considered. The domain sizes for different values of R as shown in Table 3.1 have been used in the present computations.

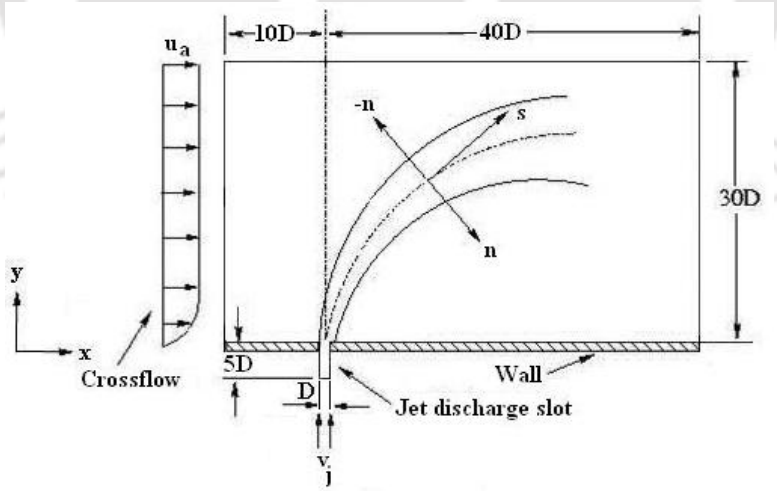

Fig. 3.1: Schematic diagram of the computational domain for R = 6.

Ramaprian and Haniu (1983) and Haniu and Ramaprian (1989) reported their experimental observations in the s-n coordinate system, where s- denotes the jet streamline direction and n- normal to it. The s-n coordinates are shown in Fig. 1.

Table 3.1: 2D Domain size for different values of *R*.

R	Normalized distance of the inlet from the centre of the jet slot (*x/D*)	Normalized distance of the outlet from the centre of the jet slot (*x/D*)	Normalized distance between the top surface and bottom wall (*y/D*)	Normalized length of the jet duct from the bottom wall (*y/D*)
6	10	40	30	5
9	10	50	40	5

3.2.2 Governing Parameter

The flow field of jet in a crossflow is strongly dependent on the momentum ratio defined as

$$J = \frac{\rho_j v_j^2}{\rho_a u_a^2} \tag{3.1}$$

where the subscripts *j* and *a* correspond to jet and crossflow, respectively. In the present work, the crossflow and the jet fluid are considered both to be water and therefore *J* is replaced by the velocity ratio as

$$R = v_j / u_a \tag{3.2}$$

From the literature review it is observed that few studies of turbulent rectangular jets in a narrow channel crossflow with a high velocity ratio have been reported. Since there are some reliable experimental results (Ramaprian and Haniu, 1983 and Haniu and Ramaprian, 1989) in some portion of the flow field (jet central plane) to compare the numerical results, we have chosen the velocity ratios of R = 6 and 9 in the present study. The width of the jet slot *D* is used as the unit length throughout the work.

3.2.3 Governing Mean Flow Equations

The 2D, steady-state, Reynolds-averaged Navier-Stokes equations constitute the governing equation of the mean flow. The equations for the incompressible fluid in the Cartesian coordinate system can be written as

Continuity:

$$\frac{\partial u}{\partial x}+\frac{\partial v}{\partial y}=0 \tag{3.3}$$

x-momentum:

$$u\frac{\partial u}{\partial x}+v\frac{\partial u}{\partial y}=-\frac{1}{\rho}\frac{\partial p}{\partial x}+\frac{\partial}{\partial x}(-\overline{u'^2})+\frac{\partial}{\partial y}(-\overline{u'v'}) \tag{3.4}$$

y-momentum:

$$u\frac{\partial v}{\partial x}+v\frac{\partial v}{\partial y}=-\frac{1}{\rho}\frac{\partial p}{\partial y}+\frac{\partial}{\partial x}(-\overline{u'v'})+\frac{\partial}{\partial y}(-\overline{v'^2}) \tag{3.5}$$

Here u and v are the mean velocities in the x- (cross-stream) and y- (jet discharge direction) respectively, and p is the mean pressure. The primed quantities represent fluctuation parts of the velocity.

3.2.4 Turbulence Models: Standard $k-\varepsilon$ Model

Eqs. (3.4) and (3.5) contain the Reynolds stress terms ($\overline{u'^2}$, $\overline{v'^2}$ and $\overline{u'v'}$), which need to be modeled by a suitable closure expressions. The accuracy of the predictions is based on the adequacy of the closure expressions in capturing the flow physics. The models used in the present work are the standard the $k-\varepsilon$ model and the $k-\varepsilon$ model with streamline curvature modification. In the standard version of $k-\varepsilon$ model, the turbulence stresses are modeled as

$$-\overline{u'^2}=2\nu_t\left(\frac{\partial u}{\partial x}\right)-\frac{2}{3}k \tag{3.6}$$

$$-\overline{v'^2}=2\nu_t\left(\frac{\partial v}{\partial y}\right)-\frac{2}{3}k \tag{3.7}$$

$$-\overline{u'v'}=\nu_t\left(\frac{\partial u}{\partial y}+\frac{\partial v}{\partial x}\right) \tag{3.8}$$

The eddy viscosity ν_t is related to the turbulence kinetic energy k and its dissipation rate ε as

$$\nu_t=c_\mu\frac{k^2}{\varepsilon} \tag{3.9}$$

Eqs. (3.6) – (3.8) represent a linear relationship between the turbulence stress and the rate of strain and form the basis of all linear two-equation models.

The distribution of turbulence kinetic energy (k) and dissipation rate (ε) in the flow field is determined from their modeled transport equations, which are

$$u\frac{\partial k}{\partial x}+v\frac{\partial k}{\partial y}=\frac{\partial}{\partial x}\left(\frac{\nu_t}{\sigma_k}\frac{\partial k}{\partial x}\right)+\frac{\partial}{\partial y}\left(\frac{\nu_t}{\sigma_k}\frac{\partial k}{\partial y}\right)+P_k-\varepsilon \tag{3.10}$$

$$u\frac{\partial \varepsilon}{\partial x}+v\frac{\partial \varepsilon}{\partial y}=\frac{\partial}{\partial x}\left(\frac{\nu_t}{\sigma_\varepsilon}\frac{\partial \varepsilon}{\partial x}\right)+\frac{\partial}{\partial y}\left(\frac{\nu_t}{\sigma_\varepsilon}\frac{\partial \varepsilon}{\partial y}\right)+C_{\varepsilon 1}\frac{\varepsilon}{k}P_k-C_{\varepsilon 2}\frac{\varepsilon^2}{k} \tag{3.11}$$

Where P_k is the rate of production of k and is given by

$$P_k=\nu_t\left[\left(\frac{\partial u}{\partial y}+\frac{\partial v}{\partial x}\right)^2+2\left(\frac{\partial u}{\partial x}\right)^2+2\left(\frac{\partial v}{\partial y}\right)^2\right] \tag{3.12}$$

The values of the model constants are: $C_\mu = 0.09$, $C_{\varepsilon 1}=1.44$, $C_{\varepsilon 2}=1.92$, $\sigma_k=1.0$, and $\sigma_\varepsilon=1.3$ (Launder and Spalding, 1974). In these formulations, the molecular viscosity is assumed to be negligible in comparison to the eddy viscosity.

3.2.5 Curvature Modification to the Standard $k-\varepsilon$ Model

Cheng and Farokhi (1992) derived the streamline curvature modification to the standard $k-\varepsilon$ model from the algebraic model proposed by Rodi (1976). In this modification the expression for the eddy viscosity is given as

$$\nu_t=\frac{k^2}{\varepsilon}\frac{2\phi}{3}\left[1-R_f-\phi\frac{P_k}{\varepsilon}\frac{R_f^2+R_f+1}{1-4R_f}\right] \tag{3.13}$$

Here ϕ is a model constant given by

$$\phi=\frac{1-C_2}{C_1-1+\dfrac{P_k}{\varepsilon}}$$

and $C_1=1.5$ and $C_2=0.76$ are the inertial and forced return-to-isotropy constants respectively. R_f is the flux Richardson number and given by

$$R_f=-\frac{\partial v/\partial x}{\partial u/\partial y} \tag{3.14}$$

The form of the flux Richardson number employed in the present work was used by Cheng and Farokhi (1992) for investigating the backward facing step flow, where the flow is predominant in the x-direction and is characterized by weak streamline curvature. The present work is also characterized by the weak streamline curvature

and the flow is predominant along the jet discharge direction in the mixing region. Hence though the flux Richardson number is not frame invariant, its application to the present flow configuration is justified as its implementation is simple and consistent with the physical nature of the flow. The flux Richardson number R_f plays an important role as it dictates the effect of streamline curvature on the turbulence structure through the amplification and diminution of the eddy viscosity. It easily follows from Eqs. (3.9) and (3.13) that

$$C_\mu = \frac{2\phi}{3}\left[1 - R_f - \phi\frac{P_k}{\varepsilon}\frac{R_f^2 + 4R_f + 1}{1 - R_f}\right] \tag{3.15}$$

Thus in this model the value of C_μ changes depending upon the value of R_f, which again is dependent on the streamline curvature. For flow with a high streamline curvature, the value of R_f becomes negative and the most destabilizing effect takes place at $R_f = -1/2$ (Piquet, 1999). Thus the correction (3.15) leads to a significant reduction in C_μ around the separation streamline, i.e., in the curved shear layer bordering the recirculation zone. Within this zone the value of C_μ would tend to zero or even change sign if a lower limit were not placed on its value. For the present case, the limit was chosen as 0.025. This value is taken as the basis that in regions where the value of C_μ is below 0.025, the concept of local equilibrium of turbulence stresses and energy on which the curvature correction is based can certainly not be expected to hold. When there is no local curvature effect, the value of $R_f = 0$ and the value of C_μ becomes 0.09, thus the model reduces to the standard *k-ε* model. Since both the turbulence models used in the present work are variants of the *k-ε* model, hereafter for simplicity and making it short, the model with streamline curvature modification to the standard *k-ε* model is termed as the curvature modification model.

3.2.6 Boundary Conditions

The different boundary conditions used in the present computations are inlet, outlet and wall. They are applied as follows

(i) **Left Boundary:** The conditions at the left boundary specified are the free stream conditions, i.e., the velocity along the jet direction is zero (v = 0) and crossflow is of a uniform velocity ($u = u_a$). The inlet boundary layer

thickness is set to *1.5D* to match the experimental conditions. Inside the boundary layer, the 1/7th power-law profile is used for the *u*-velocity component and a uniform velocity ($u = u_a$) is imposed above $y = 1.5D$. In the flow field of a turbulent jet in crossflow, considerable amount of turbulence kinetic energy is generated and the results are insensitive to the values of incoming turbulence kinetic energy via the crossflow for flow field especially with a high velocity ratio (Keimasi and Rahni, 2001). The value of the turbulence kinetic energy at the left boundary is taken from 5% turbulence intensity based on the experimental data ($k = 0.00375u_a^2$). The inlet turbulence dissipation rate is obtained from the expression suggested by Versteeg and Malalasekera (1996) as $\varepsilon = c_\mu^{3/4}(k^{1/2} / y_{\max})$, where y_{max} is the domain size in the *y* direction**.**

(ii) **Top Boundary:** It corresponds to a wall-free surface. Zero shear stresses and free stream boundary conditions are used here. Thus at the top boundary the same values of *u, v, k* and *ε* as those used, in the left boundary are used.

(iii) **Right Boundary:** At the right boundary, the normal gradients of all variables are assumed to be zero (Hoda and Acharya, 2000, Keimasi and Rahni, 2001) $\left(\frac{\partial f}{\partial x} = 0; f = (u, v, k, \varepsilon)\right)$.

(iv) **Bottom Boundary:** The whole bottom boundary, excluding the jet discharge slot, is considered as a solid wall, where the boundary conditions are applied using the standard wall functions. In this approach, an integration of the modeled equations right up to the wall is avoided and the universal behaviour of the flow variables is used to specify values at the first grid point adjacent to the wall. For velocity, the log-law is used, for the turbulence kinetic energy, a zero value is specified at the wall, while the value of dissipation at the near-wall point is set using a local equilibrium assumption as $\varepsilon = c_\mu^{3/4} k^{3/2} / (\delta y)$, where δy is the wall-normal grid spacing for the first grid point. The value of y_p^+ (the non-dimensional location of the first grid point from the wall) is taken as 11.3 (Versteeg and Malalasekera, 1996), above which the log-law is assumed to hold.

(v) **Jet Exit:** From the literature review (Catalano et al., 1989, Patankar et al., 1977 and Hwang and Chiang, 1995) it is found that in most of the numerical studies a uniform jet discharge velocity is used. Several researchers, for example Kassimatis et al. (2000) indicated that the assumption of a uniform velocity at the inlet of jet is not appropriate. For accurate prediction and to represent the actual experimental conditions it is better to include the jet slot into the computational domain. In the present study we have considered the jet slot (length $5D$) in the computational domain. The conditions at the entry to jet slot are $u = 0$ and $v = v_j$. The value of turbulence kinetic energy is taken from 6.5% turbulence intensity ($k = 0.00625 v_j^2$) and the value of dissipation rate is taken using the expression proposed by Versteeg and Malalasekera (1996) as, $\varepsilon = c_\mu^{3/4}(k^{1/2}/0.5D)$.

3.3 Numerical Procedure

All the terms of governing equations described in the previous section are non-dimensionalised with the mean jet velocity v_j and jet width D. Finite volume method is used to discretise the governing equations together with the boundary conditions specified in the previous section.

3.3.1 Computational Grids

A non-uniform grid is set up in the computational domain. The sides of the non-uniform control volumes along the x-direction are generated using the Eqs.3.16-3.17: For the upstream portion of the jet slot, the following relation is used

$$x_i = \frac{i}{i_{\max}} + \frac{\lambda}{\pi}\sin\left(\frac{\pi i}{i_{\max}}\right) \tag{3.16}$$

and for the downstream portion of the jet slot the following relation is used

$$x_i = \frac{i}{i_{\max}} - \frac{\lambda}{\pi}\sin\left(\frac{\pi i}{i_{\max}}\right) \tag{3.17}$$

The sides of the non-uniform control volumes along the *y*-direction are generated using the following relation

$$y_j = \frac{j}{j_{\max}} - \frac{\lambda}{\pi}\sin\left(\frac{\pi j}{j_{\max}}\right) \tag{3.18}$$

where *i* and *j* denote the spatial indices in the *x*- and *y*- direction respectively, i_{max} and j_{max} are their maximum values and λ is the clustering parameter. The value of λ used is 0.5. The grids are clustered near the wall in the *y*-direction as well as at the jet exit area in the *x*-direction. The distribution of the control volumes in the computational domain used for the prediction of jet in crossflow with $R = 6$ is shown in Fig. 3.2. In Fig. 3.2, the distribution of the fine mesh is shown. The fine mesh is fixed based on a grid independence study (Section 3.3.4). 172×143 (= 24596) control volumes (172 along the *x*-direction and 143 along the *y*-direction) excluding the jet duct area have been used in the fine mesh. The jet duct area comprises of 7×37 (= 259) control volumes. To avoid the occurrence of pressure oscillations in the domain, a staggered grid arrangement is employed in which the scalar variables (p, k and ε) are positioned at the centre of the control volume and the velocity components are positioned at the cell faces. The positioning of the variables is illustrated in Fig. 3.3.

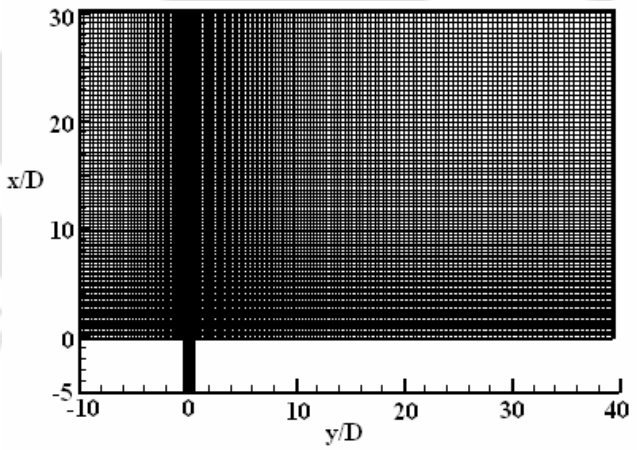

Fig. 3.2: Computational domain and finite volume grid for the jet with $R = 6$.

3.3.2 Computational Methodology

A finite volume computer code in FORTRAN 77 based on the SIMPLE algorithm (Patankar, 1980) has been developed to numerically to solve the governing equations. The momentum and the other transport equations are descritised using the power-law scheme (Patankar, 1980). A good discussion on use of various discretisation schemes

can be found in Patel and Markatos, (1986). Line-by-line iteration with alternating the sweep direction using tri-diagonal matrix algorithm is used to solve the system of linear algebraic equations.

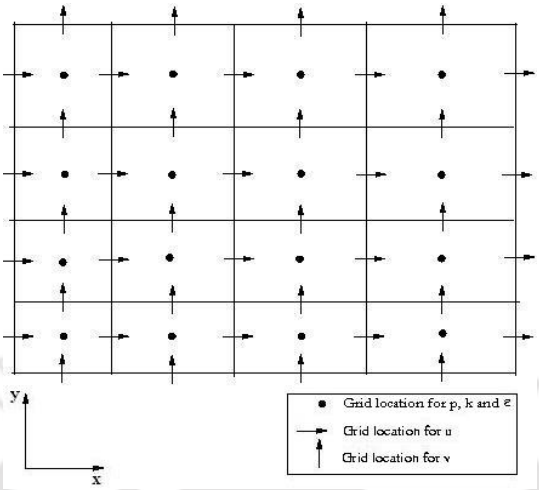

Fig. 3.3: Positioning of variables on the grid.

For any iterative process an initial guess of the unknown variables are made at the starting of the first iteration. In the computation through the curvature modification model, the initial guess is taken from the intermediate solution of the standard k-ε model for better convergence behaviour. All the variables (u, v, k and ε) are under-relaxed during each iteration. The typical values of under-relaxation parameters used are 0.3 for u and v and 0.45 for k and ε. The mass residual which represents the balance of mass in each cell is determined from the continuity equation. The mass residual is defined as

$$b = (u_w^* - u_e^*)\Delta y\Delta z + (v_b^* - v_t^*)\Delta x\Delta z + (w_s^* - w_n^*)\Delta x\Delta y \qquad (3.19)$$

Where the starred quantities (*) are the velocities before correction at each cell and subscript e, w, n, s, t and b denote the directions in east, west, north, south, top and bottom. The maximum mass residual is established as the criterion for assessing the overall convergence of the flow field. The convergence of the computation is assumed to be achieved and therefore iterations are terminated when the sum of the residual mass is less than 10^{-4} and the relative variation of variables u, v, k, and ε in the successive iteration is less than 10^{-2}. At the residual level mentioned above, the solution is found not to change for several iterations and therefore it is treated as the converged solution. Moreover the exit criterion for various equations has been taken

as $\left|\frac{\phi_i^{m+1} - \phi_i^m}{\phi_i^m}\right|_{\max} \leq 10^{-2}$, where ϕ_i represents the variable for which solution is sought.

The history of the residual fall in the numerical solution for the jet with R = 6 using the standard k- ε method is shown in Fig. 3.4. The mass residual shows some fluctuations initially with high amplitude and gradually it decays. This behaviour has no effect on the final converged solution. The residual fall history is likely to be influenced by the iteration exit criteria chosen for the variables. But to determine the exact nature of this influence, extensive numerical experiments need to be performed. The code was run on a special Linux server (16 node load clustering machine) with 8 GB RAM and 3G Hz processor speed and it took approximately 72 hours of CPU time for the full convergence of the flow field using the curvature modification model and 40 hours using the standard k- ε model.

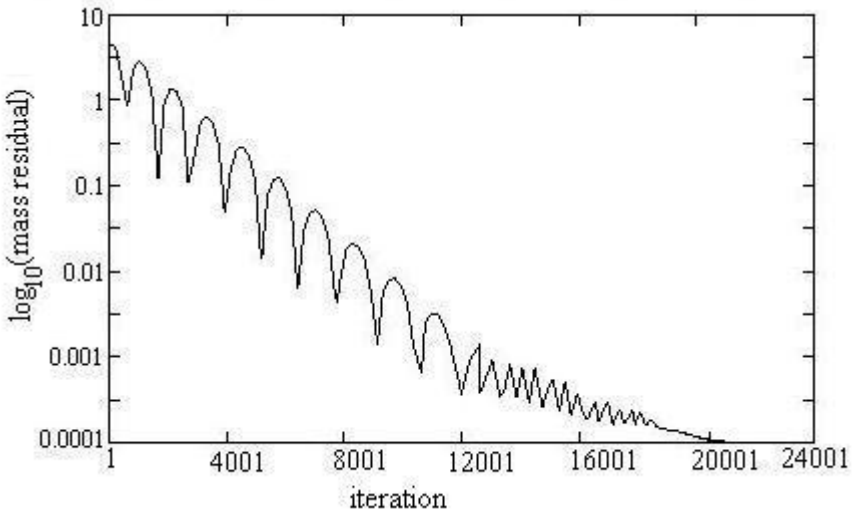

Fig. 3.4: Mass residual fall history for R = 6 (standard k-ε model).

3.3.3 Code Validation

The present code is validated against the results reported in the previous numerical studies of similar nature. The prediction of turbulence plane jets in a strong crossflow by Kassimatis et al. (2000) is used as a test case. Using streamline curvature modification model in the present code, the reattachment length and the streamwise velocity at the two different locations are compared for the jet with R = 0.8. Fig 3.5 shows that the present predictions of the streamwise velocity at two different locations at x/D = 2 and 9 agree well with those of Kassimatis et al. (2000).

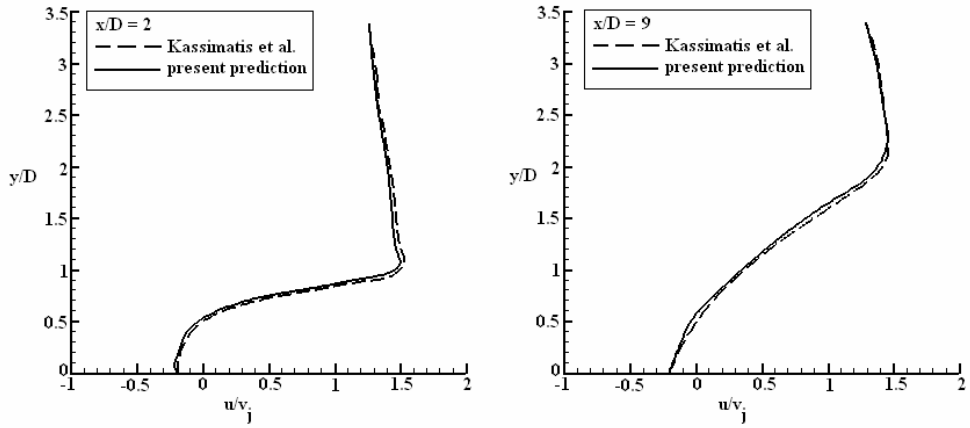

Fig. 3:5: Comparison of the present predictions using the curvature modification model with those of Kassimatis et al. (2000) for $R = 0.8$.

The recirculation region predicted by the present code for the value of $R = 0.8$ is shown in Fig. 3.6 and the comparison of the reattachment length by both the present code and by Kassimatis et al. (2000) is shown in Table 3.2. The difference between the two values is 4% and therefore the present code stands validated.

Table 3.2: Comparison of reattachment length.

Value of R	Reattachment length by present prediction (see Fig. 3.6)	Reattachment length by Kassimatis et al. (2000)
0.8	10.8	10.3

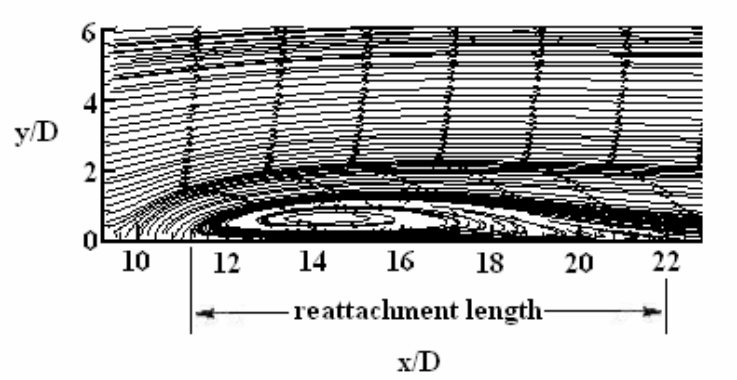

Fig. 3.6: Reattachment region predicted by the present code for $R = 0.8$.

3.3.4 Grid Sensitivity

The grid-independence test of the computations is performed with three different sets of grids, viz., 150×125 (150 along x-axis and 125 along y-axis), 172×143, and 300×240 and by comparing the prediction of the streamwise velocity for each grid for

R = 6. Similarly three different sets of grids, viz., 165×140, 200×165 and 330×250 are used for R = 9. The grids are non-uniform in both the directions and clustered near the wall and the jet source region. The velocity profile at x/D = 2 for R = 6 and 9 using the curvature modification model is shown in Fig. 3.7. It has been observed that the grid refinement in general improves the prediction by reducing the over prediction in the bottom part of the jet and increasing the peak value of the velocity. Moreover the results produced by the fine grid approach the experimental results (not shown in Fig.) than those by the other two grids. The difference between the predictions using the 2nd set and 3rd set grids is only 2%. The results that are presented in the subsequent sections are for the grid size 172×143 for R = 6 and 200×165 for R =9.

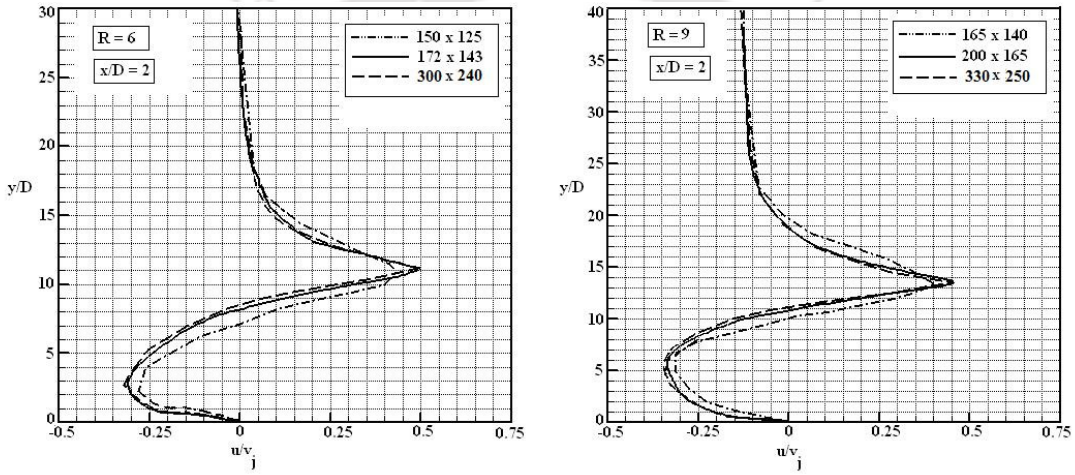

Fig. 3.7: Grid sensitivity test: Predicted profile of cross-stream component of velocity.

3.4 Results

The present computations of the mean velocity components, turbulence kinetic energy and turbulence shear stresses for the turbulent plane jet in crossflow are compared with the experimental data of Ramaprian and Haniu (1983) and Haniu and Ramaprian (1989), who reported their experimental observations in the *s*–*n* (*s*- along the streamline and *n*- normal to it) coordinate system (Fig. 3.1). They presented their results in the regions where the effect of the jet in the flow field is strong, i.e., few normalized distance along the upward and downward directions from the jet centre line. They did not present flow properties in the near-wall region. In the present work, the computations are performed in the Cartesian coordinates and the computed data are subsequently transformed to the *s*–*n* coordinates (Appendix A) for the purpose of

comparison with the experimental data. To gain an understanding of the flow physics in a clear way and to provide the near-wall flow properties we have first presented the predicted mean and turbulence flow properties in the Cartesian coordinates.

3.4.1 Components of Mean Velocity

The mean velocity of the deflected jet can be considered as having two components, one along the x-axis (in the direction of the crossflow) and the other along the y-axis (in the direction of the jet discharge). The component along the crossflow direction is referred as cross-stream component and the component along the jet direction is referred to as vertical component. Both the components have significant contribution to the resultant mean velocity in the flow configuration considered here.

The predictions of the cross-stream component of mean velocity (u/v_j) at different downstream locations are shown in Fig. 3.8 for R = 6 and in Fig. 3.9 for R = 9. The peak value of the cross-stream component is more in the near-filed (up to the location x/D = 10) and it gradually decreases downstream due to the mixing of the jet with the crossflow. A reverse flow region is observed in the bottom part and at the location of just downstream of the jet slot (x/D = 2). The length of the recirculation region predicted by the streamline curvature modification model is slightly higher than that of the standard k-ε model. The recirculation region continues up to x/D = 20 in the predictions of the streamline curvature modification which are determined by observing the value of cross-stream component. However the recirculation region predicted by the standard k-ε model ends before x/D = 20. The difference between the predictions by both the models is observed to be less in the upper part of the jet whereas in the lower part of the jet the difference is more prominent. The curvature modification model predicts higher negative velocity in the bottom part of the jet compared to the standard k-ε model, thus predicting larger recirculation region compared to that by later. Moreover the curvature modification model predicts the peak values at higher y/D positions thus showing higher penetration of the jet into the crossflow compared to that by the standard k-ε model.

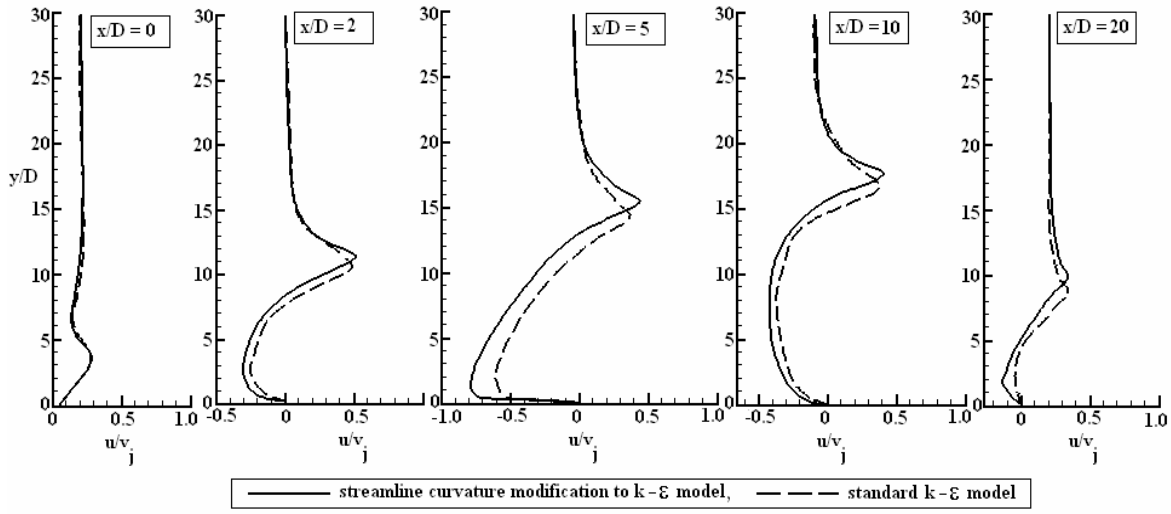

Fig. 3.8: Prediction of cross-stream component of mean velocity at different downstream locations for $R = 6$.

In the case of jet with $R = 9$ (Fig. 3.9), the profile of the cross-stream component of velocity is similar as that in the case with $R = 6$, but the size of the recirculation region and the jet penetration is more than that in the case with $R = 6$. The difference between the predictions by the two models is less in the case of $R = 9$ than that for $R = 6$ owing to less curvature for jet with $R = 9$. Therefore the curvature modification model in this case does not significantly improve the predictions in this case compared to those by the standard k-ε model.

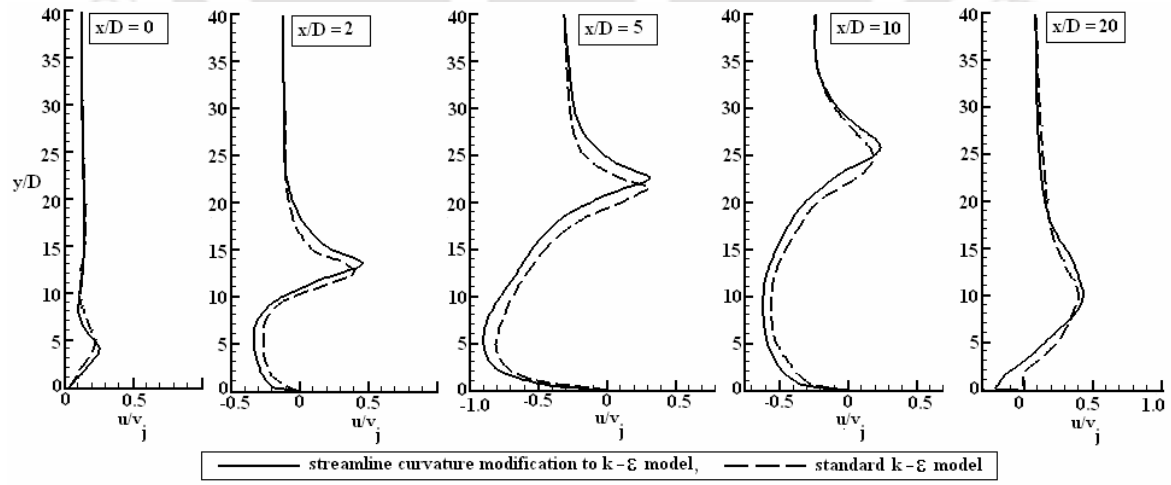

Fig. 3.9: Prediction of cross-stream component of the mean velocity at different downstream locations for $R = 9$.

The predictions of the vertical component of the mean velocity (v/v_j) by both the models at different downstream locations are shown in Figs. 3.10 and 3.11 for jets with $R = 6$ and 9, respectively. The difference in the predictions by the two models is

small near the jet exit area and further downstream, where there is no streamline curvature. The jet is almost vertical near the jet discharge, and therefore the magnitude of the vertical component is large in this region, but further downstream the jet becomes horizontal and the value of vertical velocity reduces in magnitude. The standard *k-ε* model predicts higher values of vertical component of mean velocity at the bottom part of the jet compared to the curvature modification model. In case of the jet with $R = 9$ (Fig. 3.11) the magnitude of the vertical velocity and the penetration height is more compared to the case with $R = 6$. Moreover as already mentioned, the differences between both the predictions are less in this case due to the smaller streamline curvature of the flow field.

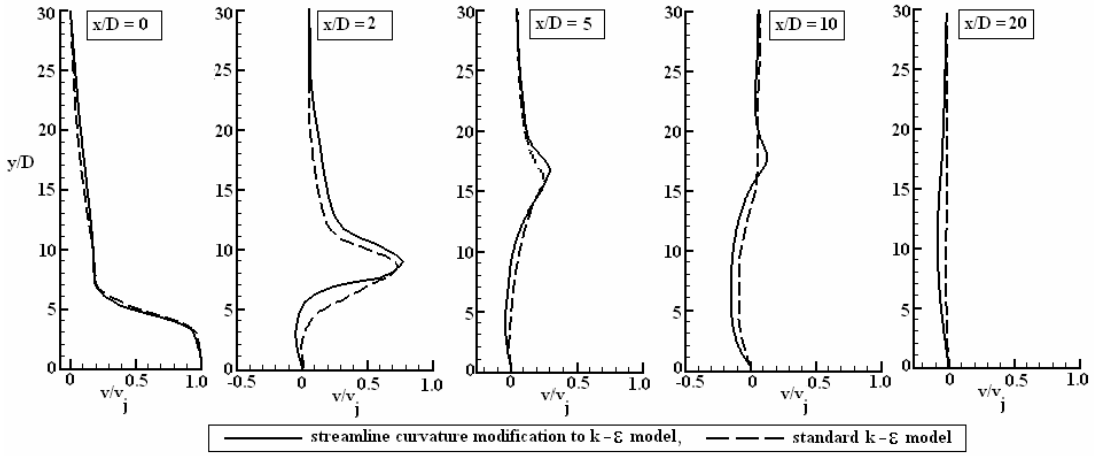

Fig. 3.10: Predicted vertical component of mean velocity at different downstream locations for $R = 6$.

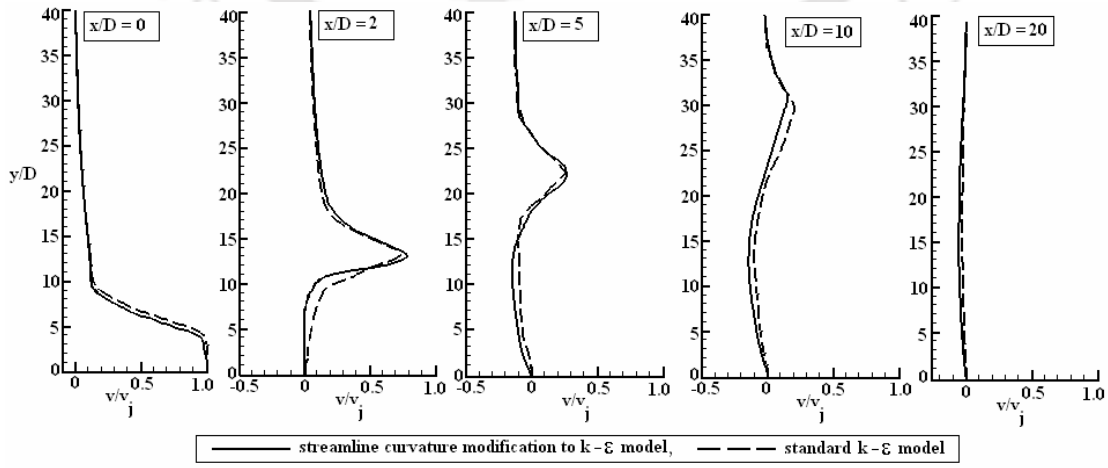

Fig. 3.11: Predicted vertical component of mean velocity at different downstream locations for $R = 9$.

3.4.2 Turbulence Kinetic Energy

Figs. 3.12 and 3.13 show the predictions of the turbulence kinetic energy for R = 6 and 9 respectively at different downstream locations. The maximum value of the turbulence kinetic energy is observed at the centre of the jet and it reaches a constant value (equal to the free stream value) at the upper part of the jet. It is observed from both the Figs. that a considerable amount of turbulence kinetic energy is generated after the jet mixes with the crossflow and gradually its value decreases owing to weaker interaction between the jet and the crossflow further downstream.

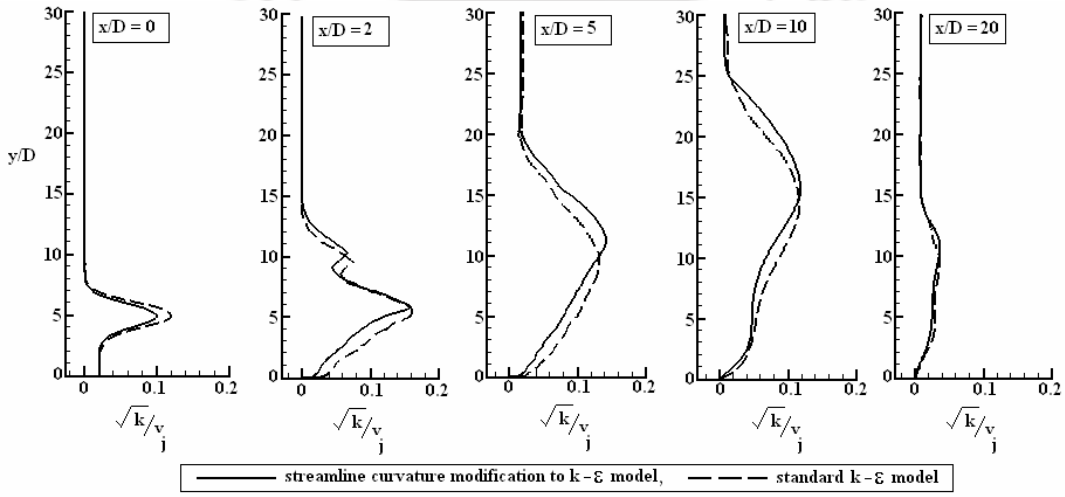

Fig. 3.12: Prediction of turbulence kinetic energy at different downstream locations for R = 6.

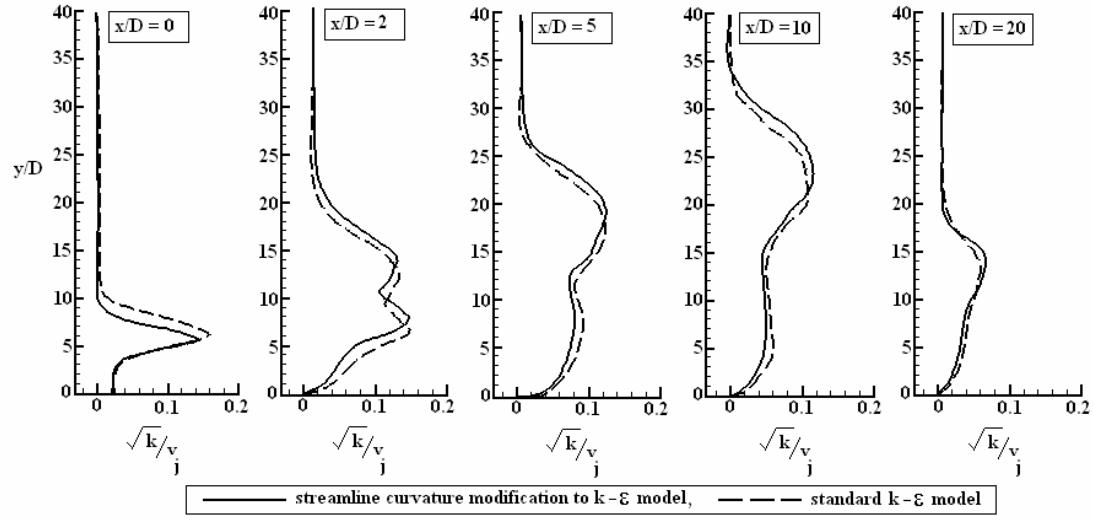

Fig. 3.13: Prediction of turbulence kinetic energy at different downstream locations for R = 9.

3.4.3 Mean Flow Structures

The predicted non-dimensional mean velocity vector plots superimposed with streamline are shown in Figs. 3.14 and 3.15 for R = 6 and 9 respectively. The overall structures of the flow field can be explained from these plots. After the discharge and some initial length, the jet trajectory is deflected in the cross-stream direction and the direction of the crossflow is altered as if a rigid obstacle blocks it. A reverse flow or recirculation is observed in the lower part of the jet which indicates the existence of the flow separation. Both the models predict the recirculation, but the size of the recirculation region predicted by the curvature modification model is larger compared to that by the standard k-ε model. Moreover the curvature modification model predicts higher penetration height compared to that by the standard k-ε model. Qualitatively the structures of flow field in the case of the jet with R = 9 is similar to the case with R = 6. In this case the penetration height and the size of recirculation region are higher than that in the earlier case. In the case of jet with R = 9, the jet is stronger and therefore the crossflow faces a bigger obstacle compared to the case with R = 6 and hence the size of the recirculation region is more in this case compared to that for R = 9. Moreover here the difference between the sizes of recirculation regions predicted by both the models are small compared to the case with R = 6.

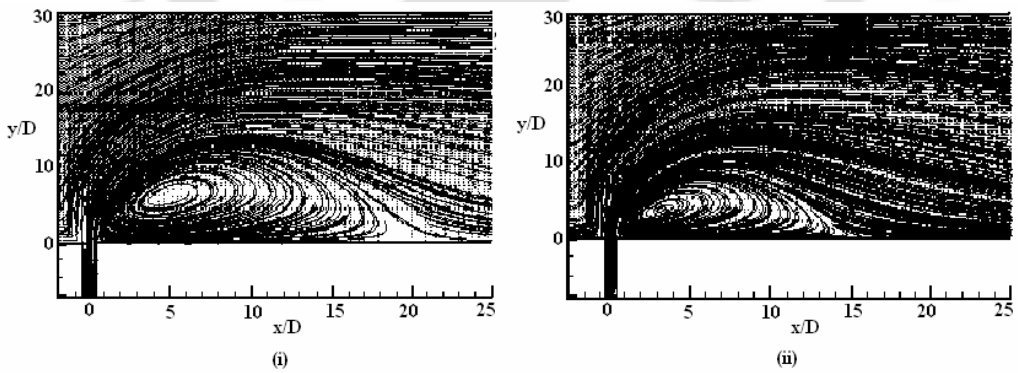

Fig. 3.14: Mean velocity vector superimposed with streamline plot for R = 6, (i) Curvature modification model and (ii) Standard k-ε model.

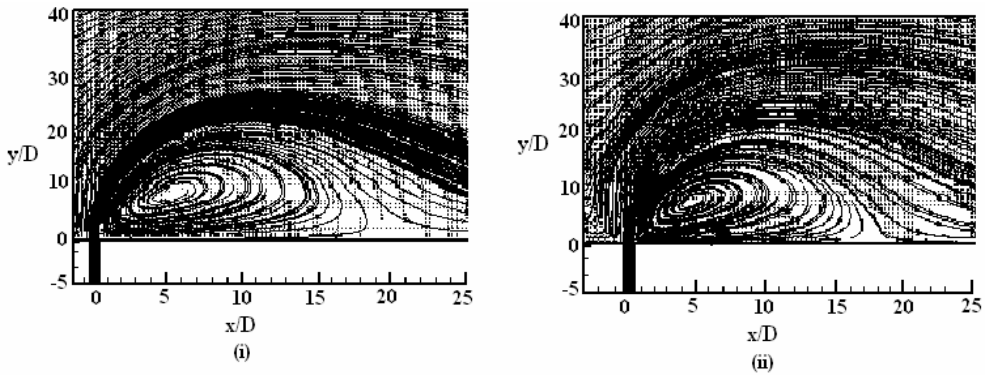

Fig. 3.15: Mean velocity vector superimposed with streamline plot for *R = 9,* (i) Curvature modification model and (ii) Standard *k-ε* model.

3.4.4 Turbulence Shear Stress

Predicted normalized shear stresses at different downstream locations are shown in Figs. 3.16 and 3.17 for jets with *R = 6* and *9,* respectively. In general the shear stress $-\overline{u'v'}$ and the velocity gradient $(\partial u/\partial y)$ have the same sign and therefore the eddy viscosity $\nu_t = -\overline{u'v'}/(\partial u/\partial y)$ is positive in all regions of the flow field. It is observed that in both cases the value of the shear stress in the upper part of the jet is more compared to that in the lower part. The value of the shear stress depends upon the velocity gradient $(\partial u/\partial y)$ thus the maxima of the shear stress $-\overline{u'v'}$ profile correspond closely to the position of maxima of the velocity gradient $(\partial u/\partial y)$. The peak value of the shear stress is observed in the jet-shear layer and is a consequence of high value of $(\partial u/\partial y)$ in the layer, where the jet and the crossflow interact with each other.

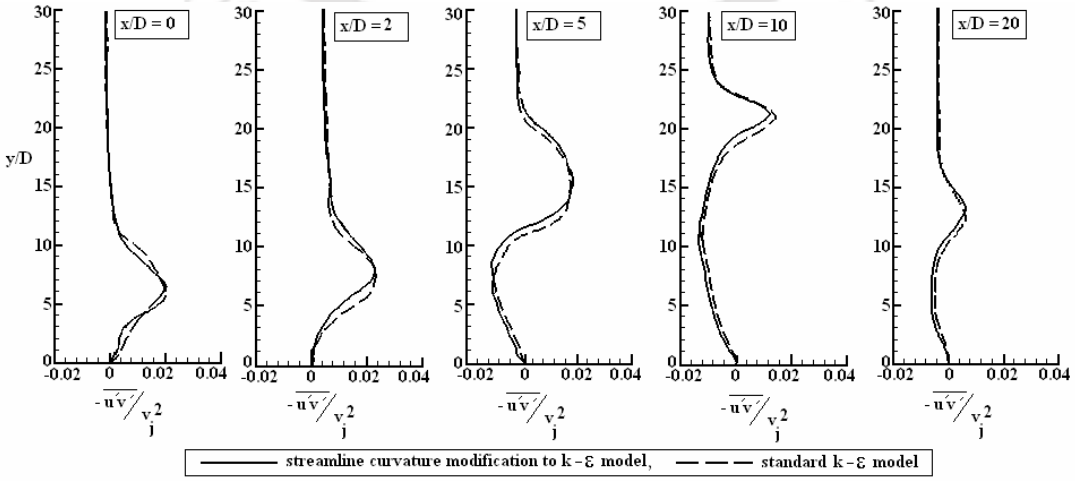

Fig. 3.16: Predicted turbulence shear stress profiles at different downstream locations for *R* = 6.

The values of the shear stress at both the upper and lower parts of the jet are opposite. At the upper edge which represents the jet-shear layer, the value of shear stress is higher, whereas the bottom part which represents the reverse flow and wake the value of shear stress is lower.

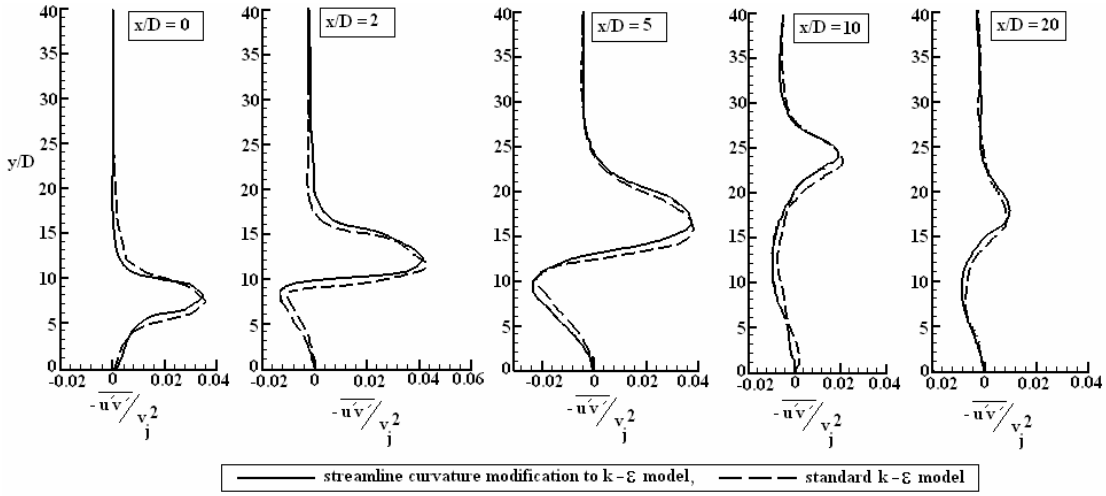

Fig. 3.17: Predicted turbulence shear stress profiles at different downstream locations for $R = 9$.

Both the models show similar profile of turbulence shear stress, but the predicted positions of the peak value of shear stress do not match (Fig. 3.16 and 3.17). For the case of jet with $R = 9$, the value of shear stress is more in the upper part of the jet than in the case of $R = 6$, but the value of shear stress in the lower part of the jet is almost same as the value in the case of $R = 6$.

3.4.5 Comparison with Measurements

In this section, the comparisons of some flow properties are made with the experimental data of Ramaprian and Haniu (1983) and Haniu and Ramaprian (1989). As said earlier Ramaprian and Haniu (1983) and Haniu and Ramaprian (1989) have reported their experimental observations in the *s–n* coordinate system (Fig. 3.1). The component of the mean velocity along the jet streamline direction is termed as the streamwise velocity (u_s) and the component along the normal to the streamline is termed as the normal component velocity (v_n). The upper part of the deflected jet ($n/D < 0$) faces and mixes with the crossflow. This part of the jet is referred to as the outer portion and the other part of the jet ($n/D > 0$) is referred to as the inner portion of the jet.

In the present flow configuration, streamline curvature will have a stabilizing effect on turbulence in the lower shear layer (inner part of the jet) and a destabilizing effect in the upper shear layer of the jet (Bradshaw, 1969). Thus the shear stress, turbulence kinetic energy and jet spreading rate would be enhanced by the curvature correction in the outer shear layer relative to the unmodified model (standard k-ε model), while the reverse would occur in the lower shear layer.

Comparisons of the normalized streamwise component of the mean velocity are shown in Figs. 3.18 and 3.19 for R = 6 at different s/D locations. The peak value of the jet is higher near the jet discharge and it decreases in the downstream locations, where the spreading of the jet is more. It is observed that the jet is not symmetric about its axis unlike a jet in quiescent ambient.

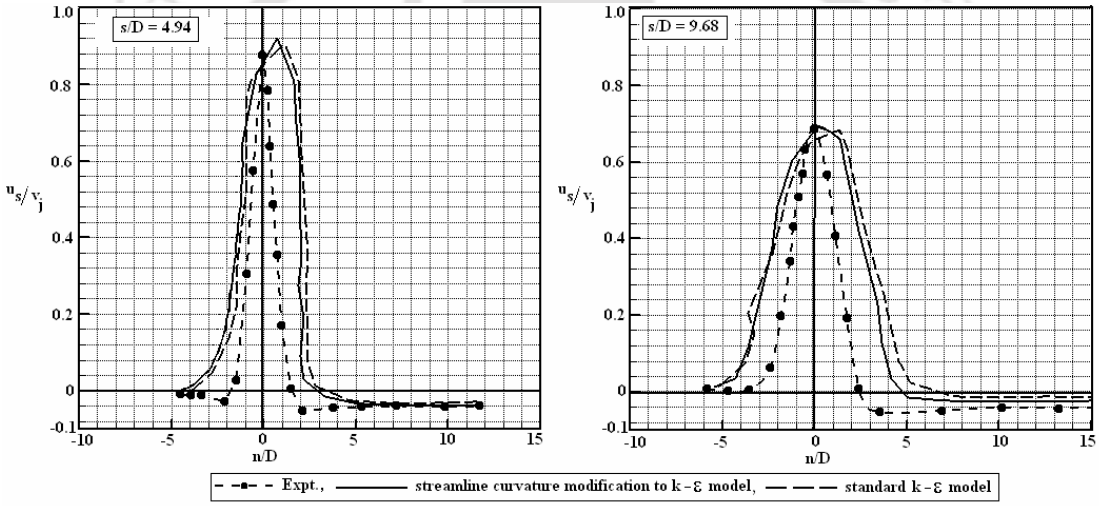

Fig. 3.18: Comparison of mean streamwise velocity with the experimental data for R = 6, s/D = 4.94 and 9.68.

The curvature modification model should show an enhanced spreading rate in the outer part ($n/D < 0$) and reduced spreading rate in the inner part ($n/D > 0$) of the jet. However due to the moving stream of the crossflow, the effects of curvature and co-flowing ambient counteract each other. Hence the spreading rate is not so distinguished in the outer part of the jet and the curvature modification model slightly over predicts compared to the standard k-ε model.

The improvement by the curvature modification model is seen in the inner part of the jet by a reduction of the spreading rate and more prominently at the edge of the

inner portion by showing a large negative velocity, thereby accurately predicting the recirculation below the jet.

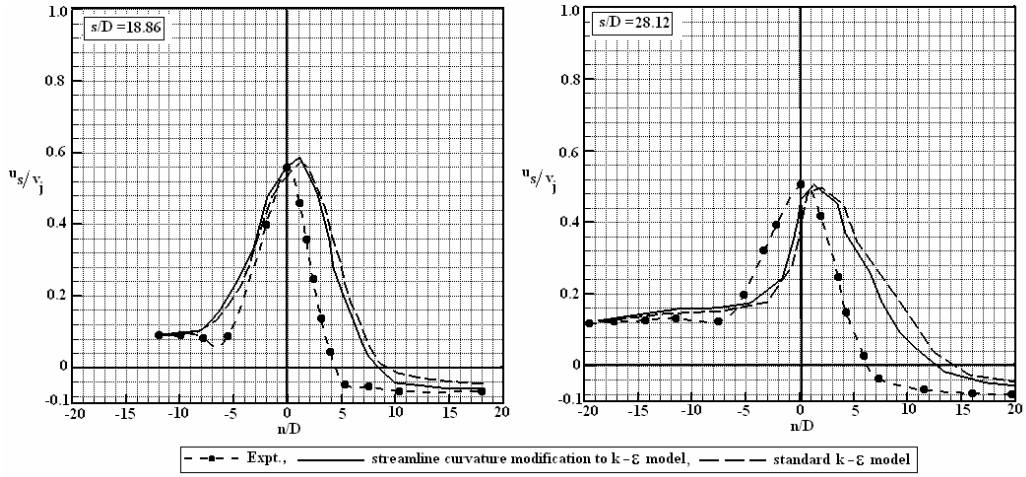

Fig. 3.19: Comparison of mean streamwise velocity with the experimental data for *R = 6, s/D* = 18.86 and 28.12.

The maximum improvement by the curvature modification model over the standard *k-ε* model is approximately 20%.

Figs. 3.20 and 3.21 show a comparison of the normalized streamwise component of mean velocity for the value of *R* = 9 at different *s/D* locations. The value of peak velocity in this case is higher than for *R* = 6 as the jet is relatively stronger in this case. In this case also due to the effect of finite edge velocity the spreading rate is reduced in the outer part of the jet. The improvement by the curvature modification model in this case is less compared to the case with *R* = 6, because the flow experiences a small streamline curvature.

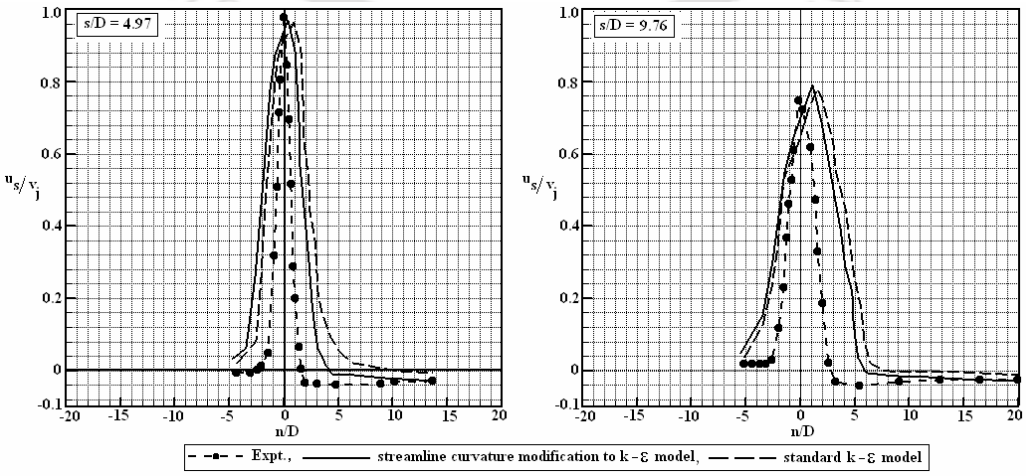

Fig. 3.20: Comparison of mean streamwise velocity with the experimental data for *R = 9, s/D* = 4.97 and 9.76.

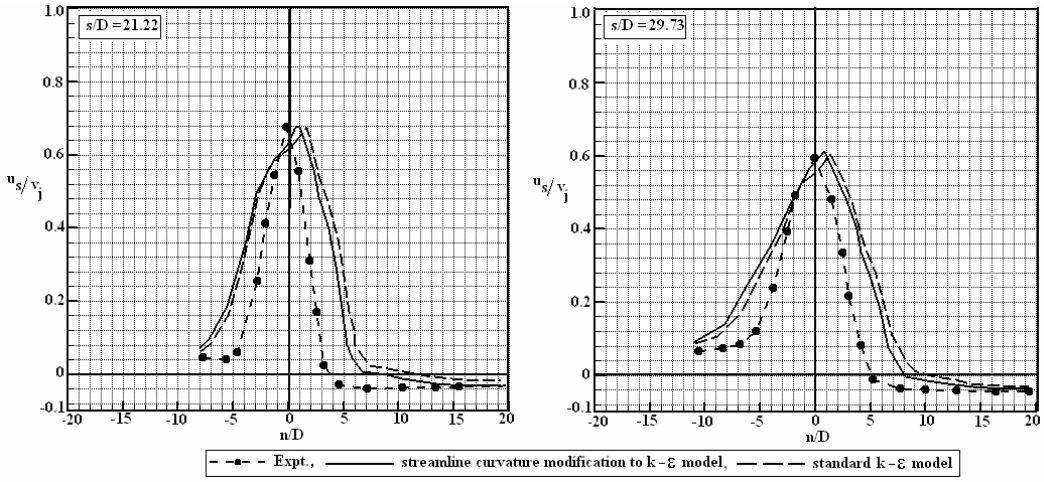

Fig. 3.21: Comparison of mean streamwise velocity with the experimental data for R = 9, s/D = 21.22 and 29.73.

Comparisons of the normal component of mean velocity (v_n/v_j) are shown in Figs. 3.22 and 3.23 for R = 6 at four different s/D locations. In the upper part of the jet the fluids show a positive component of velocity thus the making the motion upward and gradually the positive value decreases as one moves towards the jet centre. In the inner part of the jet all the fluid particles have a downward velocity. This is due to the recirculation below the jet. Thus it is observed that the recirculation determines these velocities rather than the jet turbulence. Another feature observable from Figs. 3.22 and 3.23 is that near the jet centre line in the inner part of the jet, the fluids show an upward motion making the fluids to move from the inner portion to the outer portion of the jet. Thus the entrainment rate is different at both portions of the jet. Moreover the spread of the jet at the upper and lower parts of the jet is not equal. It is more at the bottom part of the jet than that at the upper part. Due to unequal spread of the jet, profiles of the normal component of velocity show different trends at the upper and lower parts of the jet. Both the models predict the normal component of velocity well at first two downstream locations (s/D = 4.94 and 9.68), but at further downstream positions (s/D = 18.86 and 28.12) both the model show some difference of prediction from the experimental data. Comparatively the curvature modification model predicts better than the standard k-ε model especially in the inner part of the jet.

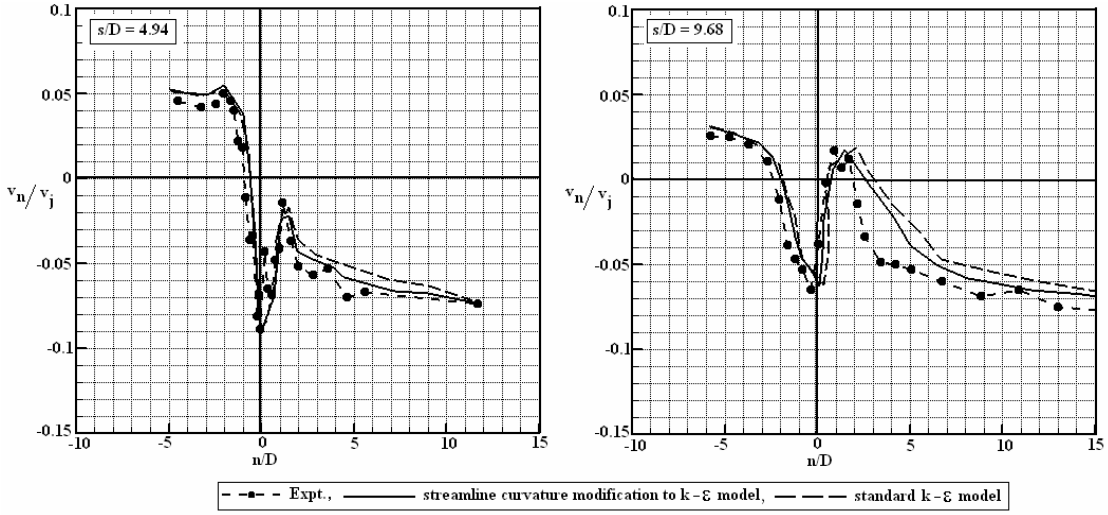

Fig. 3.22: Comparison of mean normal component velocity with the experimental data for $R = 6$, $s/D = 4.94$ and 9.68.

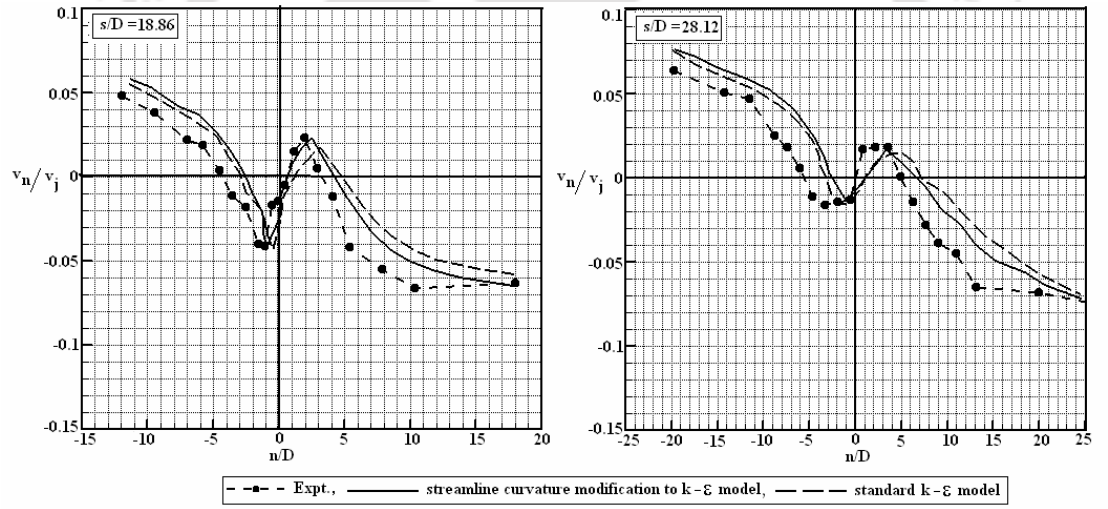

Fig. 3.23: Comparison of mean normal component velocity with the experimental data for $R = 6$, $s/D = 18.86$ and 28.12.

Comparisons of the normalized normal component profiles of the mean velocity are shown in Figs. 3.24 and 3.25 for jet with $R = 9$ at different s/D locations. In this case also due to recirculation, the n-component velocity has downward motion in the inner part of the jet. One significant difference observed in this case is that the variation of the n-component velocity with downward direction in the inner part of the jet is less compared to the case with $R = 6$. In case of jet with $R = 6$ the values of vertical velocity component reduce in the inner part of the jet and at far downstream locations ($s/D = 18.86$ and 28.12) the variation is more prominent. In the case of jet

with R = 9, the variation of velocity in the inner part of the jet is very small. In this case also the curvature modification model predicts better than the standard k-ε model in the inner portion of the jet.

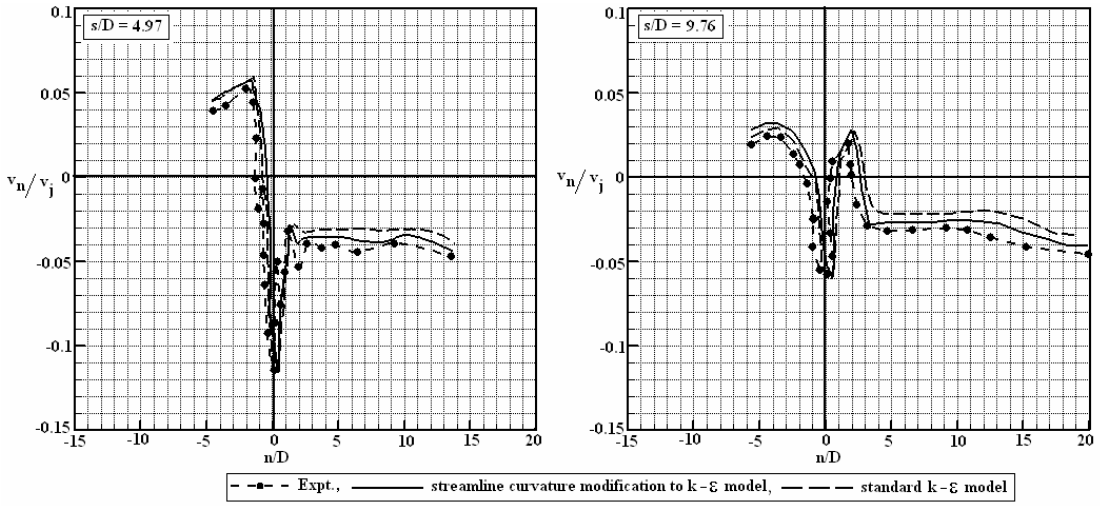

Fig. 3.24: Comparison of mean normal component velocity with the experimental data for R = 9, s/D = 4.97 and 9.76.

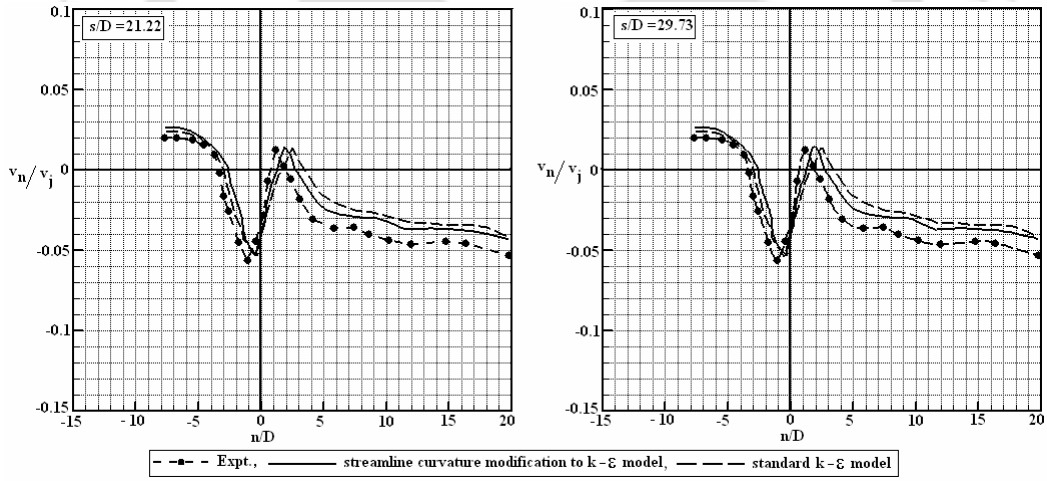

Fig. 3.25: Comparison of mean normal component velocity with the experimental data for R = 9, s/D = 21.22 and 29.73.

Comparisons of the normalized turbulence shear stresses are shown in Figs. 3.26 and 3.27 for the jet with R = 6. The value of the shear stress decreases with the distance s/D. At low s/D values, i.e., near the jet slot the value of the shear stress is large at the inner portion of the jet whereas further downstream the value of shear stress in the upper part of the jet is more than that in the lower part. According to streamline curvature effect, there should be an enhancement of the shear stress in the upper part of the jet and reduction of shear stress in the lower part of the jet. This is observed in the present investigation. Due to the combined effect of the streamline

curvature and the edge velocity, the curvature modification model does not show adequate increase of shear stresses in the outer part of the jet, but it shows an appreciable reduction of the shear stress in the inner part of the jet compared to that predicted by the standard *k-ε* model.

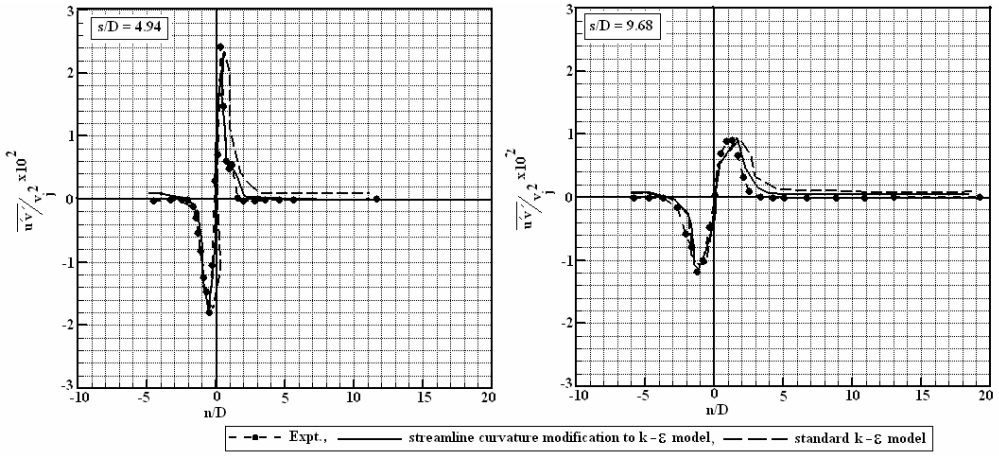

Fig. 3.26: Comparison of turbulence shear stress with the experimental data for *R = 6, s/D* = 4.94 and 9.68.

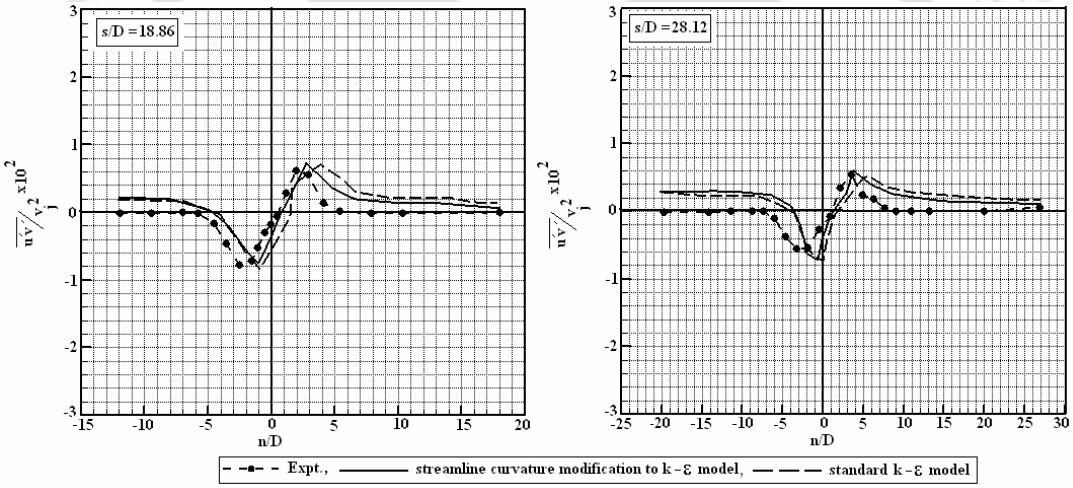

Fig. 3.27: Comparison of turbulence shear stress with the experimental data for *R = 6, s/D* = 18.86 and 28.12.

The standard *k-ε* model over predicts the shear stresses especially in the inner part of the jet. Moreover the predictions of the positive and negative peak values of the stresses by the curvature modification model match better with the experimental data than those by the standard *k-ε* model.

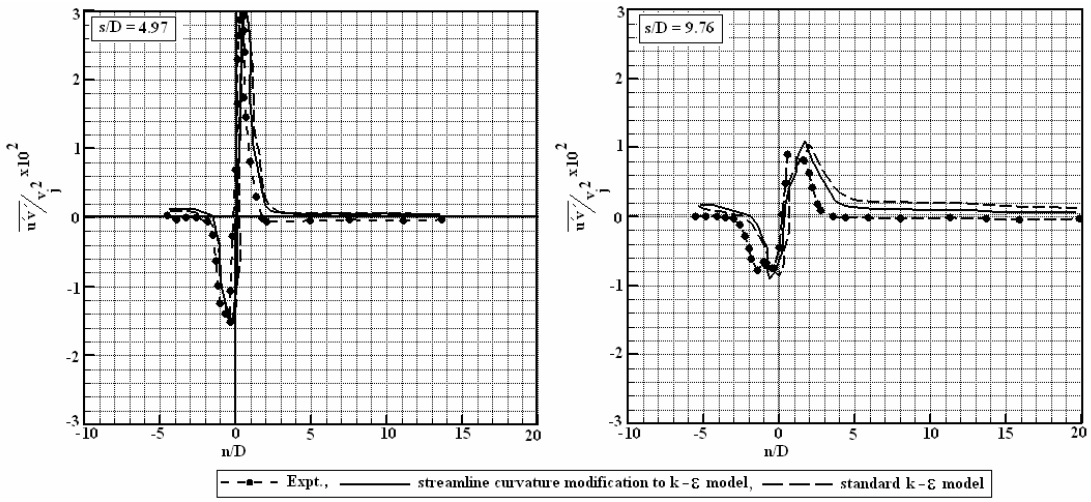

Fig. 3.28: Comparison of turbulence shear stress with the experimental data for *R = 9, s/D* = 4.97 and 9.76.

Comparisons of the normalized turbulence shear stresses are shown in Figs. 3.28 and 3.29 for the jet with *R* = 9. The value of the shear stress in the near-filed of the jet is more than that in the case of jet with *R* = 6. In this case also the curvature modification model shows improvement in the prediction especially in the inner portion of the jet but fails to match the positive and negative peak values of the shear stresses. This is due to the fact that the flow field faces less streamline curvature effect than that in the case of *R* = 6.

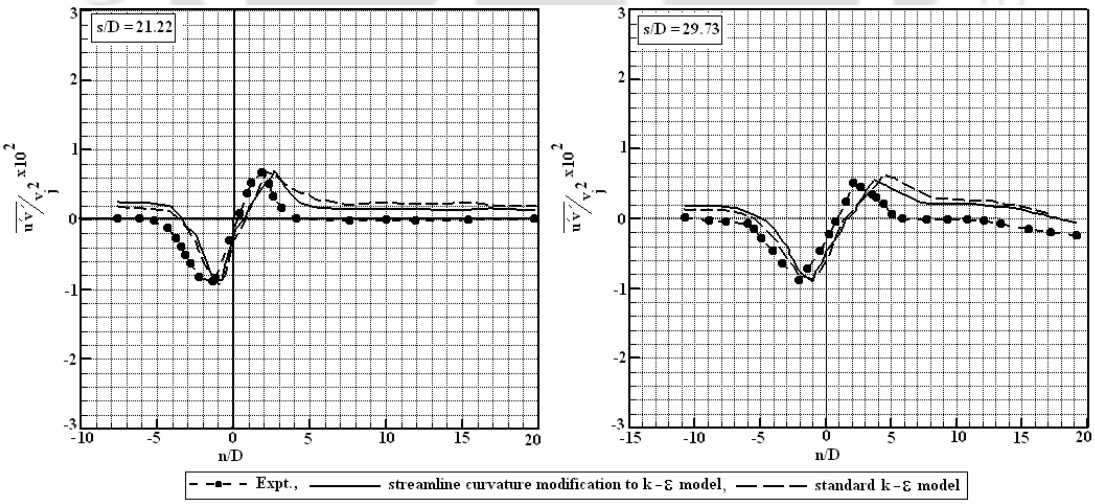

Fig. 3.29: Comparison of turbulence shear stress with the experimental data for *R = 9, s/D* = 21.22 and 29.73.

3.5 Conclusions

A 2D investigation of flow field of a plane jet in crossflow has been presented in this chapter using two different turbulence models. The 2D investigation of flow field provides sufficient information of the flow properties at the jet central plane. The streamline curvature modification produces reasonably improved results in the inner part of the jet and produces better agreement with the experimental data. The maximum improvement in the results by the curvature modification model over the standard k-ε model is observed as 20%. Therefore the inclusion of the streamline curvature effect in the standard k-ε model to predict the flow field of jet in crossflow is justified. The curvature modification model works better in case of the jet with R = 6 than in the case of jet with R = 9 due to the more streamline curvature in the flow field. Moreover the physical effect of the convex and concave streamline curvatures in the flow field is well reflected in the numerical investigation of problem of jet in crossflow due to the incorporation of the curvature effects in the turbulence model. The overall moderate agreement with the experimental data can be ascribed due to several factors, such as 2D investigation, experimental uncertainties, etc.

Chapter 4

Three-dimensional Jets in Crossflow

4.1 Introduction

We have observed from the investigation of the 2D flow field presented in the previous chapter that the agreements between the experimental and numerical results are moderate. The inclusion of the curvature modification to the standard k-ε model improves the prediction up to some extent in some selected regions only such as in the recirculation region, but not in the entire flow field. The flow field of a turbulent jet in crossflow is 3D. The accuracy of the investigation by making a simplification to 2D flow field depends on the degree of the complexity and the variations of the flow properties in the three directions present in the flow field. If these effects are weak, the flow behaviour along the central plane of a 3D flow field can be studied from a 2D investigation. In the situation where these effects have a significant effect on the flow field, a 2D investigation can only provide an approximation of the real conditions. From the literature review in Chapter 2 we have found that the flow field of jet in crossflow is chractersised by different types of vortices. Therefore several flow features and characteristics cannot be studied from a 2D investigation of such flow field.

In the present chapter, we present a 3D numerical investigation of the flow field of a jet in crossflow and compare the predictions with the experimental data of Ramaprian and Haniu (1983) and Haniu and Ramaprian (1989). It has already been discussed in the literature review in Chapter 2 that the number of studies of rectangular jet in crossflow is comparatively less compared to the case of round and square jets in crossflow. Moreover only a few studies concerning the rectangular jets in crossflow for high velocity ratios have been reported in the literature. Humber et al. (1993) experimentally studied a rectangular jet in a crossflow and found similar observations of the jet penetration and trajectory as those in the case of a round jet in crossflow, but observed more entrainment. Vincenti et al. (2003) studied plane jets in crossflow at low Reynolds number using PIV and studied the effect of the velocity ratio on the interaction between the shear layer vortices and the counter-rotating

vortices. They observed that for the velocity ratio R = 3 to 6, the shear layer of the plane jet has large fluctuations and its instability seems to be driven by the action of the crossflow leading to the formation of wake vortices. For velocity ratio higher than 6 they observed two types of shear layer vortices. Recently Plesniak and Cusano (2005) studied the scalar mixing of a confined rectangular jet in crossflow. They observed that the flow is more complex than an unconfined round jet in a crossflow. They also observed that the large-scale counter-rotating vortex pair (CRVP) structures dominate the scalar mixing of both the jet and crossflow. Ramaprian and Haniu (1983) and Haniu and Ramaprian (1989) experimentally studied a turbulent plane jet injected from a narrow slot into the crossflow in a channel. They performed experiments for three values of jet to crossflow velocity ratio R = 6, 9 and 10 both for isothermal and heated jets. There was a small clearance between the slot and the sidewalls in their experiments. Such types of flow configurations are encountered in several industrial processes such as mixing and drying of product streams, etc. Ramaprian and Haniu (1983) and Haniu and Ramaprian (1989) performed the measurements of mean and turbulence flow properties in the central plane of the jet slot. They did not study any flow properties and their variations in different transverse plane of the flow domain. Their observations did not include the flow structures near the sidewall and the effects of sidewalls on the flow structures. Moreover they did not provide any details of the flow properties near the bottom wall of the channel. They used a two-channel LDA and resistance thermometry to measure the instantaneous velocity and temperature fields. They did not resolve different vortical structures of the flow field.

One of the objectives of the present investigation is to obtain a better understanding of the flow physics than that obtained experimentally by Ramaprian and Haniu (1989) and Haniu and Ramaprian (1989) by systematically investigating the 3D flow field and resolving several issues related to the flow three-dimensionality. The formation of different types of vortices and their effects on the mean velocity fields are discussed. The present computational results are compared with the measurements of Ramaprian and Haniu (1983) and Haniu and Ramaprian (1989), which are available in the jet central plane. The predictions of some flow properties, which were absent in the experimental observations, are also reported in the present work. Sections 4.2 and 4.3 describe the flow configuration, governing equations, turbulence model, and the numerical procedure. The predictions of the mean and

turbulence quantities and their comparisons with the measurements have been reported in Section 4.4. A comparison of 2D predictions and 3D predictions is made in Section 4.5 followed by the conclusions in Section 4.6.

4.2 Governing Mean Flow Equations

The Reynolds-averaged Navier-Stokes equations for 3D, steady-state flow constitute the governing equation of the mean flow. The equations for an incompressible flow in the Cartesian coordinate system can be written as

Continuity:

$$\frac{\partial u}{\partial x}+\frac{\partial v}{\partial y}+\frac{\partial w}{\partial z}=0 \tag{4.1}$$

x-momentum:

$$u\frac{\partial u}{\partial x}+v\frac{\partial u}{\partial y}+w\frac{\partial u}{\partial z}=-\frac{1}{\rho}\frac{\partial p}{\partial x}+\frac{\partial}{\partial x}(-\overline{u'^2})+\frac{\partial}{\partial y}(-\overline{u'v'})+\frac{\partial}{\partial z}(-\overline{u'w'}) \tag{4.2}$$

y-momentum:

$$u\frac{\partial v}{\partial x}+v\frac{\partial v}{\partial y}+w\frac{\partial v}{\partial z}=-\frac{1}{\rho}\frac{\partial p}{\partial y}+\frac{\partial}{\partial x}(-\overline{u'v'})+\frac{\partial}{\partial y}(-\overline{v'^2})+\frac{\partial}{\partial z}(-\overline{v'w'}) \tag{4.3}$$

z-momentum:

$$u\frac{\partial w}{\partial x}+v\frac{\partial w}{\partial y}+w\frac{\partial w}{\partial z}=-\frac{1}{\rho}\frac{\partial p}{\partial z}+\frac{\partial}{\partial x}(-\overline{u'w'})+\frac{\partial}{\partial y}(-\overline{v'w'})+\frac{\partial}{\partial z}(-\overline{w'^2}) \tag{4.4}$$

Here *u*, *v* and *w* are the mean velocities along the directions of the crossflow direction (*x*), jet discharge (*y*) and transverse direction (*z*), respectively, and *p* is the mean pressure. The primed quantities represent the fluctuations part of the velocity.

4.2.1 Turbulence Model: Standard $k-\varepsilon$ Model

Eqs. (4.2) – (4.4) contain the Reynolds stress terms ($\overline{u'^2}, \overline{v'^2}, \overline{w'^2}, \overline{u'v'}$, $\overline{v'w'}$ and $\overline{u'w'}$), which need to be modeled by a closure approximation. In the standard $k-\varepsilon$ model, the turbulence stresses are modeled as

$$-\overline{u'^2} = 2\nu_t\left(\frac{\partial u}{\partial x}\right) - \frac{2}{3}k \tag{4.5}$$

$$-\overline{v'^2} = 2\nu_t\left(\frac{\partial v}{\partial y}\right) - \frac{2}{3}k \tag{4.6}$$

$$-\overline{w'^2} = 2\nu_t\left(\frac{\partial w}{\partial z}\right) - \frac{2}{3}k \tag{4.7}$$

$$-\overline{u'v'} = \nu_t\left(\frac{\partial u}{\partial y} + \frac{\partial v}{\partial x}\right) \tag{4.8}$$

$$-\overline{v'w'} = \nu_t\left(\frac{\partial v}{\partial z} + \frac{\partial w}{\partial y}\right) \tag{4.9}$$

$$-\overline{u'w'} = \nu_t\left(\frac{\partial u}{\partial z} + \frac{\partial w}{\partial x}\right) \tag{4.10}$$

The transport equations for turbulence kinetic energy (k) and its dissipation rate (ε) used are as follows:

$$u\frac{\partial k}{\partial x} + v\frac{\partial k}{\partial y} + w\frac{\partial k}{\partial z} = \frac{\partial}{\partial x}\left(\frac{\nu_t}{\sigma_k}\frac{\partial k}{\partial x}\right) + \frac{\partial}{\partial y}\left(\frac{\nu_t}{\sigma_k}\frac{\partial k}{\partial y}\right) + \frac{\partial}{\partial z}\left(\frac{\nu_t}{\sigma_k}\frac{\partial k}{\partial z}\right) + P_k - \varepsilon \tag{4.11}$$

$$u\frac{\partial \varepsilon}{\partial x} + v\frac{\partial \varepsilon}{\partial y} + w\frac{\partial \varepsilon}{\partial z} = \frac{\partial}{\partial x}\left(\frac{\nu_t}{\sigma_\varepsilon}\frac{\partial \varepsilon}{\partial x}\right) + \frac{\partial}{\partial y}\left(\frac{\nu_t}{\sigma_\varepsilon}\frac{\partial \varepsilon}{\partial y}\right) + \frac{\partial}{\partial z}\left(\frac{\nu_t}{\sigma_k}\frac{\partial \varepsilon}{\partial z}\right) + C_{\varepsilon 1}\frac{\varepsilon}{k}P_k - C_{\varepsilon 2}\frac{\varepsilon^2}{k} \tag{4.12}$$

Where P_k is the rate of production of k and is given by

$$P_k = \nu_t\left[\left(\frac{\partial u}{\partial y} + \frac{\partial v}{\partial x}\right)^2 + \left(\frac{\partial v}{\partial z} + \frac{\partial w}{\partial y}\right)^2 + \left(\frac{\partial u}{\partial z} + \frac{\partial w}{\partial x}\right)^2 + 2\left(\frac{\partial u}{\partial x}\right)^2 + 2\left(\frac{\partial v}{\partial y}\right)^2 + 2\left(\frac{\partial w}{\partial z}\right)^2\right] \tag{4.13}$$

The values of the model constants used are same as described in Chapter 3. It is to be mentioned here that the incorporation of streamline curvature effect in the standard $k-\varepsilon$ turbulence model in case of 3D flow field is very complex. So far there is no literature in evidence, which discusses this aspect. All the parameters in Eqs. (4.1) to (4.13) are non-dimensionalised with the mean jet velocity v_j and jet width D as follows

$$u^* = \frac{u}{v_j}, v^* = \frac{v}{v_j}, w^* = \frac{w}{v_j} \qquad x^* = \frac{x}{D}, y^* = \frac{y}{D}, z^* = \frac{z}{D} \qquad p^* = \frac{p}{\rho v_j^2}, k^* = \frac{k}{v_j^2}, \varepsilon^* = \frac{\varepsilon}{v_j^3/D}$$

After replacing all the parameters by the corresponding non-dimensional variables, Eqs. (4.1) – (4.13) retain the same forms. Hereafter for convenience the superscript * is removed from all parameters.

4.2.2 Computational Domain

A schematic diagram of the 3D computational domain and the coordinate system used in the present work is shown in Fig. 4.1. The origin is located at the centre of the jet slot. The *x*-coordinate represents the distance in the cross-stream direction, *y*- the vertical, and *z*- the spanwise direction. The computational domain includes the jet discharge slot, two sidewalls and the entire 3D region where an interaction between the jet and crossflow takes place.

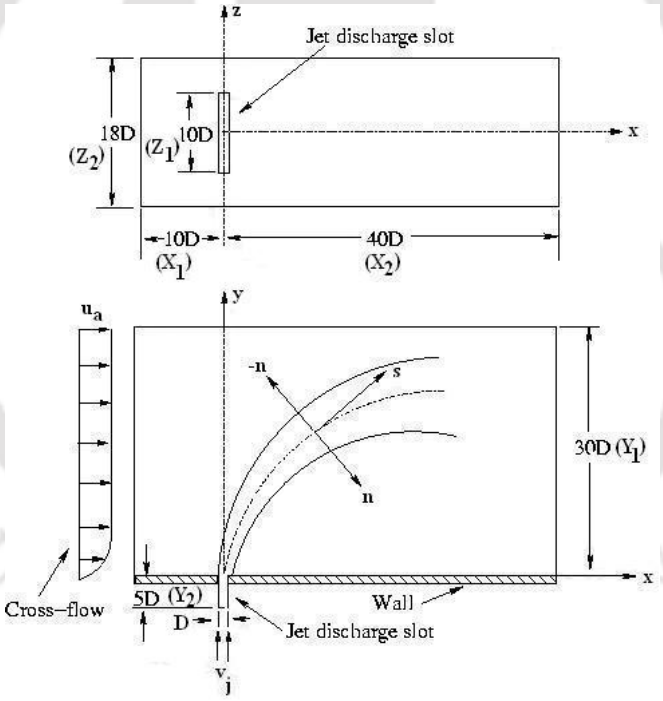

Fig. 4.1 Schematic diagram of the computational domain for $R = 6$.

The size of the computational domain depends upon the value of the jet to crossflow velocity ratio (R). For example, for $R = 6$ the computational domain extends from $10D$ upstream of the centre of the jet slot to $40D$ downstream in the crossflow direction. In the spanwise direction the distance between the two vertical sidewalls is $18D$ and the jet slot length in the spanwise direction is $10D$. Clearly the distance between the top and bottom boundaries should increase with R and it is selected in such a way so that

the free stream boundary conditions can be applied. The size of the computational domain (Fig. 4.1) used for different values of *R* are shown in Table 4.1.

Table 4.1: 3D Domain size for different values of *R*

R	X_1 (*x/D*)	X_2 (*x/D*)	Y_1 (*y/D*)	Y_2 (*y/D*)	Z_1 (*z/D*)	Z_2 (*z/D*)
6	10	40	30	5	10	18
9	10	50	40	5	10	18

4.2.3 Boundary Conditions

The different boundary conditions used in the present computations are inlet, outlet and wall. These are applied as follows

(vi) **Inlet boundary:** The boundary conditions at this plane corresponds to the crossflow conditions, i.e., the only component of the flow is along the crossflow direction ($u = u_a$) with zero components along both the vertical ($v = 0$) and spanwise directions ($w = 0$). Literature (for example, Lim et al., 1992) shows that the effect of the inlet boundary layer has small effect on the flow field for a high value of the velocity ratio as the jet is able to penetrate through a relatively thin boundary layer at the inlet. The inlet turbulence kinetic energy, turbulence dissipation rate, boundary layer thickness and the velocity profile within the boundary layer are set as the same as those for the 2D investigation (Section 3.2.6, Chapter 3).

(vii) **Top surface:** At the top surface excluding the sidewall top, the free stream condition is imposed and the values of *u, v, w, k* and ε specified are the same as those at the inlet boundary. The top of the sidewalls are treated as the wall.

(viii) **Outlet boundary:** At the outlet plane, the normal gradients of all variables are assumed to be zero $\left(\frac{\partial f}{\partial x} = 0; f = (u, v, w, k, \varepsilon)\right)$.

(ix) **Bottom surface:** The whole bottom surface, excluding the jet discharge slot, is considered as a solid wall. The no-slip condition is applied there and the standard wall functions are used to resolve the near wall turbulence. The value of y_p^+ is taken as 11.3, above which the log-law is

assumed to be valid and the value of turbulence kinetic energy and dissipation rate specified in the walls are used as those for the 2D study.

(x) **Jet inlet:** The boundary conditions at the entry to the jet channel or jet plenum are $u = 0$, $w = 0$ and $v = v_j$. The value of turbulence kinetic energy and dissipation rate are taken the same as in the 2D case.

(xi) **Sidewalls:** Sidewalls are treated with the no-slip condition and the standard wall functions are used to resolve the near wall turbulence.

4.3 Numerical Procedure

The finite volume method is used to descretise the governing equations.

4.3.1 Computational Grid

Non-uniform staggered grids are used. The sides of the non-uniform control volumes along the *x*-direction are generated using the following relations:
For the upstream portion of the jet slot, the following relation is used

$$x_i = \frac{i}{i_{\max}} + \frac{\lambda}{\pi}\sin\left(\frac{\pi i}{i_{\max}}\right) \tag{4.14}$$

and for the downstream portion of the jet slot, the following relation is used

$$x_i = \frac{i}{i_{\max}} - \frac{\lambda}{\pi}\sin\left(\frac{\pi i}{i_{\max}}\right) \tag{4.15}$$

The sides of the non-uniform control volumes along the *y*-direction are generated using the following relation

$$y_j = \frac{j}{j_{\max}} - \frac{\lambda}{\pi}\sin\left(\frac{\pi j}{j_{\max}}\right) \tag{4.16}$$

and the sides of the non-uniform control volume along the *z*-direction are generated using the following relation.

$$z_k = \frac{k}{k_{\max}} + \frac{\lambda}{\pi}\sin\left(\frac{\pi j}{k_{\max}}\right) \tag{4.17}$$

where *i, j* and *k* are spatial indices and i_{max} , j_{max} and k_{max} are their maximum values in *x*-, *y*- and *z*- directions, respectively and λ the clustering parameter with a value of 0.5. The grids are clustered near the bottom wall in the *y*-direction as

well as near both sidewalls in the z-direction. Moreover grids are clustered at the jet exit in the x-direction. The distribution of the control volumes in the computational domain used for R = 6 is shown in Fig. 4.2 where 122×90×60 (= 658800) number (122 along x-direction, 90 along the y-direction and 60 along the z-direction) of control volumes excluding the jet duct are used. The jet duct comprises 10×15×30 (= 4500) control volumes. The number of the control volumes are fixed based on a grid-independence study (described in Section 4.3.4). To avoid checkerboard flow fields, a staggered grid arrangement is employed in which the scalar variables (p, k and ε) are positioned at the centre of the control volume and the velocity components are positioned at the cell faces.

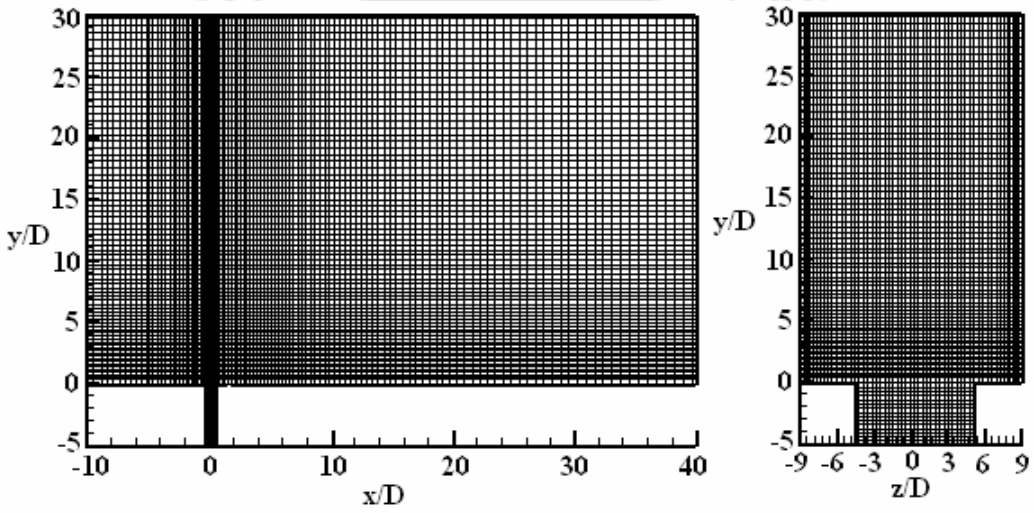

Fig. 4.2: Distribution of the control volumes in the computational domain for the jet with R = 6.

4.3.2 Computational Methodology

A computer code is developed in FORTRAN 77 by the author himself from scratch based on the SIMPLE algorithm (Patankar, 1980). The momentum and the other transport equations are descritised using the power-law scheme (Patankar, 1980). The tri-diagonal matrix algorithm with line-by-line iteration process is used to solve the system of linear algebraic equations. The line-by-line iteration is first carried out on one plane and subsequently the calculations are moved to the next plane thus covering whole domain, plane by plane. For better convergence, an alternation of sweeping direction is done. All the variables (u, v, w, k, and ε) are under-relaxed during each iteration. The value of the relaxation parameter used for u, v and w is 0.1 and for k and ε it is 0.3. The mass residual in each cell is determined from the continuity equation

and the maximum residual is established as the criteria for assessing the overall convergence of the flow field. The convergence of the computation is assumed to be achieved and therefore iterations are terminated when the normalized sum of the residual mass is less than 10^{-4} and the relative variation of variables *u, v, w, k*, and ε are less than 10^{-2} in their successive iterations. The history of the residual fall in the numerical solution for the jet with $R = 6$ using the standard k-ε model is shown in Fig. 4.3. The code was run on a special Linux server (16 nodes, load clustering machine) with 8 GB RAM and 3 GHz processor speed and it took approximately 26 days of CPU time for the full convergence of the results.

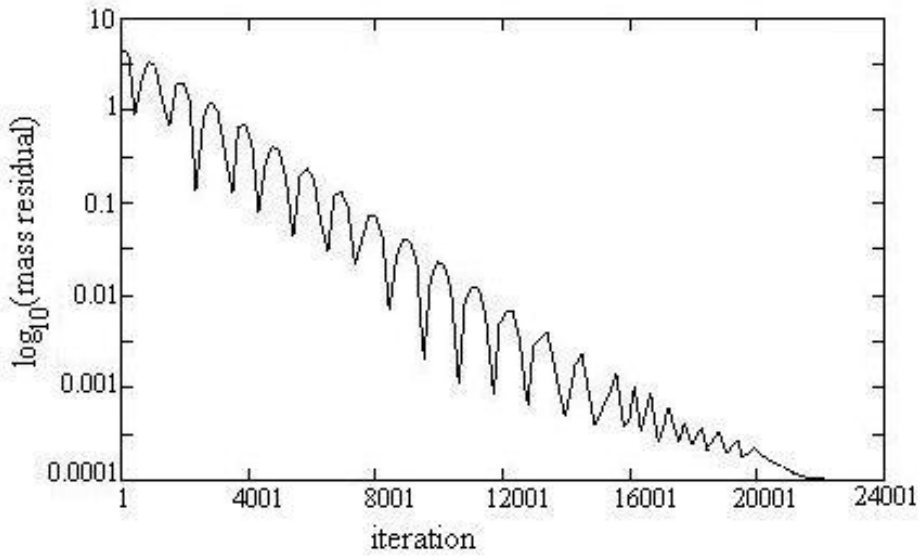

Fig. 4.3: History of mass residual fall for $R = 6$.

4.3.3 Code Validation

For testing the accuracy of the present code, it is validated with the numerical results reported by Hoda and Acharya (2000) for a square jet in a crossflow. The present code is modified according to the flow conditions of Hoda and Acharya (2000), i.e., a square jet in crossflow with a velocity ratio of $R = 0.5$. The comparison of the predicted results of the cross-stream and vertical components of the mean velocity at a location of $x/D = 5$, $z/D = 0$ for velocity ratio $R = 0.5$ obtained by the present code

with the results of Hoda and Acharya (2000) are shown in Fig. 4.4. From the comparison it is observed that the agreement between the two predictions is fairly good and the maximum difference between the two predictions is seen to be 5%. Thus the present code stands validated.

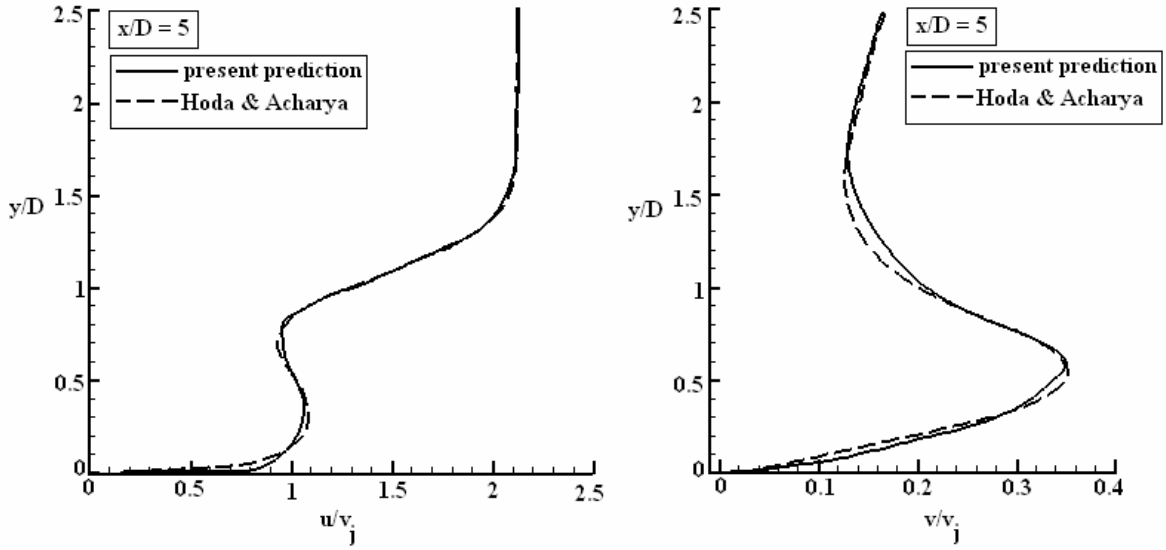

Fig. 4.4: Comparison of the present predictions with those of Hoda and Acharya (2000) for velocity ratio of $R = 0.5$, $z/D = 0$.

4.3.4 Grid Sensitivity

The grid sensitivity test of the present computation is conducted by using three different sets of grids, viz., 100×80×50 (= 400000). 100 along x-, 80 along y- and 50 along z-directions), 110×85×55 (=514250), and 122×90×60 (=658800) by comparing the cross-stream component of the mean velocity (u) profile for $R = 6$. It is to be mentioned that the ratio of smallest (coarse) number of grids and largest (fine) grids is taken as 1.647, which is almost equal to the value of 1.65 used by Hoda and Acharya (2000). Moreover the requirement of a high computational time restrict the use of finer grids. The grids are non-uniform in all the three directions and clustered near the walls and the jet source region. The velocity profiles for $R = 6$ at $x/D = 2$ using the standard $k-\varepsilon$ model is shown in Fig. 4.5. It has been observed that the grid refinement in general improves prediction by reducing the over prediction in the jet edge and increasing the peak value of the velocity. The deviation between the predictions using three different grids decreases as the mesh is refined and the difference between the predictions using the grid sizes 122×90×60 and 110×85×55 is

a maximum of 2.5%. The results that are presented in the subsequent sections are using the grid size 122×90×60 for $R = 6$ and 142×104×70 for $R = 9$.

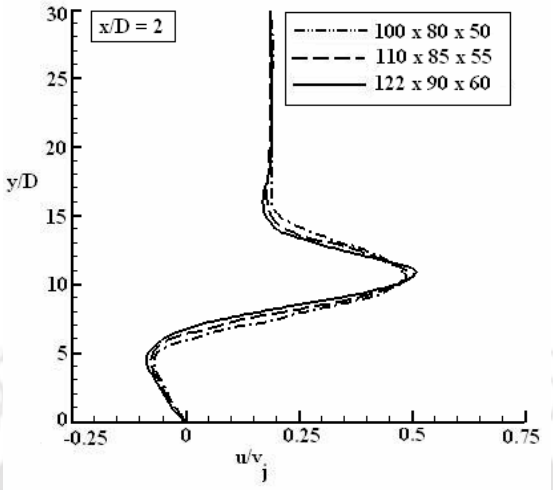

Fig. 4.5: Grid sensitivity test: predicted cross-stream component of mean velocity (u) profile for $R = 6$, $z/D = 0$.

4.4 Results

In the present work, computations are performed in the Cartesian coordinates and the computed data are subsequently transformed to the s–n coordinates for the purpose of comparison with the experiments. To gain an understanding of the flow physics in a clear way and to provide the flow properties near the bottom wall, first we have presented the predictions of the mean flow properties in the Cartesian coordinates. Before going to discuss the results, the terms used to describe the sides of the jet are first given here. The slot of the jet is rectangular. The side of the jet slot (length $10D$) which faces the crossflow first is termed as the leading edge of the jet slot and its opposite side is termed as the trailing edge. The other two sides (of length D), facing the two sidewalls are termed as the side edges of the jet slot.

4.4.1 Components of Mean Velocity

The mean velocity of the deflected jet can be considered as having three components, one along the x-axis (in the direction of the crossflow), one along the y-axis (in the direction of the jet discharge) and the other along the z-axis (in the transverse

direction). These three components are termed as the cross-stream, vertical and spanwise, respectively. All the three components have significant contribution to the resultant mean flow field in the flow configuration considered in the present work.

Figs. 4.6 to 4.10 show the variation of the cross-stream component of mean velocity (u/v_j) with distance y/D from the wall at various downstream positions (x/D) for the velocity ratio R = 6. To check the change of velocity profile in the spanwise directions, the plots of velocity (u/v_j) are shown at five different transverse planes (z/D = 0, 3, 5, 6 and -3). The main flow features, namely, the wake vortices and counter-rotating vortex pair (CRVP) are expected to be distinctly evident along these transverse planes. In Fig. 4.6, the velocity profile at the jet central plane (z/D = 0) is shown at five different downstream (x/D) positions. A reverse flow region is formed near the wall, just at the downstream of jet (x/D = 2). It is observed that the flow does not recirculate unlike in the 2D case. This is due to the entrainment process.

Immediately downstream of the jet, the low pressure in the wake of the jet induces laterally inward motion of the surrounding crossflow fluid close to the bottom wall towards the jet central plane. This behaviour can be observed clearly from the vector plots described in the Section 4.4.3 (see Fig. 4.62). The entrained fluid moves upward in the vicinity of the jet central plane (z/D = 0) and is swept up by the bent over jet. Some part of the high momentum fluid moving towards the jet central plane close to the bottom wall is re-oriented in the streamwise direction and leads to the formation of a weak wall-jet-like structure (x/D = 5 and 10). Since the crossflow is weak in this case, the wall-jet-like structure is weak compared to the case of strong crossflow, i.e., low values of the velocity ratio R (Hoda and Acharya, 2000 and Andreopoulos and Rodi, 1984). A wake-like region with low velocity is observed above the wall-jet shear layer and a shear layer with strong velocity gradient above the wake-like region is observed at the locations of x/D = 2, 5 and 10. The size of the wake-like region is comparatively larger than that reported by Hoda and Acharya (2000) and Andreopoulos and Rodi (1984) for low values of R. At further downstream location (x/D = 20) the velocity gradient in the wake-like region and jet-shear layer is diminished and the flow recovers toward a boundary layer profile.

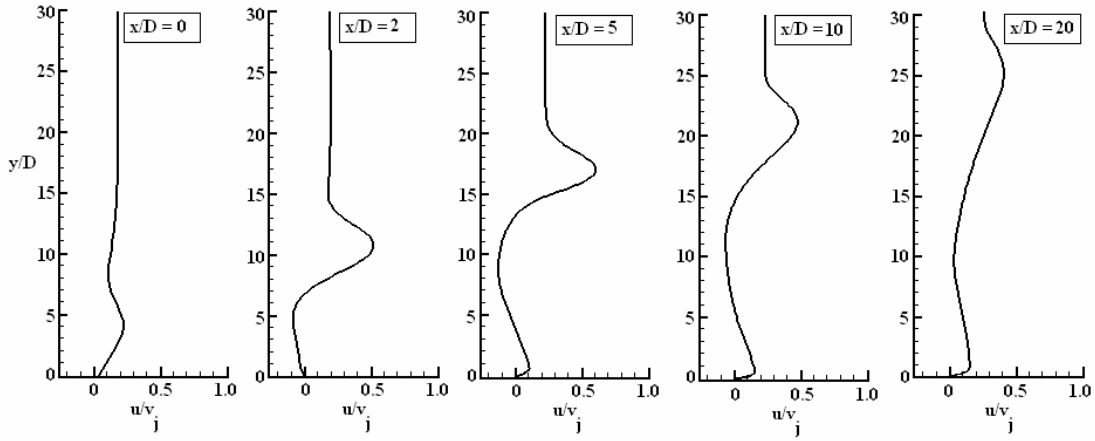

Fig. 4.6: Predictions of cross-stream component of mean velocity at different downstream locations ($z/D = 0$) for $R = 6$.

The qualitative differences of the velocity profile at various transverse planes are presented in Figs. 4.7 to 4.9. In Fig. 4.7 the cross-stream velocity profile at the jet transverse plane $z/D = 3$ is shown at five different downstream (x/D) positions. It is observed that though the trends of profiles are similar to those in the central plane the size of wake-like region is different. The size of the wake-like region is slightly smaller than the earlier case. Moreover the wall-jet-shear layer is more prominent and it is formed even at the position of $x/D = 2$.

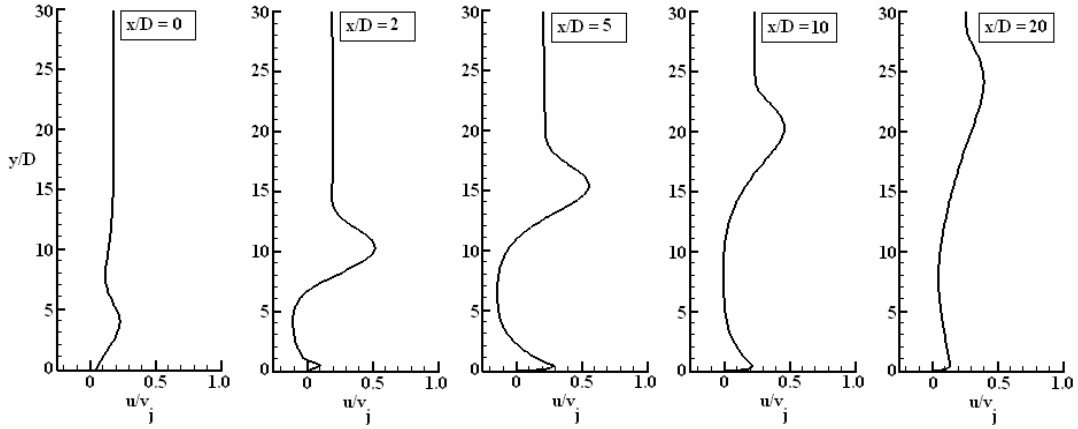

Fig. 4.7: Predictions of cross-stream component of mean velocity at different downstream locations ($z/D = 3$) for $R = 6$.

The corresponding profile at $z/D = 5$ are shown in Fig. 4.8. The velocity profile at the position x$/D = 0$ is distorted due to the shearing of jet flow with the crossflow on the transverse side. The size of wake-like region is smaller and wall-jet-like shear structure is larger than that for z$/D = 3$.

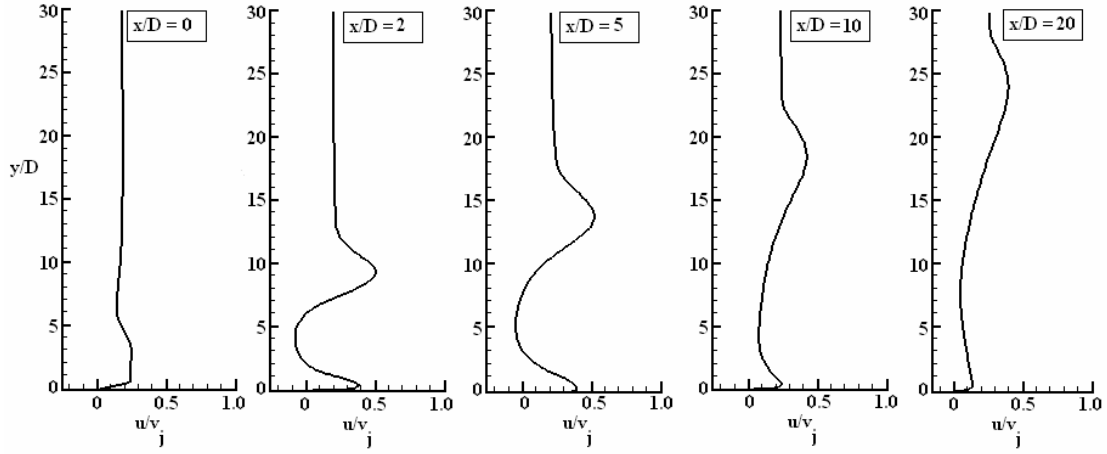

Fig. 4.8: Predictions of cross-stream component of mean velocity at different downstream locations (z/D = 5) for R = 6.

Fig. 4.9 shows the profiles at z/D = 6. The profiles at all downstream locations are expectedly different from those at the central plane (z/D = 0). The vertical height where the jet peak value occurs is less in this plane (z/D = 6) compared to those at central plane. Near the bottom wall, the wall-jet-shear layer is prominent at all downstream locations and even wall-jet-shear layer is formed at x/D = 0 with steep velocity gradients.

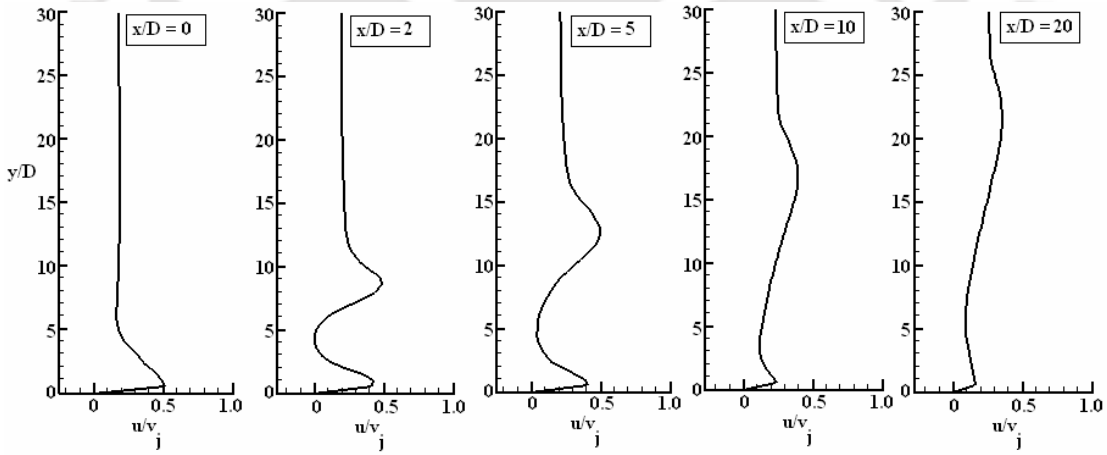

Fig. 4.9: Predictions of cross-stream component of mean velocity at different downstream locations (z/D = 6) for R = 6.

The positions of transverse planes, where cross-stream component velocity profiles are presented in the earlier paragraphs, are situated on the same side of the centre of the jet slot. The velocity profile in the transverse plane on the other side of the centre of the slot (z/D = -3) is presented in Fig. 4.10. The position of this plane is exactly opposite to the plane at z/D = 3. From the comparison of the velocity profiles at both planes (Figs.

4.7 and 4.10) it is observed that at all downstream positions these are similar in nature. Thus the profiles are symmetric about the central vertical plane (z/*D* = 0).

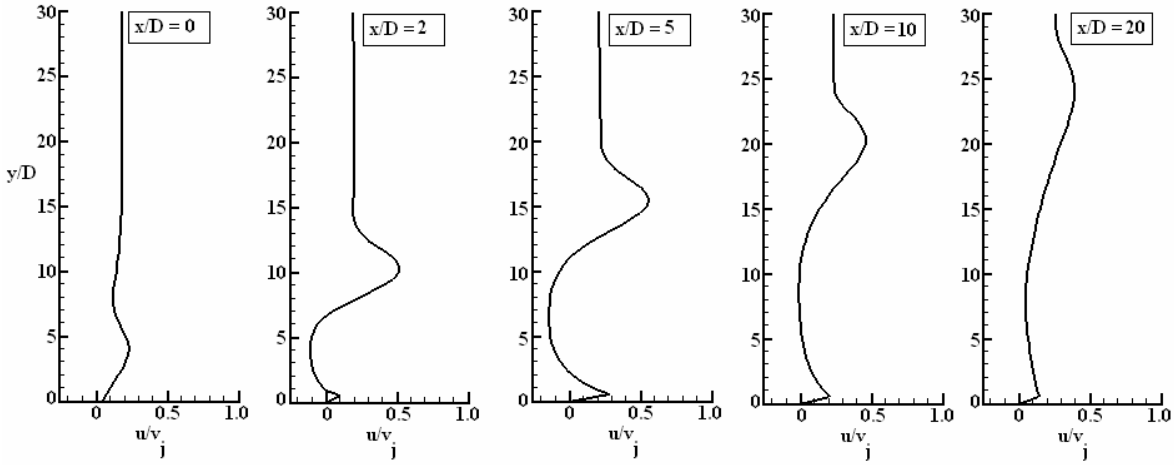

Fig. 4.10: Predictions of cross-stream component of mean velocity at different downstream locations (z/*D* = -3) for *R* = 6.

The cross-stream component of the mean velocity profile at different transverse planes (z/*D* = 0, 3, 5, 6 and -3) and at different downstream locations (x/*D* = 0, 2, 5, 10 and 20) for the velocity ratio *R* = 9 are shown in Figs. 4.11 to 4.15. The peak values of the cross-stream components are seen at higher values of *y*/*D* in Figs. 4.11 to 4.15 compared to the case of jet with *R* = 6 (Figs. 4.6 to 4.10). Thus the jet penetrates more in to the crossflow compared to the case with the velocity ratio *R* = 6. In this case also the velocity profiles show weak wall-jet-shear structures, wake-like region and the jet-shear layer structures. It is observed that the size of the wall-jet-shear structure is smaller with low velocity gradient due to the weak effect of the crossflow. In this case also the cross-stream component profiles are symmetric about the central vertical plane (z/*D* = 0).

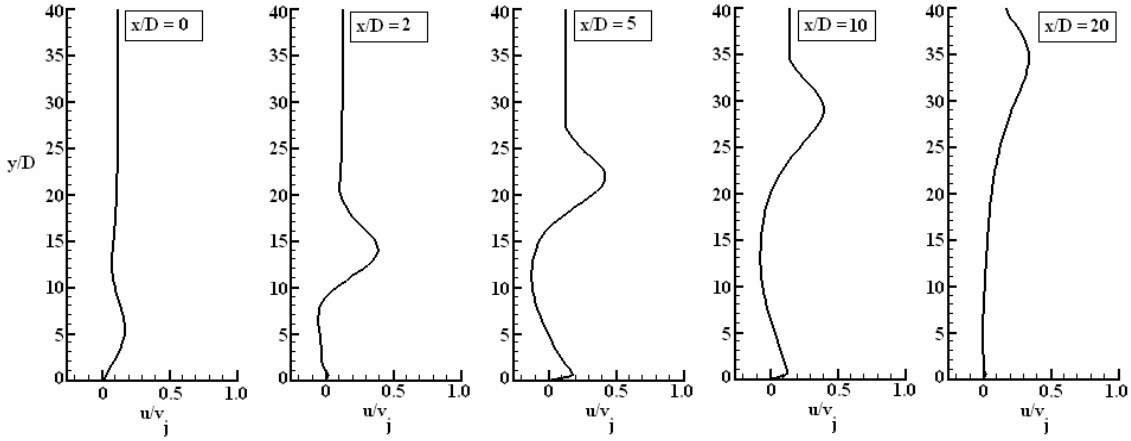

Fig. 4.11: Predictions of cross-stream component of mean velocity at different downstream locations ($z/D = 0$) for $R = 9$.

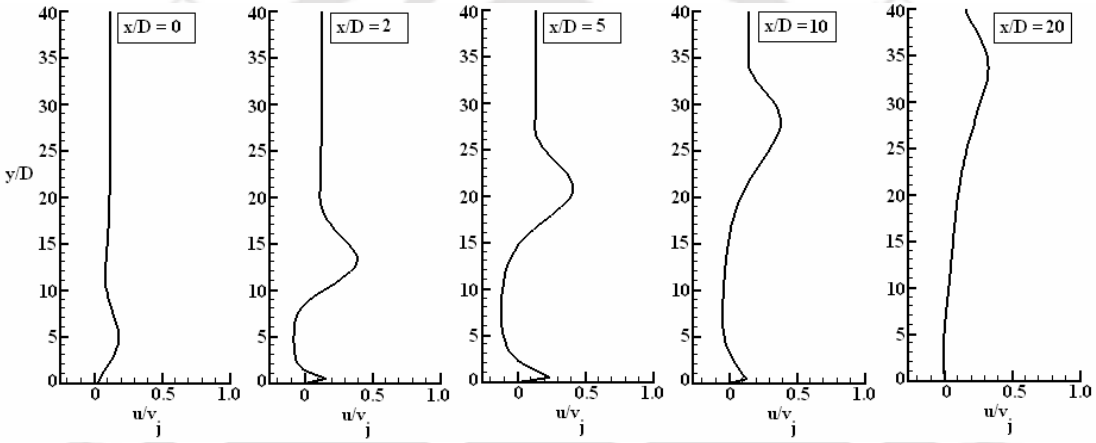

Fig. 4.12: Predictions of cross-stream component of mean velocity at different downstream locations ($z/D = 3$) for $R = 9$.

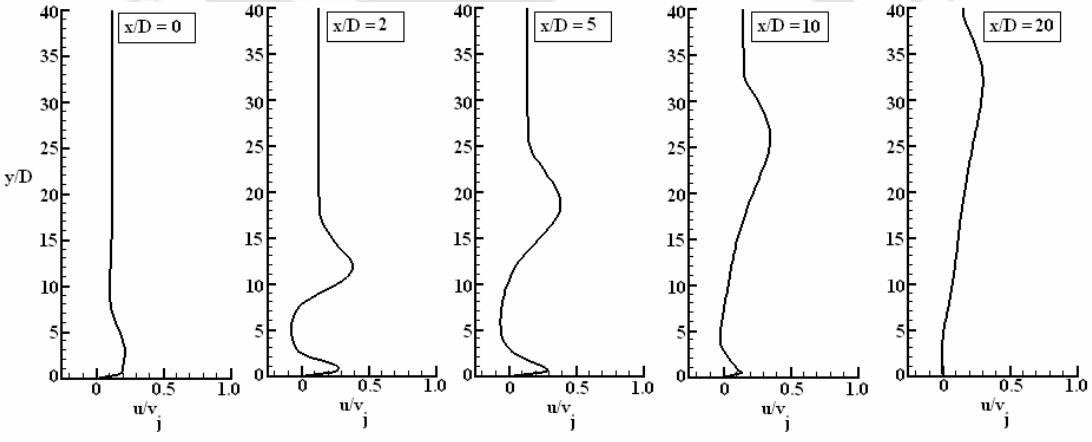

Fig. 4.13: Predictions of cross-stream component of mean velocity at different downstream locations ($z/D = 5$) for $R = 9$.

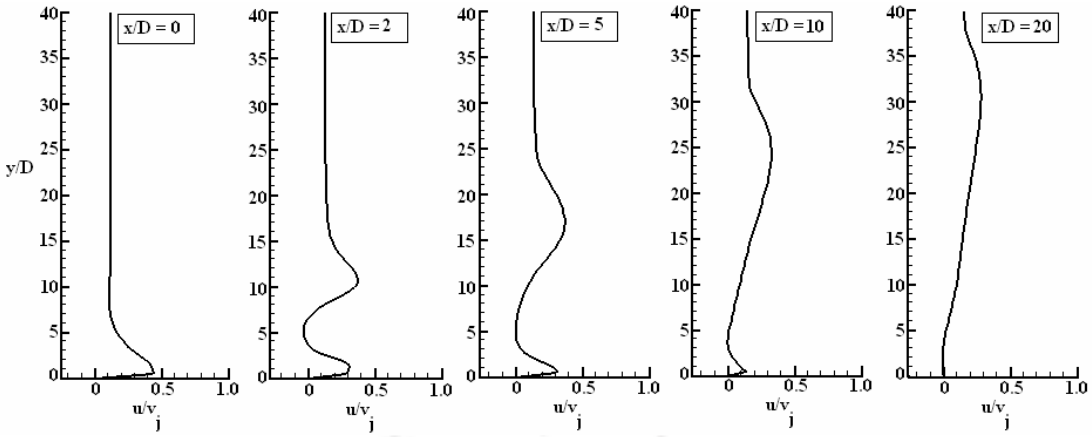

Fig. 4.14: Predictions of cross-stream component of mean velocity at different downstream locations (z/D = 6) for R = 9.

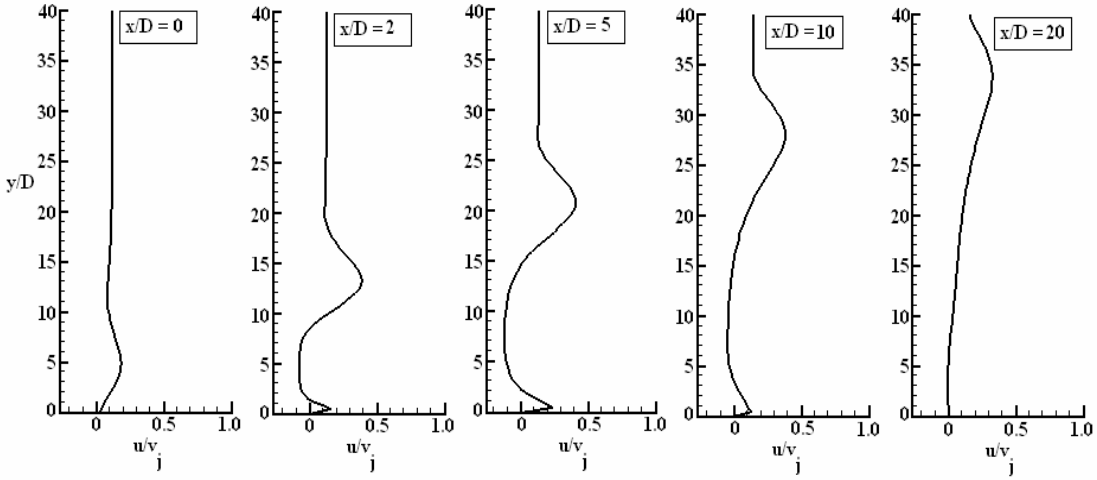

Fig. 4.15: Predictions of cross-stream component of mean velocity at different downstream locations (z/D = -3) for R = 9.

The predictions of the vertical component of the mean velocity at different transverse planes and at different downstream positions are shown in Figs 4.16 to 4.20 for the velocity ratio R = 6. Fig. 4.16 shows the downstream development of the vertical component of the mean velocity in the jet central plane (z/D = 0). At the jet discharge point (x/D = 0), the vertical component of the velocity is largely unaffected by the crossflow up to about y/D = 3, till which point the jet is almost straight. After a certain height, the jet is deflected and therefore the value of the vertical velocity component reduces. Not very far downstream of the jet slot (at x/D = 2) a wake-like region is formed not near the wall, as the near wall region is occupied by a wall-jet flow which is formed due to an inward motion of the surrounding fluid.

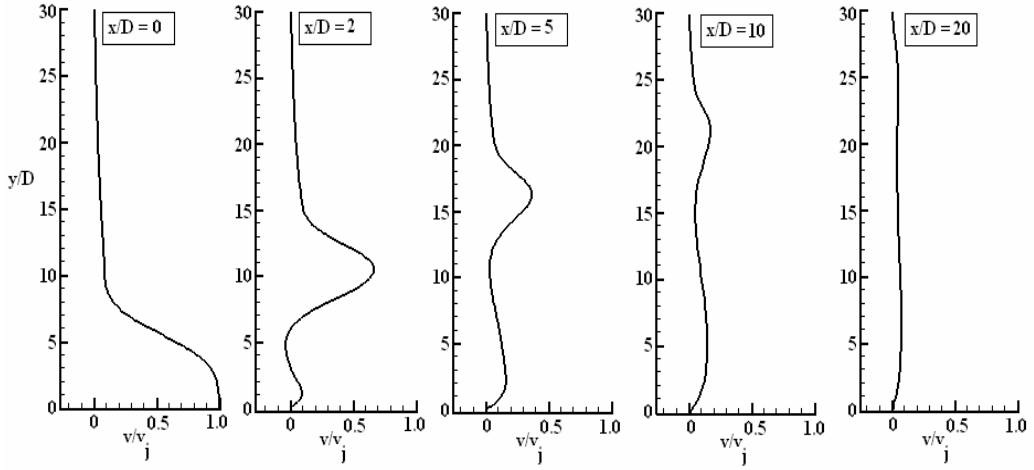

Fig. 4.16: Predictions of vertical component of mean velocity at different downstream locations ($z/D = 0$) for $R = 6$.

At $x/D = 2$, the wake-like region starts at approximately $y/D = 3$ and moves away from the wall as one goes in the downstream direction. In the wake-like region a downward motion of the fluid is observed whereas an upward motion of the fluid is observed beneath it, which explains the negative v-velocities at approximately $y/D = 4$ and positive v-velocities at approximately $y/D = 1$. Further downstream the jet becomes almost horizontal and runs parallel to the crossflow. As there is no existence of the vertical jet, the values of the vertical components are quite small at those locations.

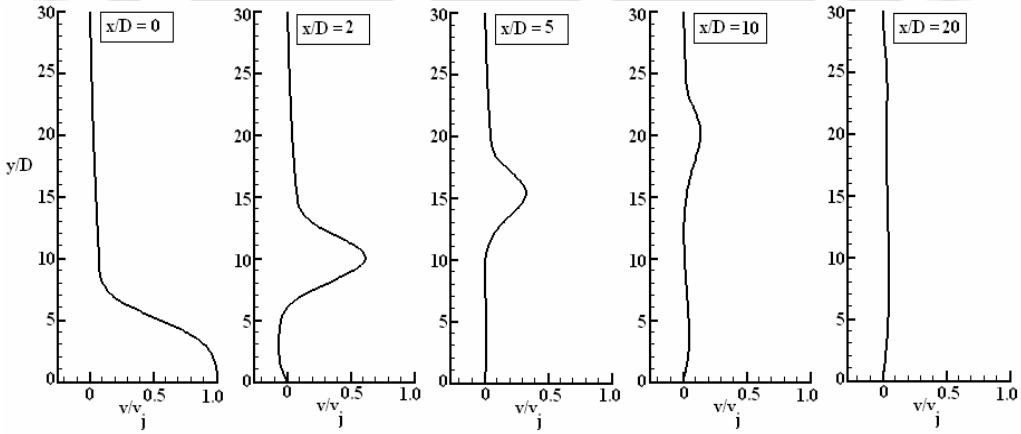

Fig. 4.17: Predictions of vertical component of mean velocity at different downstream locations ($z/D = 3$) for $R = 6$.

The changes of the vertical component profile at different transverse planes are shown in Figs. 4.17 to 4.19. The value of the vertical component near the bottom wall and at the jet exit region is reduced at the two spanwise planes $z/D = 5$ and 6 compared to that at the positions of $z/D = 0$ and 3. The velocity gradients $(\partial v / \partial y)$ in the wall-jet layer are smaller and the negative velocity in the wake-like region is reduced as one

move from the centre of the jet towards the sidewalls. The vertical penetration height reduces as one moves away from the jet centre. This is due to the entrainment and mixing of the jet with the crossflow. The shearing of the crossflow with the jet flow at the jet edge (z/*D* = 5) is seen at the location *x*/*D* = 0 (Fig. 4.18), where the vertical component of the mean velocity suddenly increases to a higher value thus producing a steep velocity gradient $(\partial v / \partial y)$. At *z*/*D* = 6 (Fig. 4.19) the influence of the jet is limited up to a small downstream location (*x*/*D* = 5). The effect of the sidewalls on the flow is observed here. The damping effect of the sidewall (at *z*/*D* = 6) produces some downward flow near the bottom wall at positions *x*/*D* = 0 and 2.

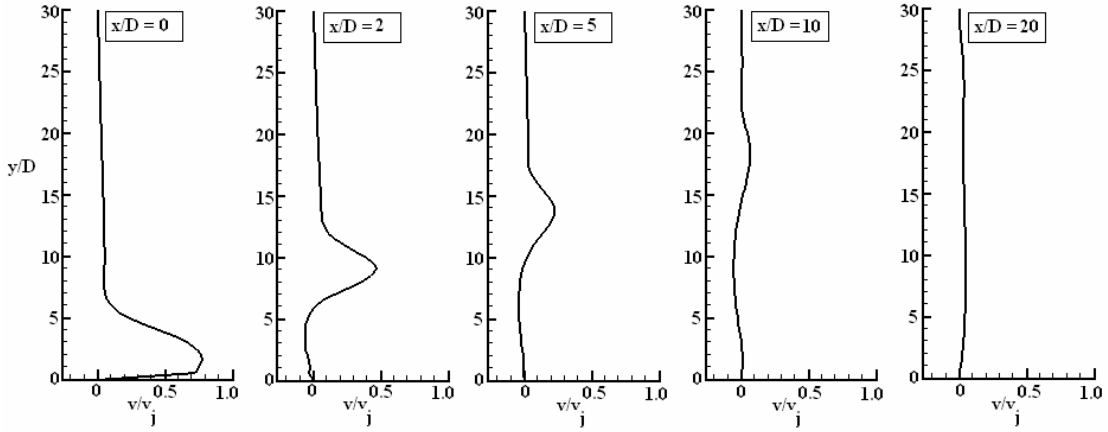

Fig. 4.18: Predictions of vertical component of mean velocity at different downstream locations (*z*/*D* = 5) for *R* = 6.

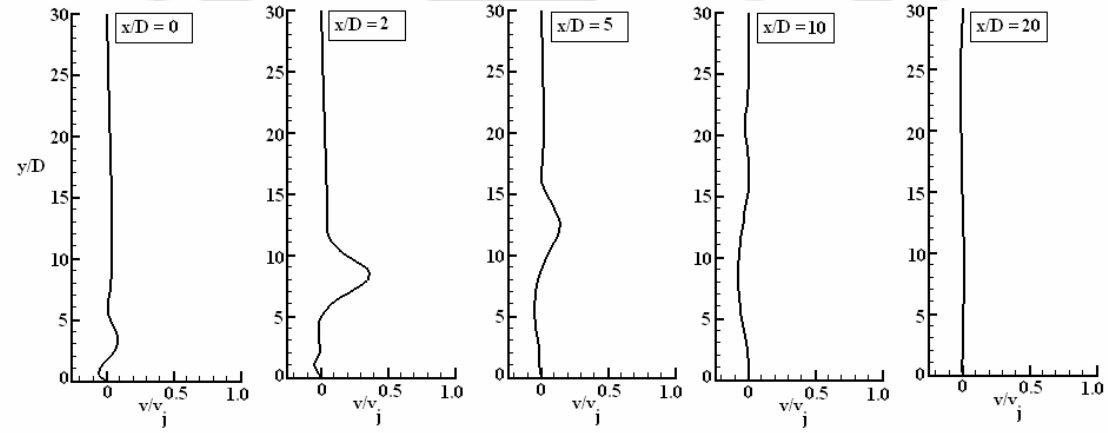

Fig. 4.19: Predictions of vertical component of mean velocity at different downstream locations (z/*D* = 6) for *R* = 6.

The profile of the vertical velocity component at *z*/*D* = -3 is shown to check the symmetry of the velocity component about the central vertical plane. When compared with Fig. 4.17, symmetry is seen to exist.

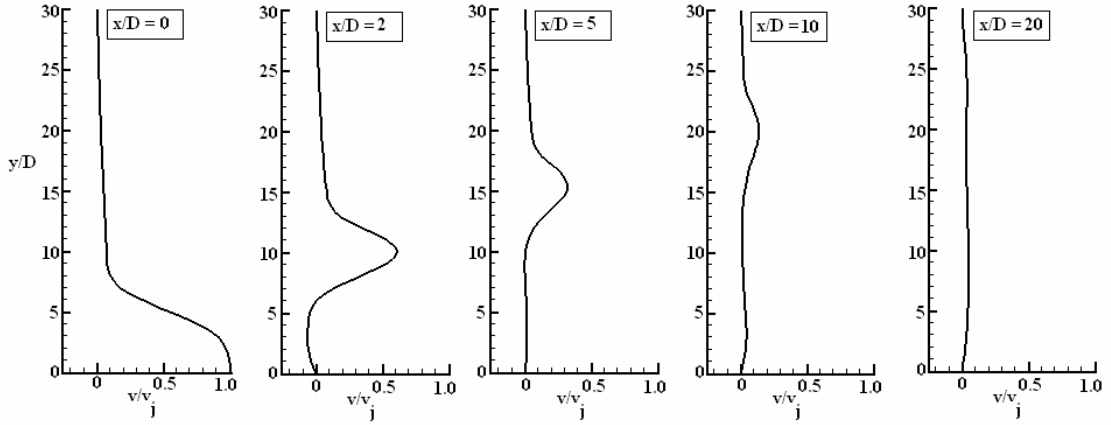

Fig. 4.20: Predictions of vertical component of mean velocity at different downstream locations (z/D = -3) for R = 6.

Figs. 4.21 to 4.25 show the vertical component of the mean velocity at different transverse planes and at different downstream locations for the velocity ratio R = 9. Qualitatively the velocity profiles are similar to the case of R = 6 (Figs. 4.16 to 4.20). Since the jet is comparatively strong in this case, the component of the vertical velocities show a high value, thus the jet trajectory is more in this case compared to the case with R = *6*. The velocity gradient $(\partial v / \partial y)$ near the bottom wall at all down stream positions at z/D = 0, is observed to be less compared to the case with R = 6. The shearing of the fluid at the jet exit point (x/D = 0) along the plane (z/D = 5) is more in this case (Fig. 4.23) compared to the case of R = 6 (Fig. 4.18). A reverse flow is observed near the bottom wall at the positions x/D = 0 and 2 in the plane z/D = 6. To check the symmetry, the velocity profiles are shown at other side of the central vertical plane at z/D = -3. It is observed that in this case also the profiles are symmetric about the central plane of the jet.

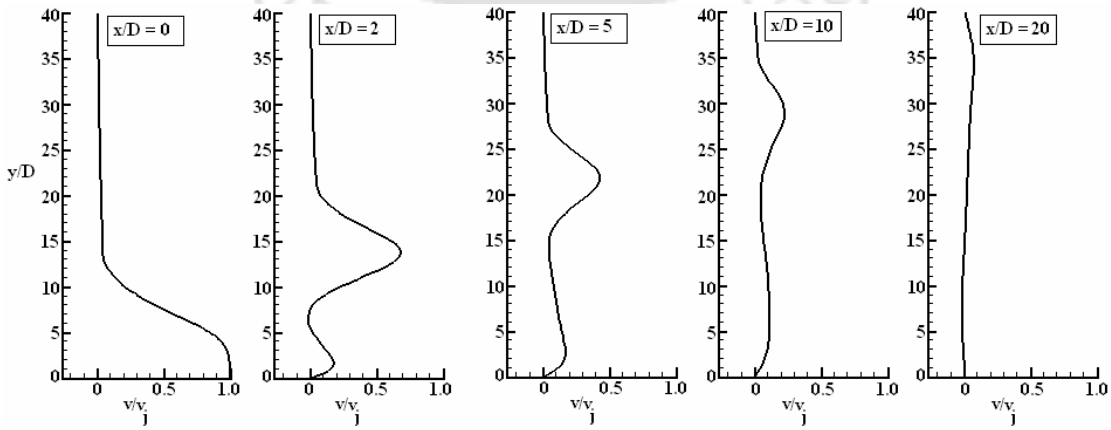

Fig. 4.21: Predictions of vertical component of mean velocity at different downstream locations (z/D = 0) for R = 9.

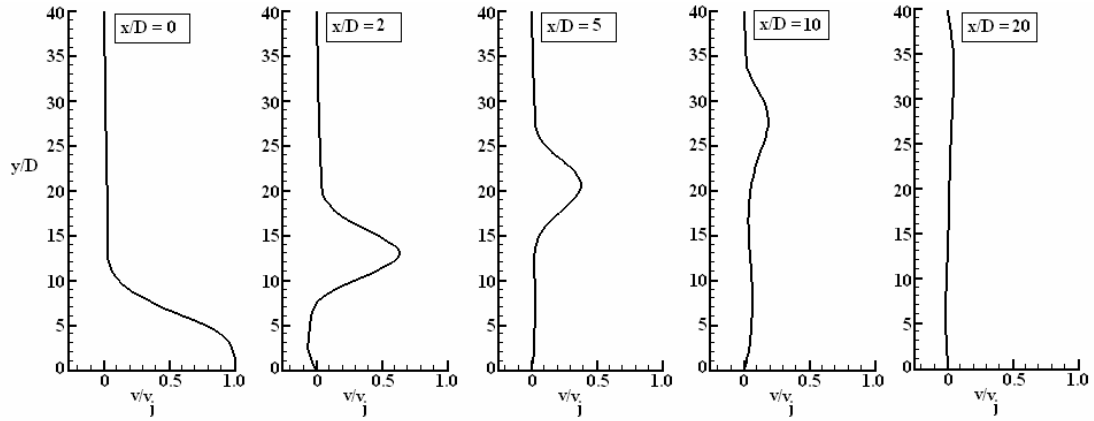

Fig. 4.22: Predictions of vertical component of mean velocity at different downstream locations ($z/D = 3$) for $R = 9$.

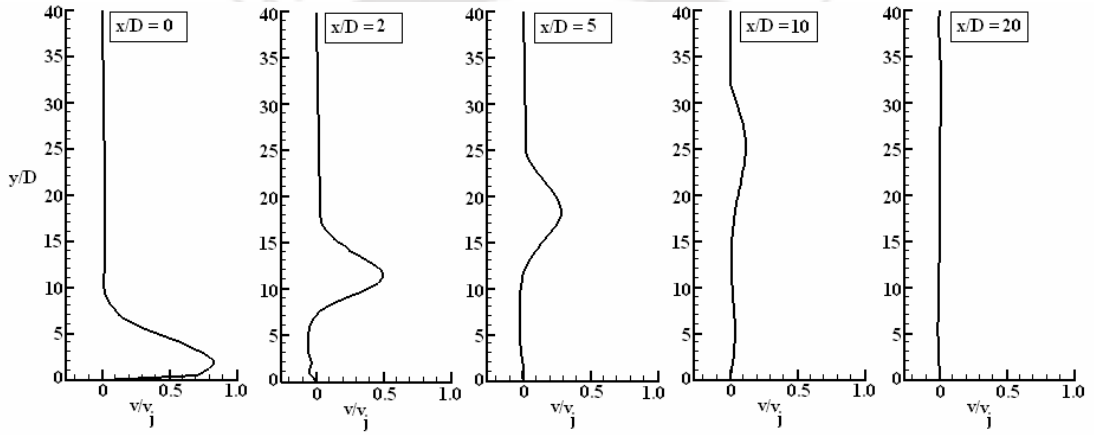

Fig. 4.23: Predictions of vertical component of mean velocity at different downstream locations ($z/D = 5$) for $R = 9$.

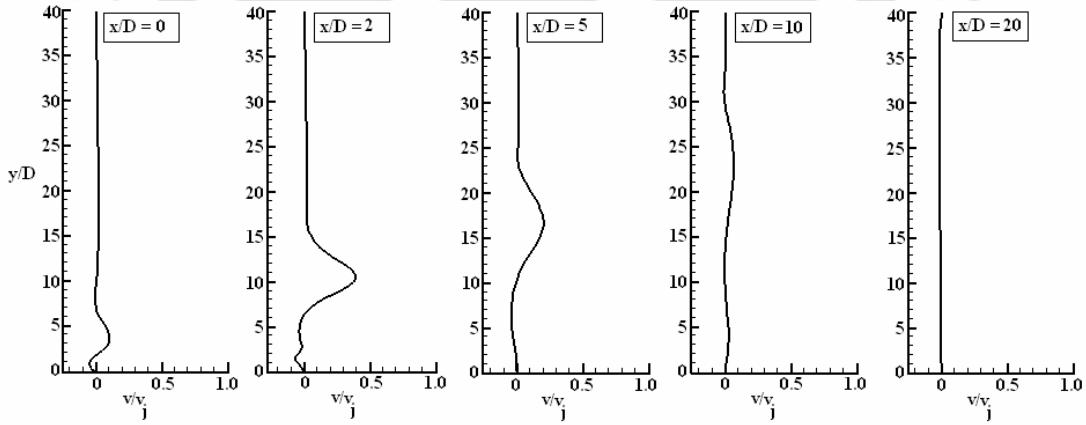

Fig. 4.24: Predictions of vertical component of mean velocity at different downstream locations ($z/D = 6$) for $R = 9$.

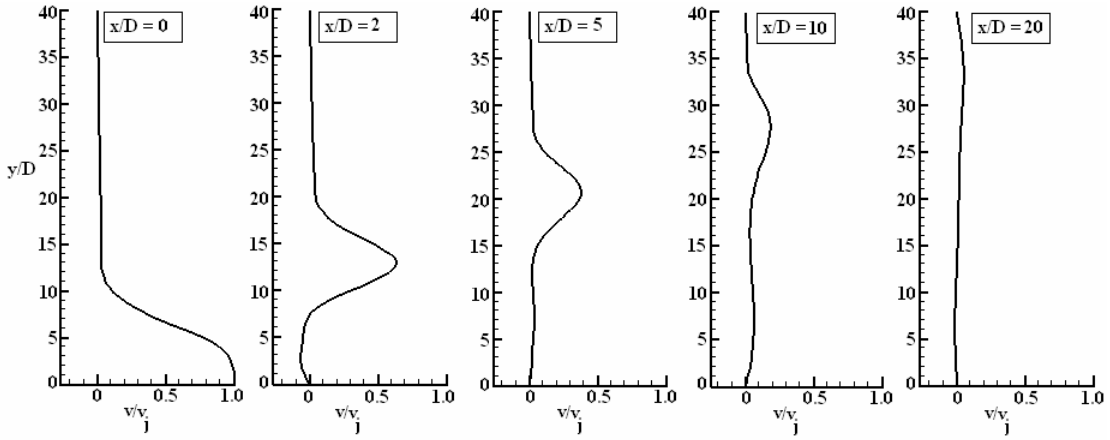

Fig. 4.25: Predictions of vertical component of mean velocity at different downstream locations (z/D = -3) for R = 9.

It is to be noted that the most of the flow features that are discussed in the present chapter were absent in the 2D investigations of the flow field. One of the important aspects of the flow three-dimensionality is manifested by the presence of transverse or spanwise component of the mean velocity in the flow field. In spite of no transverse velocity being prescribed both at the crossflow and jet inlet as boundary conditions, the fluid experiences the transverse velocity in the flow field. The secondary motion and the existence of counter-rotating vortices in the y-z and x-z planes can be depicted by the profiles of the transverse and vertical component of mean velocities. The values of the transverse velocities at the jet central plane (z/D = 0) are found to be zero (not shown in Fig.) due to symmetry of the flow. The variation of transverse velocity at different downstream positions and at different transverse planes are shown in Figs. 4.26 to 4.29 for the velocity ratio of R = 6.

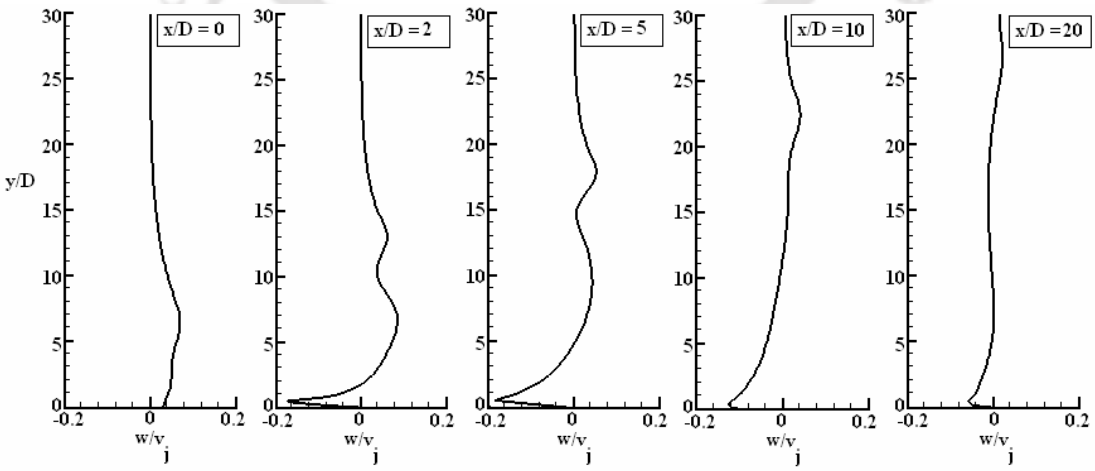

Fig. 4.26: Predictions of spanwise component of mean velocity at different downstream locations (z/D = 3) for R = 6.

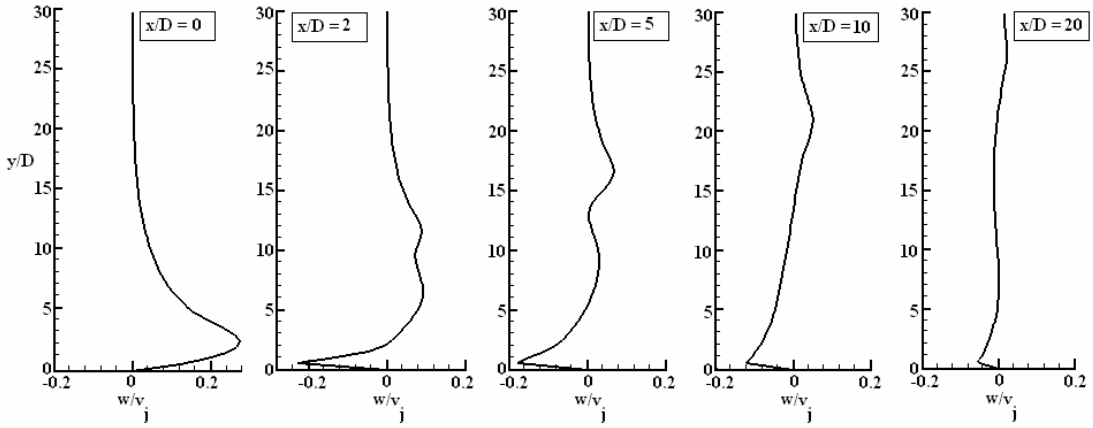

Fig. 4.27: Predictions of spanwise component of mean velocity at different downstream locations (z/D = 5) for R = 6.

The physical explanation of spanwise velocity variations can be provided with the velocity vector plots presented at different y-z and x-z planes (Section 4.4.3). Fig. 4.26 shows the variation of the spanwise component of velocity at the plane z/D = 3 at different downstream locations. At the jet exit (x/D = 0), the jet shows small components of transverse velocity acting in the direction from centre of the jet towards the sidewall immediately after leaving the jet slot i.e. y/D = 0. The value of this component is approximately 0.04 and due to this component the flow is not perfectly vertical and is deflected towards the sidewalls. Since the strength of the crossflow is relatively weak, compared to the jet, the fluids on both sides of the jet spread into the transverse direction after leaving the slot. Downstream of the jet exit (x/D = 2) the inception of the counter-rotating vortex pair (CRVP) starts and from this location, the transverse velocity is controlled by both the CRVP and the wake vortices. A low pressure region prevails in the flow field close to the bottom wall and behind the jet slot, due to which, the surrounding fluid moves towards the centre of the jet close to the bottom wall. Thus the transverse component acts in the direction from sidewall towards the central vertical plane of the jet. Velocities towards the central vertical planes close to the bottom wall are reported at all downstream positions (x/D = 2, 5, 10 and 20) and at all the planes z/D = 3, 5, and 6 (Figs. 4.26 to 4.28). Moving away from the bottom wall this variation reduces. Further downstream the low pressure region vanishes and therefore the transverse movement is not prominent giving small values of the spanwise velocity. A small variation of the spanwise velocity is seen at some vertical height (y/D = 7 to 13) at x/D = 2 at the plane z/D = 3 (Fig. 4.26). This is due to the CRVP which entrains the fluid towards the centre of the jet. The vertical height increases with the downstream distance due to jet spreading or increase of the size of the CRVP.

A higher value of transverse component of the mean velocity is observed close to the bottom wall at z/D = 5 and x/D = 0 (Fig. 4.27) indicating more spreading of the jet at that location compared to that at z/D = 3. A reverse trend of transverse component of mean velocity is observed near the bottom wall at z/D = 6 and x/D = 0 (Fig. 4.28). The transverse velocity acts towards the central vertical plane. At other down stream positions (x/D = 2, 5, 10 and 20), the profile of the transverse component of mean velocity are similar to those at the plane z/D = 5. Profiles of the transverse velocity component at z/D = - 3, opposite to the z/D = 3 (Fig. 4.26) are shown in Fig. 4.29.for checking the symmetry of the flow field. From Figs. 4.26 and 4.29 it is observed that the flow field is symmetric to the jet central vertical plane (z/D = 0).

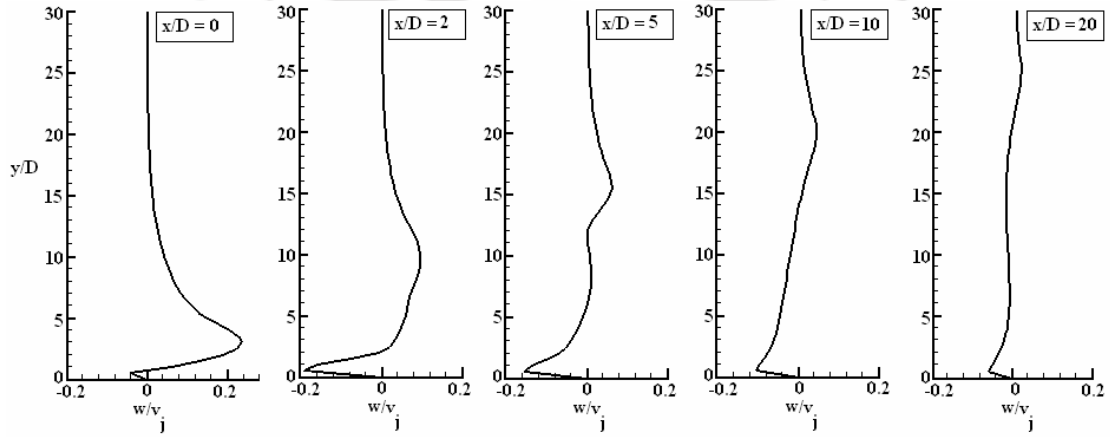

Fig. 4.28: Predictions of spanwise component of mean velocity at different downstream locations (z/D = 6) for R = 6.

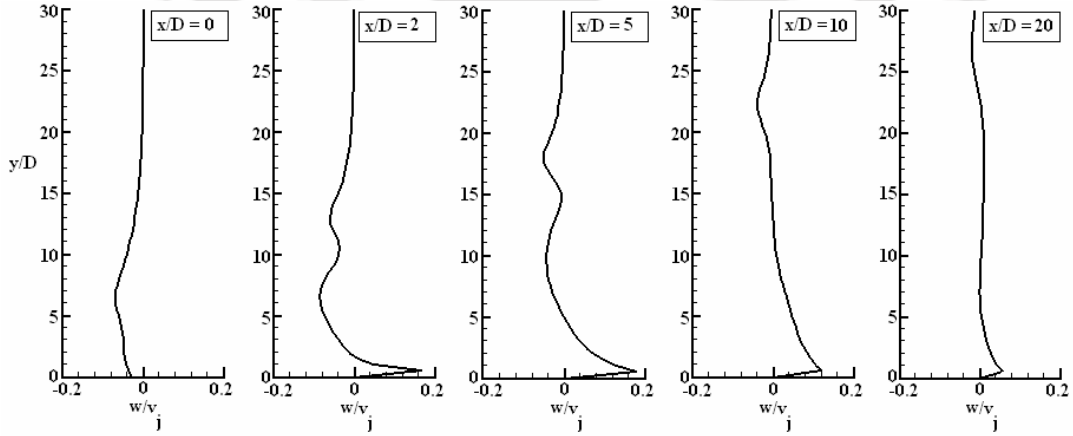

Fig. 4.29: Predictions of spanwise component of mean velocity at different downstream locations (z/D = -3) for R = 6.

The variations of the spanwise velocity at different downstream locations at different transverse planes for the velocity ratio R = 9 are shown in Figs. 4.30 to 4.33.

In this case the spreading of the jet at both sides (at x/D = 0) are observed more compared to the case of R = 6 (Figs. 4.26 to 4.29). Downstream of the jet slot (x/D = 2) the spanwise velocity is more at all the transverse planes (z/D = 3, 5 and 6) compared to the case with R = 6. Moreover the flow reversal close to the bottom wall at z/D = 6 and at the position x/D = 0 is observed to be more prominent compared to the case with R = 6. The symmetry of the flow field to the central vertical plane is well maintained in this case also by showing opposite velocity profiles at z/D = -3 compared to the profile at z/D = 3.

It may be noted that the predicted trends of the mean velocity profiles u, v and w provided so far in the present work resemble the similar predictions for square jets in crossflow (Ajersch et al., 1997, Hoda and Acharya, 2000 and Keimasi and Rahni, 2001).

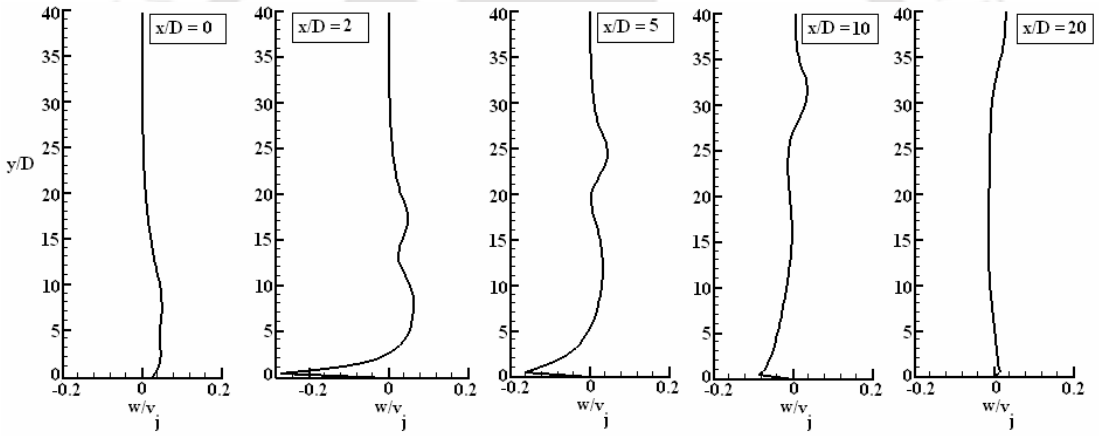

Fig. 4.30: Predictions of spanwise component of mean velocity at different downstream locations (z/D = 3) for R = 9.

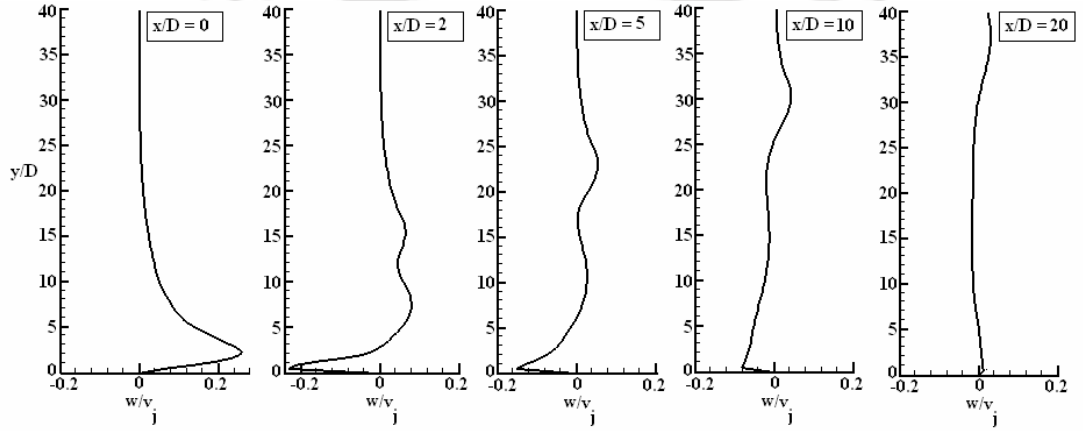

Fig. 4.31: Predictions spanwise component of mean velocity at different downstream location (z/D = 5) for R = 9.

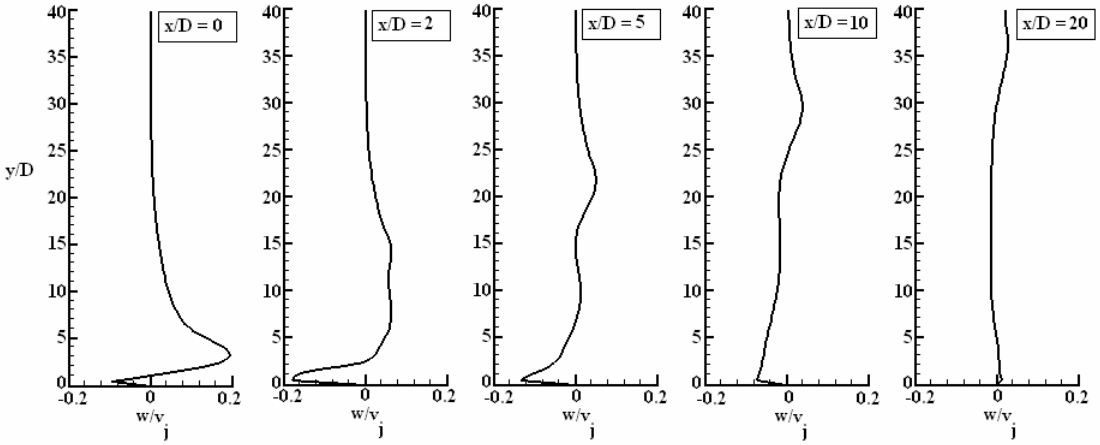

Fig. 4.32: Predictions of spanwise component of mean velocity at different downstream locations (z/D = 6) for R = 9.

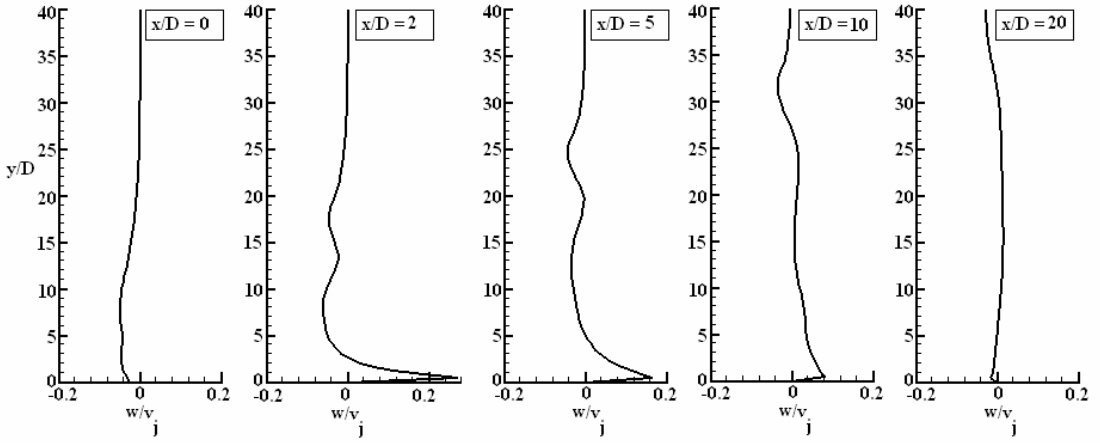

Fig. 4.33: Predictions of spanwise component of mean velocity at different downstream locations (z/D = -3) for R = 9.

To carry out further studies on the flow three-dimensionalities and the symmetry of the flow field we have shown in Figs. 4.34 to 4.36 the variations of all the components of mean velocities (u, v and w) in the spanwise direction at a vertical distance of y/D = 5 from the bottom wall at different downstream locations for the velocity ratio R = 6. Fig. 4.34 shows the variation of the cross-stream velocity in the spanwise direction at different downstream locations (x/D = 0, 5, 15 and 20). The variation of the cross-stream component can be clearly explained both from the Fig. 4.34 and the vector plot in x-z plane (Fig. 4.63, Section 4.4.3). Sufficient amount of crossflow-stream velocity is reported at the location of x/D = 0 in the vicinity of the jet slot. This shows that the jet is not completely vertical and it is already deflected at a height of y/D = 5. The cross-stream component is weakened slightly at both sides of the jet edges due to the lateral spreading of the jet. The cross-steam velocity component again increases at the gap region between the jet slot and the sidewall and

ultimately becomes zero at the sidewalls. Further downstream (x/D = 5), the flow is influenced by two wake vortices behind the jet slot (Fig. 4.63). The cross-stream velocity component shows reverse flow at the region of the wake vortex formation. The cross-stream velocity component is larger at the gap region compared to that at the position of x/D = 0 due to the contraction of the flow passage. The flow reversal disappear at the location of x/D = 10 (Fig. 4.36) and therefore the wake characteristics are reduced at the downstream locations of x/D = 15 and 20. The recovery of the cross-stream component is observed at these two locations. Two points of inflexion near the central plane are observed at all the downstream positions.

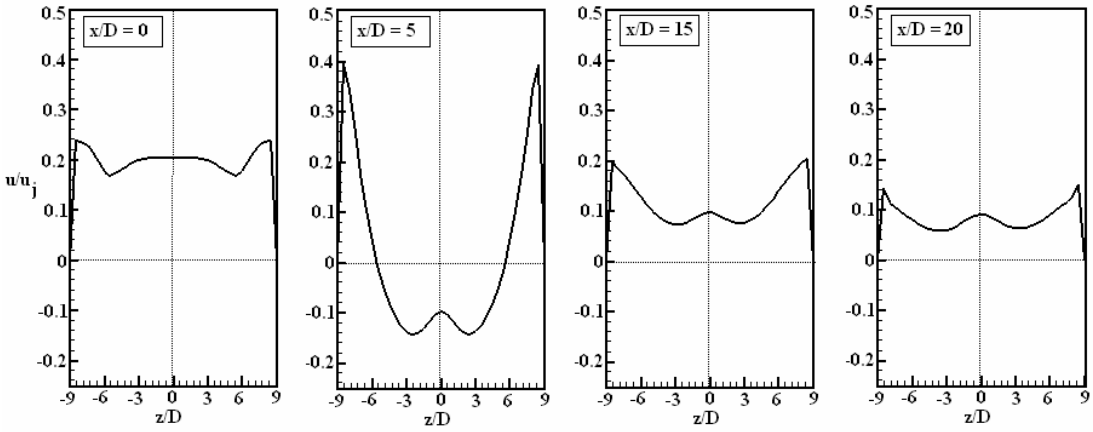

Fig. 4.34: Spanwise variation of cross-stream component of mean velocity at different downstream locations for R = 6 at vertical height y/D = 5.

The variations of the vertical component of the mean velocity in the spanwise direction at a vertical distance of y/D = 5 from the bottom wall and at different downstream locations are shown in Fig. 4.35 for the velocity ratio R = 6. The vertical component is quite strong around the centre of the jet slot (z/D = 0) at the jet exit point (x/D = 0). The value of the vertical component is approximately 0.75 and thus the jet is not completely vertical and the deflection of the jet starts even at the vertical position of y/D = 5. Moving from the centre of the jet slot towards the sidewall, the value of the vertical component reduces and it acts in opposite direction i.e. downward motion near the sidewalls. This downward motion of the jet fluid near the sidewalls can be better understood from the y-z vector plot (Fig. 4.58, Section 4.4.3).

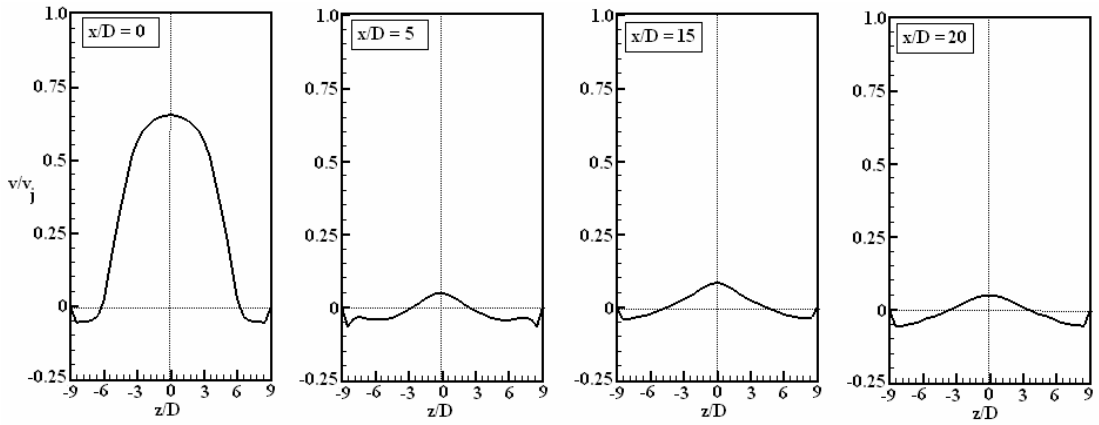

Fig. 4.35: Spanwise variation of vertical component of mean velocity at different downstream locations for $R = 6$ at vertical height $y/D = 5$.

At other downstream locations the spanwise variation of the vertical component is controlled by the CRVP. The small positive value of the vertical component at the centre of the jet slot ($z/D = 0$) is due to the upward motion of the fluid engulfed by the CRVP. The negative value of the vertical component is due to the downward motion of the fluid near the sidewall, which is also imparted by the CRVP formation.

Fig. 4.36 shows the variation of the spanwise component of the mean velocity in the spanwise directions at a vertical distance of $y/D = 5$ from the bottom wall and at different downstream locations for the velocity ratio $R = 6$. At the jet exit region ($x/D = 0$) the spanwise components are quite high at both the edges of the jet slot. The high velocity jet after emerging from the jet slot spreads at the both edges of the jet slot and moves towards the sidewall, thus reporting a high value of the spanwise component. The variation of the spanwise component can be understood more clearly from the y-z vector plot (Fig. 4.58, Section 4.4.3). The values of transverse velocity component decreases with x/D distance, which reveals that as one moves downstream, the influence of the transverse stream on the flow field at a vertical height of $y/D = 5$ is very small. Moreover the variation is controlled by the CRVP formation at all the downstream locations. Expectedly the average spanwise velocity component is zero in the symmetry plane.

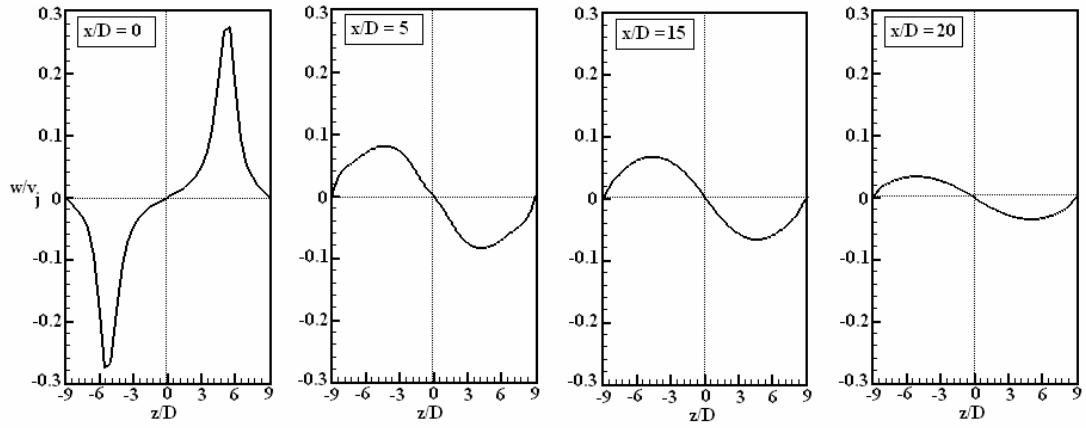

Fig. 4.36: Spanwise variation of spanwise component of mean velocity at different downstream locations for $R = 6$ at vertical height $y/D = 5$.

The spanwise variations of u, v and w velocities at different downstream locations at a vertical height of $y/D = 5$ from the bottom wall are shown in Figs. 4.37 to 4.39 for a velocity ratio $R = 9$. Fig. 4.37 shows the variation of the cross-stream component in the spanwise direction at different downstream locations.

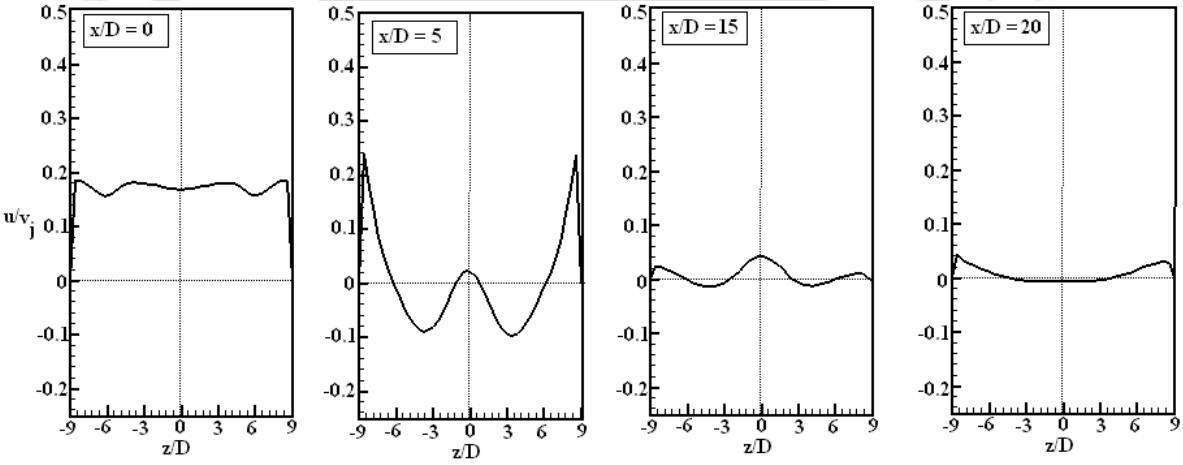

Fig. 4.37: Spanwise variation of cross-stream component of mean velocity at different downstream locations for $R = 9$ at vertical height $y/D = 5$.

The trend of the variation is same as in the case with $R = 6$, but the cross-stream component is smaller in this case. The crossflow is relatively weaker in this case and therefore the value of the cross-stream component is small. Moreover the size of the wake vortices formed are smaller than that in the case with $R = 6$ which would be explained in Section 4.4.3.

The variation of the vertical component of the mean velocity in the spanwise direction at a vertical distance of $y/D = 5$ from the bottom wall and at different downstream locations is shown in Fig. 4.38 for the velocity ratio $R = 9$.

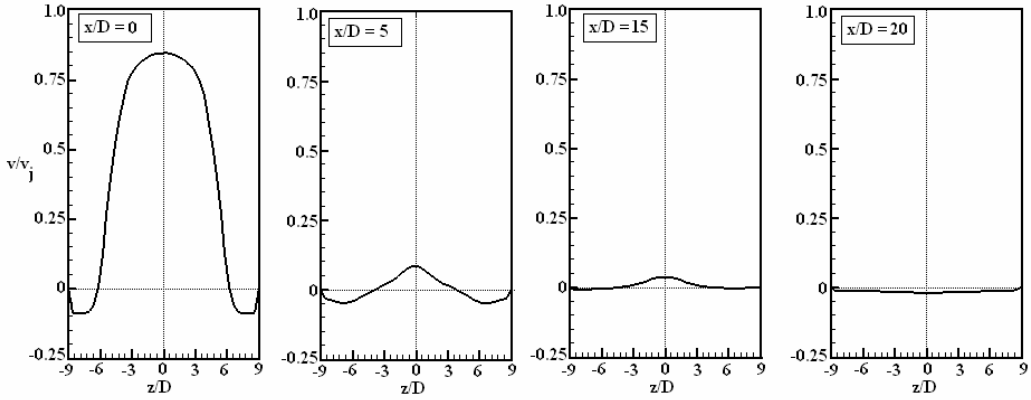

Fig. 4.38: Spanwise variation of vertical component of mean velocity at different downstream locations for $R = 9$ at vertical height $y/D = 5$.

The value of the vertical component around the centre of the jet slot ($z/D = 0$) at the jet exit point ($x/D = 0$) is higher than that in the case with $R = 6$, because of the higher strength of the jet .But at other downstream locations the values of the vertical components are smaller. The variations of the vertical components at these locations are controlled by the CRVP formation and these are formed at a higher position than that at y/D = 5 (Fig. 4.61, Section 4.4.3). Therefore the variations are very small. Similar observation is also made in case of variation of the spanwise velocity component in the spanwise direction (Fig. 4.39). The variation of the spanwise velocity at the near-field (x/D = 0 and 5) is higher, where as the variation at the far downstream locations are less due to CRVP formation at the upper position than y/D = 5 of the flow field.

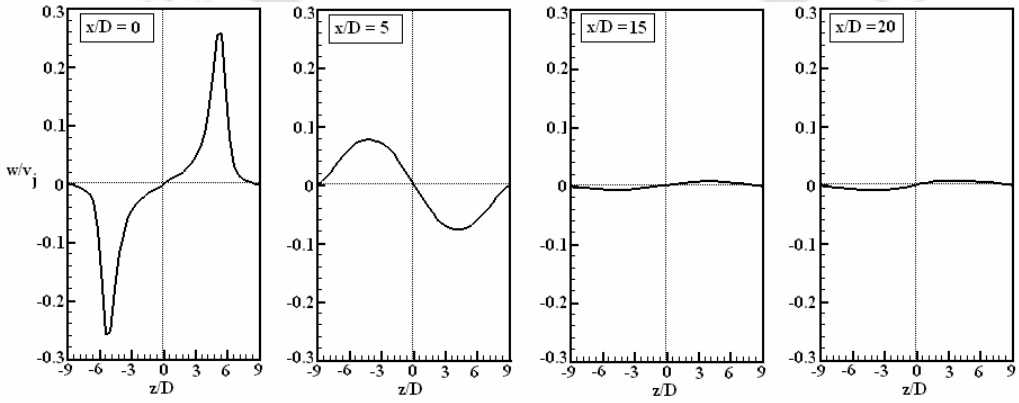

Fig. 4.39: Spanwise variation of spanwise component of mean velocity at different downstream locations for $R = 9$ at vertical height $y/D = 5$.

From the observation of the streamwise variations of u, v and w for $R = 6$ and 9 it can be concluded that the flow field is symmetric and all the variations show a

symmetry point about z/*D* = 0. This phenomenon was not observed in the case of the square jet in crossflow (Hoda and Acharya, 2000), which was slightly skewed in the transverse direction. Moreover Cusano and Plesniak (1999) also reported asymmetries of the flow field in a rectangular jet in a crossflow.

4.4.2 Turbulence Kinetic Energy and Turbulence Stresses

The prediction of the turbulence kinetic energy at different transverse planes and at different downstream locations are shown in Figs. 4.40 to 4.43 for the velocity ratio *R* = 6. The variation of the turbulence kinetic energy with the vertical distance (*y/D*) at different downstream locations in the jet central plane (z/*D* = 0) is shown in Fig. 4.40. The development of the turbulence kinetic energy can be described in three regions. The first region is the jet exit region (*x/D = 0*), where its distribution is governed by an interaction of different mechanisms. The kinetic energy is transported from the crossflow boundary layer and the jet flow. It is produced and destroyed by various mean velocity gradients. Though the generation of the kinetic energy depends upon different velocity gradients, among them the cross-stream velocity gradient ($\partial u / \partial y$) is the dominant factor. Thus the maximum value of the kinetic energy is observed at the location of the maximum velocity gradient.

The second region is at the downstream of the jet exit (*x/D* = 2 and 5). In this region the velocity gradient ($\partial u / \partial y$) becomes significantly large in the jet-shear layer and due to this, the production of the kinetic energy is high in this region.

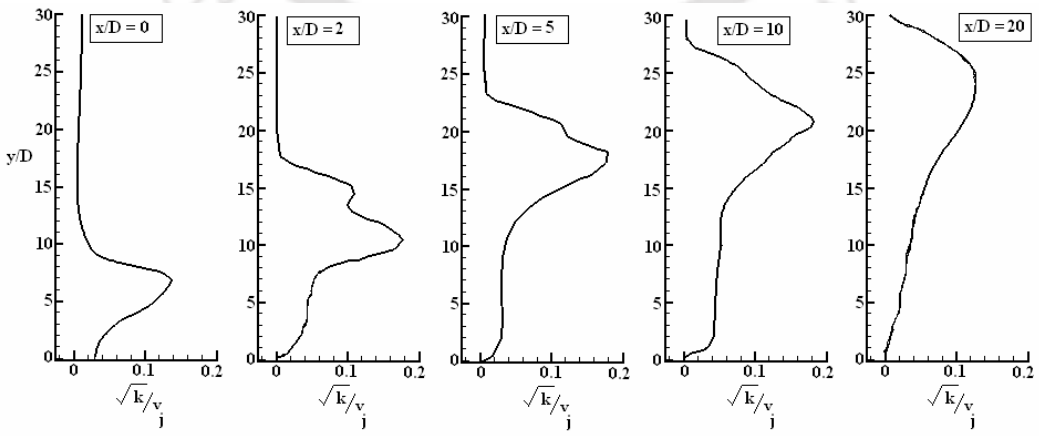

Fig. 4.40: Predictions of turbulence kinetic energy at different downstream locations (z/*D* = 0) for *R = 6*.

Due to a sharp velocity gradient in the wall-jet structure near the wall a steep increase of turbulence kinetic energy is reported near the wall. The third region is the further downstream regions (*x/D* = 10 and 20), where strong gradients of the velocity disappear thus producing less turbulence kinetic energy.

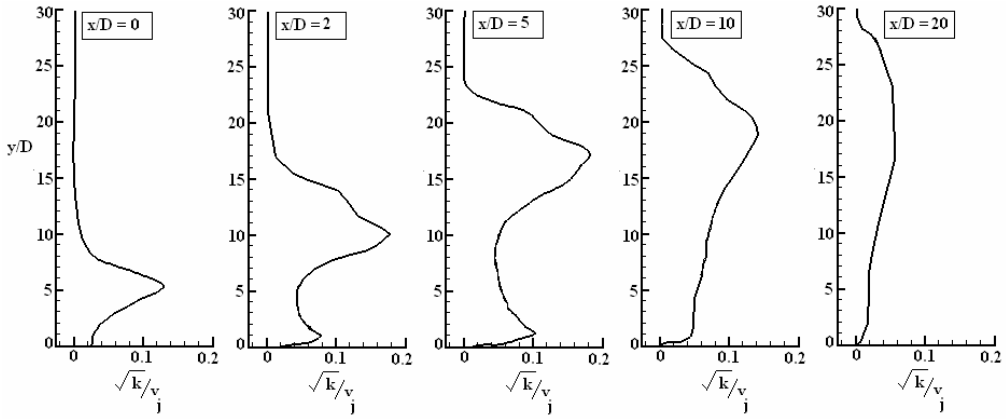

Fig. 4.41: Predictions of turbulence kinetic energy at different downstream locations (z/*D* = 3) for *R* = *6*.

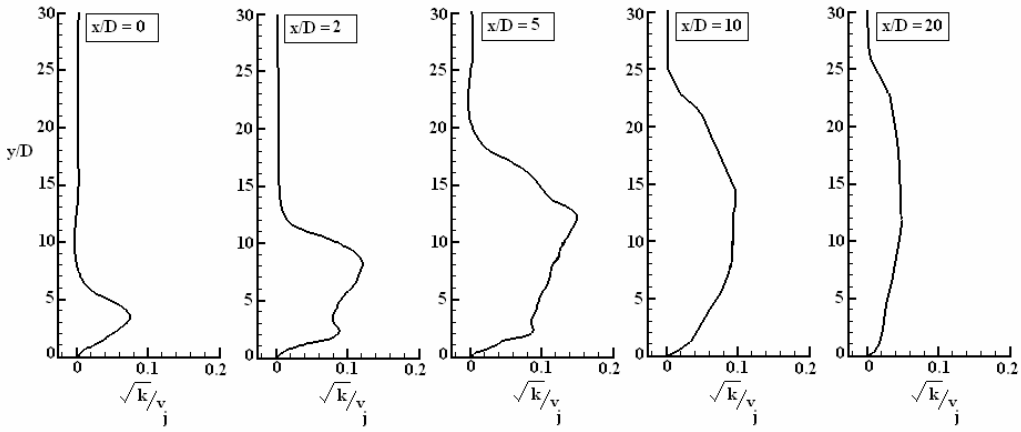

Fig. 4.42: Predictions of turbulence kinetic energy at different downstream locations (*z/D* = 6) for *R* = *6*.

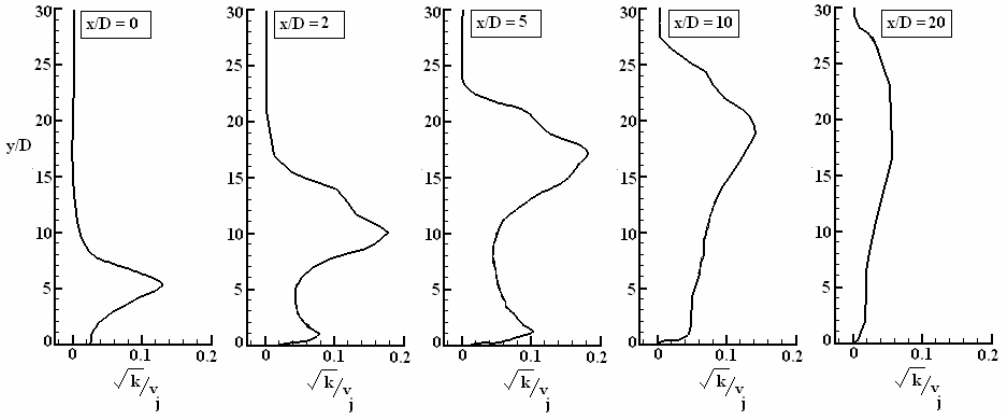

Fig. 4.43: Predictions of turbulence kinetic energy at different downstream location (*z/D* = -3) for *R* = *6*.

The variation of the kinetic energy at the plane z/D = 3 is shown in Fig. 4.41. In this plane although $(\partial u/\partial y)$ is the predominant gradient in producing turbulence kinetic energy k, the role of the spanwise velocity gradient $\partial w/\partial y$ should not be underestimated. In the wake-like region where there is entrainment of the fluid towards the jet central plane, the streamlines converge $(\partial w/\partial y < 0)$ and the production of k is reduced. The higher value of kinetic energy at the wall-jet region is observed in this plane due to a strong velocity gradient of the w-component. Fig. 4.42 shows the variation of the kinetic energy at the plane z/D = 6 for R = 6. The value of the k at the wall-jet region is higher in this case compared to the earlier two cases due to a high value of $\partial u/\partial y$. However the value is smaller at the upward position of the flow field due to lesser gradients of all components of mean velocity than that in earlier two cases.

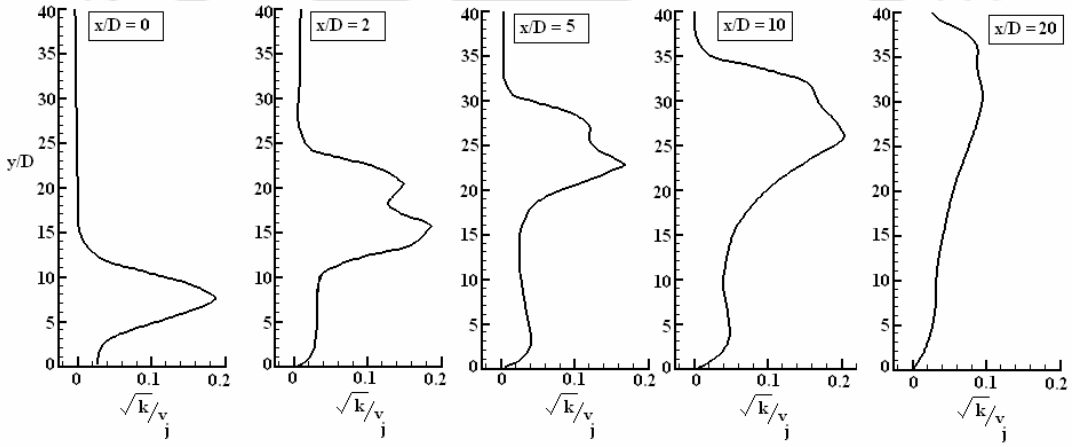

Fig. 4.44: Predictions of turbulence kinetic energy at different downstream locations (z/D = 0) for R = 9.

The observation of the symmetry of the profile of turbulence kinetic about the jet centre plane is made by comparing the profiles at z/D = - 3 (Fig. 4.43) with the profile at z/D = 3 (Fig. 4.41).

The prediction of the turbulence kinetic energy at different transverse planes and at different downstream locations are shown in Figs. 4.44 to 4.47 for the velocity ratio R = 9. Fig. 4.44 shows the variation of turbulence kinetic energy at z/D = 0. The trend of the kinetic energy profile is same as that in the case with R = 6. However the value of the kinetic energy is more in this case due to a stronger effect of the jet. A high value of turbulence kinetic energy is transported from the jet flow. At other two transverse planes (z/D = 3 and 6), the kinetic energy profiles show some qualitative difference.

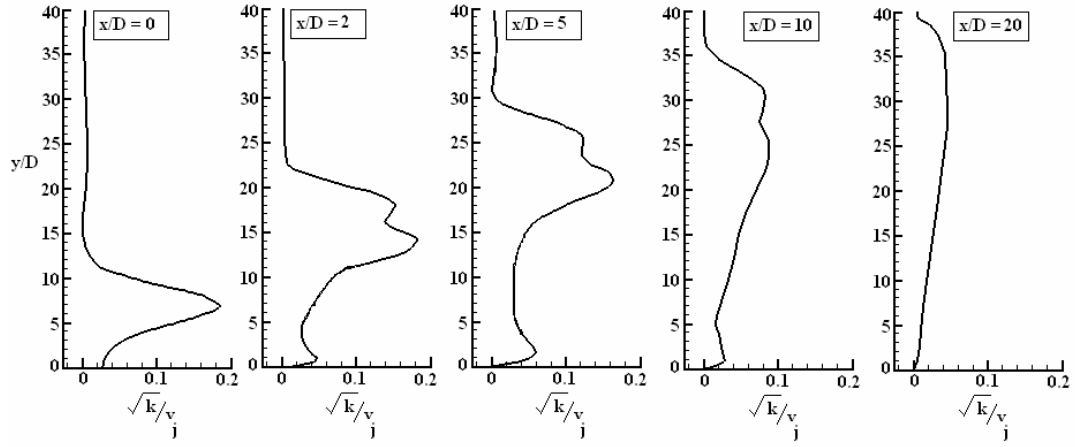

Fig. 4.45: Predictions of turbulence kinetic energy at different downstream locations (z/*D* = 3) for *R* = *9*.

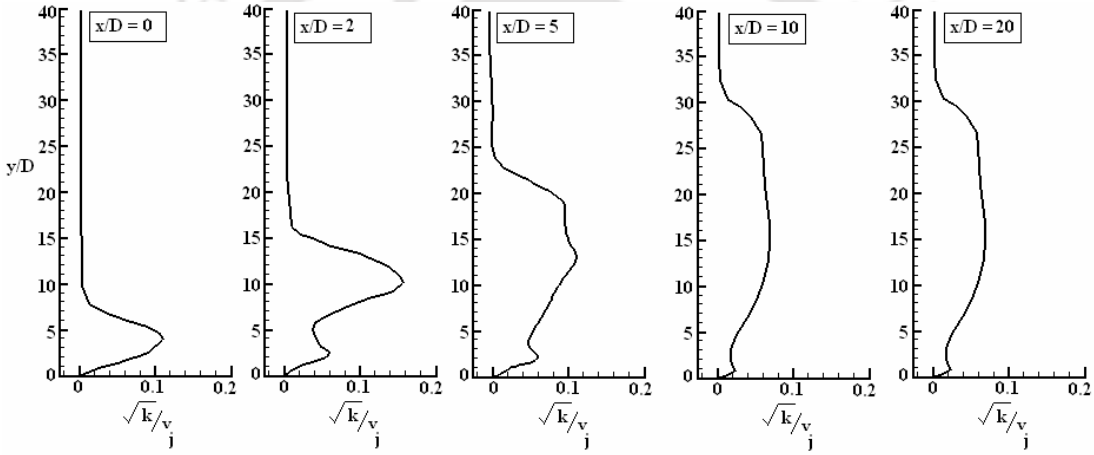

Fig. 4.46: Predictions of turbulence kinetic energy at different downstream locations (*z/D* = 6) for *R* = *9*.

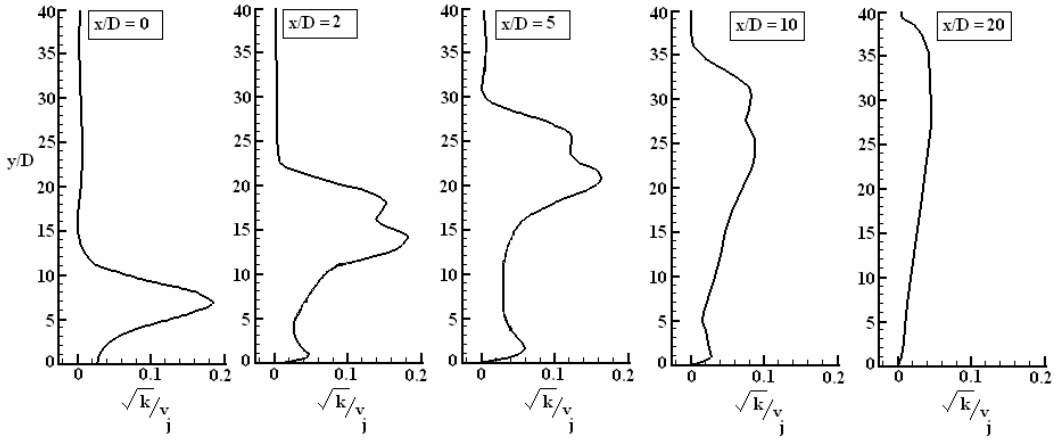

Fig. 4.47: Predictions of turbulence kinetic energy at different downstream locations (*z/D* = -3) for *R* = *9*.

Two peak values of the turbulence kinetic energy profiles are more distinguished in this case (Figs. 4.45 and 4.46) compared to the case of R = 6 (Figs. 4.41 and 4.42). Moreover the value of turbulence kinetic energy at the wall-jet region is less compared to the case of R = 6 due to a weak velocity gradient $\partial u/\partial y$ in that region. The turbulence kinetic energy profile is also symmetric for R = 9 about jet centre plane (z/D = 0), which can be observed by comparing Figs. 4.45 and 4.47.

The prediction of turbulence shear-stress profile at two different planes (z/D = 0 and 5) and at different downstream locations are shown in Figs. 4.48 and 4.49 for the velocity ratio R = 6. Fig. 4.48 shows the development of turbulence shear stress at jet centre plane (z/D = 0) and at different downstream positions. In general the shear stress $-\overline{u'v'}$ and the velocity gradient ($\partial u/\partial y$) have the same sign and therefore the eddy viscosity $\nu_t = -\overline{u'v'}/(\partial u/\partial y)$ is positive in all regions of the flow field. The maxima of the shear stress $-\overline{u'v'}$ profile correspond closely to the position of maxima of the velocity gradient ($\partial u/\partial y$).

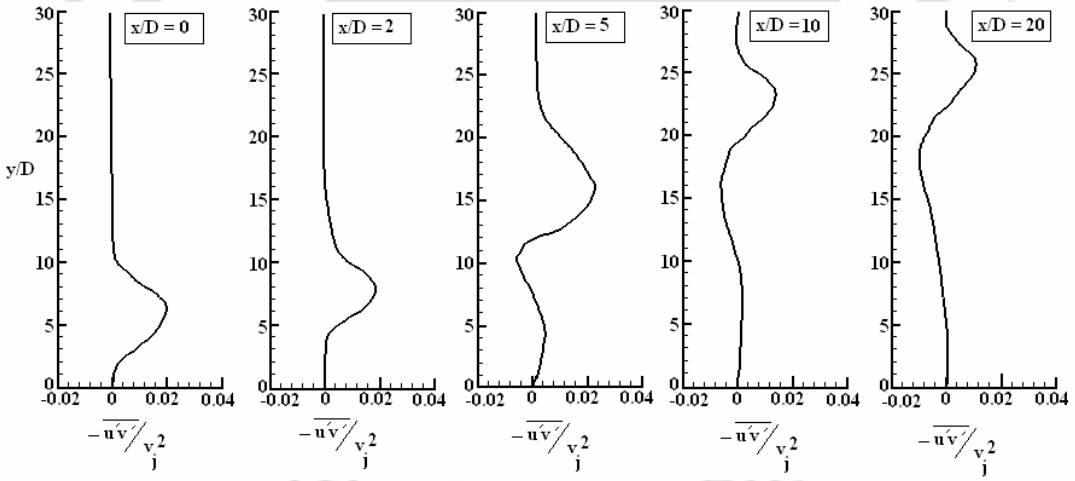

Fig. 4.48: Predictions of turbulence shear stress at different downstream locations (z/D = 0) for R = 6.

In the crossflow direction initially the maximum value of shear stress increases as the shear layer with a higher velocity gradient which is developed over the wake-like region. Further downstream the maximum of shear stress decreases as the velocity gradient becomes smaller. Near the jet exit region (x/D = 0 and 2) there is no wake-like region and therefore the shear stress shown represents only the jet-shear layer.

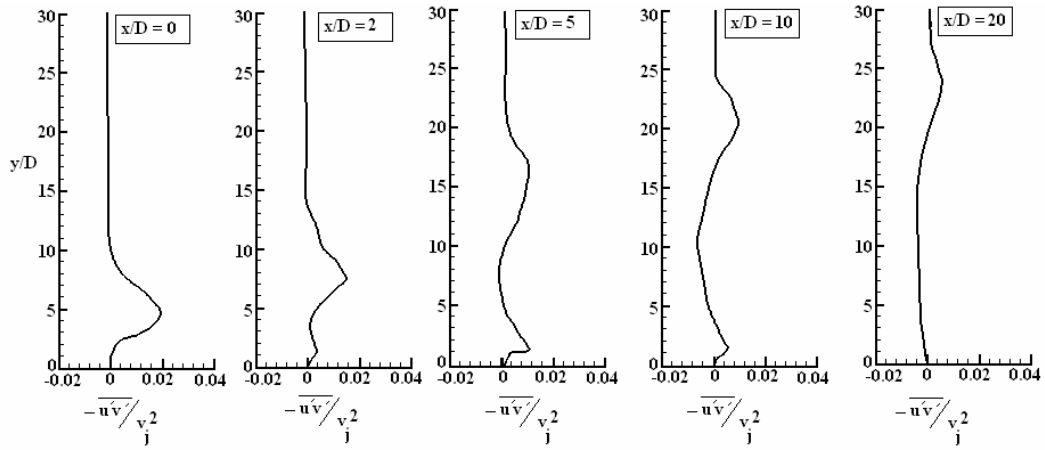

Fig. 4.49: Predictions of turbulence shear stress at different downstream locations (z/D = 5) for R = 6.

Downstream of the jet exit region the shear stress distinctly shows the wake-like region, where the value of the shear stress is low. In this region the shear stress shows a trend of increasing the value due to the wall-jet structures, further downstream it decreases in the wake-like region, reaches a minimum value and again increases in the jet-shear layer. After reaching the maximum value in the jet-shear layer, the value of the shear stress again decreases where the jet and the crossflow does not have much interaction.

The prediction of the shear stress at the jet edge plane (z/D = 5) at different downstream locations is shown in Fig. 4.49 for R = 6. The profiles follow the trends of the velocity gradient ($\partial u / \partial y$) shown in Fig. 4.8. In this plane the value of the shear stress is significantly higher in the wall-jet layer compared to that in the jet central plane (z/D = 0). The maximum value of the shear stress in the jet-shear layer is lower compared to that at z/D = 0 due to lesser velocity gradient.

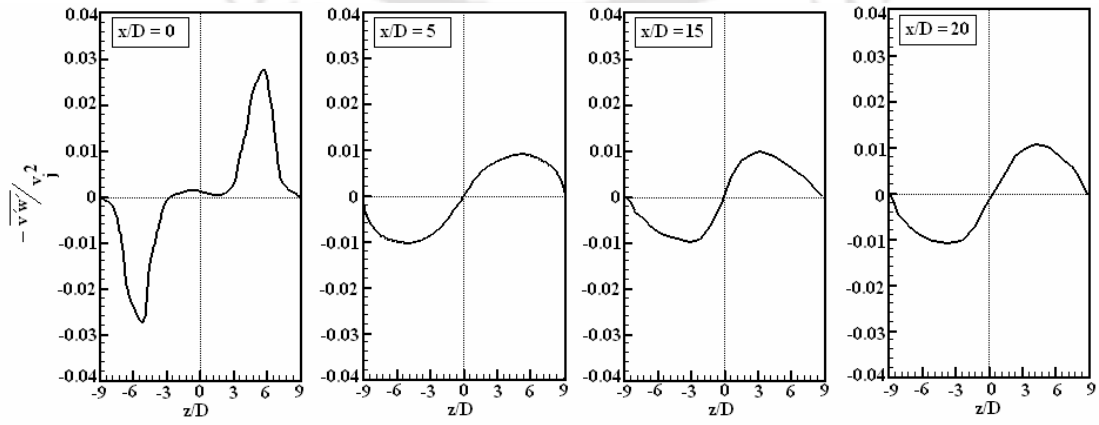

Fig. 4.50: Variation of turbulence shear stress in spanwise direction at different downstream locations for R = 6, y/D = 5.

The shear stress $\overline{v'w'}$ represents the transverse turbulence mixing and is associated with the transverse spreading of the jet in the vertical (*y-z)* plane. The variations of the shear stress $\overline{v'w'}$ in the spanwise directions at a vertical distance of *y*/*D* = 5 from the bottom wall and at different downstream locations are shown in Fig. 4.50 for the velocity ratio *R* = 6. At the jet exit region (*x*/*D* = 0) the value of the shear stress is quite high near both the side edges of the slot (*z*/*D* = 5 and -5). The high velocity jet after leaving the slot interacts with the slower moving crossflow thus producing a shear layer near both the edges where the shear stress is quite high. Downstream of the slot the shear stress is governed by the CRVP formation and the value of the shear stress reduces due to a reduced velocity gradients. The value of the shear stress at the plane of symmetry (*z*/*D* = 0) is zero.

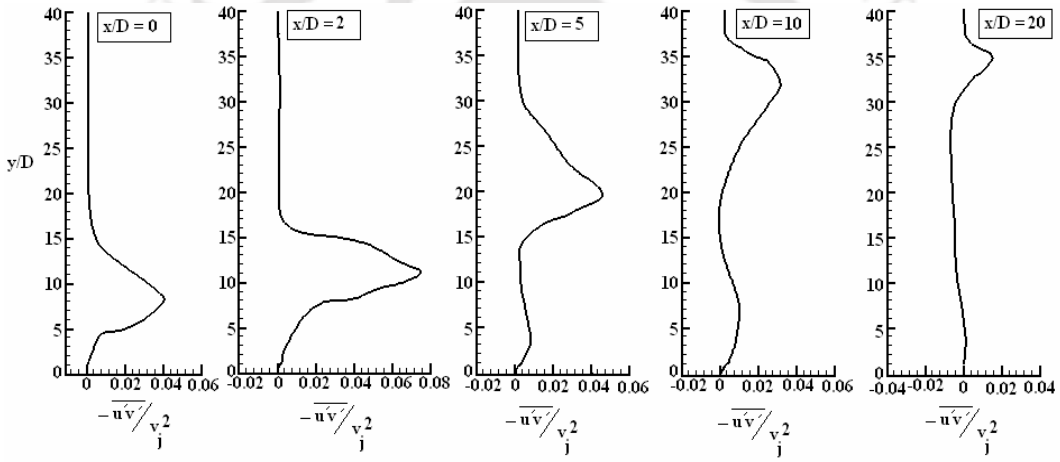

Fig. 4.51: Predictions of turbulence shear stress at different downstream locations (z/*D* = 0) for *R* = *9*.

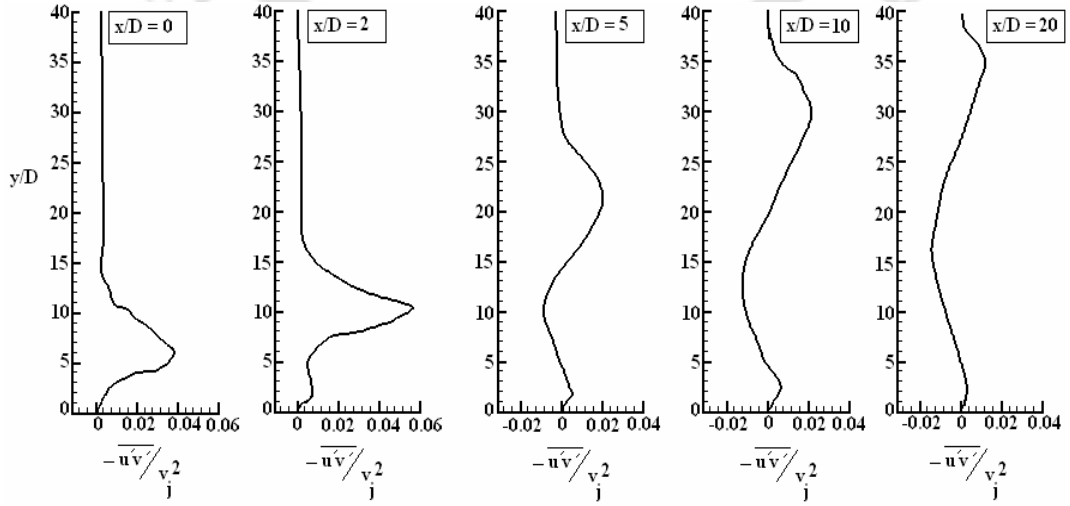

Fig. 4.52: Predictions of turbulence shear stress at different downstream locations (z/*D* = 5) for *R* = *9*.

The predictions of the turbulence shear-stress profiles at two different planes (z/*D* = 0 and 5) and at different downstream locations are shown in Figs. 4.51 and 4.52 for the velocity ratio *R* = 9. The trend of the profiles is similar to the case with *R* = 6, but the value of the shear stress is higher compared to the case with *R* = *6*. Moreover the shear stress predictions in the three regions of wall-jet, wake-like and jet-shear layer are also observed more prominent in this case.

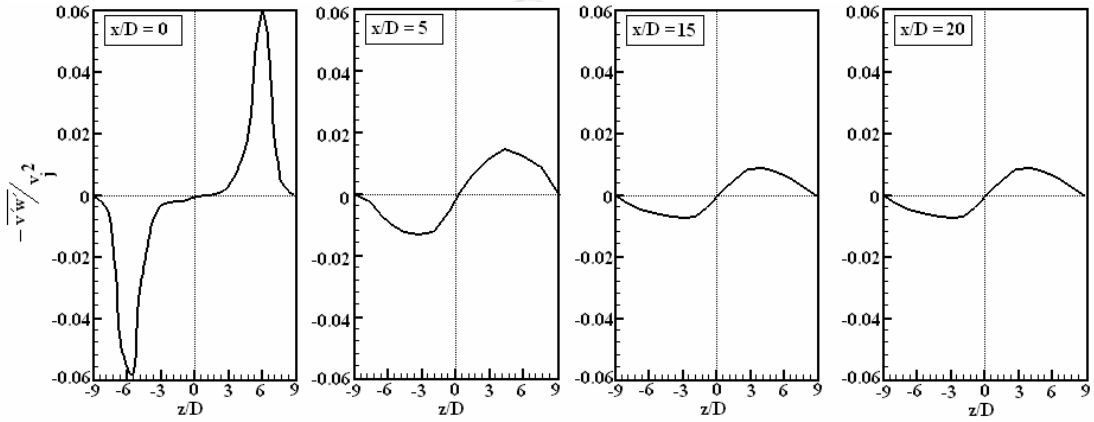

Fig. 4.53: Variation of turbulence shear stress in spanwise direction at different downstream locations for *R* = *9*, *y/D* = 5.

The value of shear stress $\overline{v'w'}$ is higher at the jet exit region *x/D* = 0 near both the edges of the jet compared to the case with *R* = 6. At the downstream positions the value of the stresses are the similar to the case with *R* = 6.

4.4.3 Flow Structures and Their Effects on Flow Field

After discussing the variations of the mean velocity and turbulence quantities, we present the gross behaviour of the flow fields and their structures in this section. The discussion concerns the mean structures without reference to the instantaneous flow field. It will be shown that the dominant flow patterns are well represented by the mean velocity field predicted in the present work.

The predicted non-dimensional mean velocity vectors superimposed with streamline plot at four different *x*-*y* planes in the spanwise direction for the velocity ratio *R* = 6 are shown in Figs. 4.54 and 4.55. The four planes chosen are the central vertical plane (*z*/*D* = 0) and planes at *z*/*D* = 3, 5 and 6. The jet trajectory is deflected in the streamwise direction and the direction of the crossflow is altered as if an

obstacle blocks it. However, due to the effect of the jet entrainment and the motion of the jet, the flow field of a jet in crossflow is not exactly the same as that over a rigid obstacle. It is to be noted that, the jet-shear-layer vortices form and dominate the initial portion of the jet and which are a result of the Kelvin-Helmholtz instability (Fric and Roshko, 1994). Since the present study deals with the steady mean flow field, these vortices are not captured in the present investigation. A wake-like region with a complex flow pattern is formed in the lee side of the jet. Very close to the bottom wall, a reverse flow region is formed and the crossflow fluid has been observed to enter this region. After entering, the crossflow travels upstream and observed to be lifted upward by the jet fluid and to be carried downstream together with it. Unlike the flow field in the 2D case, the flow does not recirculate in the present highly 3D case. Here the reverse flow is restricted to a region which is close to the bottom wall.

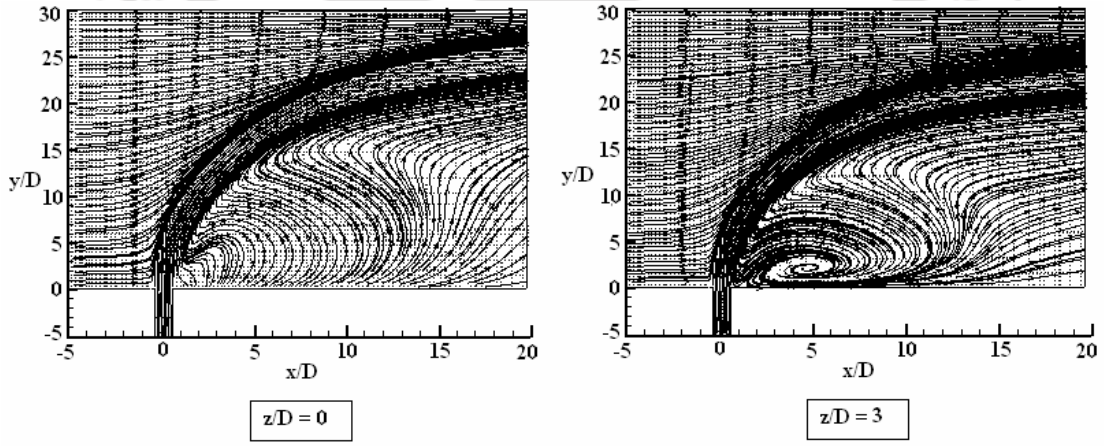

Fig. 4.54: Mean velocity vector plots superimposed with streamline at different spanwise locations, z/D = 0 and 3 for R = 6 in x-y plane.

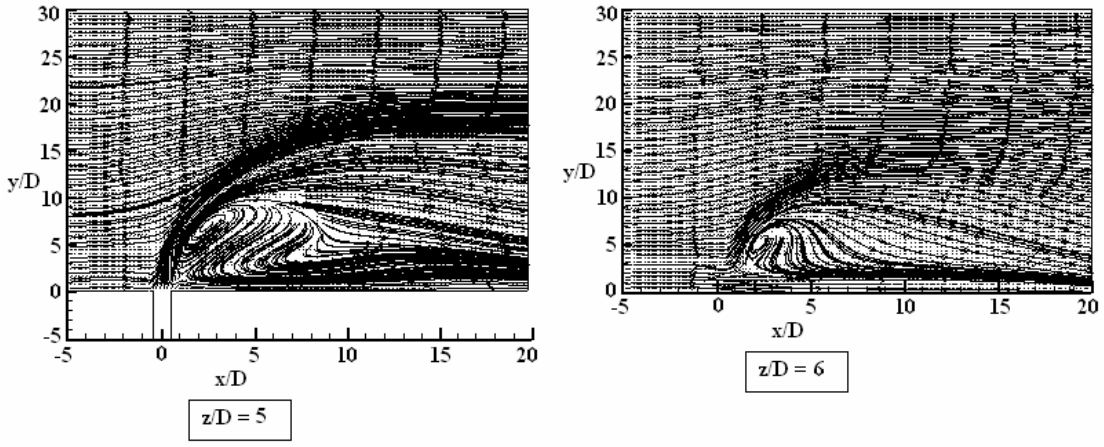

Fig. 4.55: Mean velocity vector plots superimposed with streamline at different spanwise locations, z/D = 5 and 6 for R = 6 in x-y plane.

The vertical penetration of the jet is more at the central plane (z/*D* = 0) than at the other three planes due to the lateral spread of the jet near the side edge of the jet discharge slot. It is also observed that the structures and extent of the reverse flow regions downstream of the jet are different at the three spanwsise planes, thereby demonstrating the three-dimensionality of the flow

Figs. 4.56 and 4.57 show the predicted non-dimensional mean velocity vectors superimposed with streamlines at four different *x*-*y* planes in the spanwise direction for the velocity ratio *R* = 9. In this case the jet trajectory is different from that in the case with *R* = 6. The undisturbed length of the jet is more in this case and the jet penetration into the crossflow is more compared to the case with *R* = 6. An interesting effect of the velocity ratio on the flow field is observed in the size of the reverse flow region. For the velocity ratio *R* = 9, the length of the reverse flow zone is decreased by as much as three slot widths or over 20% compared to that for the velocity ratio *R* = 6. The length of the reversed flow region is a function of the pressure field induced by the jet on the wall. At high velocity ratio, the jet lifts from the wall rapidly, so the fluid is rapidly drawn into the jet from the crossflow boundary layer. Therefore the effect of the jet upon the crossflow boundary layer fluid does not persist as far downstream as in the case of a low velocity ratio owing to the proximity of the jet to the wall. At a low velocity ratio the jet remains comparatively close to the wall for a large distance downstream and therefore affects the crossflow boundary layer fluid over a large distance.

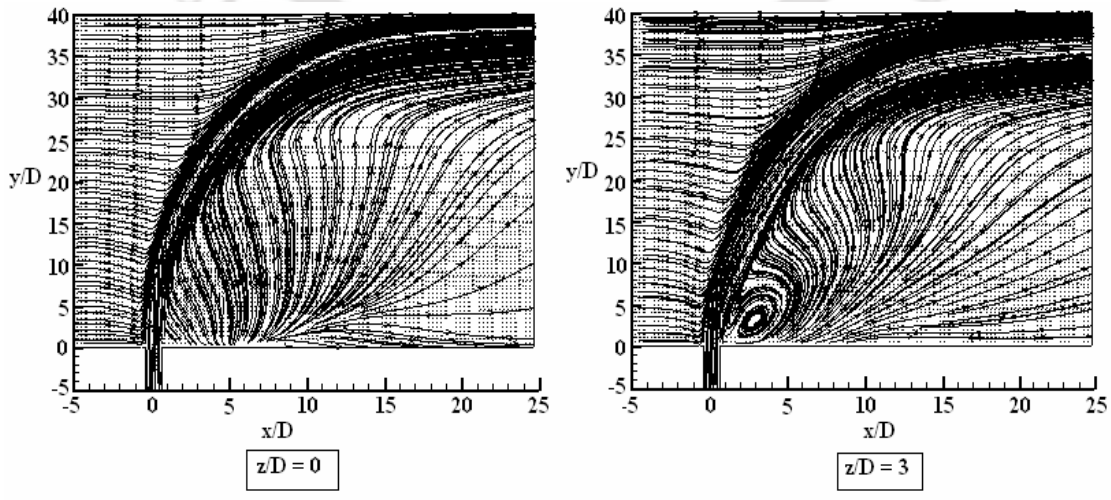

Fig. 4.56: Mean velocity vector plots superimposed with streamline at different spanwise locations, *z/D* = 0 and 3 for *R* = 9 in *x*-*y* plane.

In this case also the flow structures at other spanwise planes (z/D = 3, 5, 6 are different than the flow structure at the jet centre plane (z/D = 0). The jet penetration at the spanwise planes z/D = 5 and 6 (Fig. 4.57) is more compared to the penetration at the corresponding planes in case of R = 6 (Fig. 4.55). The jet is relatively strong and therefore its spread is more in the spanwise direction compared to the case with R = *6.* Therefore the existence of the jet is felt more in the spanwise planes compared to the case with R = 6.

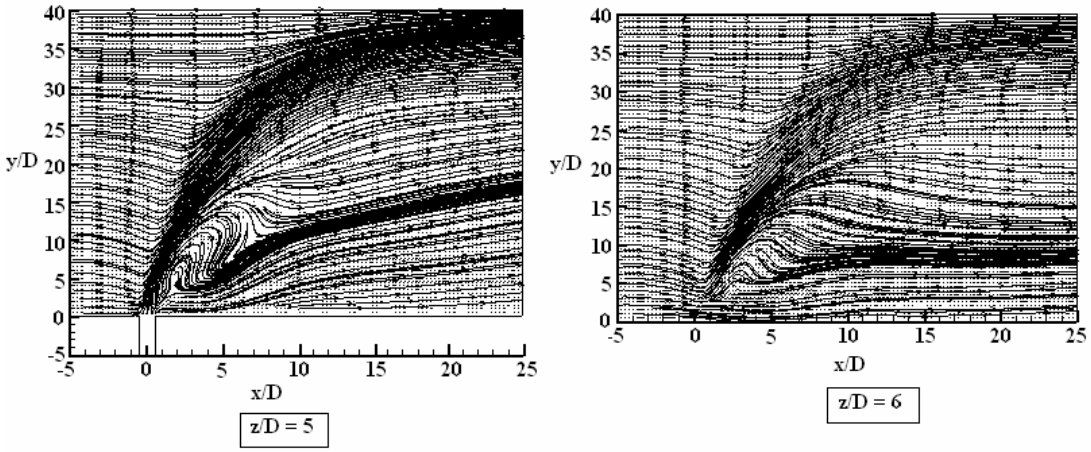

Fig. 4.57: Mean velocity vector plots superimposed with streamline at different spanwise locations, z/D = 5 and 6 for R = 9 in x-y plane.

Figs. 4.58 and 4.59 show the mean velocity field at different y-z planes at various downstream locations (x/D = -0.5, 0, 0.5, 2, 5, 10, 15 and 20) for the velocity ratio R = 6. The first plane is located 0.5D upstream of the centre of the jet slot and therefore it is the plane at the leading edge of the jet slot. The crossflow boundary layer fluid not only starts to react to the upcoming jet but also moves away from the bottom wall. The jet pushes the crossflow in the lateral direction at the edge of the discharge slot since the strength of the jet is more than that of the crossflow. At the centre of the jet slot (x/D = 0), a strong vertical component of the jet velocity is observed. The high velocity jet-shears the relatively slow moving crossflow boundary layer and an inception of two vortical structures is observed at both sides of the jet slot. According to Yuan et al. (1999) these two vortices are formed inside the jet slot itself and they are discharged along with the jet flow.

The roll-up of the crossflow fluid into the cross-streamwise vortices at the edges of the jet is seen at the trailing edge of the jet slot (x/D = 0.5) and the vortices formed

due to the shearing of the crossflow boundary layer flow have moved away slightly from the bottom wall. Downstream of the discharge slot (x/D = 2), the two vortices formed at the edge of the jet move further up from the bottom wall. Due to the absence of a shearing action of the jet the two vortices become weaker and their shape starts to distort. Additionally a pocket of vorticity has appeared on each side of the slot centreline with the same sign of rotation as the vorticity on its respective side. Further downstream of the jet slot (x/D = 5), the vortices produced at the side edge start to weaken and the two vortices formed at each side of the slot centre plane start to enlarge. The continued development of the CRVP which grows larger in size is observed at the planes x/D = 10, 15 and 20, respectively.

The size of the vortex pair at the plane x/D = 10 becomes very large. The pressure drop in the wake-like region induces an inward motion, transporting the fluid from the crossflow towards the jet centre plane. The development of the CRVP appears to be full fledged at x/D = 15, which grow in size and assume the shape of a kidney. Far downstream the kidney shape of the CRVP is observed to be reduced.

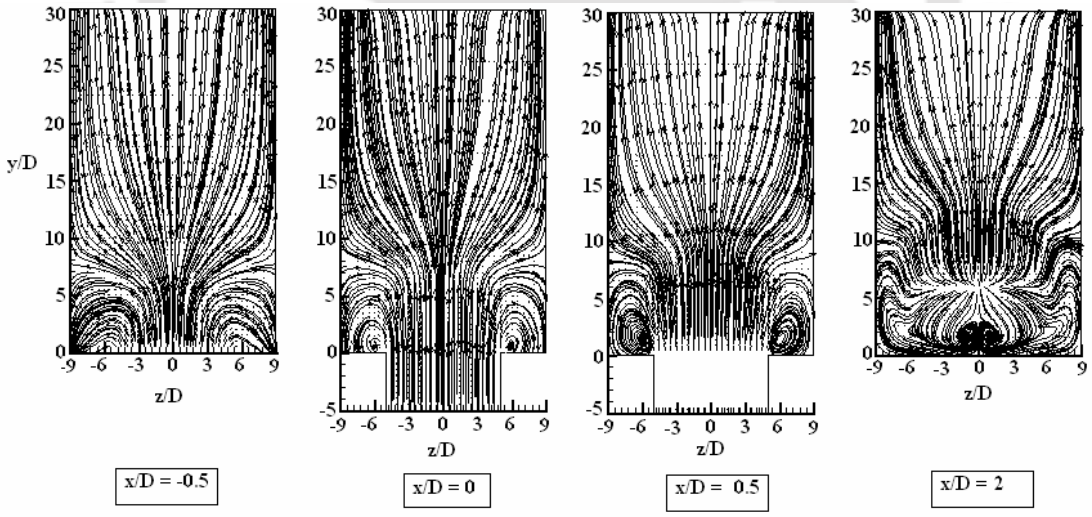

Fig. 4.58: Mean velocity vector plots superimposed with streamline at different downstream locations, x/D = -0.5, 0, 0.5 and 2 for R = 6 in y-z plane.

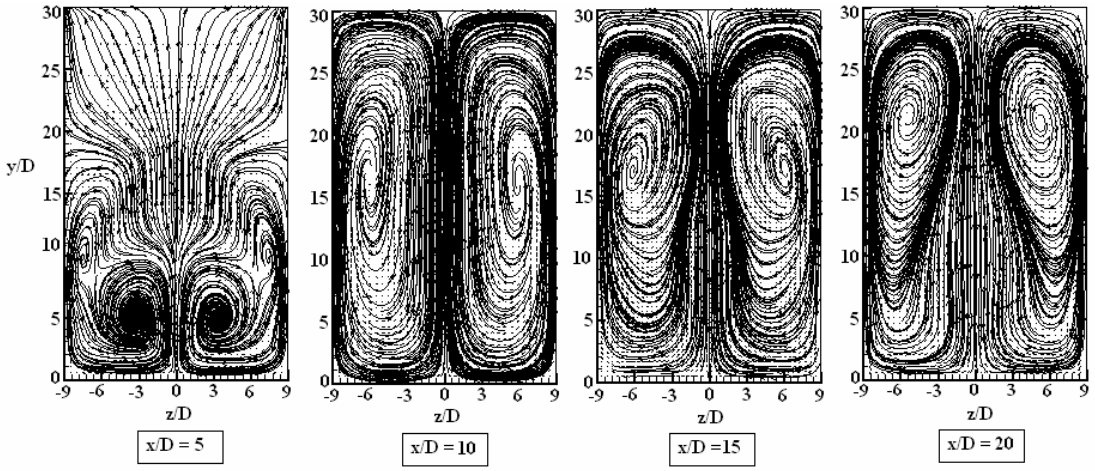

Fig. 4.59: Mean velocity vector plots superimposed with streamline at different downstream locations, x/D = 5, 10, 15 and 20 for R = 6 in y-z plane.

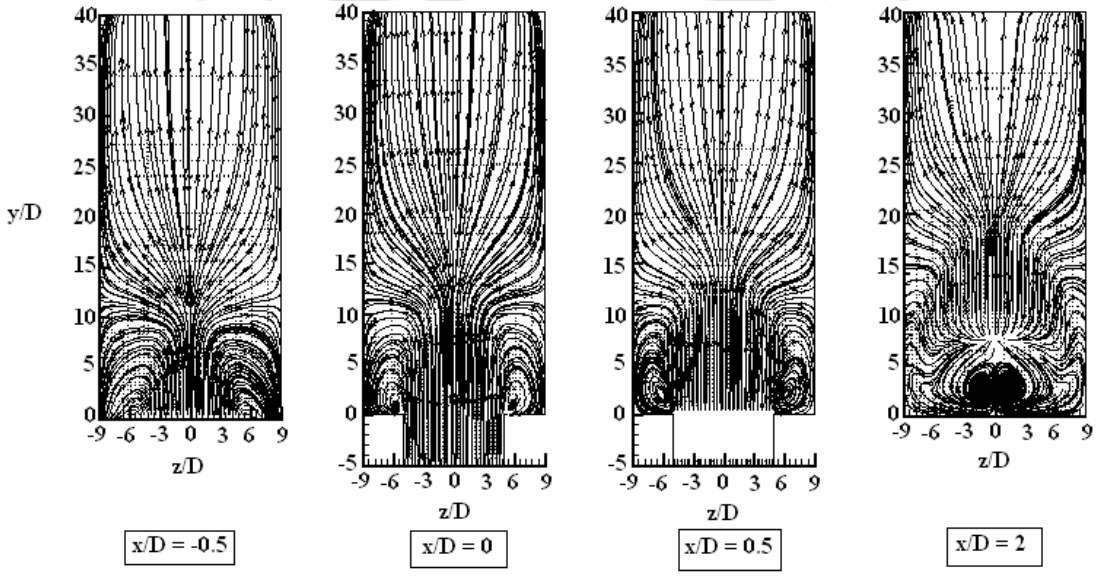

Fig. 4.60: Mean velocity vector plots superimposed with streamline at different downstream locations, x/D = -0.5, 0, 0.5 and 2 for R = 9 in y-z plane.

The mean velocity field at different y-z planes at various x/D locations (x/D = -0.5, 0, 0.5, 2, 5, 10, 15 and 20) for the velocity ratio R = 9 is shown in Figs. 4.60 and 4.61. The mechanism of formation of the two vortices at the side edges of the jet is similar to the case with R = 6. However their size and the extent of the affected flow field are more in this case compared to the case with R = 6. The shearing of the crossflow boundary layer flow at the centre plane of the jet (x/D = 0) is more due to a higher velocity of the jet and the size of the two vortices formed at the side edge of the jet is bigger than that in the case with R = 6. The roll-up of the crossflow fluid into the cross-streamwise vortices at the trailing edge of the jet slot (x/D = 0.5) looks similar to the previous case. The sizes of the two central vortices formed at the downstream

locations (x/D = 2) are bigger in this case. Further downstream (x/D = 5, 10, 15 and 20) the structures of the flow field are quite different from those for R = 6. At all these planes the sizes of the CRVP are elongated. At the plane x/D = 10, the two vortex centres are somewhat far from the central plane (z/D = 0). At farther downstream locations (x/D = 15 and 20) the vortex centres come closer to the central plane and also move up. Also the fluid beneath the two CRVP experiences some changes of patterns and direction of rotation. The direction of this rotation is opposite to the rotation of CRVP. At the plane x/D = 20 the bottom part of fluid rotates in the opposite direction and forms other vortices.

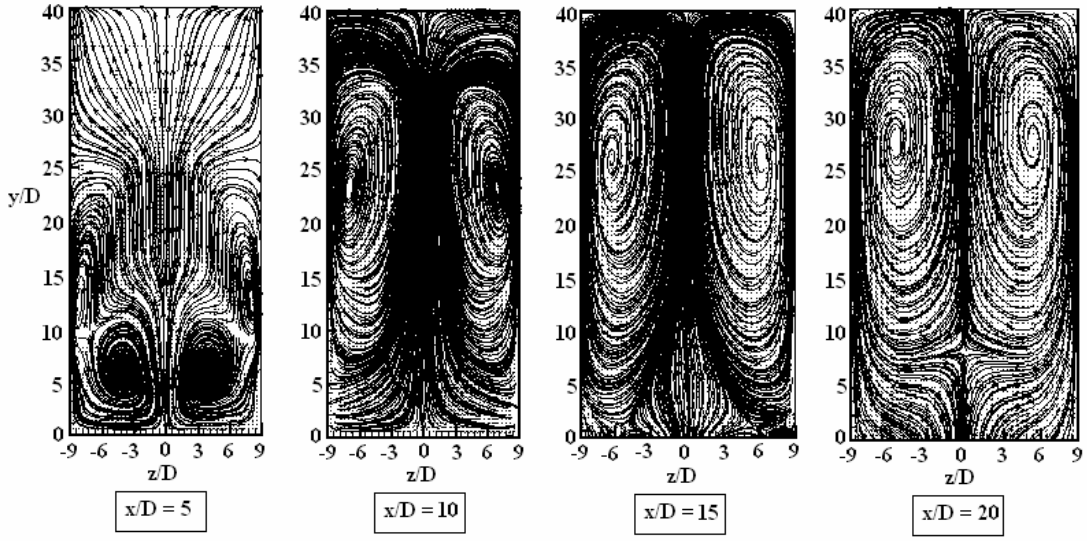

Fig. 4.61: Mean velocity vector plots superimposed with streamline at different downstream locations, x/D = 5, 10, 15 and 20 for R = 9 in y-z plane.

Figs. 4.62 and 4.63 show the mean velocity distributions of the jet stream into the crossflow at four different x-z planes parallel to the bottom wall for the velocity ratio R = 6. The first plane (y/D = 1) is located near to the bottom wall. The approaching crossflow boundary layer encounters an adverse pressure gradient ahead of the vertical jet. Since the jet is not a bluff body the separation of the crossflow does not occur but it embraces the side edges of the jet thus forming weak structures of horse shoe vortices. Downstream of the jet slot the jet/crossflow mixture accelerates and converges upon the spanwise centreline (z/D = 0). Immediately downstream of the jet, two vortices roll up. These vortices are both stable spiral nodes and are consistent with the time-averaged 'wake' vortices numerically predicted by Rudman (1996), Hale et al. (2000) and Peterson and Plesniak (2004).

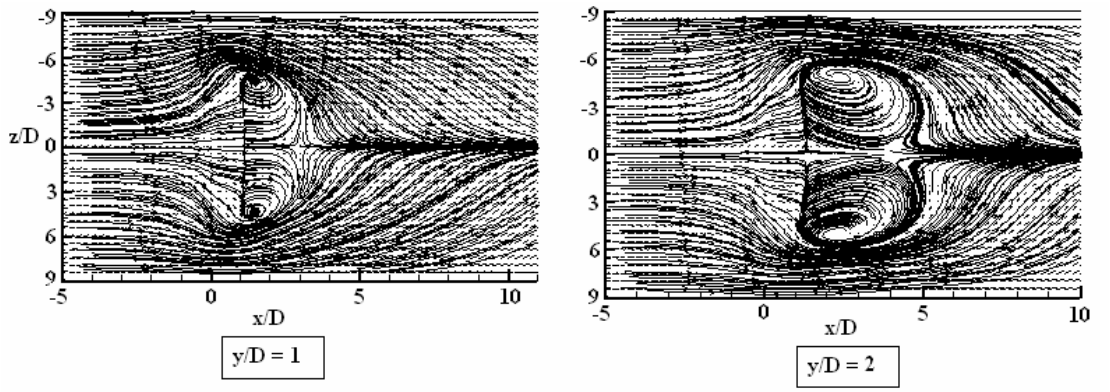

Fig. 4.62: Mean velocity vector plots superimposed with streamline at different vertical heights, *y/D* = 1 and 2 for *R* = 6 in *x*-*z* plane.

It is to be noted that these structures are different from the wake vortex structures reported by Fric and Roshko (1994), which were inherently unsteady. To distinguish them from the wake vortices observed by Fric and Roshko (1994), the steady 'wake' vortices are referred by Peterson and Plesniak (2004) as the downstream spiral separation node (DSSN) vortices.

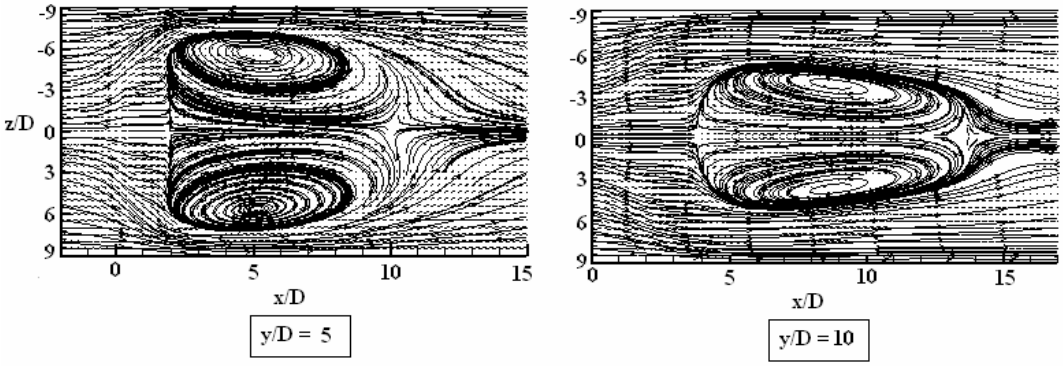

Fig. 4.63: Mean velocity vector plots superimposed with streamline at different vertical height, *y/D* = 5 and 10 for *R* = 6 in *x*-*z* plane.

Continuing away from the bottom wall to the plane at *y/D* = 2, the pair of vortices appear to have advected downstream and grown in size. Further away from the bottom wall (*y/D* = 5), the jet is still almost vertical and expands in the spanwise direction producing a larger wake effect. Therefore the sizes of the two vortices are bigger than those at two other planes. At the plane y/*D* = 10, the contribution of the crossflow to the in-plane velocity magnitude increases owing to the bending of the jet. Therefore blocking effect of the jet is lesser and the free stream velocity at this plane is larger in magnitude than that in the first three planes. Therefore the sizes of the two vortices are reduced in the *y*- direction. As the jet bends and produces no blockage,

the vortices diminish and disappear above the plane y/D = 15 (not shown in Fig. 4.63).

A contour plot of the spanwise component of the mean velocity at different x-z planes is shown in Fig. 4.64. Since the spanwise component plays a leading role in the formation of the CRVP and wake vortices, this plot illustrates the evolution of the flow structures and can give some insight to the formation of those vortices. The first plane corresponds to in-hole contours of the spanwise velocity at a depth of D from the bottom wall

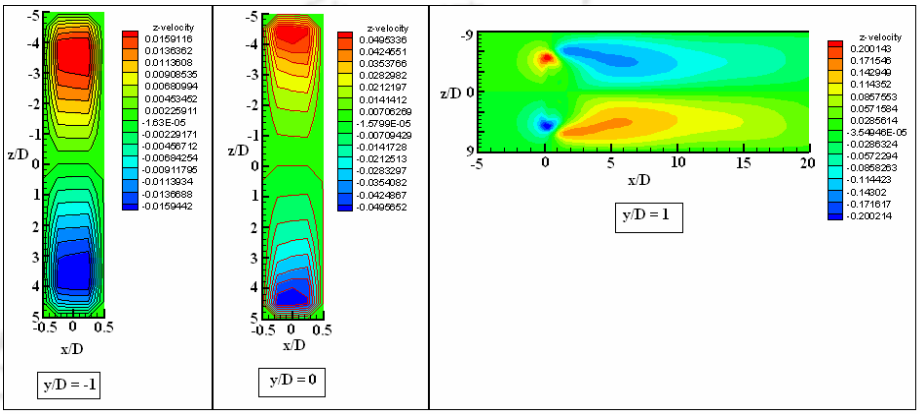

Fig. 4.64: Mean z velocity contour plots at different vertical planes for R = 6.

It is seen that the values of the spanwise velocity at both sides of the jet slot are opposite to each other, thus the tendency of the formation of vortices starts inside the duct itself. The contours of the spanwise velocity at the plane y/D = 0, just before the fluid exits into the crossflow, differ from the previous case. The high-value spanwise components take the position of the side edge and they concentrate there and get ready to exit. The contours of the spanwise velocity at a vertical height y/D = 1 from the bottom wall show different directions of the jet fluid and the crossflow fluid. Looking in the crossfow direction from the inlet boundary the direction of the spanwise velocity at the right side edge of jet slot is towards the sidewall. These components make the fluid to move in clockwise direction in the right side vortices of DSSN. Just downstream of the jet, the direction of the components are opposite and move towards the centre and they are responsible for the anti-clockwise movement of the right side of wake or DSSN vortices, which can be seen in Figs. 4.62 and 4.63.

.

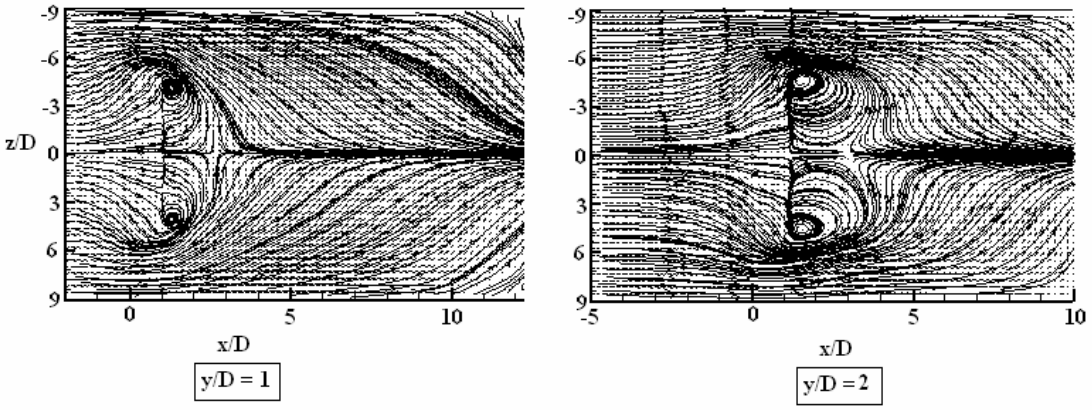

Fig. 4.65: Mean velocity vector plots superimposed with streamline at different vertical height, *y/D* = 1 and 2 for *R* = 9 in *x*-*z* plane.

The mean velocity distributions of the jet stream into the crossflow at four different *x*-*z* planes parallel to the bottom wall for velocity ratio *R* = 9 are shown in Figs. 4.65 and 4.66. In the first two planes (*y/D* = 1 and 2) the DSSN vortices are seemed to be weaker than those in the case with *R* = 6 and cover a relatively small area

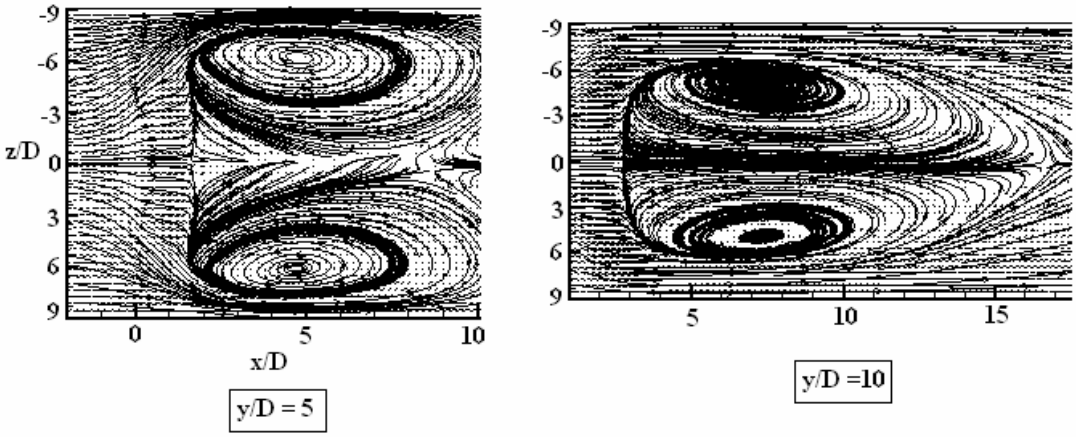

Fig. 4.66: Mean velocity vector plots superimposed with streamline at different vertical height, *y/D* = 5 and 10 for *R* = 9 in *x*-*z* plane.

One reason for this behaviour may be that for a high velocity ratio, the lift of the crossflow boundary layer flow is large in the jet development region close to the bottom wall (*y/D* = 1 and 2). The lifted crossflow boundary layer draws the fluid from the DSSN vortices thus having a weak effect in the formation of DSSN. At upward planes (*y/D* = 5 and 10) the sizes of DSSN and the areas covered by them are more than those in the case with *R* = 6. In these vertical locations the lifting of the crossflow fluid stops and the jet is comparatively stiffer than that in the case with *R* = 6 and therefore the wake effect is strong.

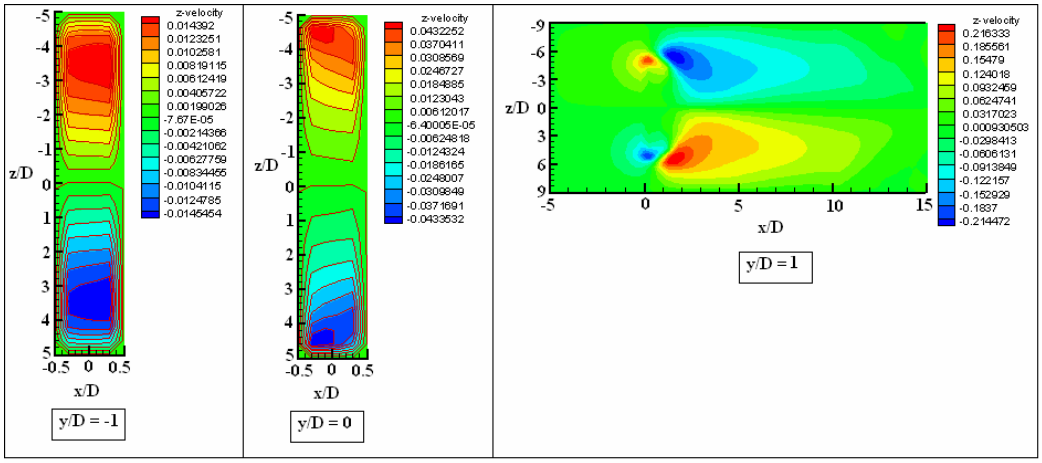

Fig. 4.67: Mean z velocity contour plots at different vertical planes for $R = 9$.

A contour plot of the spanwise component of the mean velocity at different x-z planes for the velocity ratio $R = 9$ is shown in Fig. 4.67. The spanwise velocity components have similar characteristics as in the case of $R = 6$, but their values are higher in this case compared to the case with $R = 6$.

4.4.4 Comparison with Measurements

In this section a comparison of some predicted flow properties is made with the experimental data of Ramaprian and Haniu (1983) and Haniu and Ramaprian (1989). As stated earlier Ramaprian and Haniu (1983) and Haniu and Ramaprian (1989) have reported their experimental observations in the s–n coordinate system whereas the present predictions in the Cartesian coordinates are converted to the s–n coordinates for the purpose of comparison with the experimental data.

A comparison of the normalized streamwise component of mean velocity (u_s/v_j) in the jet central vertical plane ($z/D = 0$) at four different downstream locations (s/D = 4.94, 9.68, 18.86 and 28.12) with the experimental data for the velocity ratio $R = 6$ is shown in Figs. 4.68 and 4.69. The overall agreement of the predictions by the models at two locations of $s/D = 4.94$ and 9.68 is better than that at the far downstream positions of $s/D = 18.86$ and 28.12. The first two positions are in the vicinity of the jet exit region, where experimental conditions are used as the boundary conditions in the numerical predictions. Far downstream the present computations over predict the jet spread in the upper part and at the lower part of the jet. Moreover the positions of the peak values do not match with the experimental data.

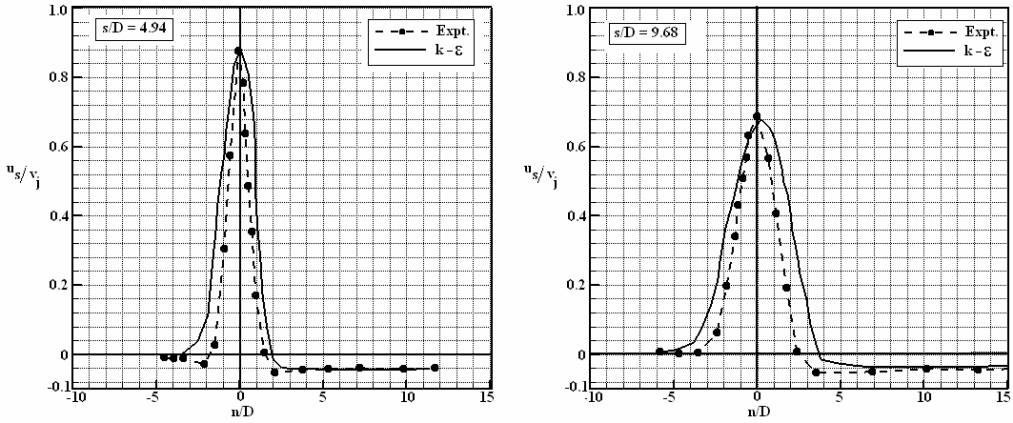

Fig. 4.68: Comparison of mean streamwise velocity at jet central plane ($z/D = 0$) for R =6, s/D = 4.94 and 9.68.

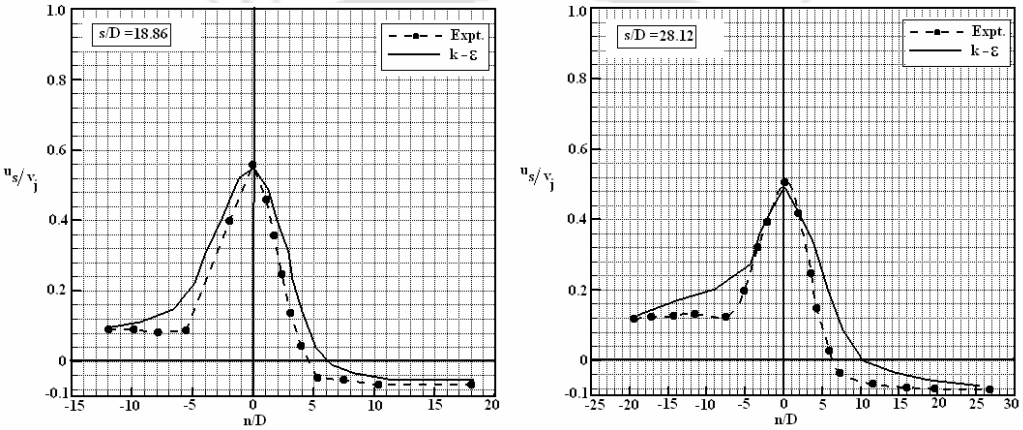

Fig. 4.69: Comparison of mean streamwise velocity at jet central plane ($z/D = 0$) for R =6, s/D = 18.86 and 28.12.

A comparison of the normalized s-component profiles of the mean velocity (u_s/v_j) in the jet central vertical plane ($z/D = 0$) at four different downstream locations (s/D = 4.97, 9.76, 21.22 and 29.73) with the experimental data for the velocity ratio $R = 9$ are shown in Figs. 470 and 4.71. The agreement with the experimental data is better in the upper and lower part of the jet at all s/D locations compared to the case with $R = 6$. However the present prediction slightly underpredicts the paek values.

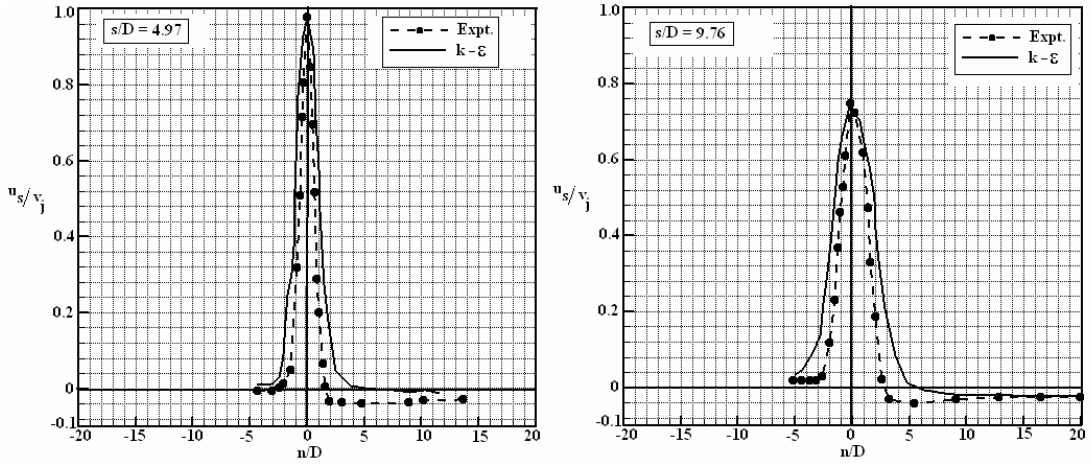

Fig. 4.70: Comparison of streamwise velocity at jet central plane (z/D =0) for R = 9, s/D = 4.97 and 9.76

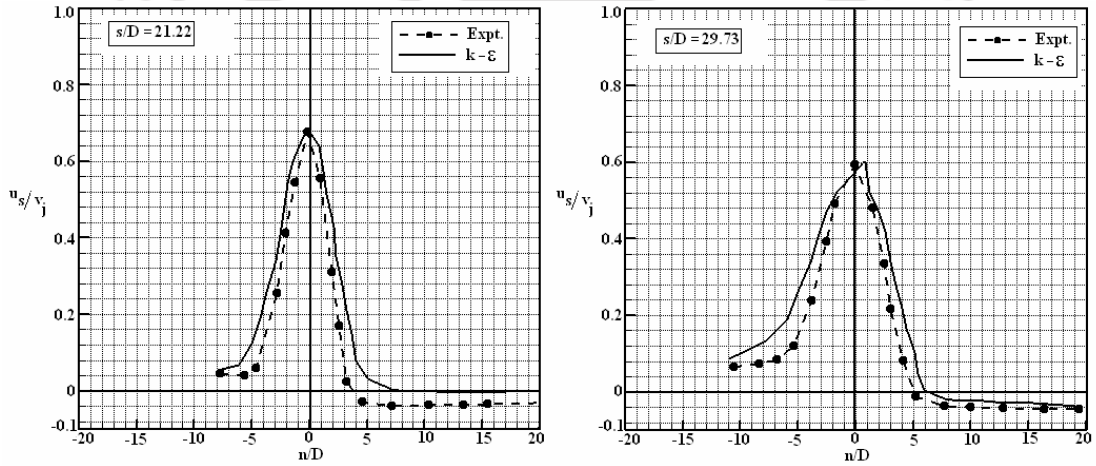

Fig. 4.71: Comparison of streamwise velocity at jet central plane (z/D = 0) for R = 9, s/D = 21.22 and 29.73.

.

Figs. 4.72 and 4.73 show a comparison of the normalized normal component profiles of the mean velocity (v_n/v_j) in the jet central vertical plane (z/D = 0) at four downstream locations with the experimental data for velocity ratio R = 6. The predictions agree well with the experimental data, both quantitatively and qualitatively.

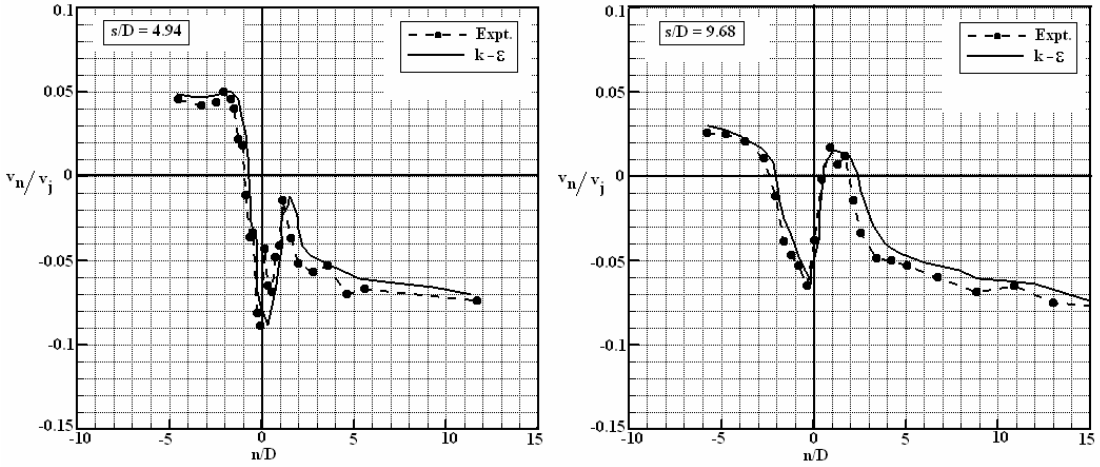

Fig. 4.72: Comparison of normal component velocity at jet central plane (z/D = 0) for R = 6, s/D = 4.94 and 9.68.

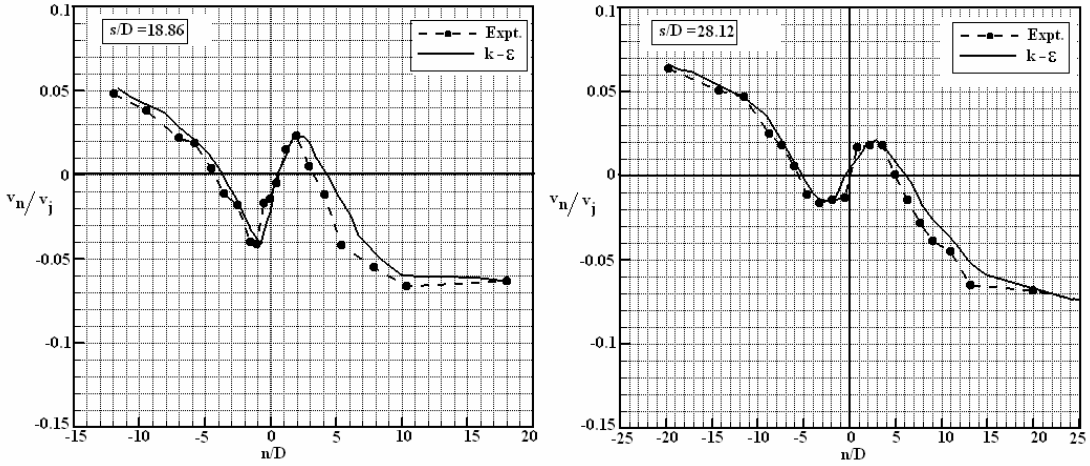

Fig. 4.73: Comparison of normal component velocity at jet central plane (z/D = 0) for R = 6, s/D = 18.86 and 28.12.

The comparison of the normalized normal component velocity profiles of the mean velocity (v_n/v_j) in the jet central vertical plane (z/D = 0) at four different downstream locations with the experimental data for the velocity ratio R = 9 are shown in Figs. 4.74 and 4.75. The agreement is better in this case compared to the case with R = 6.

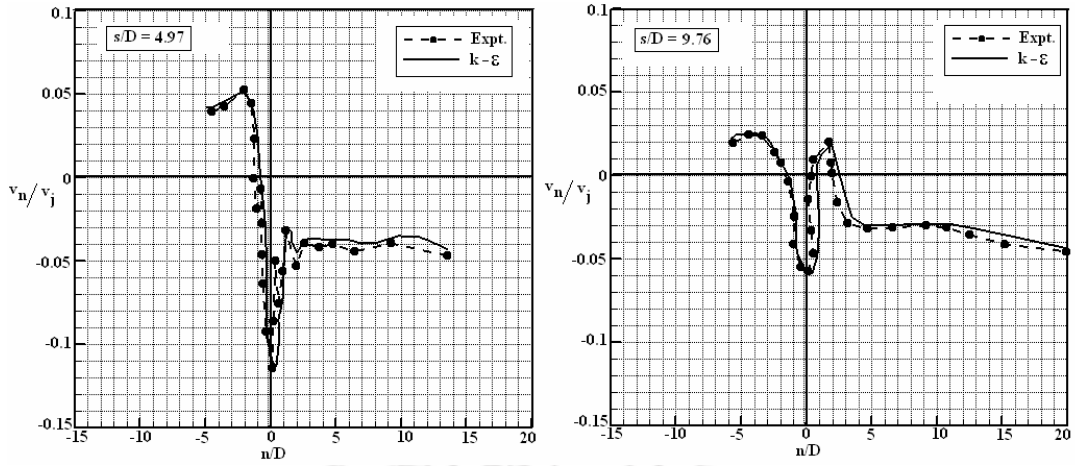

Fig. 4.74: Comparison of normal component velocity at jet central plane (z/D =0) for R = 9, s/D = 4.97 and 9.76.

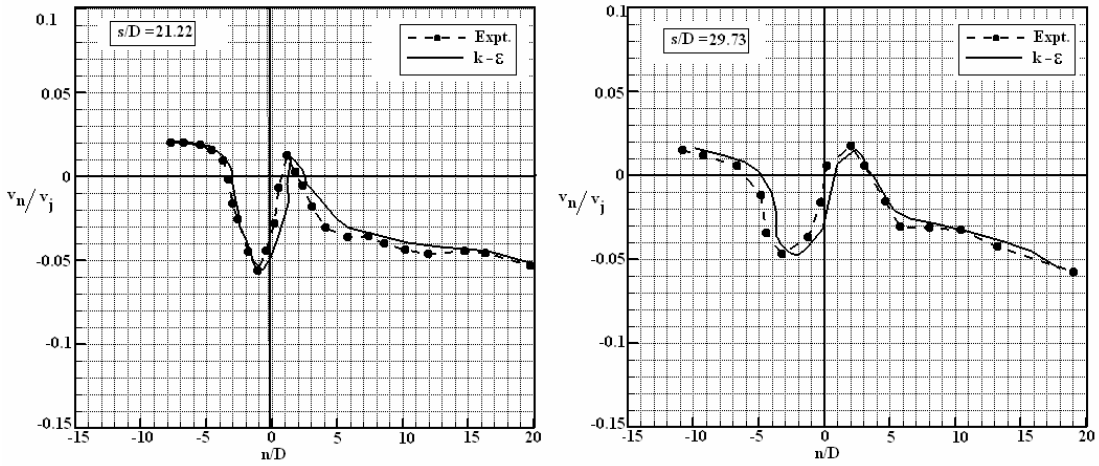

Fig. 4.75: Comparison of normal component velocity at jet central plane (z/D =0) for R = 9, s/D = 21.22 and 29.73.

A comparison of the turbulence shear stress profiles in the jet central vertical plane (z/D = 0) at four downstream locations (s/D = 4.94, 9.68, 18.86 and 28.12) for the velocity ratio R = 6 is shown in Figs. 4.76 and 4.77. The large peak values observed in the experimental data and in the present predictions are due to the high values of velocity gradients in the jet-shear-layer region. As in the case of the velocity predictions the agreement of the shear predictions near the jet exit regions are better than those in the downstream locations.

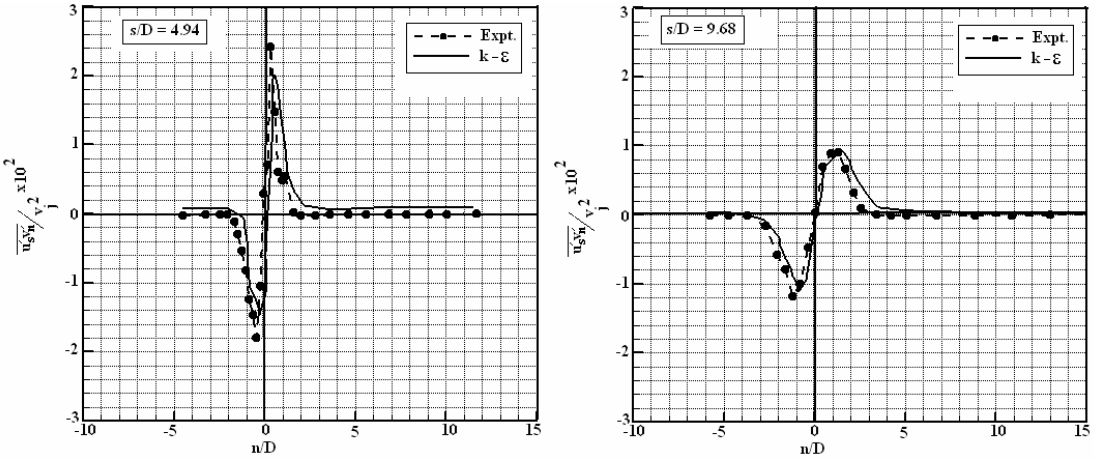

Fig. 4.76: Comparison of turbulence shear stress at jet central plane ($z/D = 0$) for $R = 6$, $s/D = 4.94$ and 9.68.

The present computations over predict the shear stresses especially in the inner half of the jet, where the flow faces reverse flow. Moreover the predicted positions of the maximum and minimum shear stress values do not match with the experimental data.

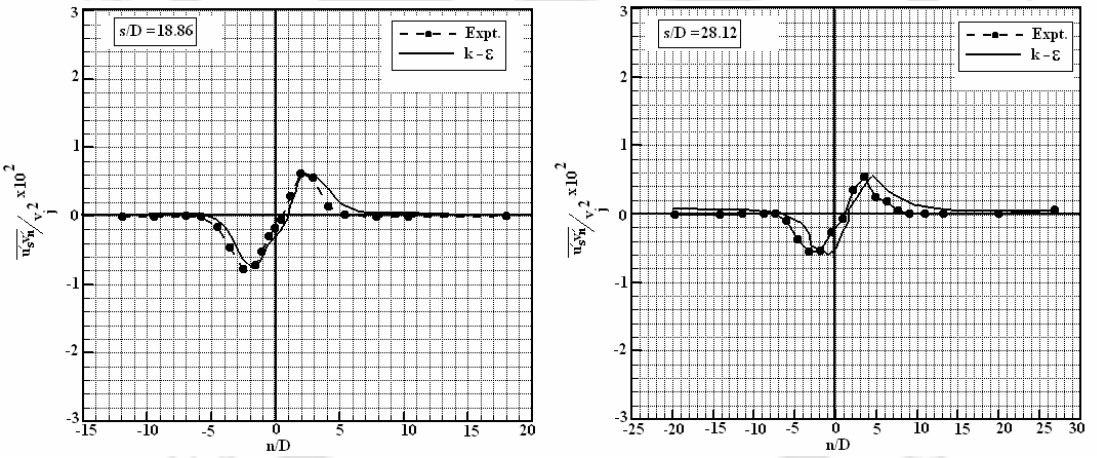

Fig. 4.77: Comparison of turbulence shear stress at jet central plane ($z/D = 0$) for $R = 6$, $s/D = 18.86$ and 28.12.

Figs. 4.78 and 4.79 show a comparison of the turbulence shear stress profiles in the jet central vertical plane ($z/D = 0$) at four downstream locations for the velocity ratio $R = 9$. The value of the shear stress near the jet exit region ($s/D = 4.97$) is quite high in this case compared to the case with $R = 6$. In this case also the large peak values of shear stress are observed due to high values of velocity gradient in the jet-shear-layer region. The agreement of the shear stress predictions in this case is better than that in the case with $R = 6$.

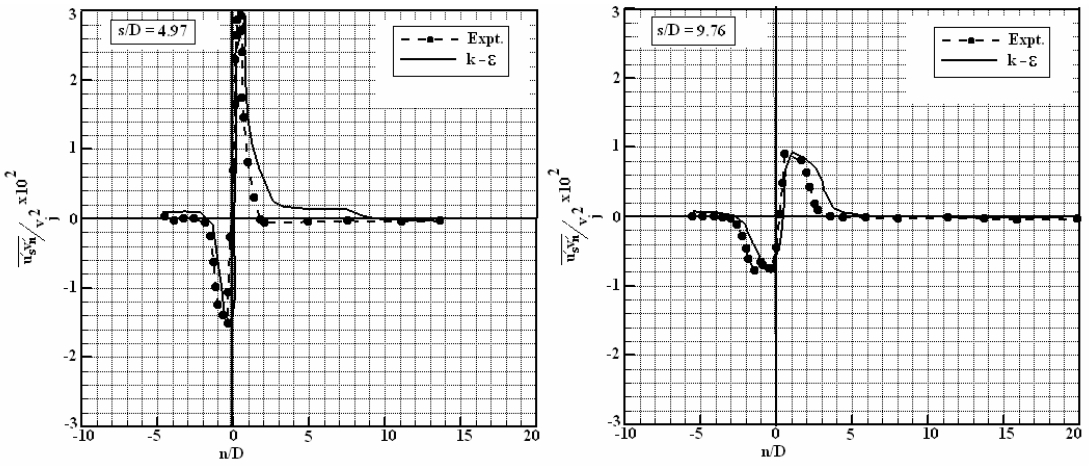

Fig. 4.78: Comparison of turbulence shear stress at jet central plane ($z/D = 0$) for $R = 9$, $s/D = 4.97$ and 9.76.

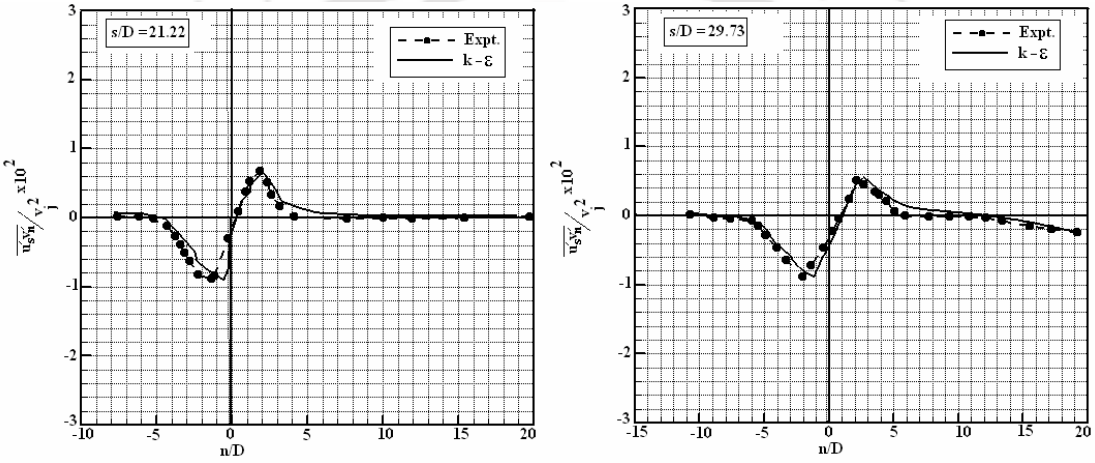

Fig. 4.79: Comparison of turbulence shear stress at jet central plane ($z/D = 0$) for $R = 9$, $s/D = 21.22$ and 29.73.

4.5 Comparison of 2D and 3D Results

We have presented the computational results of 2D flow fields in the Chapters 3. The 2D investigations represent the flow field at the jet central plane ($z/D = 0$) with an assumption that there is no spanwise variation of the fluid properties in the flow field. However, we have observed from the 3D investigation in this chapter that the flow field shows significant variations in the spanwise direction. The flow field is also characterised by different types of vortices, which eventually become 3D. In such conditions a 2D investigation can produce only an approximate analysis of the flow configuration at the jet central plane. Both the degree of approximations of 2D investigations and the accuracy of the 3D investigations can be observed by

comparing the 2D and 3D numerical results with the experimental data. In order to achieve this objective, a comparison of the 2D and 3D numerical results of the rectangular jet in crossflow with the measurements of Ramaprian and Haniu (1983) and Haniu and Ramaprian (1989) is presented in this section. It is to be noted that only the standard k–ε model is used in both the predictions of 2D and 3D flow field.

4.5.1 Mean Velocity Components

A comparison of the normalized streamwise component of the mean velocity (u_s/v_j) at the jet central vertical plane (z/D = 0) with the experimental data at four different downstream locations (s/D = 4.94, 9.68, 18.86 and 28.12) for the velocity ratio R = 6 is shown in Figs. 4.80 and 4.81.

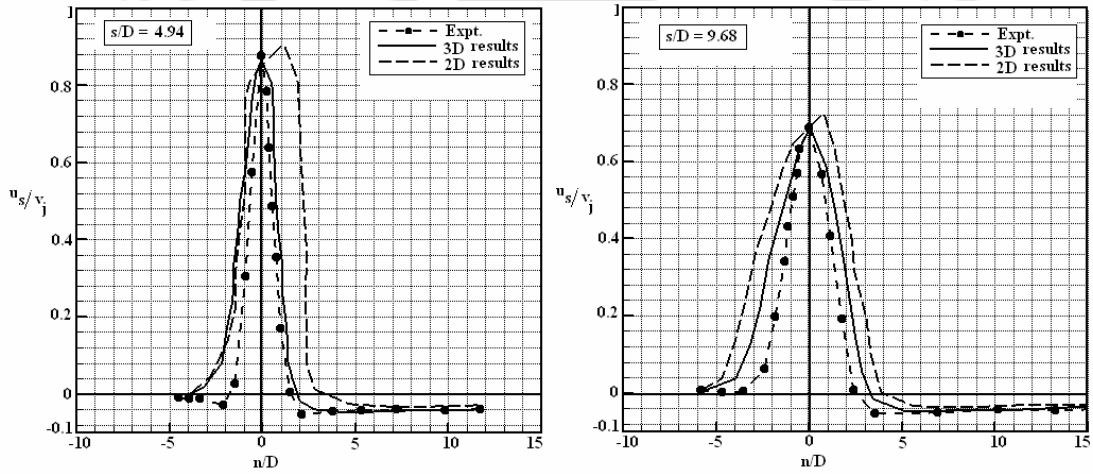

Fig. 4.80: Comparison of mean streamwise velocity at jet central plane (z/D = 0) for R = 6, s/D = 4.94 and 9.68.

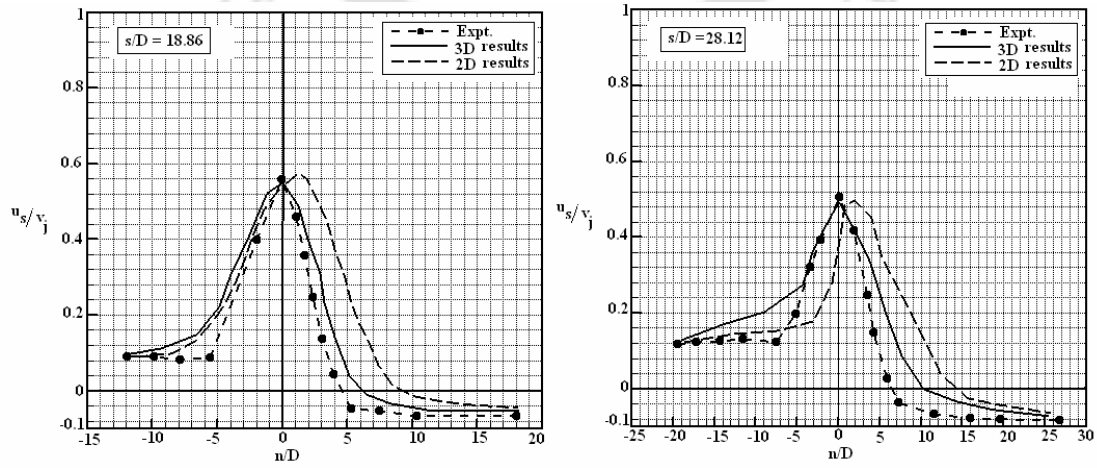

Fig. 4.81: Comparison of mean streamwise velocity at jet central plane (z/D = 0) for R = 6, s/D = 18.86 and 28.12.

It is observed that the 2D predictions show a higher spread of the jet especially in the inner part of the jet than that by the 3D predictions. The position of the peak value predicted by 3D investigation matches well with the experimental data, whereas a deviation is observed between 2D investigation and the experimental data (Figs. 4.80 and 4.81). The position of the jet maximum value is shifted towards the bottom of the jet in the later case. The difference between the two results is more at the downstream positions than in the near-field of the jet. The poor predictions of 2D investigations in the inner portion can be ascribed to the inability of capturing the entrainment and other secondary effects of the flow field.

Figs. 4.82 and 4.83 show a comparison of the normalized streamwise component of the mean velocity (u_s/v_j) at the jet central vertical plane (z/D = 0) at four different downstream locations (s/D = 4.97, 9.76, 21.22 and 29.73) with the experimental data for the velocity ratio R = 9. In this case also the spread of the jet from the 2D prediction is observed to be more than that from the 3D predictions. Moreover the peak velocity value is under predicted in 2D investigation except in the position of s/D = 9.76, where the peak velocity is over predicted by the 2D investigation.

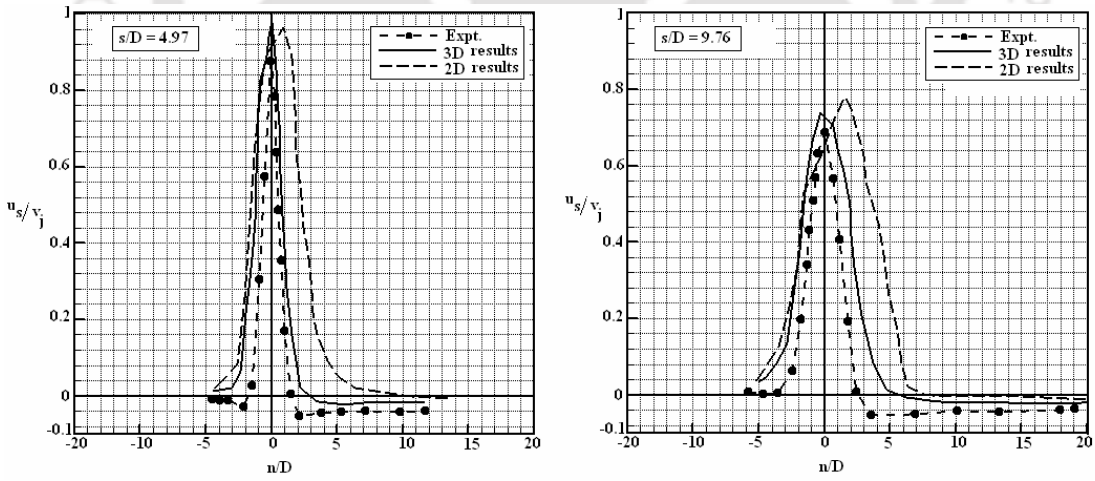

Fig. 4.82: Comparison of mean streamwise velocity at jet central plane (z/D = 0) for R = 9, s/D = 4.97 and 9.76.

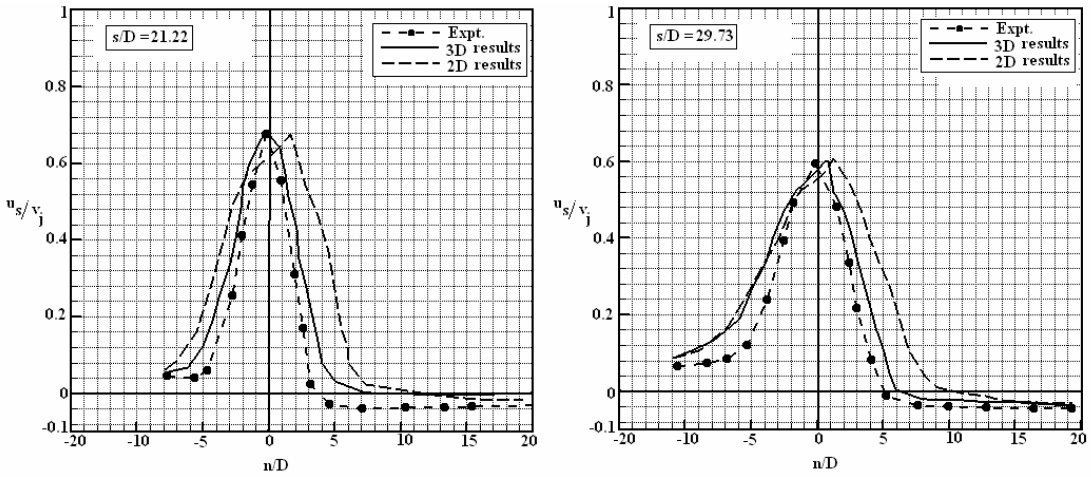

Fig. 4.83: Comparison of mean streamwise velocity at jet central plane (z/D = 0) for R = 9, s/D = 21.22 and 29.73.

A comparison of the normalized normal component of the mean velocity (v_n/v_j) at the jet central vertical plane (z/D = 0) at four different downstream locations (s/D = 4.94, 9.68, 18.86 and 28.12) with the experimental data for the velocity ratio R = 6 is shown in Figs. 4.84 and 4.85. The agreement of the 3D predictions with the experimental data is better than that by the 2D predictions. In the bottom portion of the jet, the 2D prediction produces poor agreement with the experimental data compared to that by the 3D prediction. This is may be due to the same reasons as that mentioned for the streamwise velocity (Figs. 4.80 and 4.81).

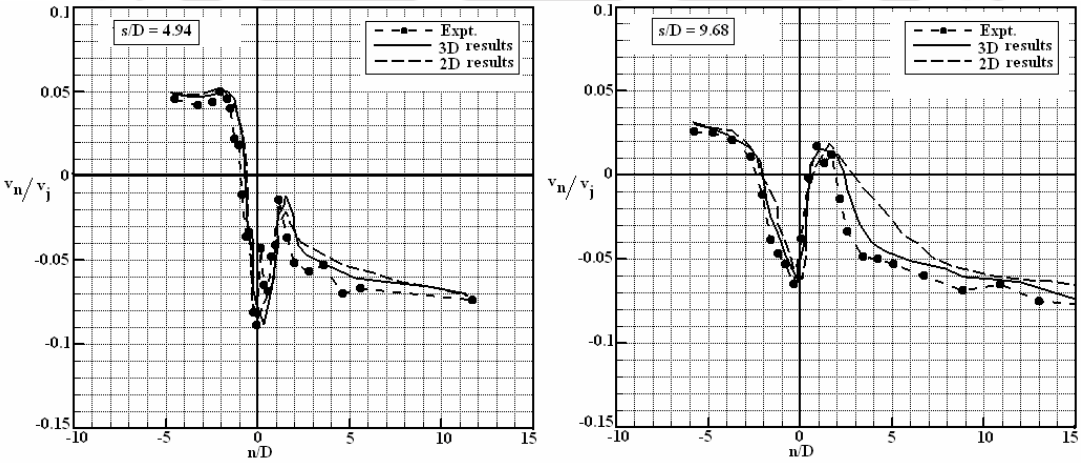

Fig. 4.84: Comparison of mean normal component velocity at jet central plane (z/D = 0) for R = 6, s/D = 4.94 and 9.68.

A comparison of the normal component of the mean velocity (v_n/v_j) at the jet central plane (z/D = 0) for R = 9 is shown in Figs. 4.86 and 4.87. Similar observations

as in the case of R = 6 can be made here. It is observed that the agreement of 2D predictions in the bottom part of the jet at far downstream positions (Figs. 4.86 and 4.87) with the experimental data is worse than that in the case of R = 6 (Figs. 4.84 and 4.85).

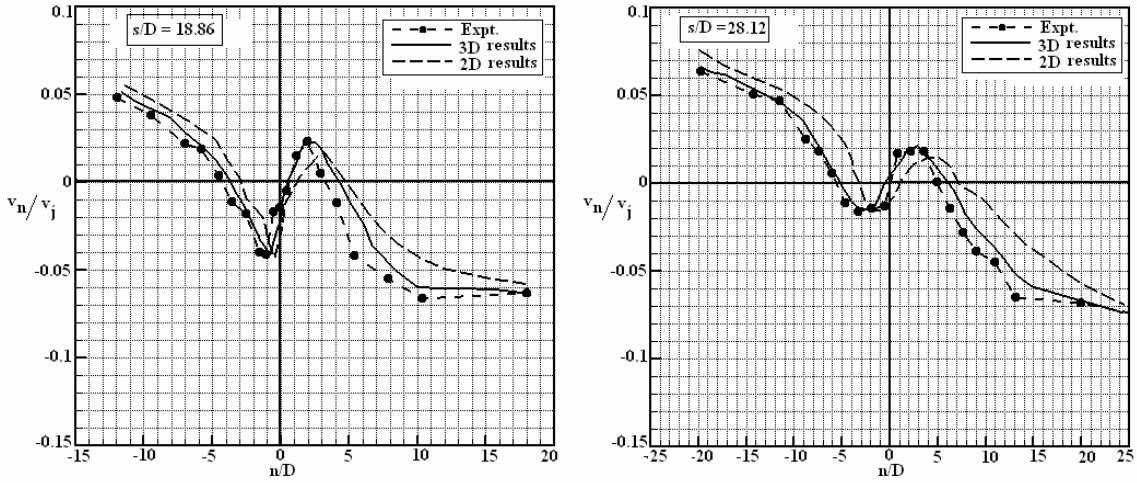

Fig. 4.85: Comparison of mean normal component velocity at jet central plane (z/D = 0) for R = 6, s/D = 18.86 and 28.12.

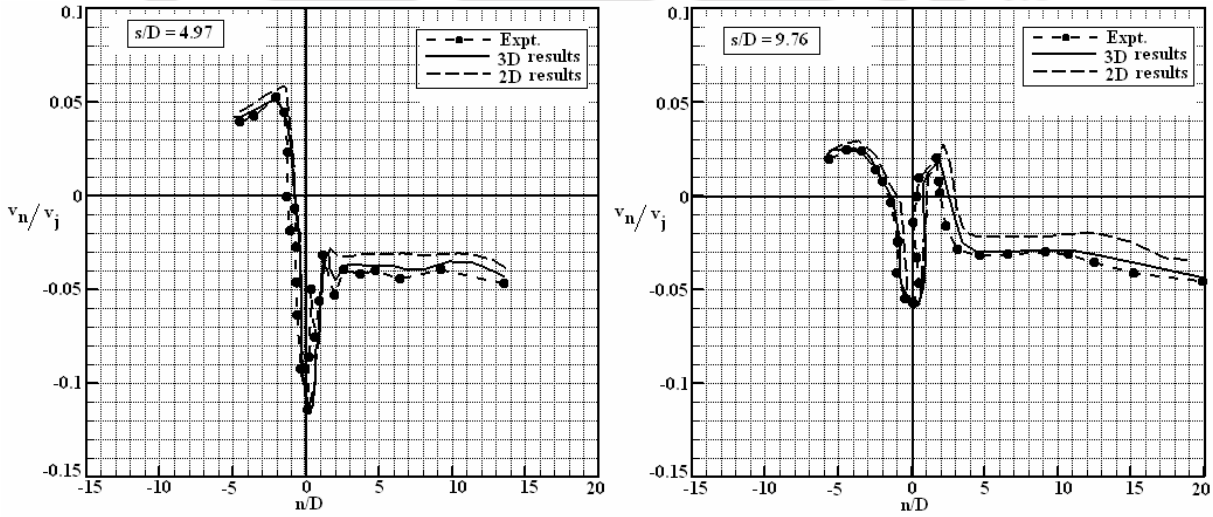

Fig. 4.86: Comparison of mean normal component velocity at jet central plane (z/D = 0) for R = 9, s/D = 4.97 and 9.76.

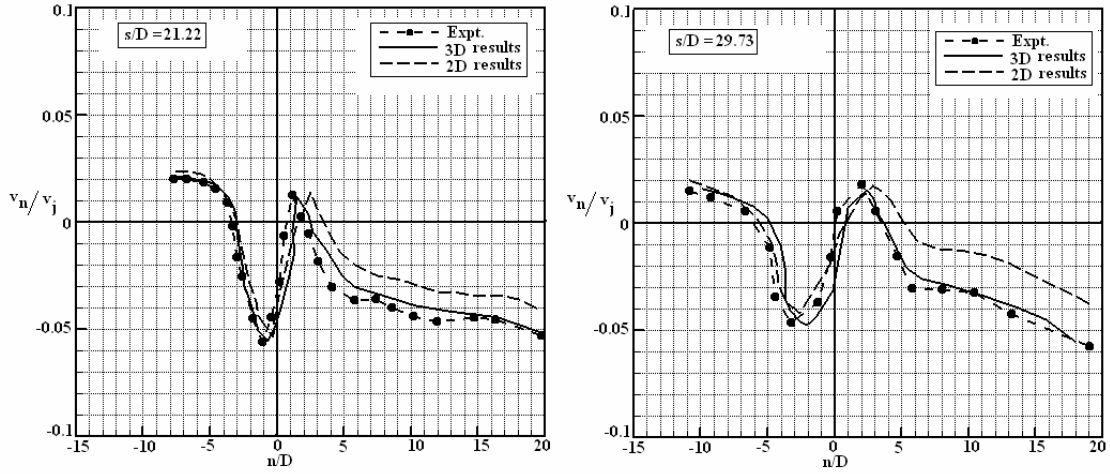

Fig. 4.87: Comparison of mean normal component velocity at jet central plane (z/D = 0) for R = 9, s/D = 21.22 and 29.73.

4.5.2 Turbulence Shear Stress

A comparison of the normalized turbulenc shear stress at the jet central vertical plane (z/D = 0) at four different downstream locations (s/D = 4.94, 9.68, 18.86 and 28.12) with the experimental data for the velocity ratio R = 6 is shown in Figs. 4.88 and 4.89. The profile of the turbulence shear stress is governed by the velocity gradient. Thus the turbulence shear stress profile should also show the same behaviour as that of the mean velocity. The 2D predictions over predict whereas the 3D predictions are in good agreement with the experimental data. Moreover the location of the maximum shear stress predicted by the 2D investigations does not match with the experimental data.

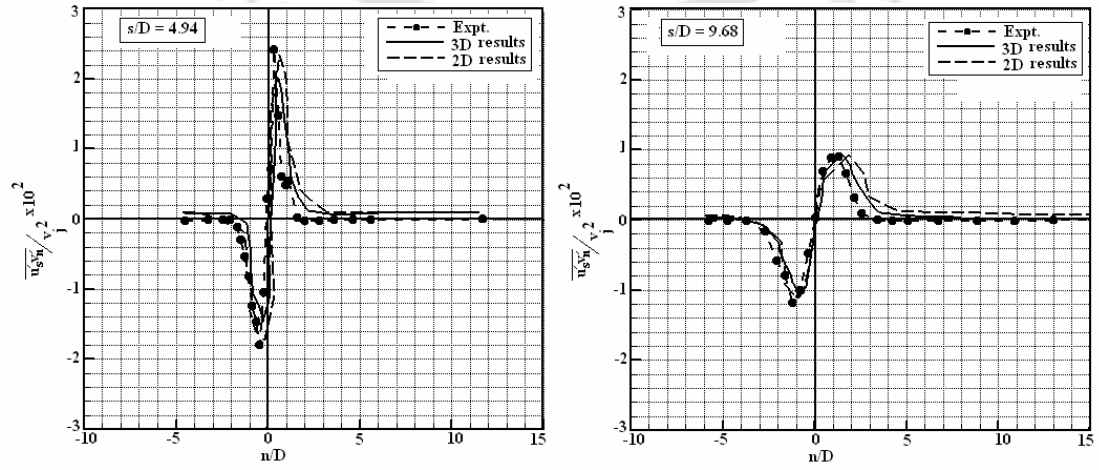

Fig. 4.88: Comparison of turbulence shear stress at jet central plane (z/D = 0) for R = 6, s/D = 4.94 and 9.68.

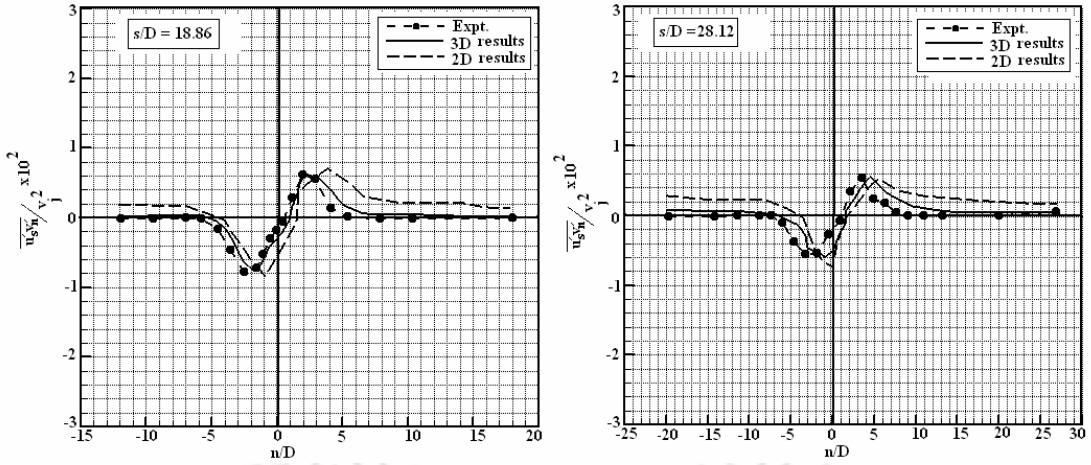

Fig. 4.89: Comparison of turbulence shear stress at jet central plane ($z/D = 0$) for $R = 6$, $s/D = 18.86$ and 28.12.

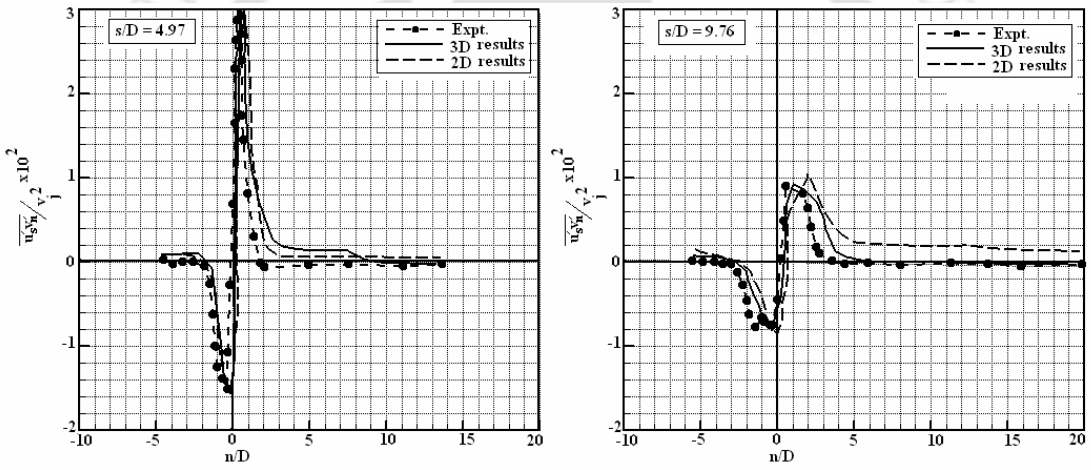

Fig. 4.90: Comparison of turbulence shear stress at jet central plane ($z/D = 0$) for $R = 9$, $s/D = 4.97$ and 9.76.

In case of the velocity ratio $R = 9$ (Figs. 4.90 and 4.91) similar observations of the trend of shear stress as observed in case $R = 6$ are made. The position of the maximum shear stress in the 2D predictions is shifted more towards the inner part of the jet in case of $R = 9$ especially in the downstream position than that in the case with $R = 6$.

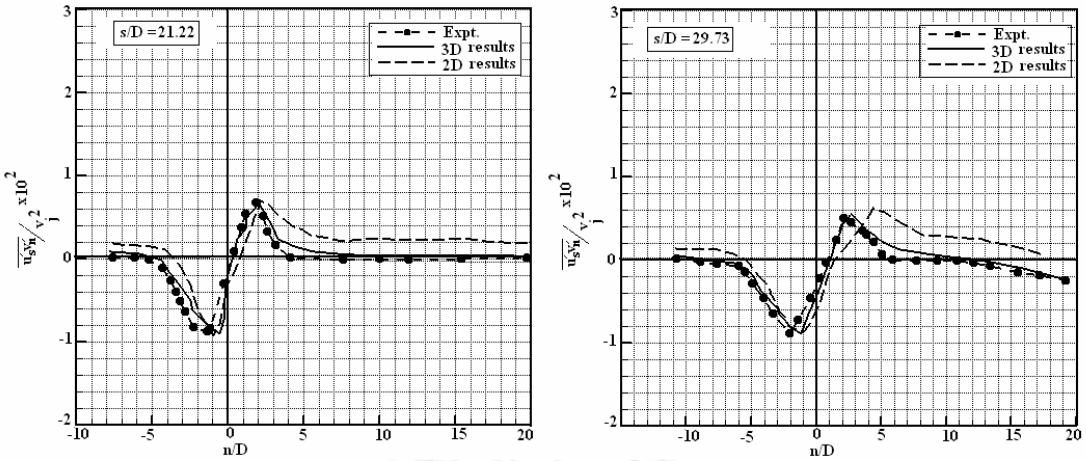

Fig. 4.91: Comparison of turbulence shear stress at jet central plane ($z/D = 0$) for $R = 9$, $s/D = 21.22$ and 29.73.

4.6 Conclusions

A 3D numerical investigation of the mean flow field of a rectangular jet in crossflow has been presented in this chapter. The governing equations, turbulence model and the computational methodology employed are also presented. The predictions of the mean velocity field and the turbulence properties are presented in the Cartesian coordinates to facilitate the explanation of the near wall flow field. The variations of all the flow properties along the jet discharge direction at different spanwise planes and at different downstream locations are discussed. Moreover the variations of the flow properties in spanwise directions are also presented. Thus a detailed 3D investigation of the flow field is made. Also a comparison of the 2D and 3D predictions of important flow properties is made in this chapter. From the investigation it is concluded that the flow field exhibits a 3D nature. The standard k-ε model is used as the turbulence model and it has performed well by reproducing many physical and realistic results which are similar with the results reported in the literature. The model also produces reasonably good agreement with the experimental data. The effect of the velocity ratio on the flow field is discussed for the two velocity ratios $R = 6$ and 9. The velocity ratio is found to affect the flow features such as the trajectory and the lateral spread of the jet and the low velocity region downstream of the jet. The turbulence properties such as the turbulence kinetic energy and shear stress are also affected by the velocity ratio. The formations of different types of vortices in the flow field are discussed. The present predictions capture well the steady structures of the

wake vortices and counter-rotating vortex pair. However, the structure of the horse shoes vortices is captured weakly and the unsteady structure of shear layer vortices is not captured. The length scales of these vortices are significantly greater than those of eddies containing the turbulence energy and are therefore considered to be associated with the mean flow rather than the turbulence. The effect of the velocity ratio on the formation of these vortices is also observed. A high value of the velocity ratio was associated with the reduced size of the wake vortices and the reverse flow region downstream of the jet slot. Due to the omission of several 3D effects, the 2D numerical investigation produces a relatively poor agreement with the experimental data. A good agreement between the predictions of the 3D flow field and the experimental data is observed compared to that from the 2D investigation. The present investigation has produced quite a bit of new information of the flow field and thus provides a deeper insight to the flow physics than that provided by Ramaprian and Haniu (1983) and Haniu and Ramaprian (1989).

Chapter 5

Three-dimensional Heated Jets in Crossflow

5.1 Introduction

In Chapters 3 and 4, we have presented the results of numerical investigations of 2D and 3D flow fields of a rectangular jet in crossflow. In both the Chapters we have carried out the investigations by assuming the entire flow field to be isothermal. In many applications the flow field of a heated jet in cold crossflow is encountered such as exhaust gas issuing from the exhaust stacks of most power plants, and behind steam locomotives, etc. In most of these practical problems, jets and plumes are either discharged vertically or at an angle to a crossflow. In such flow conditions, the jet and crossflow interactions, the resulting temperature downstream of the jet, thermal spread or the trajectory and physical path of the jet are extremely important factors for design. Accordingly, when the temperature field is strongly affected by the velocity field and can be regarded as a passive scalar, it is necessary to understand the mean and fluctuating characteristics of the thermal spread and mixing in such jets in a crossflow. The flow behaviour and heat transfer analysis of a heated jet in crossflow are reported by several researchers (Ramaprian and Haniu, 1983, Wark and Foss, 1998, Haniu and Ramaprian, 1989, Chen and Hwang, 1991, Sherif and Pletcher, 1991, Nishiyama et al., 1993, Sarkar and Bose, 1995, Hwang and Chiang, 1995, Shi et al., 2003, and Said et al., 2003).

In the present work, we have used the standard k–ε model for investigating the 2D and 3D flow fields of an isothermal jet. We have also used the streamline curvature modification model in the investigation of 2D flow field of an isothermal jet in crossflow. The streamline curvature modification model showed the improvement in the prediction over the standard k–ε model in some region of the flow fields especially in the inner part of the jet. We did not make any comparison of the performance of the standard k-ε model with any other model in investigating the 3D flow field. In the present chapter we present a comparison of the performance of the standard k–ε model with a Reynolds stress transport (RST) model. The RST model is known to work better than the standard k–ε model in investigating the flow fields that are highly anisotropic and characterized by streamline curvature effects like the flow field of jets

in crossflow (Demuren, 1993). In RST model, the transport equations for different components of Reynolds stresses are solved and therefore it has the ability to produce better results than those produced by the other two equation models. Demuren (1993) has observed that a RST model reproduces peak vorticity and CRVP strength very well and predicts Reynolds stresses better than those predicted by the standard k–ε model. Moreover, this model is computationally much less expensive than the use of either LES or DNS.

Only a few investigators report the use of RST model for computing the flow field of jet in crossflow. Ince and Leschziner (1990, 1993) used a high Reynolds number RST model with wall functions to study the flow field of single and multiple jets in a crossflow. Demuren (1993) also reported predictions with a high Reynolds number model using a multigrid method and obtained fairly good predictions of the mean flow field. Jansson and Davidson (1996) applied near-wall corrections to the basic linear model and solved a low-Reynolds number RST model to predict effusion cooling in a double-row discrete-hole configuration. They reported better predictions than those by a two-layer k–ε model. Hale et al. (2000) used commercial flow solver FLUENT to study the surface heat transfer associated with a row of short-hole jets in a crossflow. They used a RST model along with the non-equilibrium wall functions and a two-layer zonal approach and found a better performance by two-layer zonal method than that by RST model. Hale et al. (2000) investigated multiple round jets in a crossflow. However, no work on the study of plane jet in crossflow using Reynolds stress transport model has been reported in the literature.

In the present chapter the flow field of a slightly heated jet in crossflow is discussed. The governing time-averaged momentum equations in three directions and the energy equation are solved for the same computational domain as given in Chapter 4. A RST model is used for resolving the turbulence in the flow field. The computations are carried out using the commercial code FLUENT 6.2.16 based on the finite volume method. Comparisons of the predictions by the RST model and the standard k–ε model, described in the Chapter 4, are made with the experimental data of Ramaprian and Haniu (1983) and Haniu and Ramaprian (1989). A description of the governing equations, turbulence model and computational domain is presented in Section 5.2. Section 5.3 describes the computational methodology. The predictions of the mean and turbulence quantities and their comparisons with the measurements are described in Section 5.4, followed by the conclusions in Section 5.5.

5.2 Governing Mean Flow Equations

The Reynolds-averaged continuity, three momentum equations and energy equation are the governing equations. We assume the flow to be steady in mean. The equations may be expressed using the Cartesian tensor notation as follows

Continuity:

$$\frac{\partial}{\partial x_j}\left(u_j\right)=0 \tag{5.1}$$

Momentum:

$$\frac{\partial}{\partial x_j}\left(u_i u_j\right)=-\frac{\partial p}{\rho \partial x_i}+\frac{\partial}{\partial x_j}\left[-\overline{u_i' u_j'}\right] \tag{5.2}$$

Energy:

$$\frac{\partial(u_j T)}{\partial x_j}=\frac{\partial}{\partial x_j}\left[\frac{\nu_t}{\sigma_t}\frac{\partial T}{\partial x_j}\right] \tag{5.3}$$

Here u_i s denote the mean velocities, p the mean pressure and T the mean temperature. σ_t denotes turbulence Prandtl number and is defined as the ratio of the thermal diffusivity and eddy diffusivity. In many applications one can get results of modest accuracy by using a constant value of σ_t (Biswas and Eswaran, 2002). The value of the turbulence Prandtl number used in the present work is 0.85.

It is to be noted that the jet discharge and the flow in the entire computational domain are assumed to be fully turbulent and thus independent of the value of Reynolds number. The discharged jet is at a slightly higher temperature than that of the crossflow with a temperature difference of 5.7°C for the velocity ratio R = 6 and 6.1^{0}C for R = 9 according to the experimental conditions. The value of the exit buoyancy Richardson number ($R_{bj}=\frac{\Delta\rho_j g D}{\rho_a v_j^2}$) due to the heating is quite low thus ensuring a negligible buoyancy effect with temperature playing the role of a passive scalar only. A physical quantity that is transported by the flow but in turn does not alter the flow field is called a passive scalar. In such a condition, a passive scalar such as temperature is transported only by the forced convective flow. In many engineering applications, the distribution of some passive scalar such as concentration is

important. Therefore in the present thesis we have also studied the distribution of passive scalar. It is logical to use the momentum ratio ($=\frac{\rho_j v_j^2}{\rho_a u_a^2}$) in the formulation of investigation of heated jet in crossflow, but since both the jets and crossflow are of the same fluid (water), the change of density for a small temperature difference was assumed to be negligible. Thus the momentum ratio is equivalent to the square of velocity ratio.

5.2.1 Turbulence Models: Reynolds Stress Transport (RST) Model

Transport equations for six individual components of Reynolds stresses ($\overline{u_i' u_j'}$) are solved numerically. The exact form of the Reynolds stress transport equations may be derived by taking moments of the exact momentum equation. This is a process wherein the exact momentum equations are multiplied by a fluctuating property, the product then being Reynolds-averaged. However, several terms in the exact equation are unknown and modeling assumptions are required to close the equations. The exact equations of stresses used for the present investigations can be written in the tensor notation as:

$$\underbrace{\frac{\partial}{\partial x_k}\left(u_k \overline{u_i' u_j'}\right)}_{C_{ij}=Convection} = \underbrace{-\frac{\partial}{\partial x_k}\left[\overline{u_i' u_j' u_k'} + \overline{p'(\delta_{kj} u_i' + \delta_{ik} u_j')}\right]}_{D_{ij}^T=Turbulent\ Diffusion} \underbrace{-\left(\overline{u_i' u_k'}\frac{\partial u_j}{\partial x_k} + \overline{u_j' u_k'}\frac{\partial u_i}{\partial x_k}\right)}_{P_{ij}=Stress\ Production}$$

$$+ \underbrace{\frac{p'}{\rho}\overline{\left(\frac{\partial u_i'}{\partial x_j} + \frac{\partial u_j'}{\partial x_i}\right)}}_{\phi_{ij}=Pressure\ Strain} \underbrace{- 2\nu_t \overline{\frac{\partial u_i'}{\partial x_k}}\,\overline{\frac{\partial u_j'}{\partial x_k}}}_{\varepsilon_{ij}=Dissipation} \qquad (5.4)$$

Since the jet discharge and the flow in the entire computational domain are assumed to be fully turbulent, the effect of the molecular viscosity is assumed to be negligible, and therefore the molecular diffusion term of the Reynolds stress equations is neglected.

To obtain the boundary conditions for the Reynolds stresses at different boundary zones, the equation for the turbulence kinetic energy (k) is solved. Moreover the equation for the dissipation rate (ε) of k is solved to obtain the dissipation rate (ε_{ij}) of Reynolds stress tensor. In both the equations a few minor modifications are made to the original form of the equations. The equations are as follows.

$$\frac{\partial}{\partial x_i}(ku_i) = \frac{\partial}{\partial x_j}\left(\frac{\nu_t}{\sigma_k}\frac{\partial k}{\partial x_j}\right) + \frac{1}{2}P_{ii} - \varepsilon \tag{5.5}$$

$$\frac{\partial}{\partial x_i}(\varepsilon u_i) = \frac{\partial}{\partial x_j}\left(\frac{\nu_t}{\sigma_\varepsilon}\frac{\partial \varepsilon}{\partial x_j}\right) + \frac{1}{2}C_{\varepsilon 1}P_{ii}\frac{\varepsilon}{k} - C_{\varepsilon 2}\frac{\varepsilon^2}{k} \tag{5.6}$$

where P_{ii} is the production of k and $\sigma_k = 0.82$, $\sigma_\varepsilon = 1.0$, $C_{\varepsilon 1} = 1.44$, $C_{\varepsilon 2} = 1.92$ are the model constants. Although Eq. (5.5) is solved globally throughout the computational domain, the values of k obtained are used only for boundary conditions. In every other case, k is obtained by taking the trace of the Reynolds stress tensor: $k = \frac{1}{2}\overline{u_i' u_i'}$ (5.7)

Among the various terms of Reynolds stress transport equation (5.4), the convection term (C_{ij}) and the production term (P_{ij}) do not require any modelling. However, the turbulence diffusion term (D_{ij}^T), the pressure strain term (ϕ_{ij}), and the dissipation term (ε_{ij}) need to be modelled to close the set of governing equations.

Modelling the Turbulence Diffusion Term (D_{ij}^T)

In most cases, the turbulence diffusion term is modelled by the Daly-Harlow (1970) model. However the model sometimes results in numerical instabilities. Therefore in FLUENT the turbulence diffusive term is modelled as suggested by Lien and Leschziner (1994). In this modelling the diffusive term is simplified by using a scalar turbulence diffusivity as:

$$D_{ij}^T = \frac{\partial}{\partial x_k}\left(\frac{\nu_t}{\sigma_k}\frac{\partial \overline{u_i' u_j'}}{\partial x_k}\right) \tag{5.8}$$

where $\sigma_k = 0.82$ (Lien and Leschziner, 1994).

Modelling the Pressure Strain Term (ϕ_{ij})

This term is modelled in FLUENT with a linear pressure strain model as suggested by Gibson and Launder (1978), Fu et al. (1987) and Launder (1989a, 1989b). However the highly anisotropic nature of the flow due to the streamline curvature near the jet discharge, resulting from a strong interaction between the jet discharge and crossflow, suggests that the production term and the pressure strain correlation play a dominant

role in the prediction of turbulence stresses. The later process is especially important in producing the anisotropy of normal stress components. The quadratic pressure strain model proposed by Speziale et al. (1991), which is known to improve the accuracy of flow field with streamline curvature, is used to model the pressure-strain term of the Reynolds stress transport equation (5.4). The model is written as

$$\phi_{ij} = -(C_1\varepsilon + C_1^* p')b_{ij} + C_2\varepsilon(b_{ik}b_{kj} - \frac{1}{3}b_{mn}b_{mn}\delta_{ij}) + (C_3 - C_3^*\sqrt{b_{ij}b_{ij}})kS_{ij} +$$

$$C_4 k(b_{ik}S_{jk} + b_{jk} - \frac{2}{3}b_{mn}S_{mn}\delta_{ij}) \qquad (5.9)$$

Where b_{ij} is the Reynolds stress anisotropy tensor defined as

$$b_{ij} = -\left(\frac{-\overline{u_i'u_j'} + \frac{2}{3}k\delta_{ij}}{2k}\right)$$ and the mean strain rate S_{ij} is defined as

$$S_{ij} = \frac{1}{2}\left(\frac{\partial u_j}{\partial x_i} + \frac{\partial u_i}{\partial x_j}\right)$$

The model constants are $C_1 = 3.4$, $C_1^* = 1.8$, $C_2 = 4.2$, $C_3 = 0.8$ and $C_3^* = 1.3$.

Modelling the Dissipation Term (ε_{ij})

This is modelled in terms of dissipation rate (ε) of turbulence kinetic energy as proposed by Sarkar and Balakrishnan (1990). The modelled dissipation term is written as follows

$$\varepsilon_{ij} = \frac{2}{3}\delta_{ij}\varepsilon \qquad (5.10)$$

An additional dilatation dissipation term, which takes care of the compressible effect in the flow field, has been neglected in Eq. (5.10).

It is to be noted that a Reynolds stress transport model is applicable only for fully turbulence flows and not applicable in the vicinity of a solid wall. In the near wall region, the molecular viscosity affects the generation, destruction and transport of the Reynolds stresses. Wall functions account for the shortcomings of the RST model in the near wall region. In the present work, the standard wall functions are used for resolving the near wall turbulence in the model. The values of Reynolds stresses are calculated from the adjacent wall cells by employing the wall functions. The

Reynolds stresses at the wall adjacent cell are computed in terms of k. Further details of the Reynolds stress transport model used in the present work are given in the FLUENT-6.2 (2005) manual.

5.2.2 Computational Domain

We have used the same computational domain as given by Fig. 4.1, Chapter 4 and the domain size for different values of R used is according to Table 4.1.

5.2.3 FLUENT 6.2.16

FLUENT is a commercial CFD code developed and marketed by Fluent Inc, which is based on the finite volume method. The code employs state-of-the-art computer programs for modeling fluid flow and heat transfer in different geometries. It is written in C and makes full use of the flexibility and power offered by this language. Due its robustness and providing solutions for varieties of fluid flow problem FLUENT is extensively used for many industrial problems as well as fundamental research (Zhao et al., 2004, Kaiser et al., 2004, Christopher et al., 2005, Laccarino, 2001, Shi et al., 2003 and Vijayan and Balaji, 2004, etc).

5.2.4 Computational Mesh

The commercial software Gambit 2.1.6 is used to create the geometry and mesh of the present computational domain. Since the geometry is Cartesian, hexahedral elements are used for meshing the geometry. A non-uniform grid is used and the grids are clustered at the jet exit and near wall regions. The structure of the computational mesh is kept the same as that used for the isothermal jet in crossflow (Chapter 4). However, the numbers of control volumes used in the present case is larger than those used in the later. This is done by comparing the results of FLUENT code with those by the in-house code developed by the author employing the same turbulence model (standard $k-\varepsilon$ model) for R = 6. The difference between the two codes using the same conditions was found to be 1.57%. The number of control volumes excluding the jet duct used are 150×95×65 (= 926250) for R = 6. The jet duct comprised 12×16×30 (= 5760) control volumes.

5.2.5 Boundary Conditions

A wide range of boundary conditions are available in FLUENT and for a particular problem one has to select the most appropriate boundary conditions. Before applying the boundary conditions in FLUENT, different boundary zones are made in the computational domain. Different types of boundary conditions are used for different boundary zones of the flow domain. The different boundary conditions used in the present computations with reference to the FLUENT are inlet, outflow, free surface and wall.

(xii) **Crossflow Inlet:** FLUENT provides several types of boundary zones at the flow inlet such as the velocity inlet type, pressure inlet type, and mass flow inlet type. The velocity inlet types of boundary conditions are used at the crossflow inlet. In this type of boundary conditions the velocity and scalar properties at the flow inlet are defined. Thus the velocity components are prescribed as $u = u_a$, $v = 0$ and $w = 0$. The crossflow inlet boundary layer thickness is set to $1.5D$ by adapting the boundary at the velocity inlet zone to match with the experimental conditions. Inside the boundary layer, the $1/7^{th}$ power-law profile is used for the u-velocity component. A user defined function (UDF) is used to introduce this profile at the inlet. The values of turbulence quantities at the crossflow inlet used are based on the turbulence specification method where the turbulence intensity and a length scale are prescribed. The value of the turbulence kinetic energy is taken from the 5% turbulence intensity based on the experimental data. The domain length in the vertical direction is used as the length scale to represent the turbulence dissipation rate. The values of Reynolds stresses at the flow inlet are taken from the prescription of turbulence kinetic energy by assuming the isotropy of the turbulence as: $\overline{u_i'^2} = \frac{2}{3}k$, $\overline{u_i'u_j'} = 0$. The non-dimensionalised temperature of 0.9813 for R = 6 and 0.9800 for R = 9 is specified at the crossflow inlet which is maintained at a temperature of 300K.

(xiii) **Top Surface:** The top surface is assumed to be a wall-free surface having the zero shear stress. No convective and diffusive flux is assumed to occur

across this surface. To represent these conditions symmetric conditions are employed in FLUENT and therefore this condition is used at the top surface.

(xiv) **Outflow:** This represents the outlet of the computational domain (i.e. the right face). Here the normal gradients of all variables are made zero through the outflow boundary condition in FLUENT.

(xv) **Bottom Boundary:** The entire bottom boundary excluding the jet discharge is considered as a solid wall. The wall-boundary conditions are applied at the bottom boundary. To treat the near wall turbulence the standard wall functions are activated at the time of choosing the RST model. At the wall, FLUENT computes the near-wall values of Reynolds stresses in terms of k by using the standard wall functions. To define the thermal boundary conditions at the wall, FLUENT has different types of thermal conditions such as the fixed heat flux, fixed temperature, convective heat transfer, etc. In the present work the fixed temperature is applied at the wall. The non-dimensionalised temperature of the wall was set in the same way as described in the crossflow inlet boundary condition (= 300K)

(xvi) **Jet Exit:** At the jet exit, the velocity inlet type of boundary conditions are used where the velocity components are prescribed as $u = 0$, $v = v_j$, $w = 0$. The turbulence quantities are specified in the same way as in the case of crossflow inlet. The turbulence kinetic energy is specified based on 6% turbulence intensity and the length scale was taken as the width of the slot D. The non-dimensionalised temperature of 1.0 was set as the jet stream temperature for both the cases of $R = 6$ and 9.

(xvii) **Sidewalls:** At the sidewalls of the channel, the wall boundary conditions are used.

5.3 Computational Methodology

The computations are carried out by using the software FLUENT 6.2. The basic steps of the solution methods with the software are the same as in a conventional CFD technique: (1) Create the basic geometry and the grids for computational domain; (2) Starting the appropriate 2D or 3D solver; (3) Import and check the grids; (4) Select

the solver information and choose the basic equations to be solved; (5) Specify the boundary conditions; (6) Adjust the solution control parameters; and (7) Initialize the flow field and the start the iteration process. Two types of numerical methods for solving the basic equations of the flow field are available in FLUENT: (1) Segregated solver and (2) Coupled solver. In the segregated method continuity, momentum, energy and other transport equations are solved sequentially, whereas they are solved simultaneously in the coupled solution method. Since in the present flow configuration, the temperature is a passive scalar only, we have selected the segregated solver method. The momentum equations are discretised using the 2nd order upwind scheme and all transport equations are discretised using the power-law scheme. SIMPLE algorithm is used for coupling the pressure-velocity field. In the segregated solution method of FLUENT, each discrete governing equation is linearized implicitly with respect to the equation's dependent variable which results in a linear system of equations. A point implicit (Gauss-Seidel) linear equation solver is used in conjunction with an algebraic multigrid (AMG) method to solve the resultant system of equations for the dependent variable in each cell.

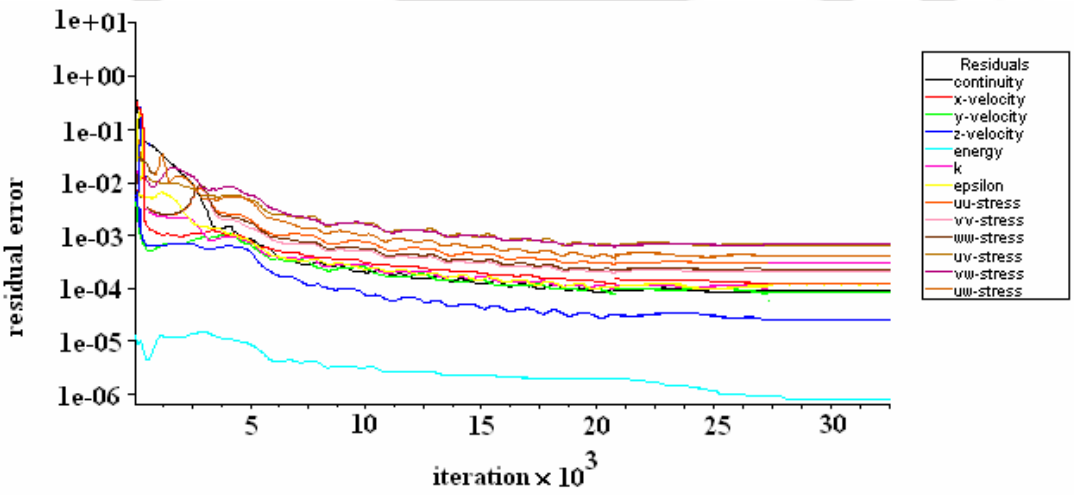

Fig. 5.1: History of residual fall for R = 6.

All the variables (u, v, w, k, and ε) are under-relaxed in each iteration. The solution is assumed to be converged when the normalized residual of the energy equation is lower than 10^{-6} and the normalized residuals of continuity and other variables are less than 10^{-3}. The history of the residual fall in the numerical solution for the jet with R = 6 is shown in Fig. 5.1. The computations are performed on a Pentium 4 machine with

512 Mb RAM, 1.6 GHz processor speed and it takes approximately 34 days of CPU time to obtain the converged solution.

5.3.1 Code Validation

The present FLUENT code is validated by testing the present computations with the result reported by Hoda et al. (2000), who performed numerical investigations for a square jet in a crossflow for the velocity ratio of 0.5 using two versions of RST model and by performing LES. For validation, the present FLUENT code employed the Chen (1995) model which was also used by Hoda et al. (2000). The Chen (1995) model uses the Daly and Harlow (1970) model for modeling the turbulence diffusion of RST equation and the quadratic pressure strain model for the pressure strain term.

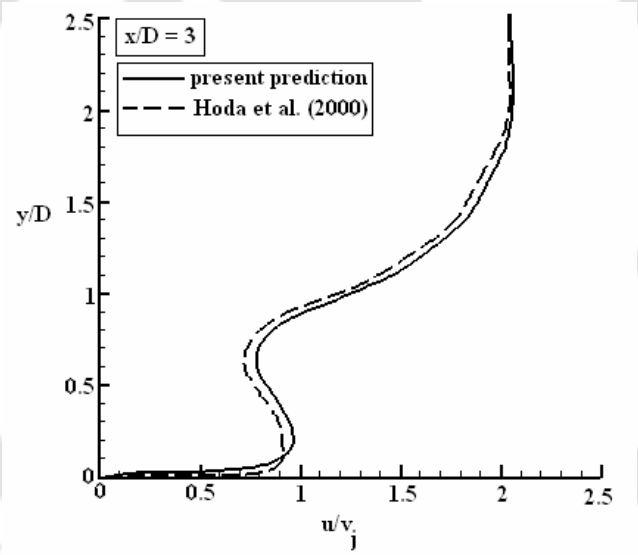

Fig. 5.2: Comparison of the present prediction with the results of Hoda et al. (2000) for the velocity ratio of $R = 0.5$, $z/D = 0$.

The wall reflection correction term was also included in the code. A comparison of predicted results of the cross-stream component of the mean velocity at a location of $x/D = 3$, $z/D = 0$ for the velocity ratio $R = 0.5$ by the present code with the results of Hoda et al. (2000) is shown in Fig. 5.2. The agreement between the two predictions is fairly good and the maximum difference between the two is 11.5%.

5.3.2 Grid Sensitivity

The grid sensitivity test of the present computation is conducted by using three different sets of grids, viz., 130×85×55 (130 along *x*-, 85 along *y*- and 55 along *z*-directions), 140×90×60, and 150×95×65 by comparing the cross-stream component of the mean velocity (*u*) profile for $R = 6$. The velocity profiles for $R = 6$ at the plane $z/D = 0$ and at the location $x/D = 2$ using the RST model is shown in Fig. 5.3. It has been observed that the grid refinement in general improves the prediction by reducing the higher prediction in the near wall region and increasing the peak value of the jet velocity. The deviation between the predictions using the three different grids decreases as the mesh is refined and the difference between the computations using the grid sizes 150×95×65 and 140×90×60 is 3.4%. The results that are presented in the subsequent sections are using the grid size of 150×95×65 for the velocity ratio $R = 6$ and 174×110×76 for $R = 9$.

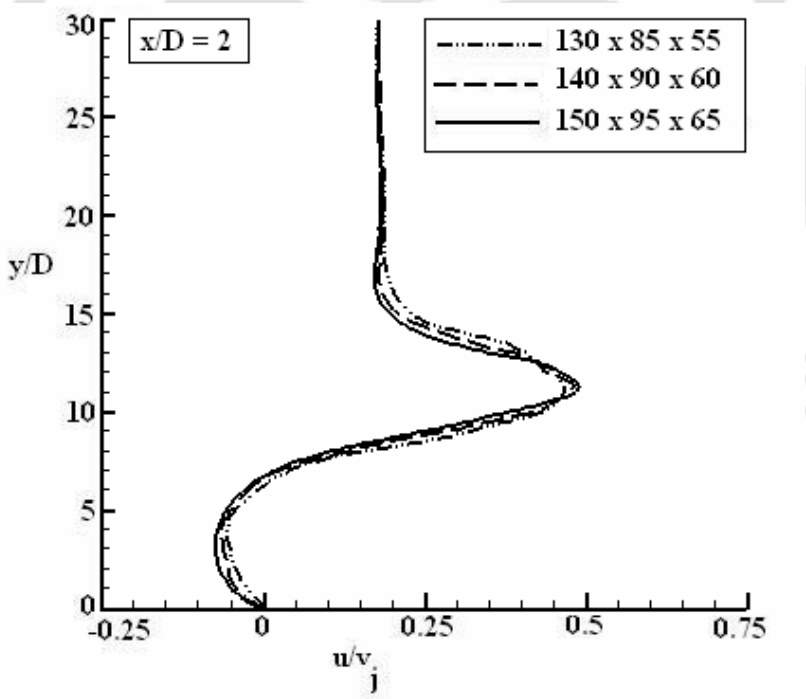

Fig. 5.3: Grid sensitivity test: predicted cross-stream component of the mean velocity (*u*) profile for $R = 6$, $z/D = 0$.

5.4 Results

The predictions of the mean flow properties and turbulence properties are presented in this section. Since the flow physics is discussed in details in Chapter 4, a qualitative comparison of the predictions by RST model and the standard *k-ε* model is presented in the present chapter. The comparisons are shown in Cartesian coordinates to facilitate an explanation of the near wall flow features.

5.4.1 Components of Mean Velocity

A comparison of the variation of cross-stream component of mean velocity (u) with distance *(y/D)* from the bottom wall at various downstream positions (*x/D)* and at different spanwise planes for the velocity ratio $R = 6$ is shown in Figs. 5.4 to 5.8. The different spanwise planes considered are at $z/D = 0$, 3, 5, 6 and -3. At the jet discharge region ($x/D = 0$) both the models show quite similar predictions since the same experimental conditions are used in both models at that location. Similar observations of small difference in the predictions of both the models are made at all other three spanwise planes ($z/D = 3$, 5 and 6) in the jet discharge region. At other downstream positions, the RST model predicts a higher penetration of the jet in to the crossflow as indicated by the recovery to the crossflow value at a higher *y/D* location than that by the standard *k-ε* model.

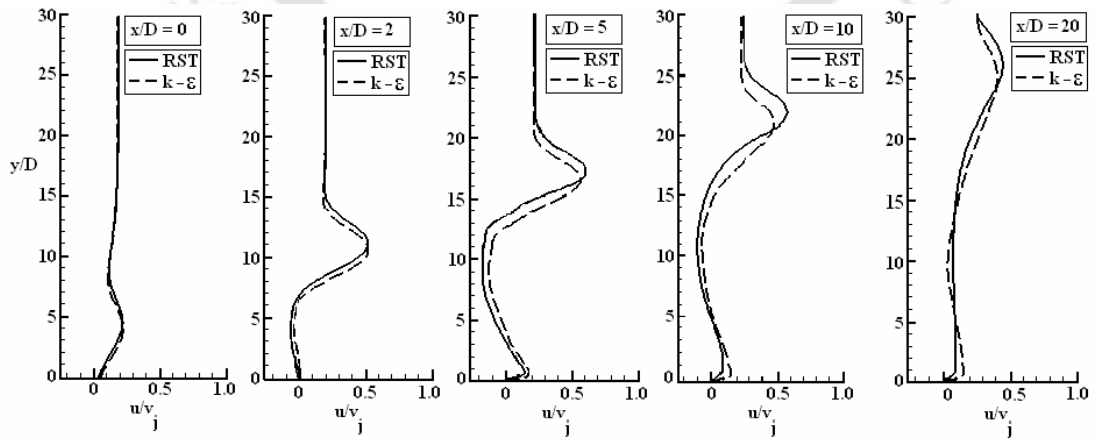

Fig. 5.4: Comparison of the cross-stream component of the mean velocity at different downstream locations ($z/D = 0$) for $R = 6$.

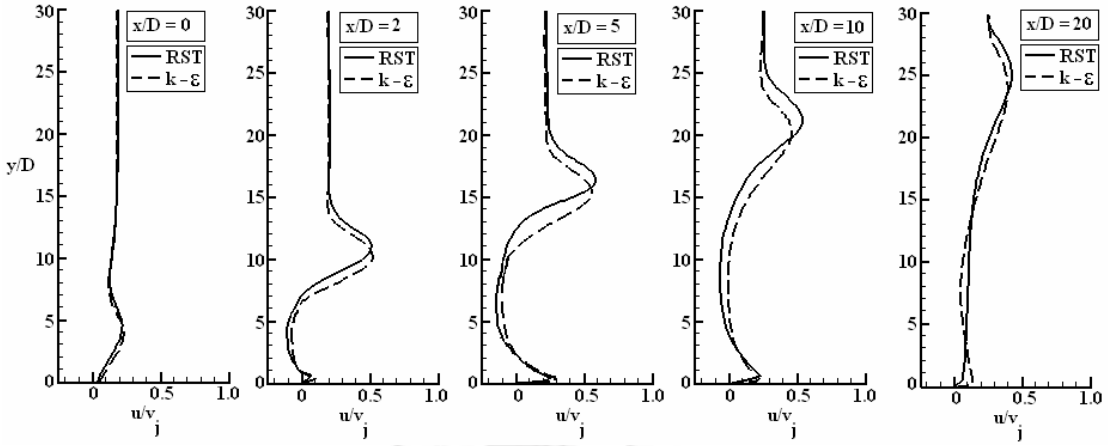

Fig. 5.5: Comparison of the cross-stream component of the mean velocity at different downstream locations (z/D = 3) for R = 6.

It is observed that the locations of the peak velocity predicted by both the models do not match. The RST model predicts a higher jet trajectory compared to that by the standard k-ε model. The standard k-ε model predicts higher values of velocity in the lower part of the jet. Near the bottom wall, i.e., in the wall-jet layer, the k-ε predicts a sharper gradient of velocity at all the downstream locations compared to that by the RST model. At the spanwise plane, which is outside of the jet slot (z/D = 6, Fig. 5.7) the difference between the two predictions is relatively small. Far downstream (at x/D = 20) a significant difference between the two predictions in the near wall and wake-like regions is observed at all the transverse planes. This is due to the fact that the RST model captures some secondary vortices, which are not captured by the k-ε model. A discussion on the secondary vortices will be presented in Section 5.4.3.

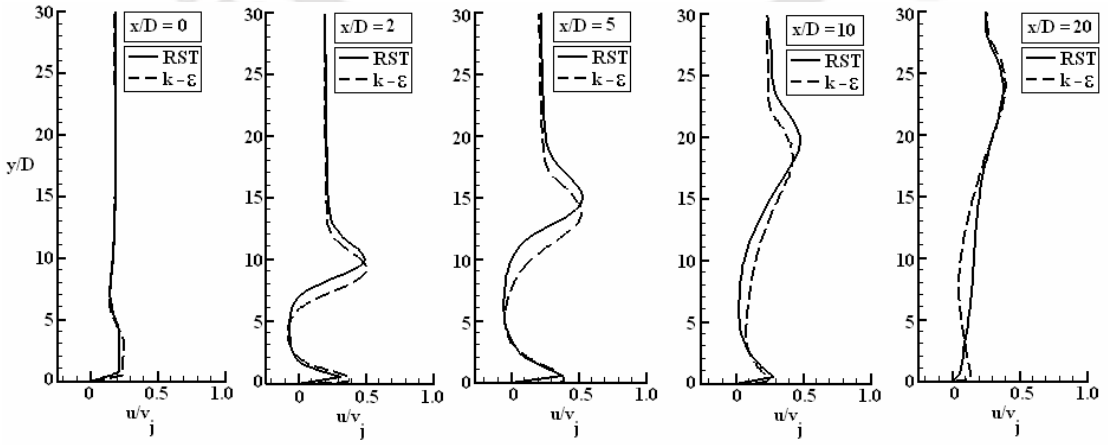

Fig. 5.6: Comparison of cross-stream component of the mean velocity at different downstream locations (z/D = 5) for R = 6.

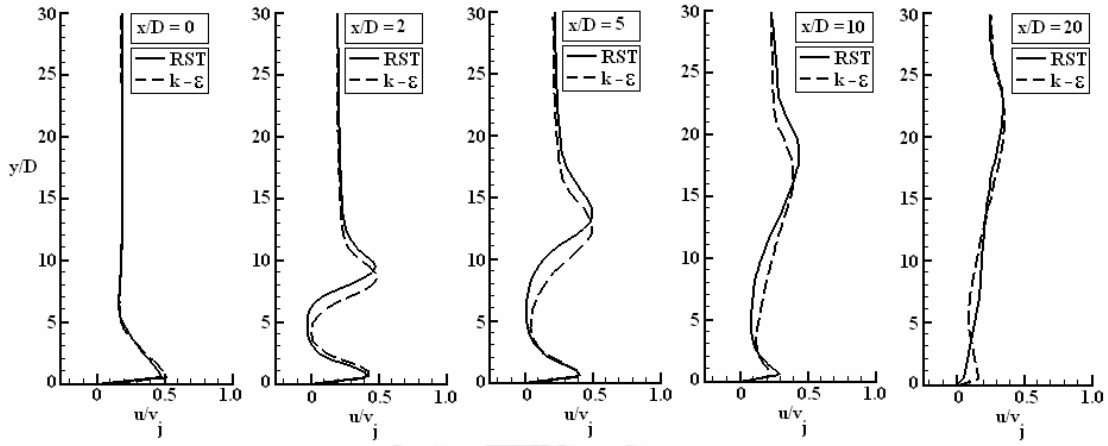

Fig. 5.7: Comparison of cross-stream component of mean velocity at different downstream locations (z/D = 6) for R = 6.

Like the k-ε model, the RST model also shows the symmetry of the cross-stream component to the central vertical plane (z/D = 0) by showing the same flow pattern which are observed from the predictions of cross-stream component at z/D = 3 and -3 (Figs. 5.5 and 5.8).

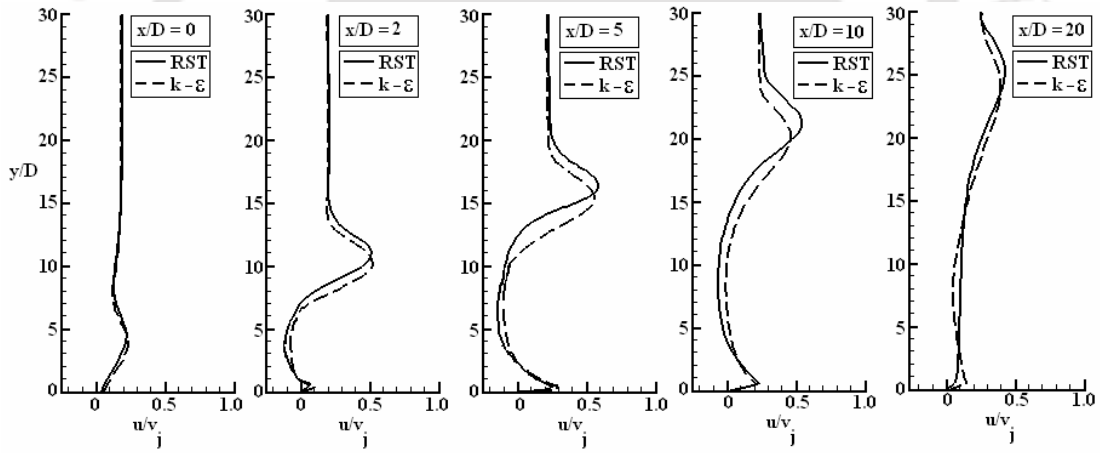

Fig. 5.8: Comparison of cross-stream component of mean velocity at different downstream locations (z/D = -3) for R = 6.

Figs. 5.9 to 5.13 show the variation of the cross-stream component of mean velocity at different downstream locations and at different spanwise planes for the velocity ratio R = 9. In this case also the RST model predicts a higher jet penetration compared to that by the standard k-ε model. Far downstream (x/D = 20) the difference between the two predictions in the bottom part of the jet is quite large due to the predictions of secondary vortices by the RST model. In this case also the RST model shows the flow to be symmetric to the jet central vertical plane (z/D = 0).

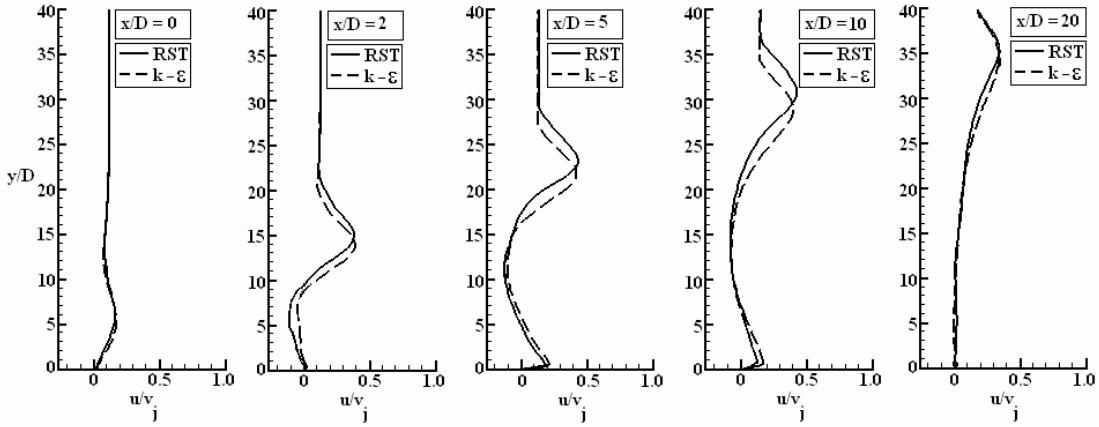

Fig. 5.9: Comparison of cross-stream component of mean velocity at different downstream locations ($z/D = 0$) for $R = 9$.

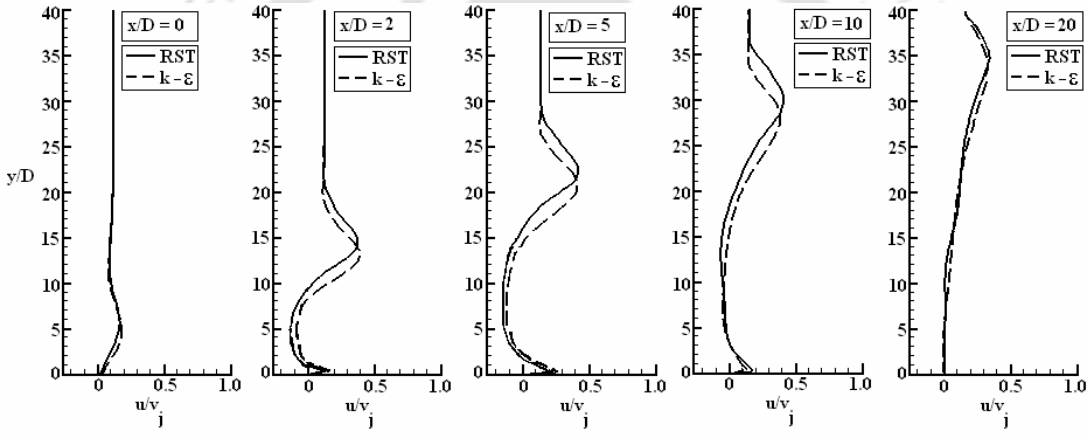

Fig. 5.10: Comparison of cross-stream component of the mean velocity at different downstream locations ($z/D = 3$) for $R = 9$.

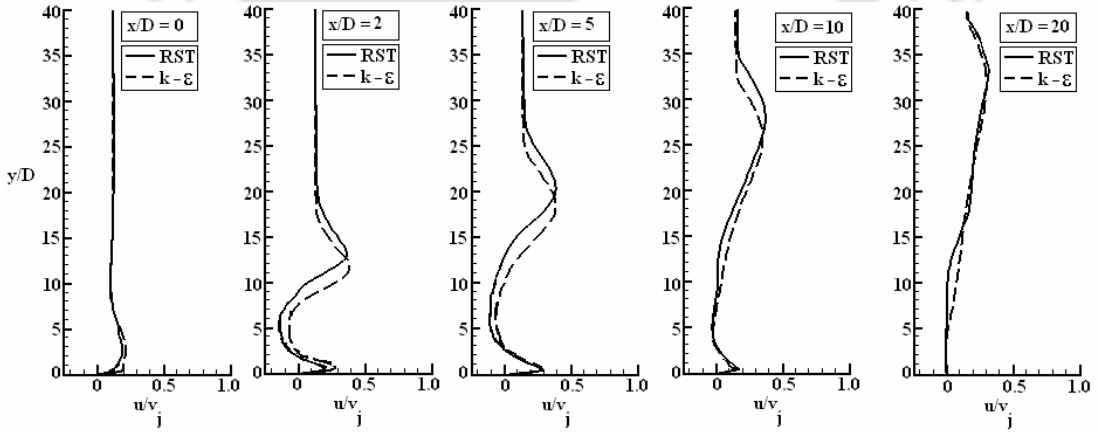

Fig. 5.11: Comparison of cross-stream component of the mean velocity at different downstream locations ($z/D = 5$) for $R = 9$.

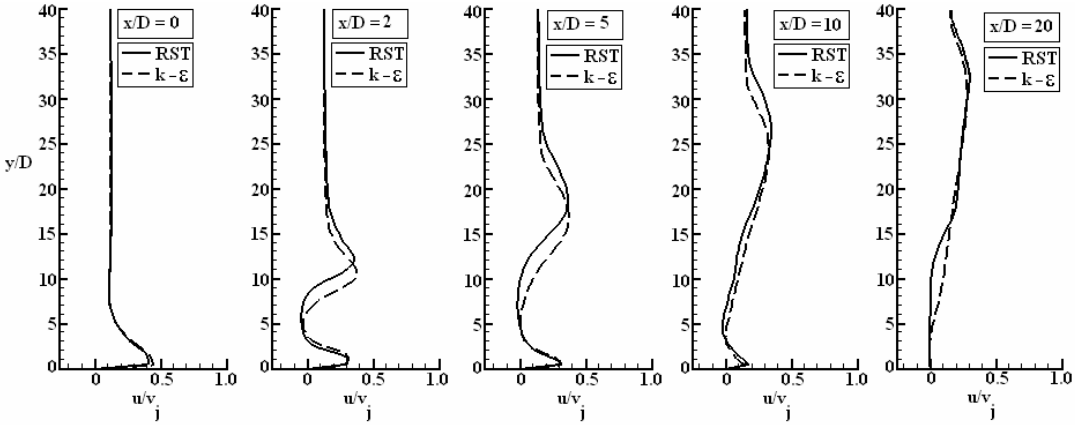

Fig. 5.12: Comparison of cross-stream component of the mean velocity at different downstream locations (z/D = 6) for R = 9.

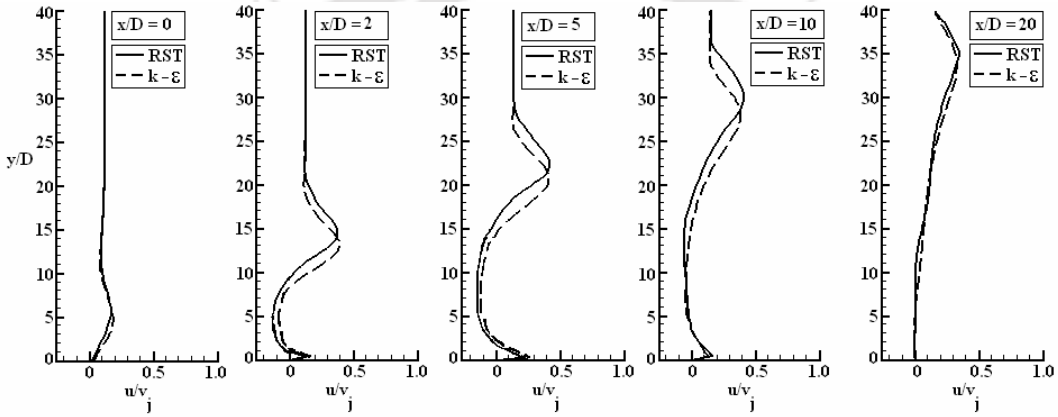

Fig. 5.13: Comparison of cross-stream component of the mean velocity at different downstream locations (z/D = -3) for R = 9.

Figs. 5.14 to 5.18 show the comparison of the vertical component of mean velocity on different spanwise planes and at different downstream locations for R = 6. Vertical velocities near the bottom wall are quite strong just downstream of the jet slot, as the jet is almost vertical in this region. As the jet moves downstream the vertical velocity reduces in magnitude and further downstream the jet becomes almost horizontal and the values of the vertical components are quite low. The RST model predicts higher values of the vertical component of mean velocity in the upper part of the jet and thus it predicts a higher jet trajectory compared to that by the standard k-ε model. The standard k-ε model predicts higher value of the vertical component in the wake-like region. At the spanwise planes z/D = 0 and 3 the difference in the predictions by the two models is observed to be small at downstream locations of x/D = 15 and 20. However, in the spanwise planes z/D = 5 and 6 the difference in the predictions in the

bottom part of the deflected jet is found to be large at far downstream positions (*x/D* = 15 and 20).

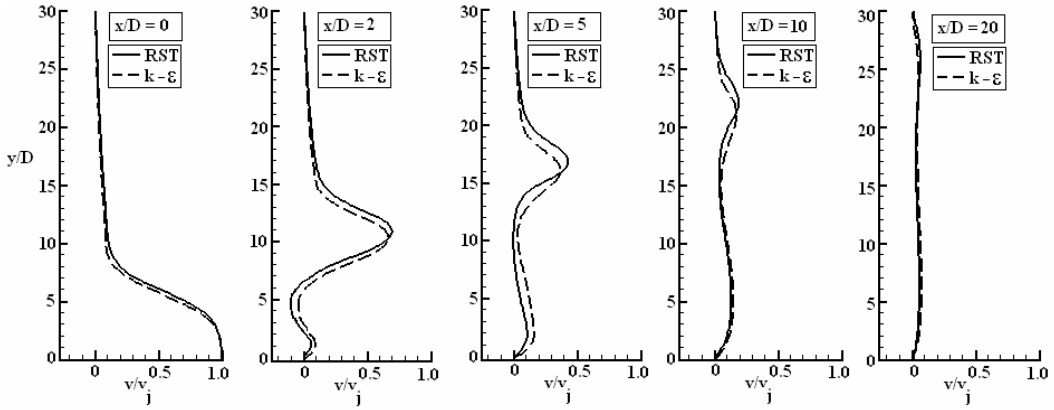

Fig. 5.14: Comparison of vertical component of the mean velocity at different downstream locations (*z/D* = 0) for *R* = 6.

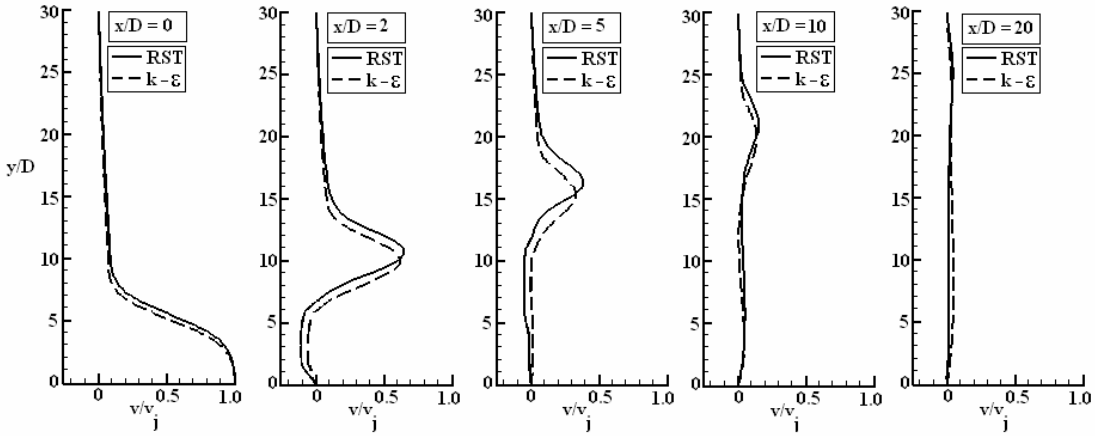

Fig. 5.15: Comparison of vertical component of the mean velocity at different downstream locations (*z/D* = 3) for *R* = 6.

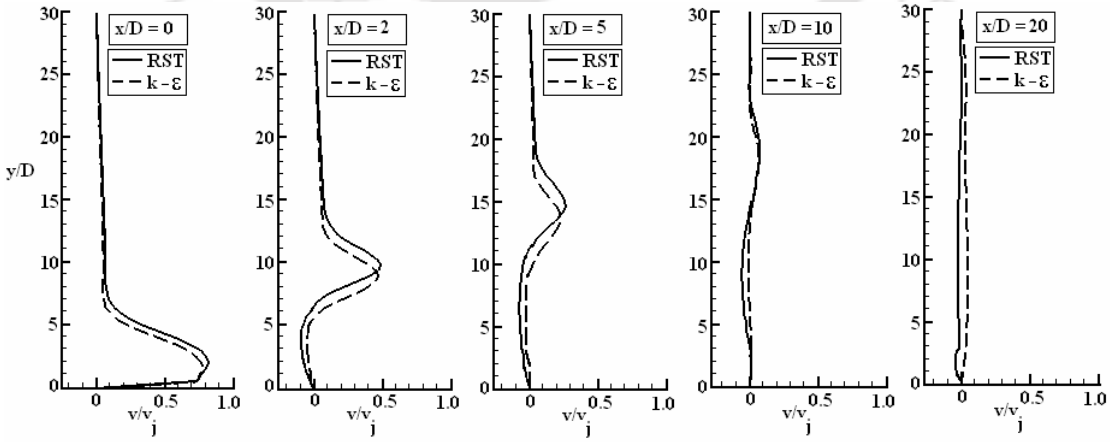

Fig. 5.16: Comparison of vertical component of the mean velocity at different downstream locations (z/*D* = 5) for *R* = 6.

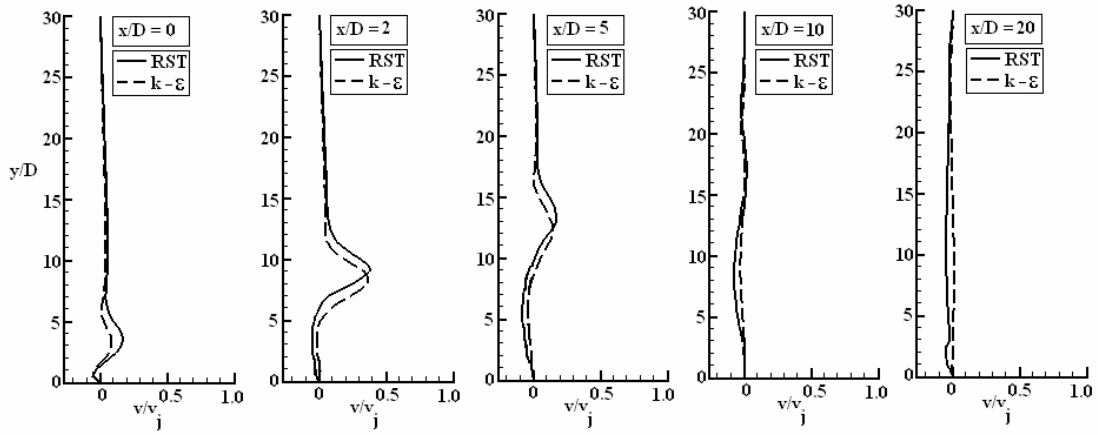

Fig. 5.17: Comparison of vertical component of the mean velocity at different downstream locations (z/D = 6) for R = 6.

In this case also the RST model shows the symmetric about the central vertical plane (z/D = 0), which can be observed by comparing the velocity profiles at z/D = 3 and z/D = -3 (Figs. 5.15 and 5.18).

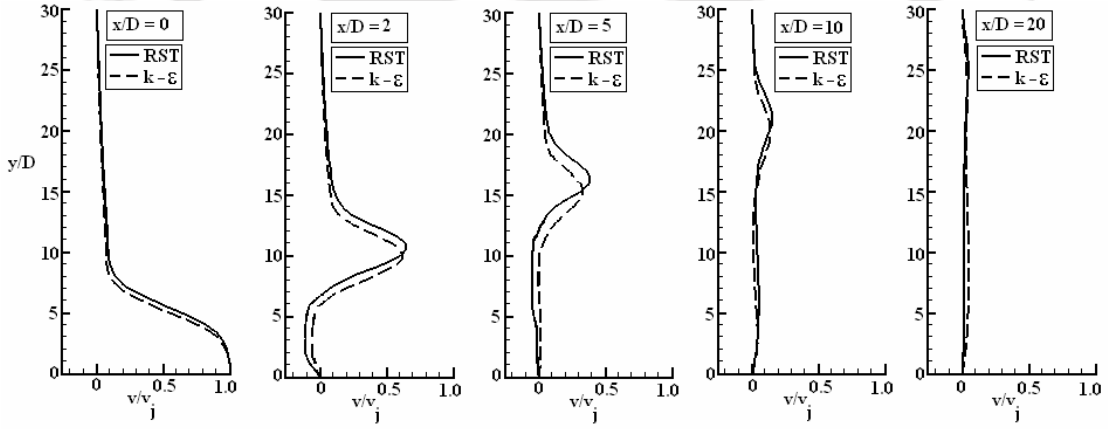

Fig. 5.18: Comparison of vertical component of the mean velocity at different downstream locations (z/D = -3) for R = 6.

A comparison of the vertical component of mean velocity on different spanwise planes and at different downstream locations for R = 9 is shown in Figs. 5.19 to 5.23. In this case also the RST model predicts higher values of the vertical component at the upper part of the jet whereas the standard k-ε model predicts higher predictions at the bottom part of the jet. The difference between the two predictions is found to be large at downstream positions just after the jet discharge (x/D = 2 and 5) for all the spanwise planes.

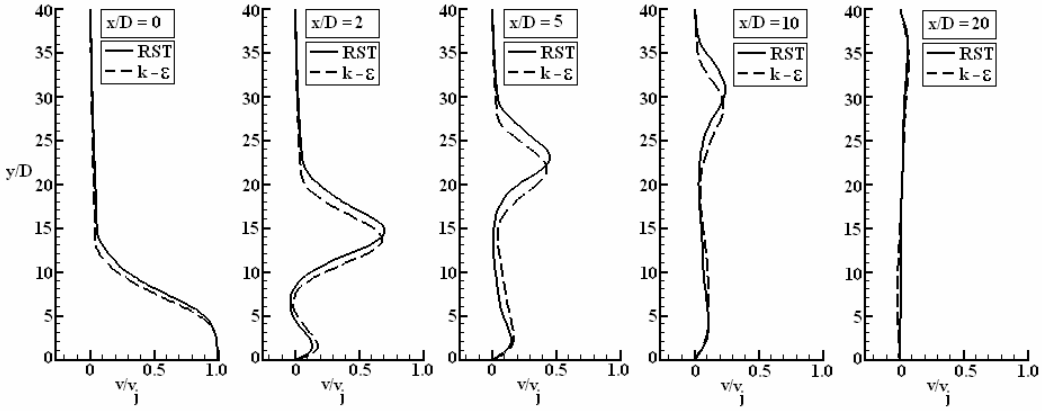

Fig. 5.19: Comparison of vertical component of mean velocity at different downstream locations ($z/D = 0$) for $R = 9$.

The difference of the two models in predicting the flow field at the bottom part of the computational domain is found to be small at far downstream locations in the jet central plane ($z/D = 0$). At other spanwise planes ($z/D = 3$, 5 and 6) a significant difference in the predictions at the bottom part of the jet at far downstream positions ($x/D = 15$ and 20) is observed.

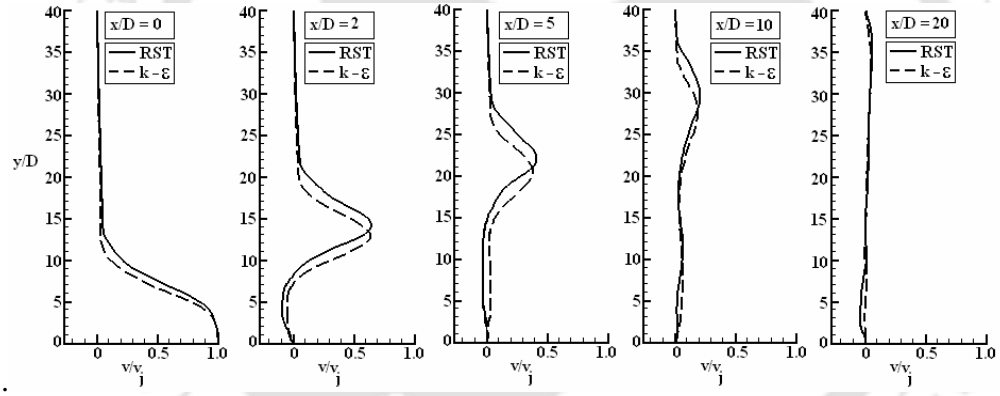

Fig. 5.20: Comparison of the vertical component of mean velocity at different downstream locations ($z/D = 3$) for $R = 9$.

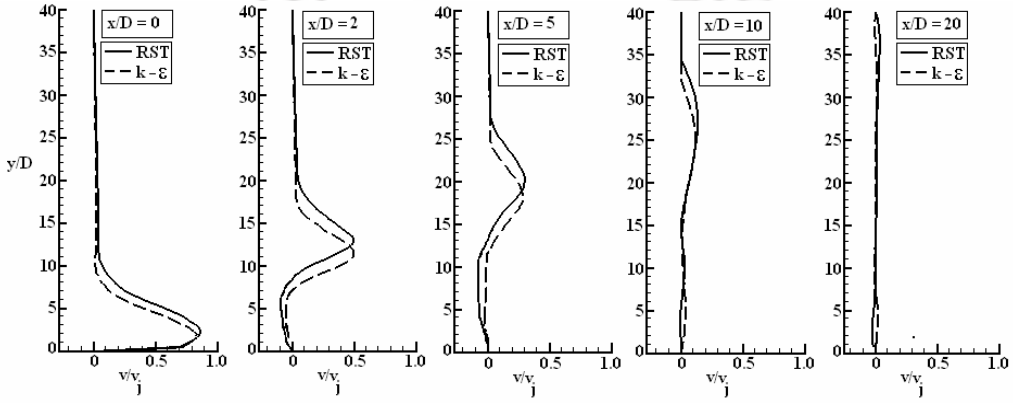

Fig. 5.21: Comparison of vertical component of mean velocity at different downstream locations ($z/D = 5$) for $R = 9$.

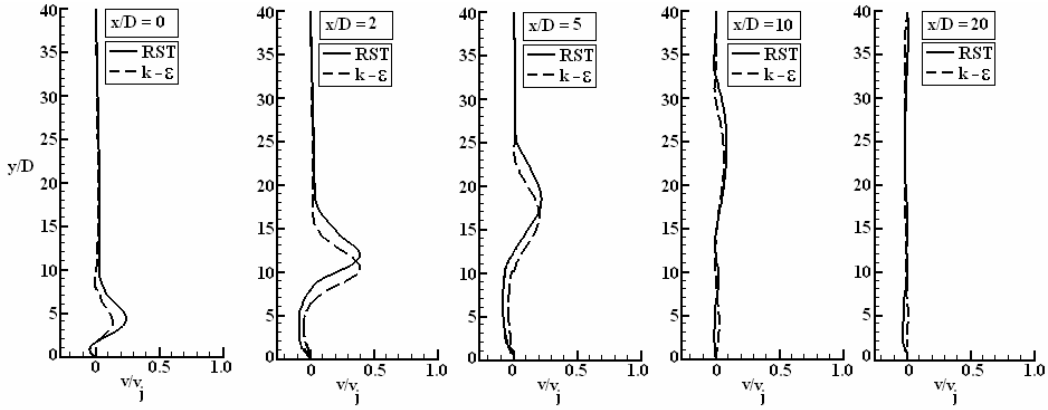

Fig. 5.22: Comparison of vertical component of mean velocity at different downstream locations (z/D = 6) for R = 9.

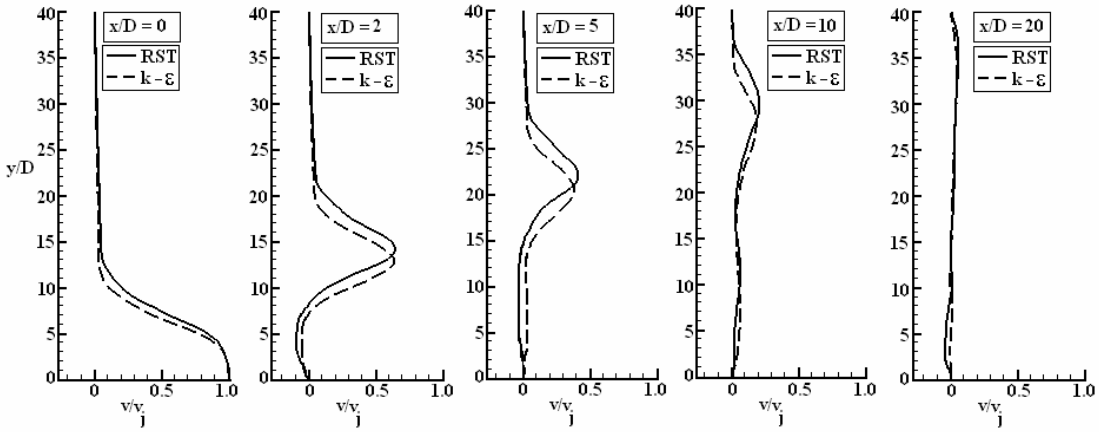

Fig. 5.23: Comparison of vertical component of mean velocity at different downstream locations (z/D = -3) for R = 9.

Comparisons of the variation of the spanwise component of the mean velocity on different spanwise planes and at different downstream locations for R = 6 are shown in Figs. 5.24 to 5.27. The predicted values of the transverse velocities by both the models on the jet central vertical plane (z/D = 0) are found to be zero (not shown here) due to symmetry of the flow. The difference between the two predictions in the jet discharge region on all the planes is found to be small. At this location, both the models show spreading of the jet after exiting from the jet slot by showing that transverse flow is taking place from the jet centre plane (z/D = 0) towards the sidewalls. At all other downstream positions, the standard k-ε model predicts higher values of the spanwise velocity near the sidewall, thus producing a stronger transverse movement of the fluid compared to that by RST model. Far downstream (x/D = 20) the differences of prediction near the bottom wall by both the model are observed to be large due to the prediction of secondary vortices by the RST model.

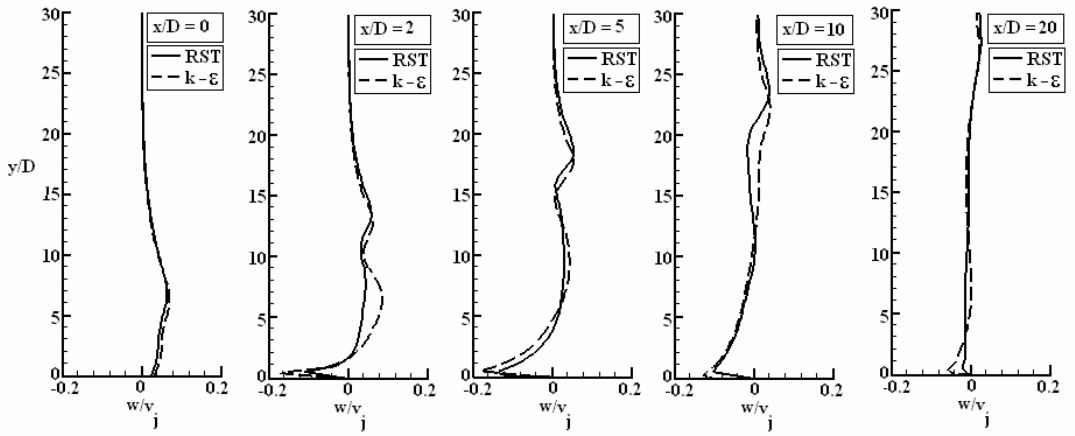

Fig. 5.24: Comparison of spanwise component of mean velocity at different downstream locations (z/D = 3) for R = 6.

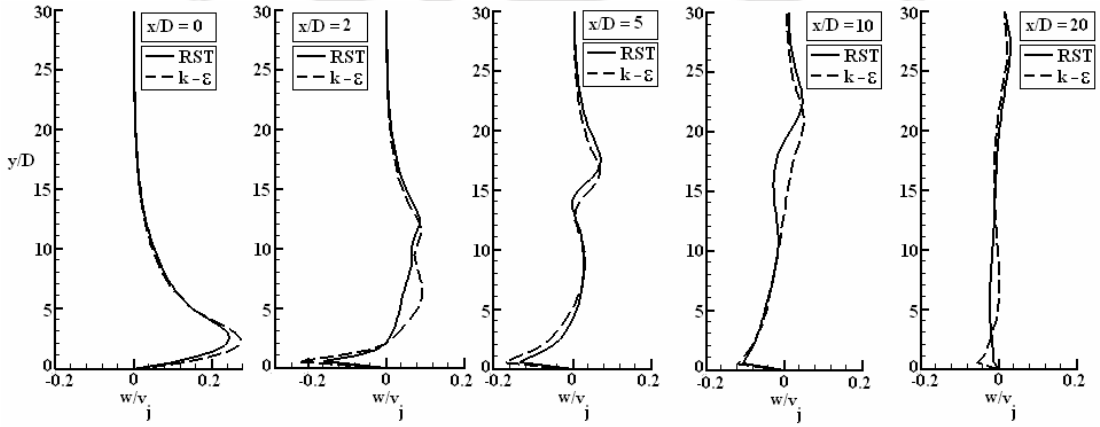

Fig. 5.25: Comparison of spanwise component of mean velocity at different downstream locations (z/D = 5) for R = 6.

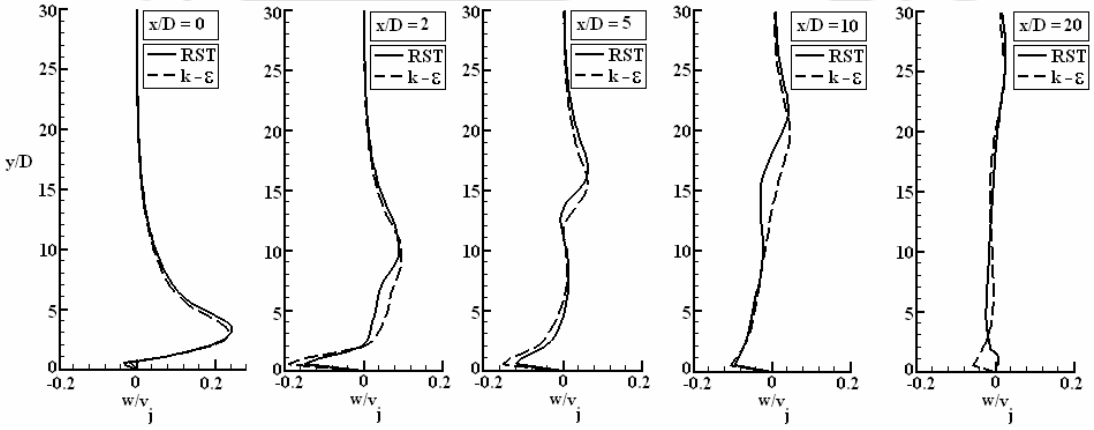

Fig. 5.26: Comparison of spanwise component of mean velocity at different downstream locations (z/D = 6) for R = 6.

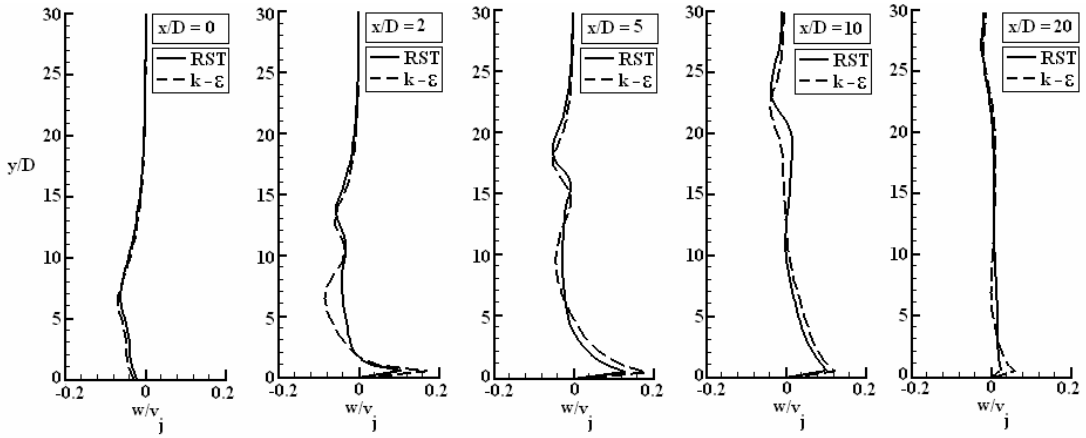

Fig. 5.27: Comparison of spanwise component of mean velocity at different downstream locations (z/D = -3) for R = 6.

It is observed that the spanwise velocity profiles at z/D = 3 (Fig. 5.24) and z/D = -3 (Fig. 5.27) are similar thus both the models show the symmetry of the spanwise velocity to the jet central vertical plane (z/D = 0).

Figs. 5.28 to 5.33 show a comparison of the spanwise component of the mean velocity at different spanwise planes and at different downstream locations for R = 9. In this case also the standard k-ε model predicts higher values of the spanwise velocity near the bottom wall region than those by the RST model. The difference between the two models at far downstream locations in the spanwise planes z/D = 5 and 6 are observed to be large in this case than that in the case of R = 6. The RST model predicts the complex flow field by showing some variations of velocity at vertical position of y/D = 3 to 10 whereas the standard k-ε model is unable to capture those variations.

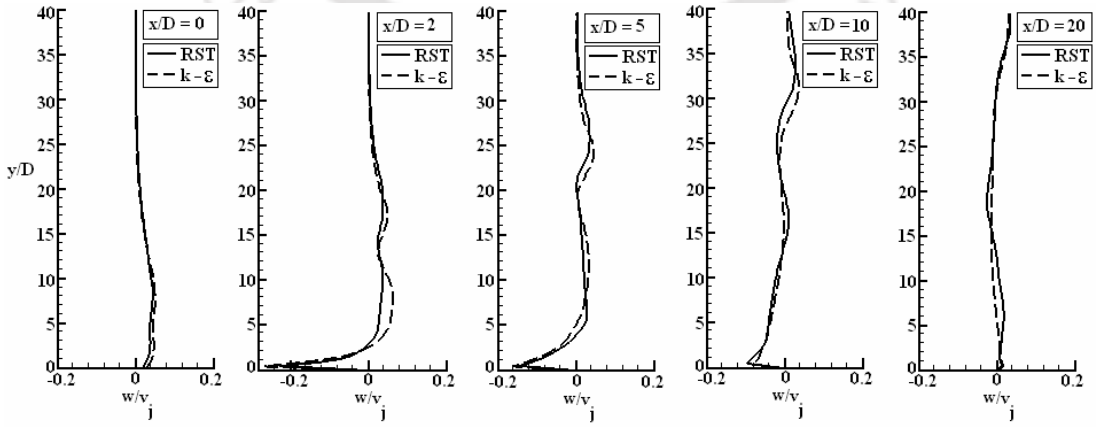

Fig. 5.28: Comparison of spanwise component of mean velocity at different downstream locations (z/D = 3) for R = 9.

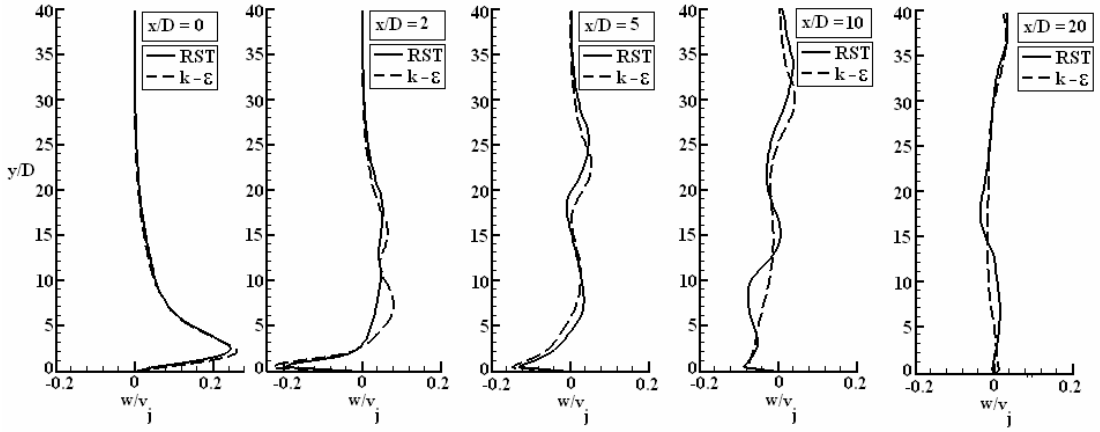

Fig. 5.29: Comparison of spanwise component of mean velocity at different downstream locations (z/D = 5) for R = 9.

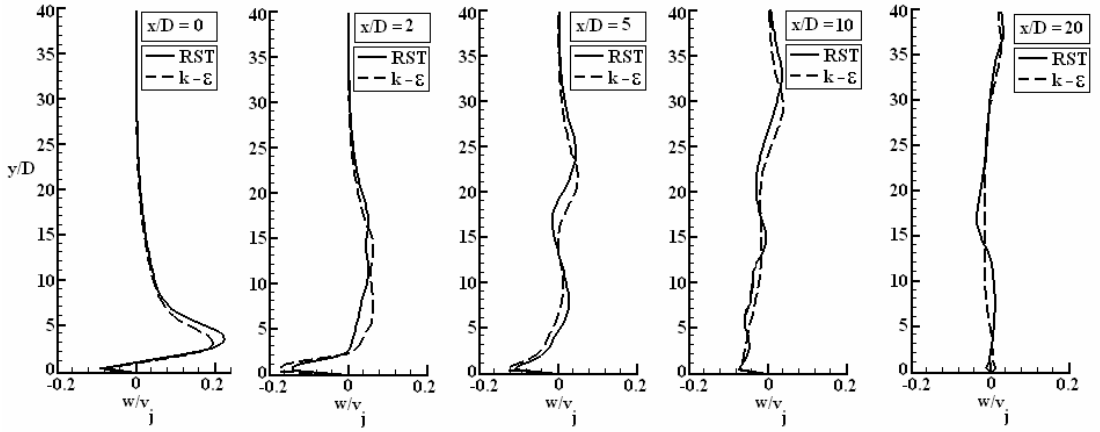

Fig. 5.30: Comparison of spanwise component of mean velocity at different downstream locations (z/D = 6) for R = 9.

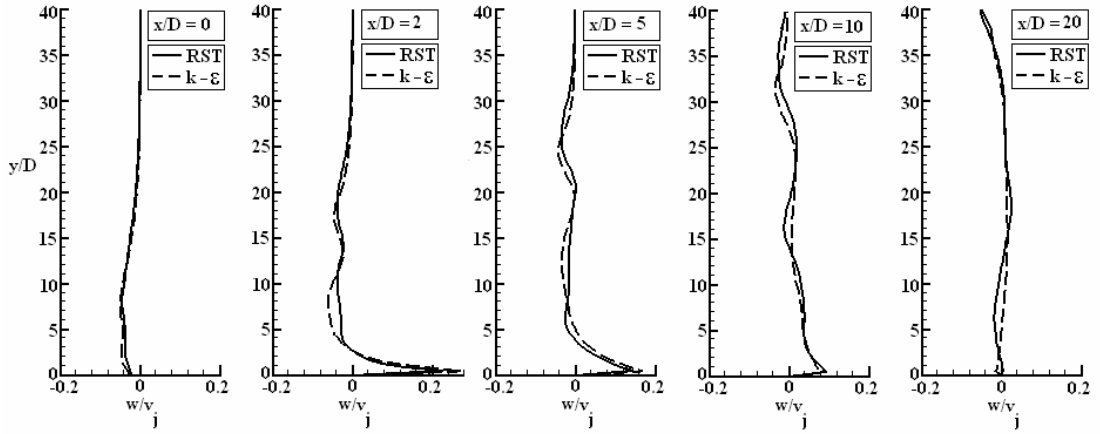

Fig. 5.31: Comparison of spanwise component of mean velocity at different downstream locations (z/D = -3) for R = 9.

A comparison of the variation of the cross-stream component of mean velocity in the spanwise direction at a height *y/D* = 5 from the bottom wall and at different downstream locations for velocity ratio *R* = 6 is shown in Fig. 5.32. The standard *k-ε* model predicts higher values than those by the RST model, which is in accordance with the variation of cross-stream component in the vertical direction (Fig. 5.4 to 5.7). Thus the standard *k-ε* model predicts a weaker wake effect by showing less drop of the cross-stream component compared to that by the RST model. Both the model show a symmetric variation of the cross-stream component of the mean velocity about the jet central vertical plane (*z/D* = 0).

A comparison of the variation of the vertical component of mean velocity in the spanwise direction at a height *y/D* = 5 from the bottom wall and at different downstream locations for *R* = 9 is shown in Fig. 5.33.

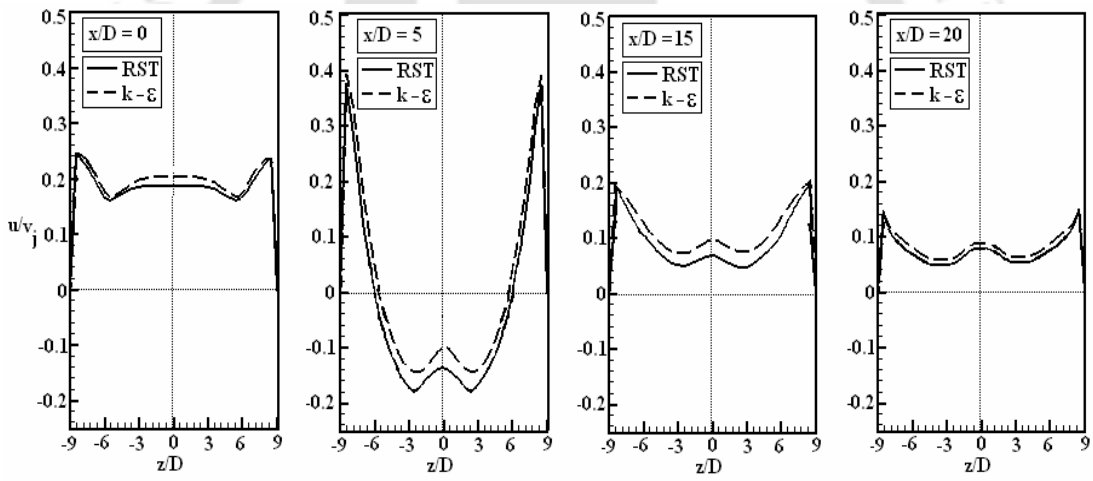

Fig. 5.32: Comparison of spanwise variation of cross-stream component of mean velocity at different downstream locations for *R* = 6 at a height *y/D* = 5.

The RST model predicts a higher variation of the vertical component in the spanwise direction compared to that by the standard *k-ε* model. Both the models show a vertically upward movement of the fluid at the jet centre plane (z/*D* = 0), which represents an upward movement of the fluid due to the CRVP. In this case also both the models show the symmetric behaviour of the variation about the central vertical plane (*z/D* = 0).

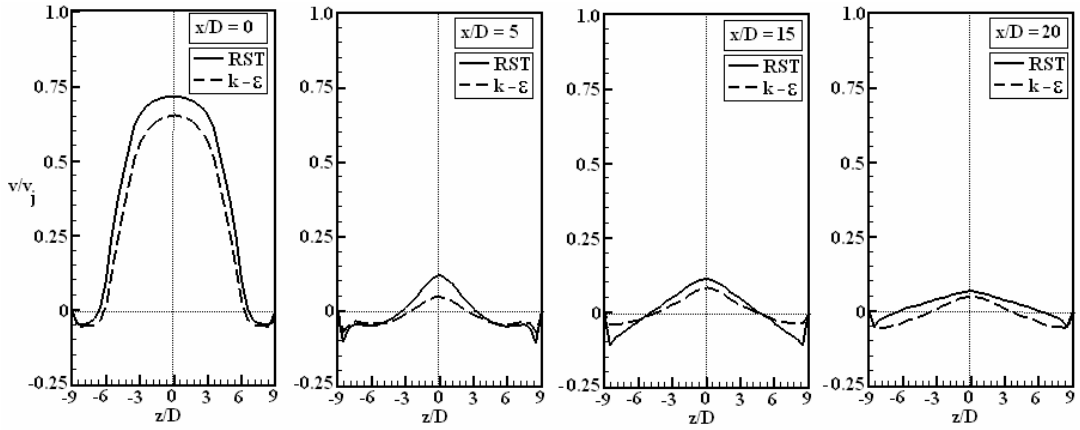

Fig. 5.33: Comparison of spanwise variation of vertical component of mean velocity at different downstream locations for $R = 6$ at a height $y/D = 5$.

The variation of the spanwise component of the mean velocity in the spanwise direction is shown in Fig 5.34 for the velocity ratio $R = 6$. The standard k-ε model shows more variation of the spanwise velocity component compared to that by RST model. As discussed in the Chapter 4 this variation is due to the formation of CRVP and therefore by predicting a large spanwise component, the standard k-ε model predicts bigger size of CRVP compared to that by RST model.

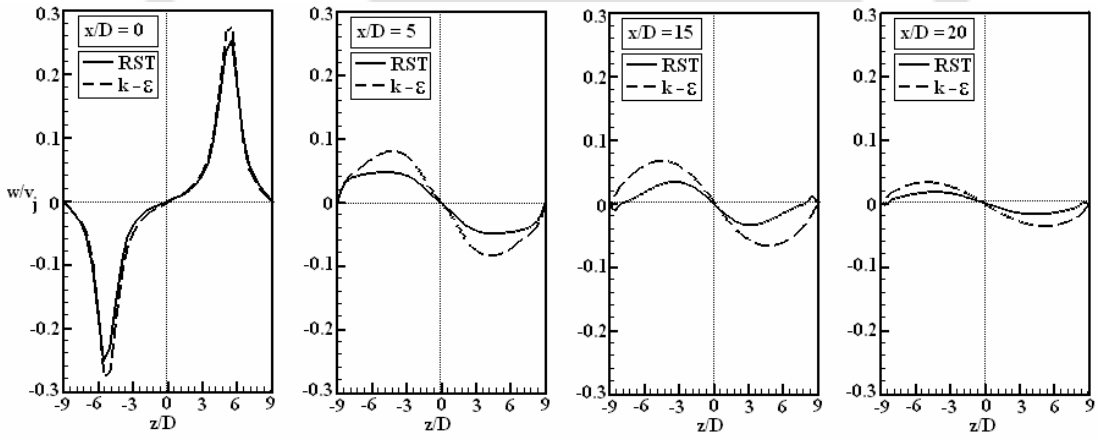

Fig. 5.34: Comparison of spanwise variation of spanwise component of mean velocity at different downstream location for $R = 6$ at a height $y/D = 5$.

Variations of all the three velocity components (cross-stream, vertical and spanwise) in the spanwise direction for velocity ratio $R = 9$ are shown in Figs. 5.35, 5.36 and 5.37, respectively. Both the models show similar behaviour as in the case of $R = 6$.

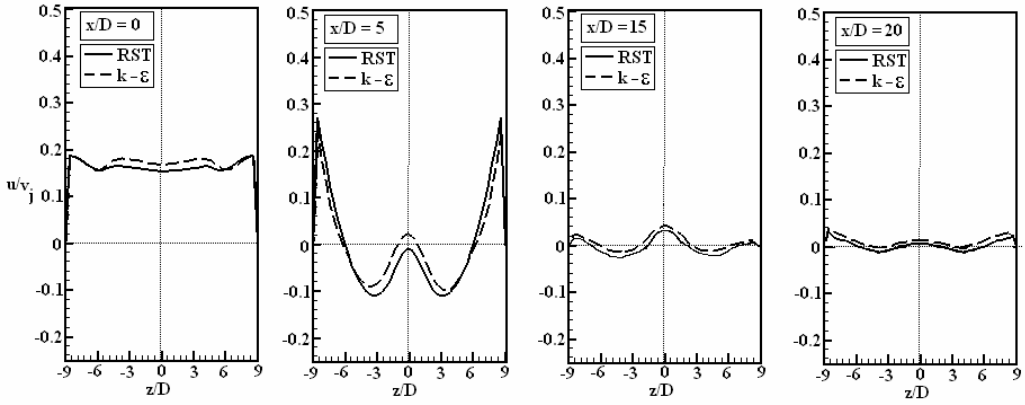

Fig. 5.35: Comparison of spanwise variation of cross-stream component of mean velocity at different downstream locations for $R = 9$ at a height $y/D = 5$.

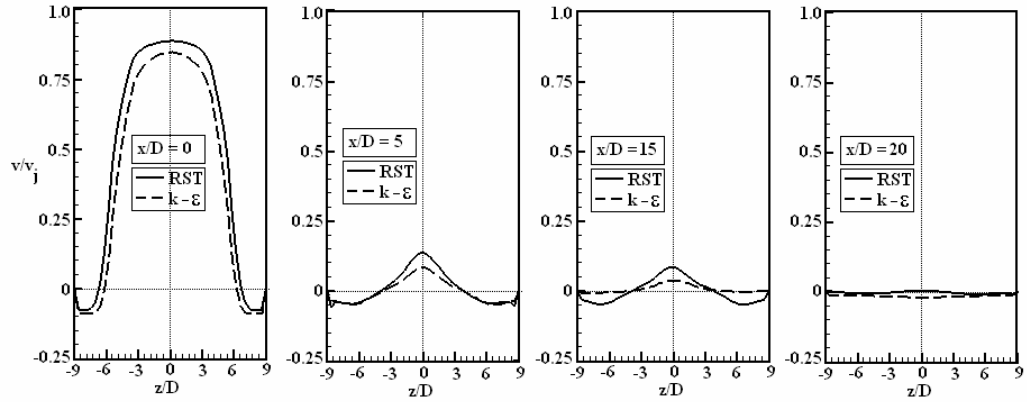

Fig. 5.36: Comparison of spanwise variation of vertical component of mean velocity at different downstream locations for $R = 9$ at a height $y/D = 5$.

The standard k-ε model predicts larger variation of the cross-stream component compared to that by RST model. However, the RST model predicts higher vertical component than that by the standard k-ε model and the standard k-ε model predicts higher values of spanwise component than that by the RST model. It is observed that the difference between the predictions by the two models in this case is less compared to the case with $R = 6$. The variation of the cross-stream component is smaller than that in the case with $R = 6$ (Fig. 5.35). The predicted magnitudes of the vertical component at far downstream positions ($x/D = 15$ and 20) are quite small. Moreover the variation of the spanwise component at far downstream positions ($x/D = 15$ and 20) are also quite small. This may be due to the fact that the CRVP takes the position of the upper part of the flow domain for the velocity ratio $R = 9$ (Section 5.4.3, Fig. 5.60). Both the models show symmetric variation of all the three components of the velocity about the plane $z/D = 0$.

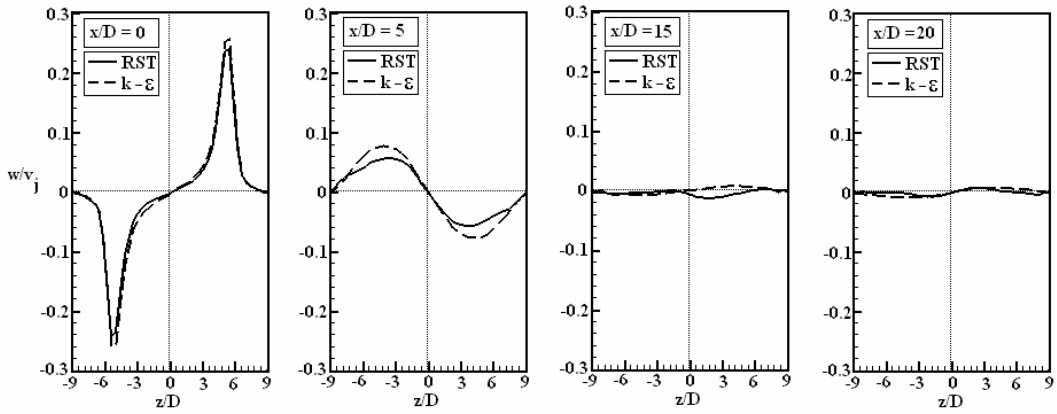

Fig. 5.37: Comparison of spanwise variation of spanwise component of mean velocity at different downstream location for $R = 9$ at a height $y/D = 5$.

5.4.2 Turbulence Kinetic Energy and Turbulence Stress

Comparisons of the predicted turbulence kinetic energy at different transverse planes and at different downstream locations are shown in Figs. 5.38 to 5.41 for the velocity ratio $R = 6$. The standard k-ε model predicts a higher value in the lower part of the jet, whereas the RST model predicts higher values of kinetic energy in the upper part of the jet. The difference between the two models is high at the downstream regions of the jet and it decreases far downstream. A slightly higher prediction of k near the wall regions by the standard k-ε model is observed. Above the wall-jet layer, i.e. in the wake-like region the dissipation exceeds the production (Andreopoulos and Rodi, 1984), which try to reduce the kinetic energy value. Thus a reduced value of kinetic energy is observed between two maxima at the wall-jet layer and at the jet centreline and this trend continues till the existence of the wake-like region.

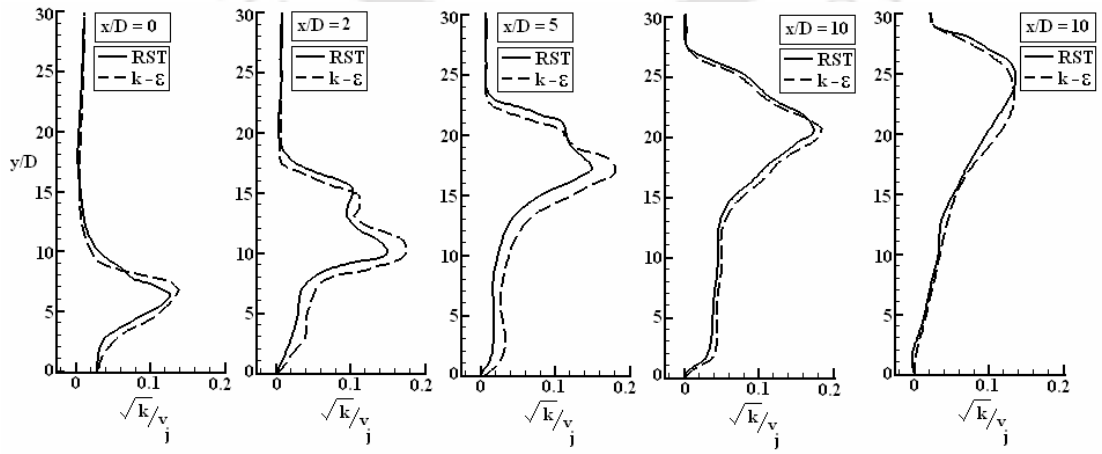

Fig. 5.38: Comparison of turbulence kinetic energy at different downstream locations ($z/D = 0$) for $R = 6$.

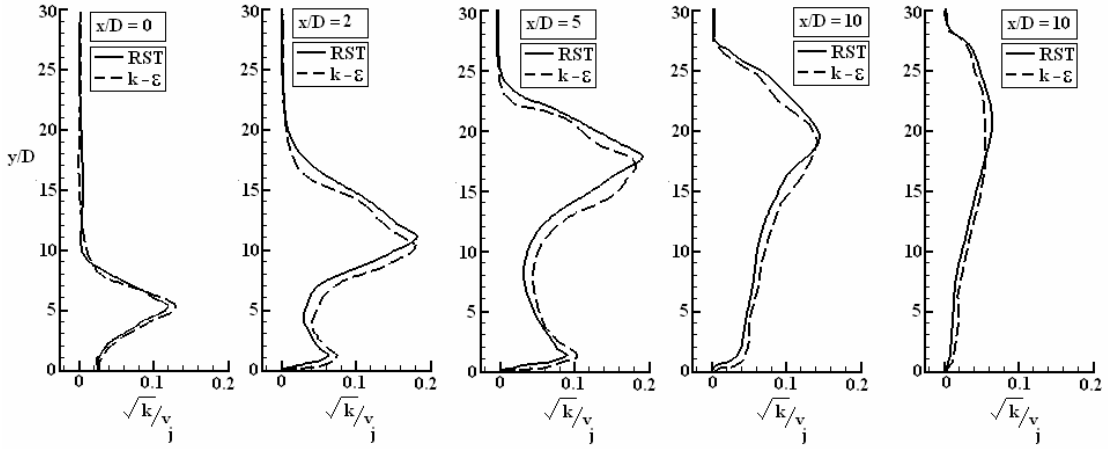

Fig. 5.39: Comparison of turbulence kinetic energy at different downstream locations (z/D = 3) for R = 6.

We have already observed that the RST model predicts the lower values of velocity in the wake-like region, thus affecting the production term of turbulence kinetic energy. In the wake-like region the dissipation reduces the value of the kinetic energy and therefore its value should be small. The RST model predicts this accurately, but the standard k-ε model over predicts the kinetic energy in the wake-like region. Both the models show the symmetry of the k profile about the jet central vertical plane (z/D = 0), which can be observed by comparing the profiles at z/D = 3 (Fig. 5.39) and at z/D = -3 (Fig. 5.41).

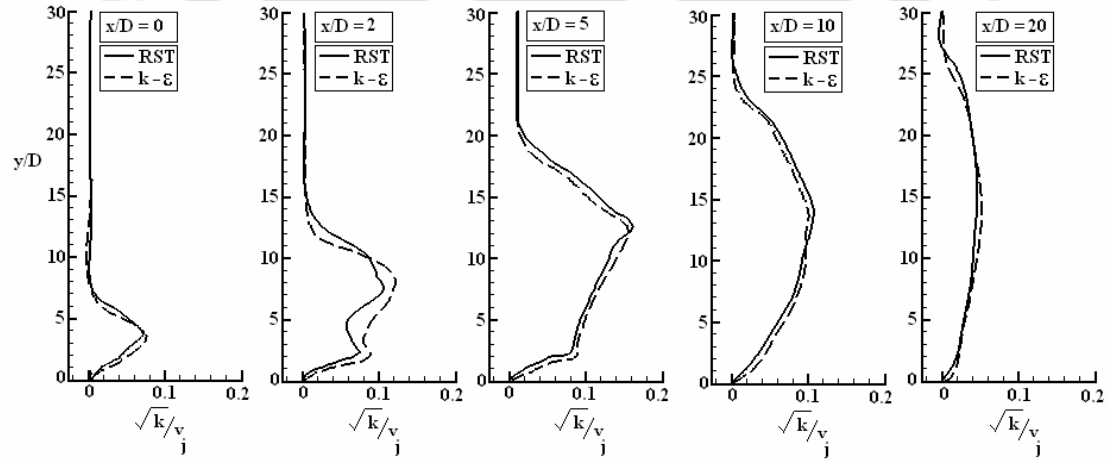

Fig. 5.40: Comparison of turbulence kinetic energy at different downstream location (z/D = 6) for R = 6.

Comparisons of turbulence kinetic energy for R = 9 are shown in Figs. 5.41 to 5.45. In this case also the standard k-ε model predicts higher values at the wall-jet and wake-like layer and RST model predicts higher values at the jet-shear layer.

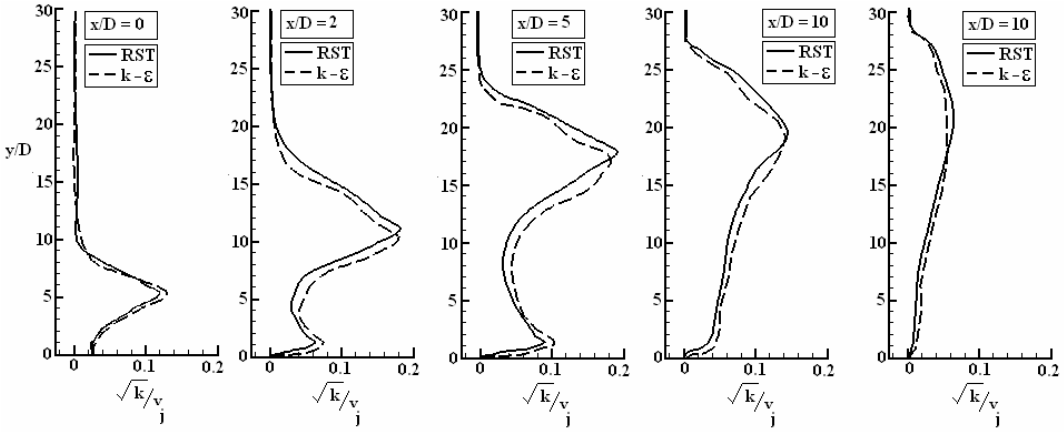

Fig. 5.41: Comparison of turbulence kinetic energy at different downstream location (z/D = -3) for R = 6.

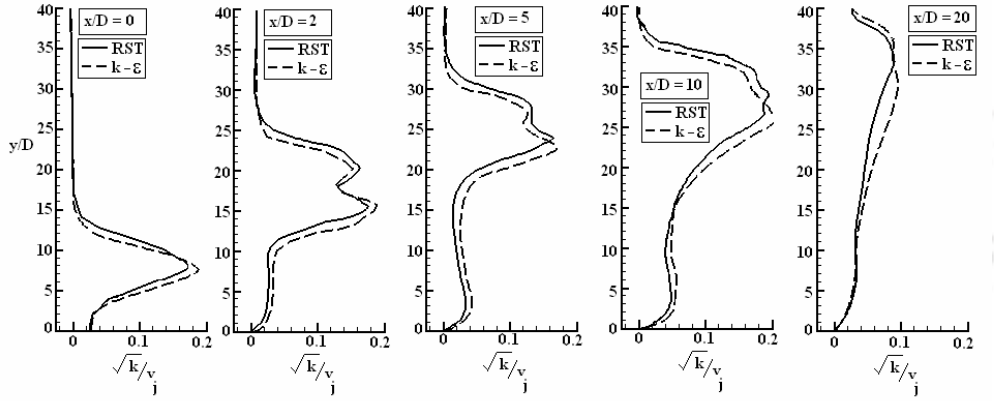

Fig. 5.42: Comparison of turbulence kinetic energy at different downstream locations (z/D = 0) for R = 9.

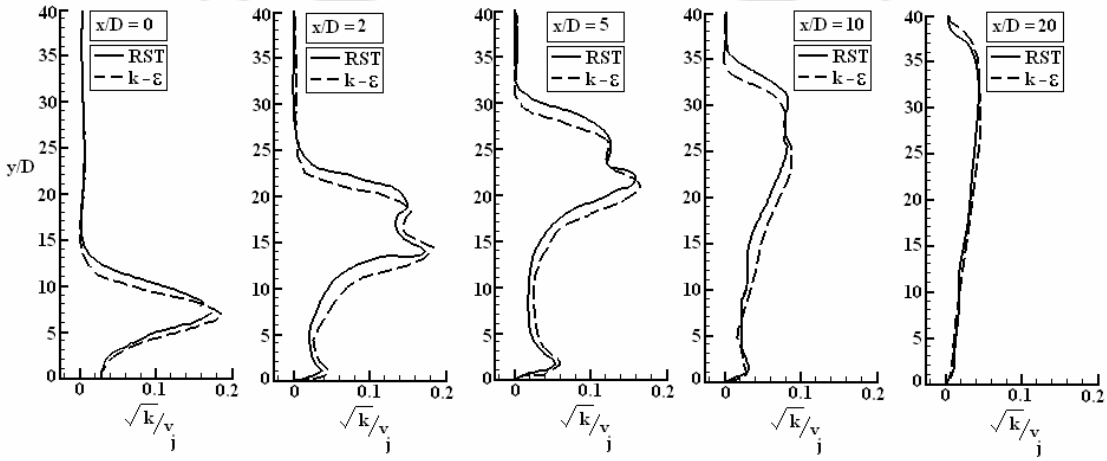

Fig. 5.43: Comparison of turbulence kinetic energy at different downstream locations (z/D = 3) for R = 9.

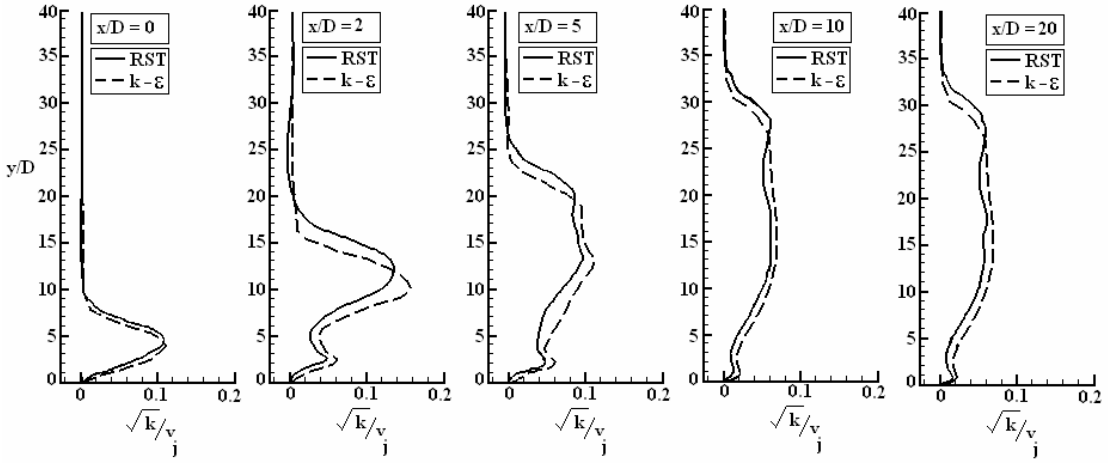

Fig. 5.44: Comparison of turbulence kinetic energy at different downstream locations (z/D = 6) for R = 9.

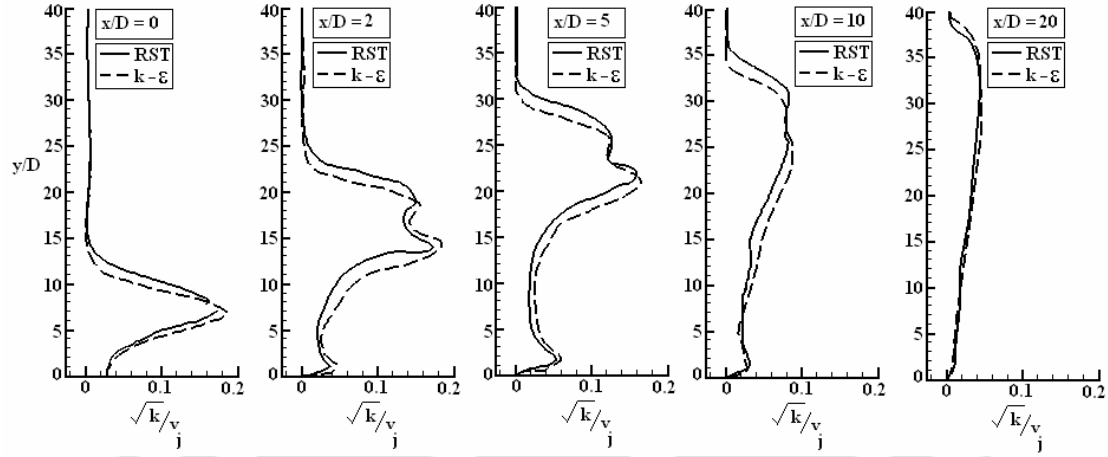

Fig. 5.45: Comparison of turbulence kinetic energy at different downstream locations (z/D = -3) for R = 9.

Comparison of the predicted Reynolds shear ($\overline{u'v'}$) stress at two different spanwise planes for R = 6, is shown in Figs. 5.46 and 5.47. At the jet central plane (z/D = 0) the difference in the predictions by both the models are small compared to that at the spanwise plane of z/D = 5. The values of the shear stress follow the mean velocity gradient ($\partial u / \partial y$). The standard k-ε model predicts higher values at the wall-jet layer and in the wake-like region whereas the RST model predicts higher values at the upper part of the jet-shear layer. Moreover the RST model predicts the maxima values of shear stress at larger vertical heights than those by the standard k-ε model.

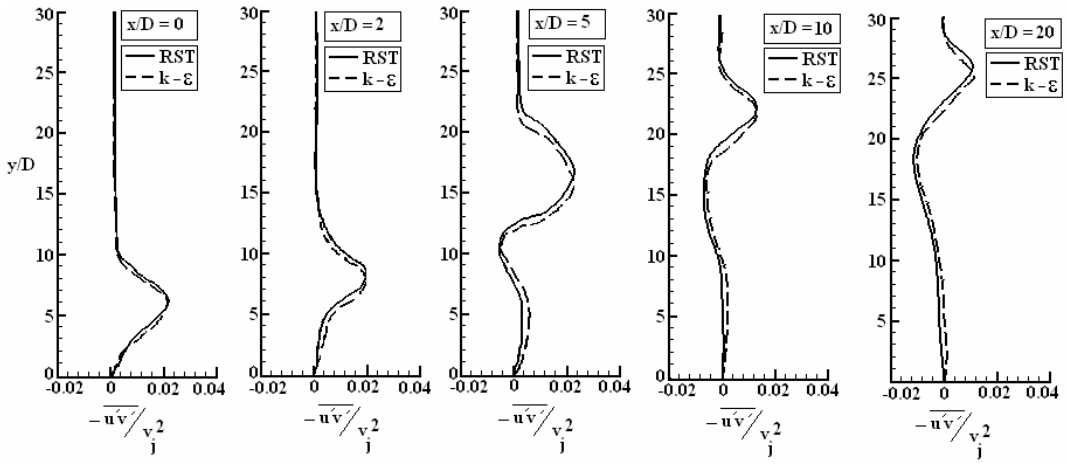

Fig. 5.46: Comparison of turbulence shear stress at different downstream locations ($z/D = 0$) for $R = 6$.

On the plane $z/D = 5$, both the models show an increase of the shear stress in the near wall region, showing a noticeable wall-jet structure. The standard k-ε model predicts more shear stress at the wall-jet layer and at the wake-like region than that by the RST model.

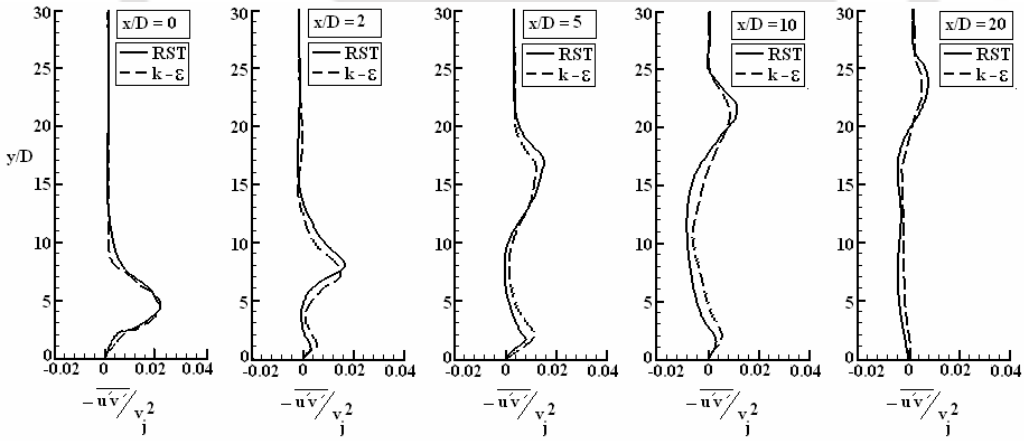

Fig. 5.47: Comparison of turbulence shear stress at different downstream locations ($z/D = 5$) for $R = 6$.

A comparison of the shear stress $\overline{v'w'}$ in the spanwise direction at a vertical height of $y/D = 5$ is shown in Fig. 5.48. It is observed that both the models show almost same behaviour. However the standard k-ε model predicts more value of the shear stress in the jet exit region ($x/D = 0$). Both the models show a symmetric variation of the shear stress to the jet central vertical plane ($z/D = 0$).

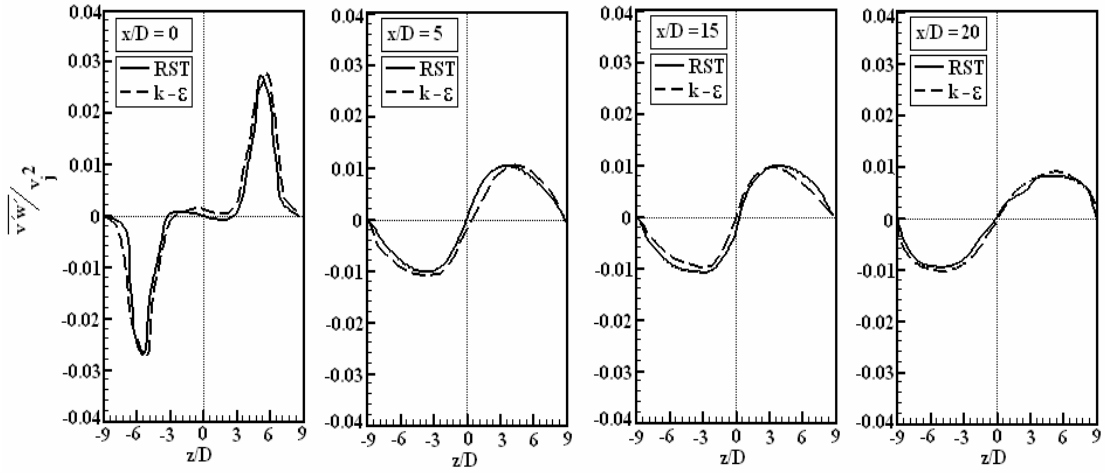

Fig. 5.48: Comparison of turbulence shear stress in spanwise direction at different downstream locations for R = 6.

A comparison of the shear stress for the velocity ratio R = 9 is shown in Figs. 5.49 and 5.50. Here the values of the shear stress are larger compared to the case with R = 6. The shear stress profiles predicted by both the models show the same trend as in the case of R = 6. However the difference of vertical heights predicted by both the models, at which the peak value of the shear stress occurs is more in this case than the case of R = 6. A comparison of the shear stress $\overline{v'w'}$ in the spanwise direction at a vertical height of y/D = 5 for R = 9 (Fig. 5.48) shows the same behaviour of higher prediction by the standard k-ε model compared to that by RST model and the symmetry of the profile to the jet central vertical plane as observed in the case of R = 6.

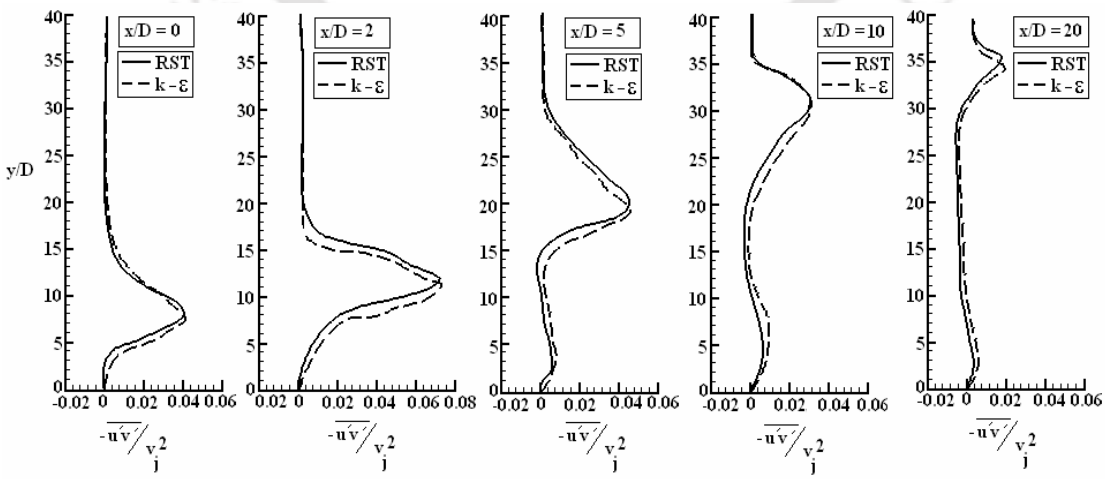

Fig. 5.49: Comparison of turbulence shear stress at different downstream location (z/D = 0) for R = 9.

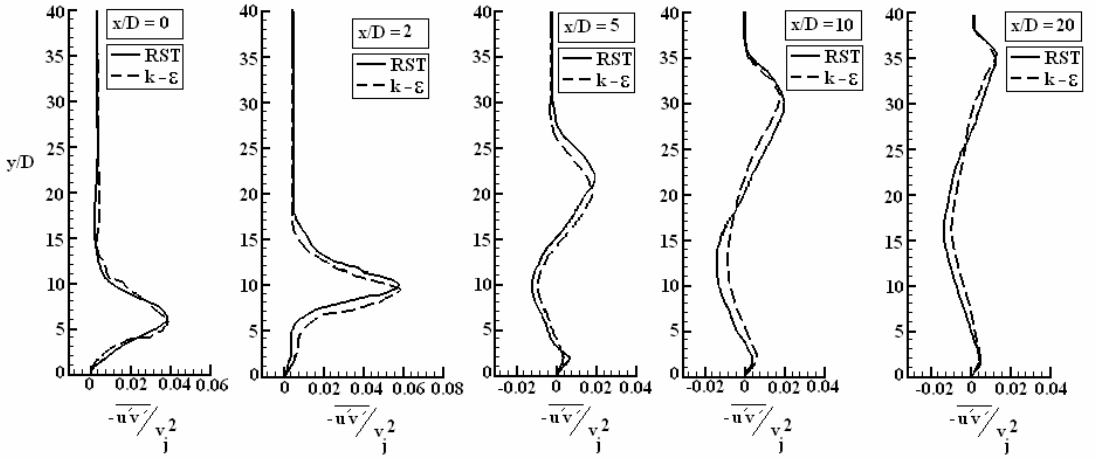

Fig. 5.50: Comparison of turbulence shear stress at different downstream location (z/D = 5) for R = 9.

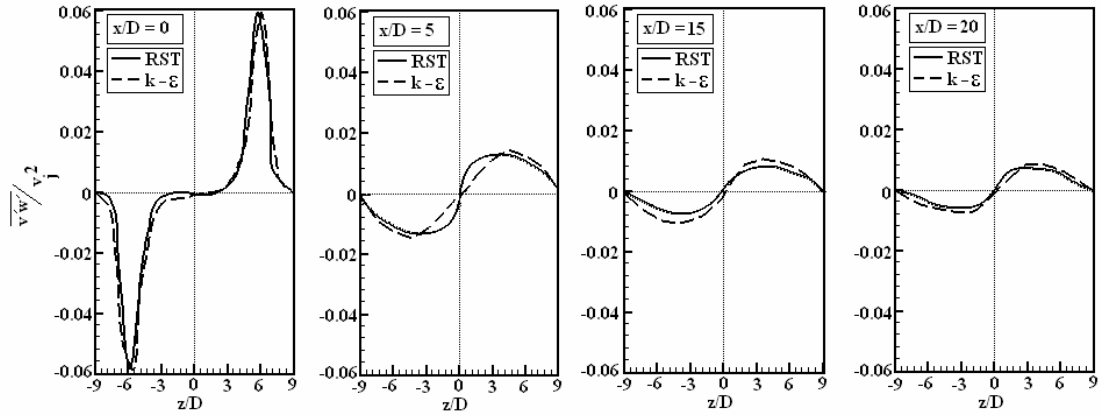

Fig. 5.51: Variation of turbulence shear stress in spanwise direction at different downstream location for R = 9.

5.4.3 Flow Structures and Their Effects on the Flow Field

The predicted mean velocity vectors superimposed with streamline plots at four different x–y planes in the spanwise direction by the RST model for R = 6 are shown in Figs. 5.52 and 5.53. It is observed from these plots that the RST model predicts a higher jet penetration of the jet into the crossflow compared to that shown in the mean x-y vector plot predicted by the standard k-ε model (Fig 4.54 and 4.55), which is already discussed in Chapter 4. The reverse flow region predicted by the RST model is large in the jet central plane (z/D = 0) as well at the other three spanwise planes. In the case of velocity ratio R = 9 also the RST model predicts a higher penetration of the jet and a larger reverse flow region at the bottom part of the jet as shown in Figs. 5.54 and 5.55.

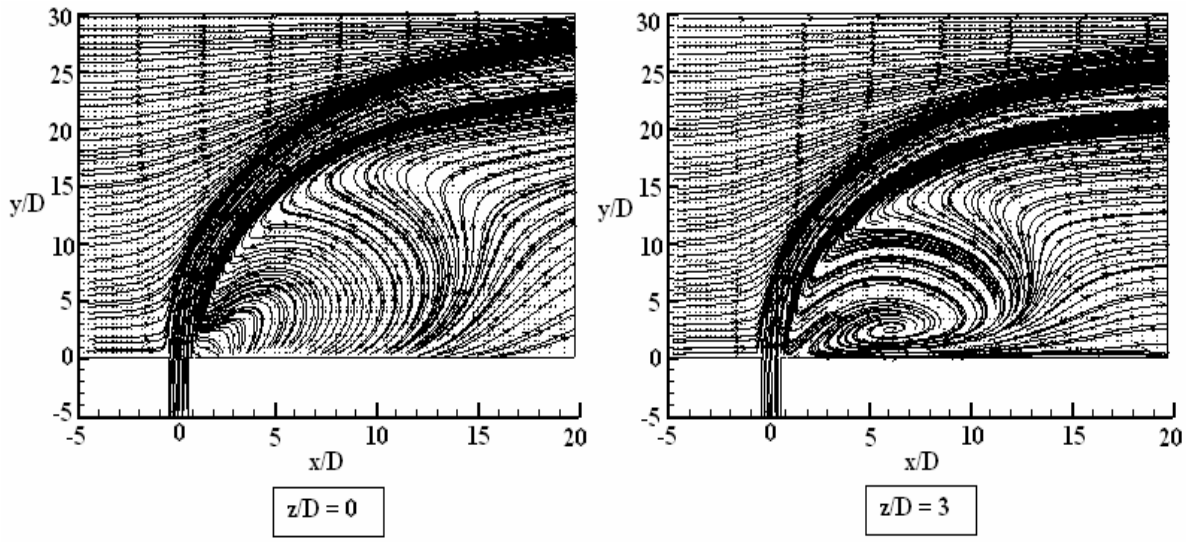

Fig. 5.52: Mean velocity vector plots superimposed with streamline at different spanwise locations predicted by RST model for R = 6, z/D = 0 and 3 in x-y plane.

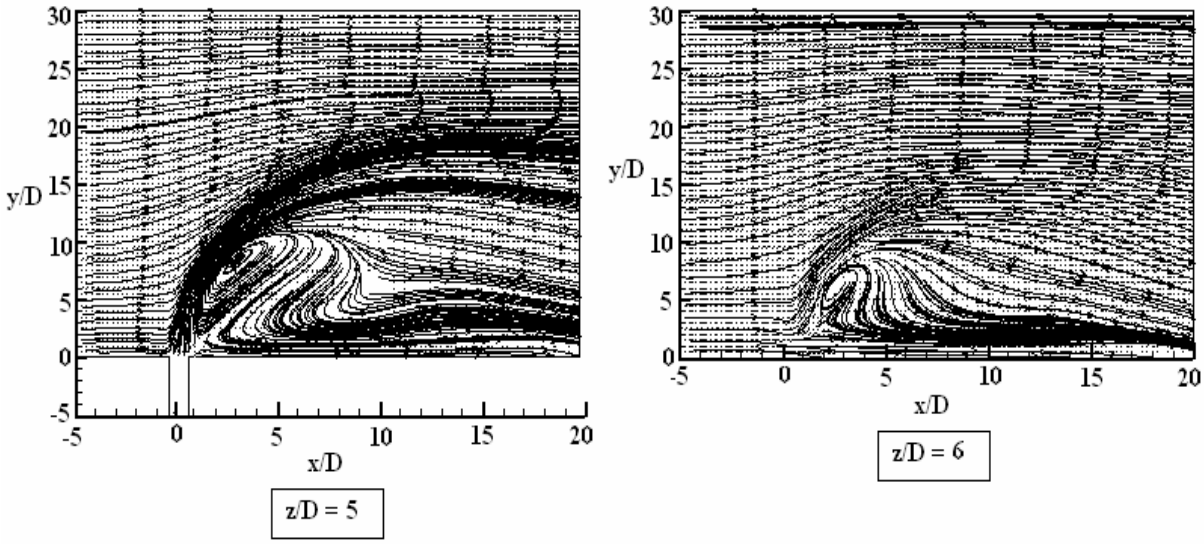

Fig. 5.53: Mean velocity vector plots superimposed with streamline at different spanwise locations predicted by RST model for R = 6, z/D = 5 and 6 in x-y plane.

The flow structures predicted by the RST model in the spanwise planes at z/D = 5 and 6 (Fig. 5.55) are completely different from the corresponding predictions by the standard k-ε model (Fig. 4.57, Chapter 4). A reverse flow region is captured by the RST model even at the spanwise planes at z/D = 5 and 6. Moreover the existence of the jet at those planes is observed more prominent in this case compared to that by the standard k-ε model.

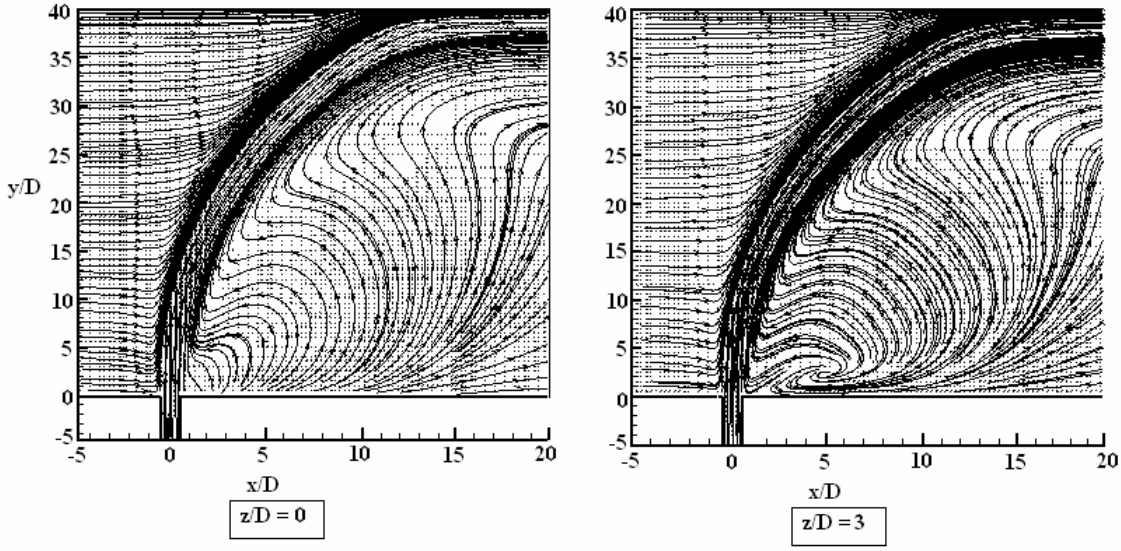

Fig. 5.54: Mean velocity vector plots superimposed with streamline at different spanwise locations predicted by RST model for R = 9, z/D = 0 and 3 in x-y plane.

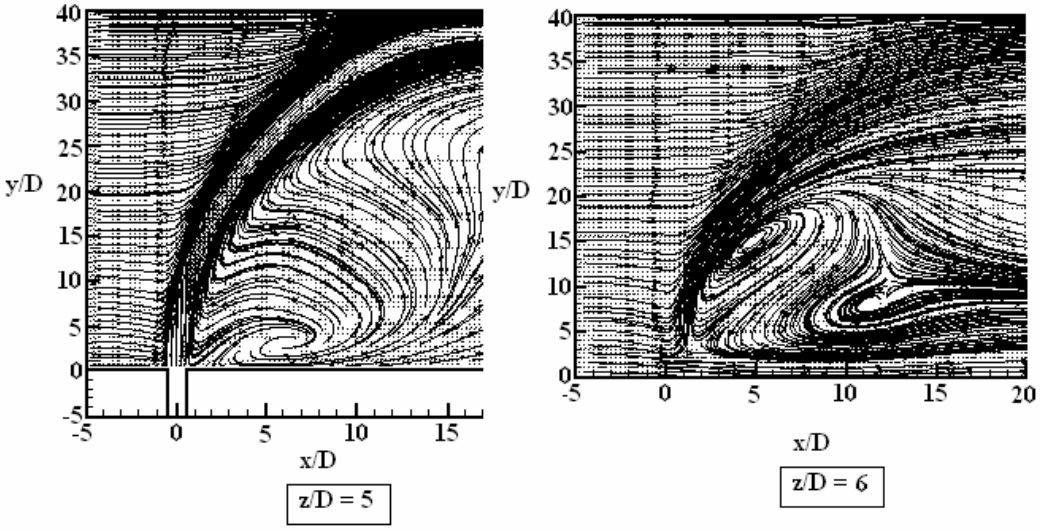

Fig. 5.55: Mean velocity vector plots superimposed with streamline at different spanwise locations predicted by RST model for R = 9, z/D = 5 and 6 in x-y plane.

The y-z mean velocity vector plots predicted by the RST model at different downstream locations for the velocity ratio R = 6 are shown in Figs. 5.56 and 5.57. The structures of the flow field at the first four locations, i.e., up to the location x/D = 2 are observed to be the same as those predicted by the standard k-ε model. The inception of the CRVP in the flow field are same up to the locations of x/D = 5, but the size of the vortices are slightly bigger than those predicted by the k-ε model. At far downstream locations the RST model shows significant difference of the flow field. For example the standard k-ε model showed the maximum growth of the size of the

CRVP at the position *x/D* = 15 (Fig. 4.59, Chapter 4), downstream of which the sizes of vortices start to diminish. In the prediction by the RST model the maximum growth of the CRVP is observed at the position of *x/D* = 20.

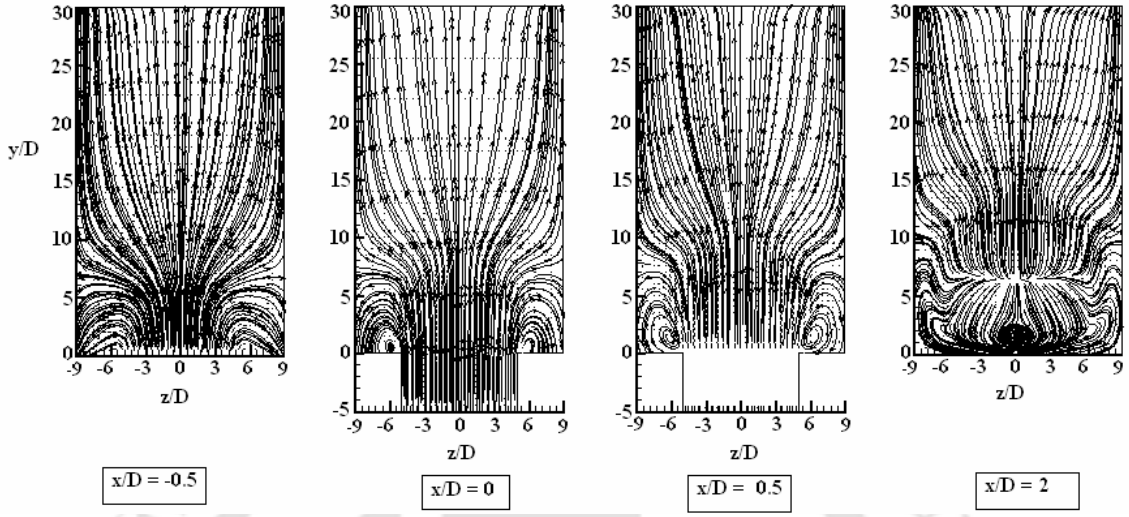

Fig. 5.56: Mean velocity vector plots superimposed with streamline at different locations predicted by RST model for *R* = 6, *x/D* = -0.5, 0, 0.5 and 2 in *y*-*z* plane.

The most important feature of the prediction by the RST model is the capturing of a pair of secondary vortices at the bottom for *x/D* = 20. The rotation of these two secondary vortices is opposite to that of the two primary CRVPs and their formation pattern is same as that of the secondary vortices in a lid driven cavity. One of the secondary vortices is shown in an enlarged view in Fig. 5.58.

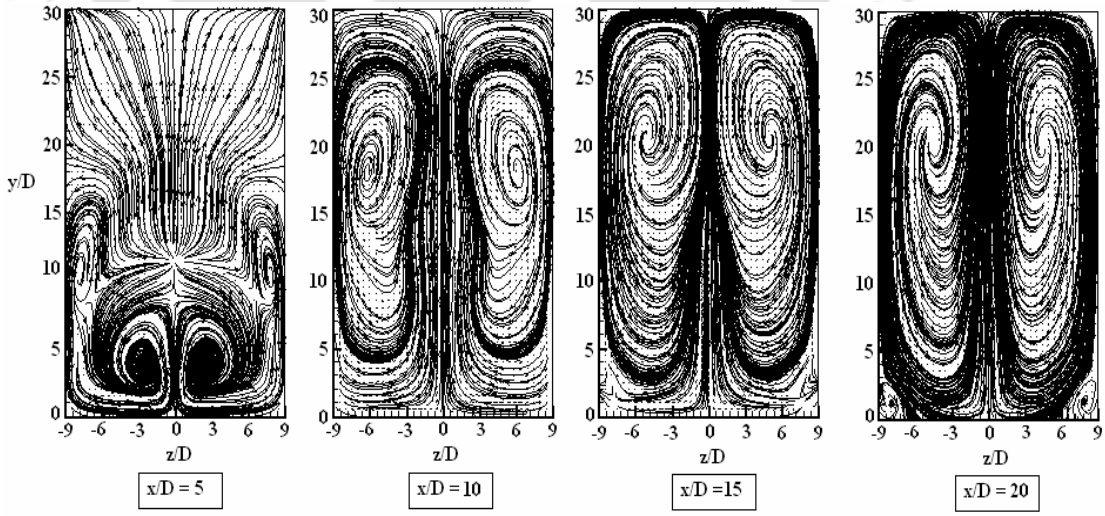

Fig. 5.57: Mean velocity vector plots superimposed with streamline at different locations predicted by RST model for *R* = 6, *x/D* = 5, 10, 15 and 20 in *y*-*z* plane.

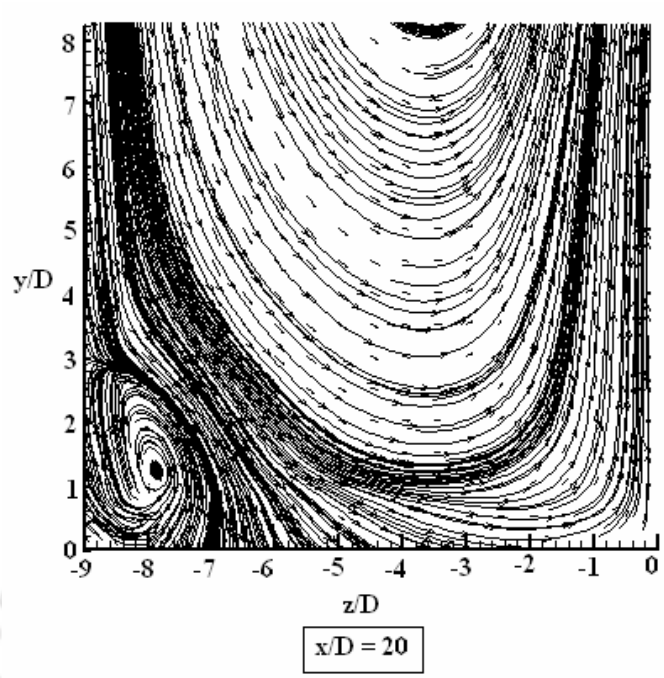

Fig. 5.58: A zoomed view of the secondary vortex at the bottom corner predicted by RST model for $R = 6$.

In the case of $R = 9$ also the RST model predicts similar flow patterns as predicted by the k-ε model up to the location of $x/D = 2$. After this position the RST model shows some qualitative difference of the flow structure than those predicted by the k-ε model.

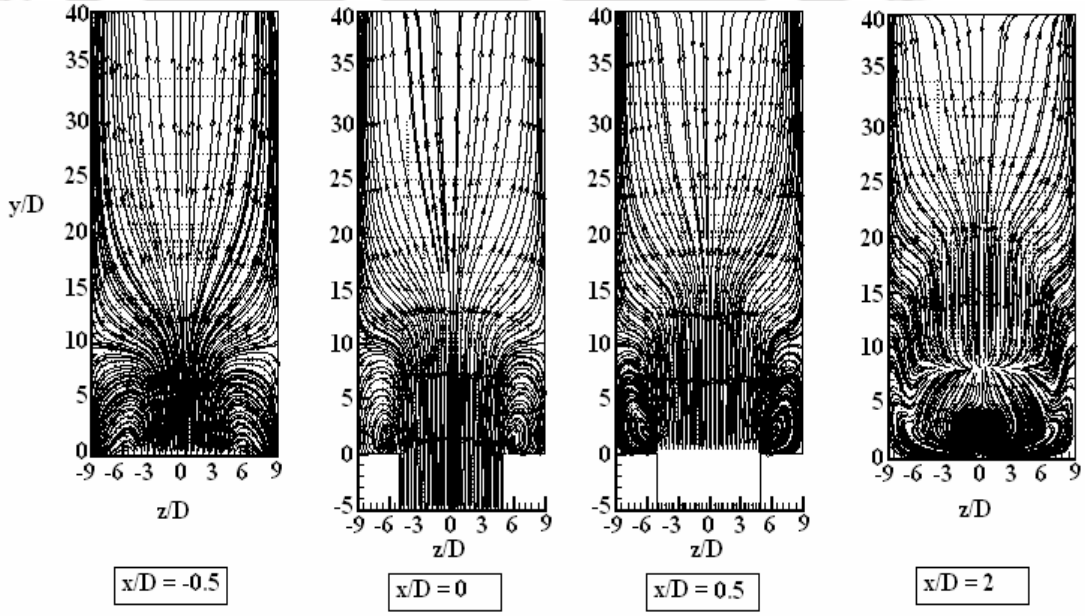

Fig. 5.59: Mean velocity vector plots superimposed with streamline at different locations predicted by RST model for $R = 9$, x/D = -0.5, 0, 0.5 and 2 in y-z plane.

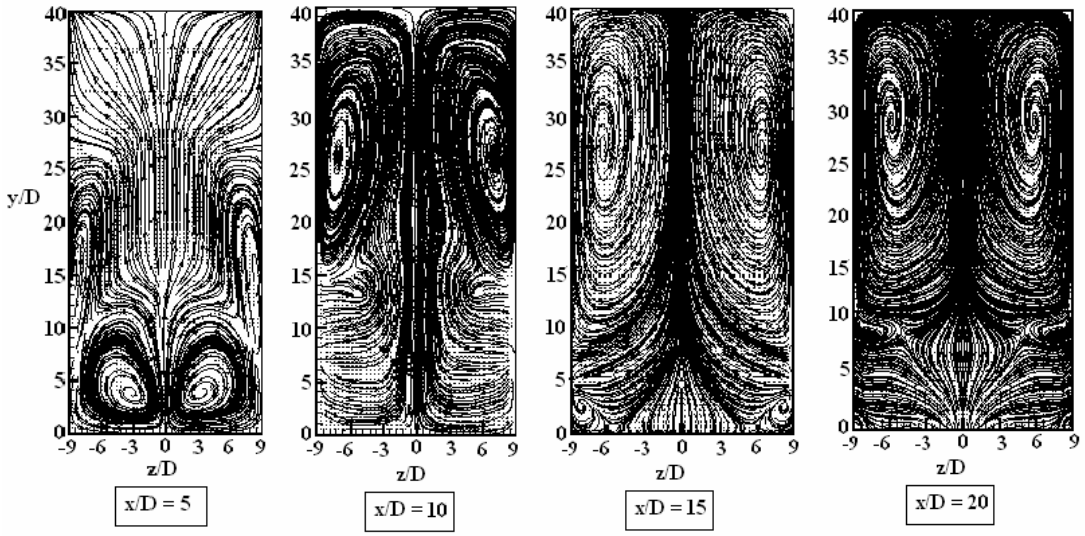

Fig. 5.60: Mean velocity vector plots superimposed with streamline at different locations predicted by RST model for $R = 9$, $x/D = 5$, 10, 15 and 20 in y-z plane.

At the position $x/D = 10$, the CRVP forms at the upper part of flow domain and the sizes of the two CRVPs are smaller than those predicted by the standard k-ε model (Fig. 4.61, Chapter 4). Downstream of this at $x/D = 15$, the two secondary vortices start to form at the two bottom corners. As the flow progresses the main CRVP centres move to an upward position. Enlarged views of the secondary vortices at the two locations $x/D = 15$ and 20 are shown in Fig. 5.61.

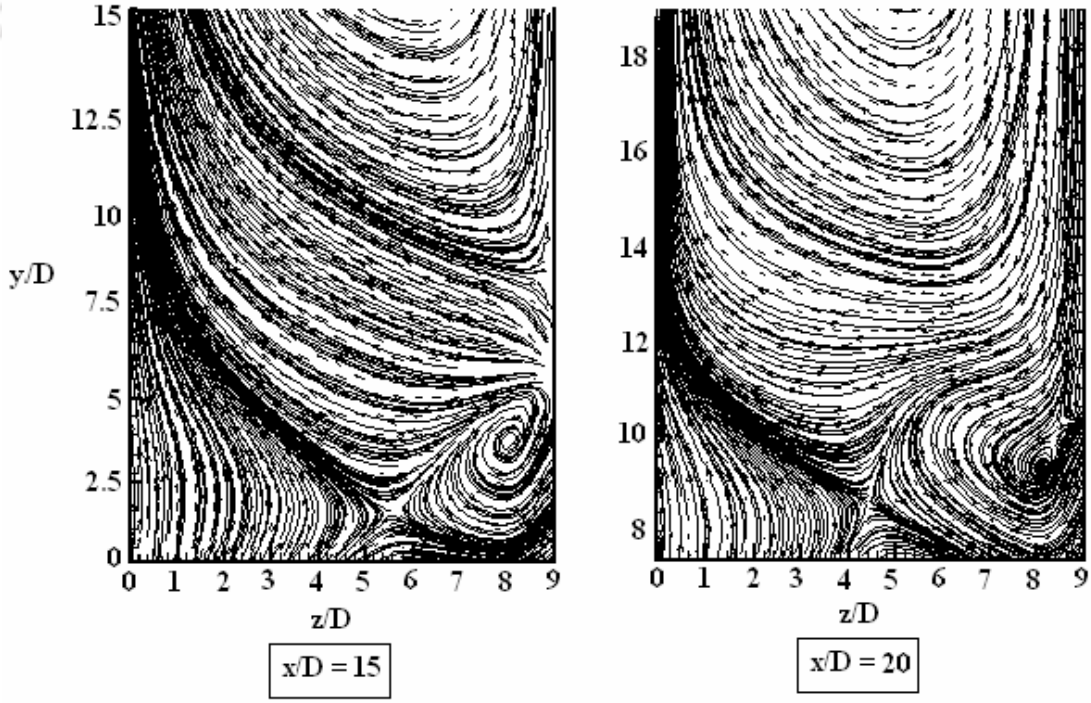

Fig. 5.61: Development of secondary vortices at the downstream locations predicted by RST model for $R = 9$.

The *x-z* plane mean velocity vector plots predicted by the RST model at different vertical positions for the velocity ratio R = 6 are shown in Figs. 5.62 and 5.63. The RST model shows some difference of structures of the DSSN vortices (already described in Chapter 4) in respect to their sizes and the orientation. At the first two vertical positions shown (Fig. 5.62), the sizes of the DSSN vortices are comparatively bigger than those predicted by the standard *k-ε* model (Fig. 4.62, Chapter 4).

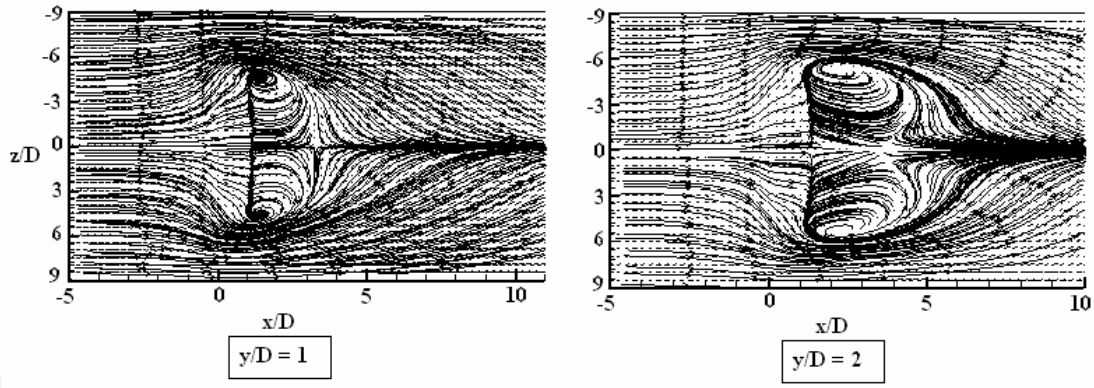

Fig. 5.62: Mean velocity vector plots superimposed with streamline at differnt vertical heights, *y/D* = 1 and 2 predicted by RST model for R = 6 in *x-z* plane.

At the position of *y/D* = 5 the DSSN vortices predicted by the RST model are of larger size than those predicted by standard *k-ε* model and they are oriented towards the sidewalls. However, at the position of *y/D* = 10 the size and position of the DSSN vortices are similar to those predicted by the standard *k-ε* model.

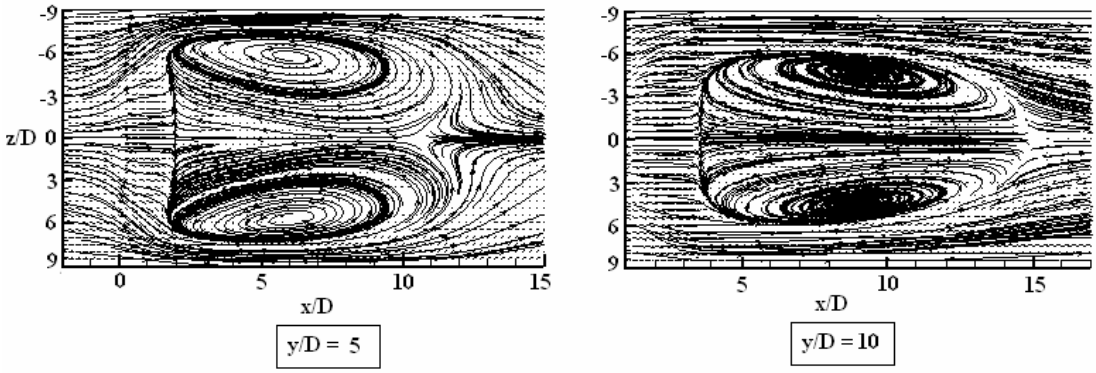

Fig. 5.63: Mean velocity vector plots superimposed with streamline at different vertical heights, *y/D* = 5 and 10 predicted by RST model for R = 6in *x-z* plane.

The contour plots of the spanwise component of the mean velocity at different *x-z* planes are shown in Fig. 5.64. It is observed from these plots that inside the jet discharge slot the components at both sides are opposite to each other, and thus the

tendency of the formation of vortices starts at the inside of the slot itself. This is also observed in the case of the standard k-ε model (Fig. 4.64, Chapter 4). From the values of contours of spanwise components it is observed that the values are slightly smaller than those predicted by the standard k-ε model. Thus the RST model predicts smaller values of spanwise components than those predicted by k-ε model.

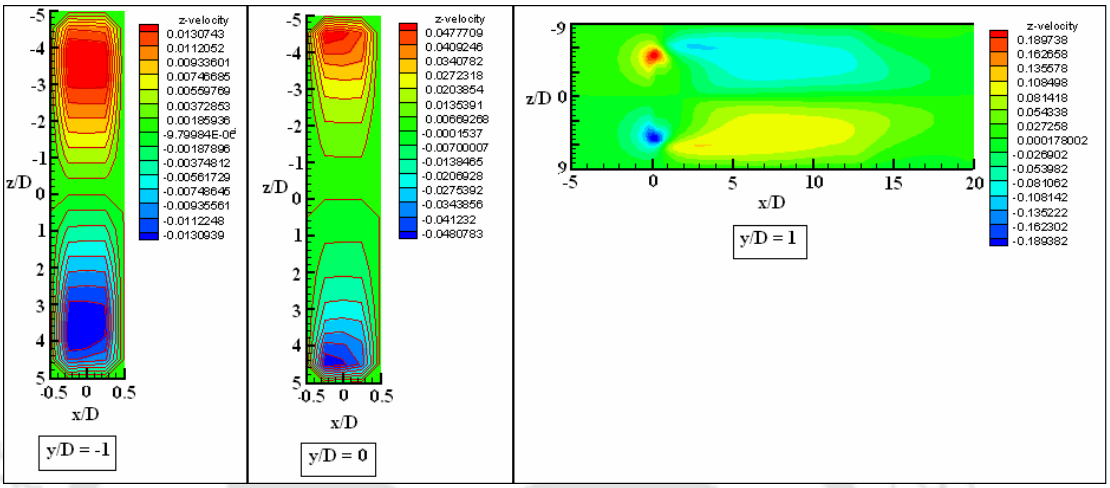

Fig. 5.64: Contour plot of mean z- velocity at different vertical planes predicted by RST model for R = 6.

The x-z plane mean velocity vector plots predicted by the RST model at different heights for R = 9 are shown in Figs 5.65 and 5.66. Compared to the standard k-ε model (Figs. 4.65 and 4.66, Chapter 4) the position of the DSSN vortices predicted by RST model (Figs. 5.65 and 5.66) lies somewhat downstream and their shapes are slightly different.

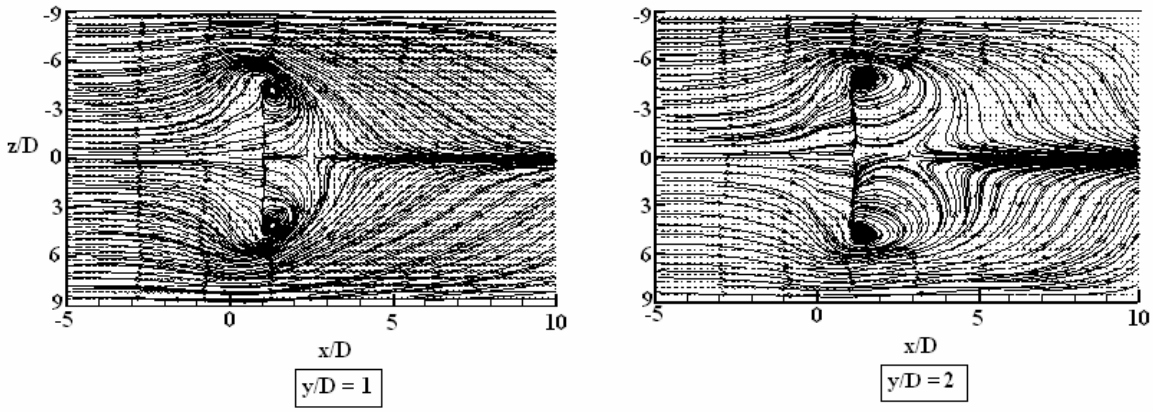

Fig. 5.65: Mean velocity vector plots superimposed with streamline at different vertical heights, y/D = 1 and 2 predicted by RST model for R = 9 in x-z plane.

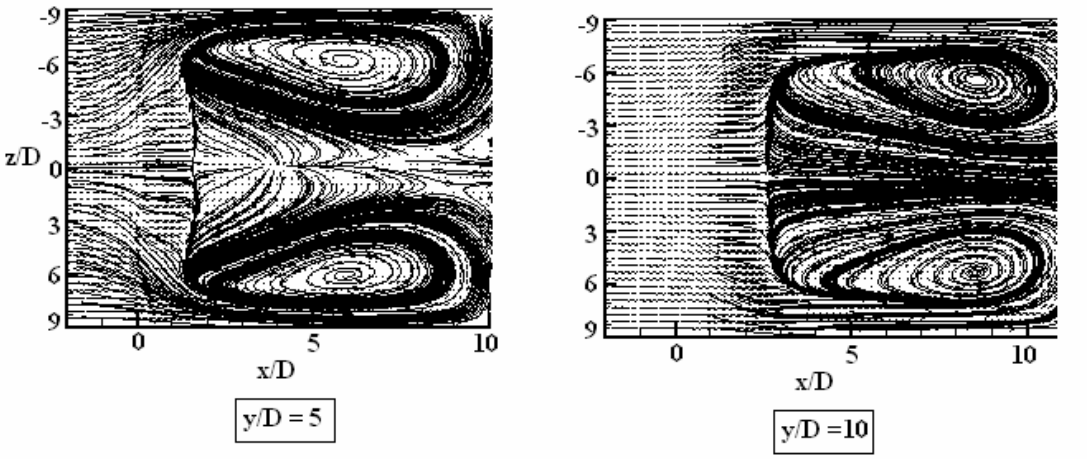

Fig. 5.66: Mean velocity vector plots superimposed with streamline at different vertical heights, *y/D* = 5 and 10 predicted by RST model for *R* = 9, in *x*-*z* plane.

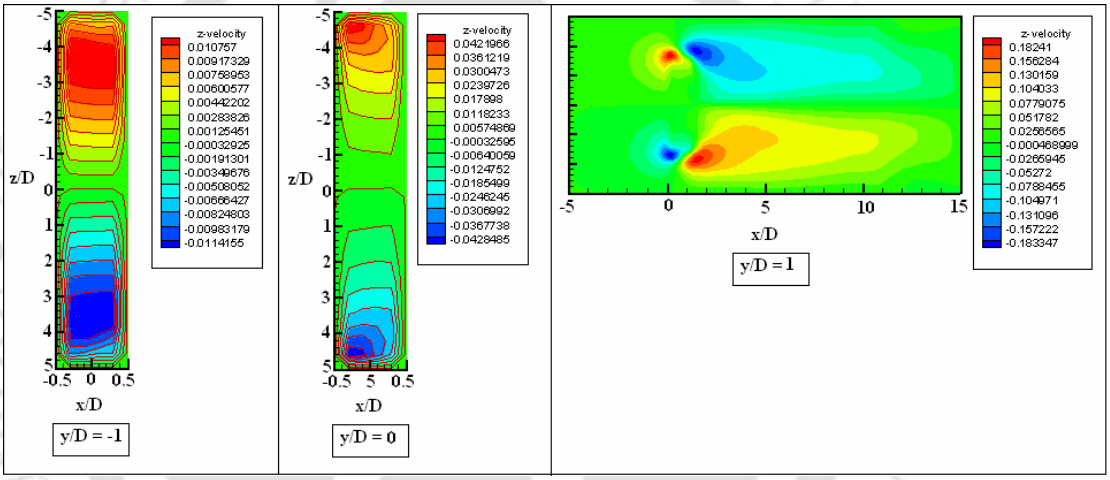

Fig. 5.67: Mean *z*- velocity contour plot at different vertical planes predicted by RST model for *R* = 9.

In case of *R* = 9 also the values of the spanwise component predicted by the RST model (Fig. 5.67) are smaller compared to those by the standard *k*-*ε* model (Fig. 4.67).

5.4.4 Mean Temperature Field

It is already explained in Section 5.2 that the jet is slightly heated (5.7 K for *R* = 6 and 6.1 K for *R* = 9). Due to a small temperature difference the changes of density are assumed to be negligible and therefore the flow field is assumed to be unaffected by the temperature field. The temperature distribution can provide good information about the mixing behaviour of the jet with the crossflow.

The variations of the normalized mean temperature with the vertical height (*y/D*) predicted by RST model at different spanwise planes and at different downstream locations for the velocity ratio $R = 6$ are shown in Figs. 5.68 to 5.71. At the jet slot ($x/D = 0$), it is observed that the peak of the mean temperature is near the wall, which indicates the high temperature of the jet stream at the jet inlet. Further downstream the temperature peak moves upwards along with the jet and this spread is controlled by the velocity field. It is observed that moving from the bottom wall the value of temperature gradually increases to a maximum or peak value and decreases monotonically thereafter. The distribution of the mean temperature at the upper and lower halves of the jet is different. This is due to the fact that the distribution of the temperature in the lower half of the jet is controlled by the reverse flow. It is observed that the temperature profile show similar trends as the vertical component of the mean velocity. It may be due to the fact that the prescribed boundary condition of the temperature at the jet inlet is similar to the vertical component of the mean velocity. It is also observed that though the jet is slightly heated compared to the crossflow, the decay rate of the temperature with downstream distance is quite small, due to a weak crossflow.

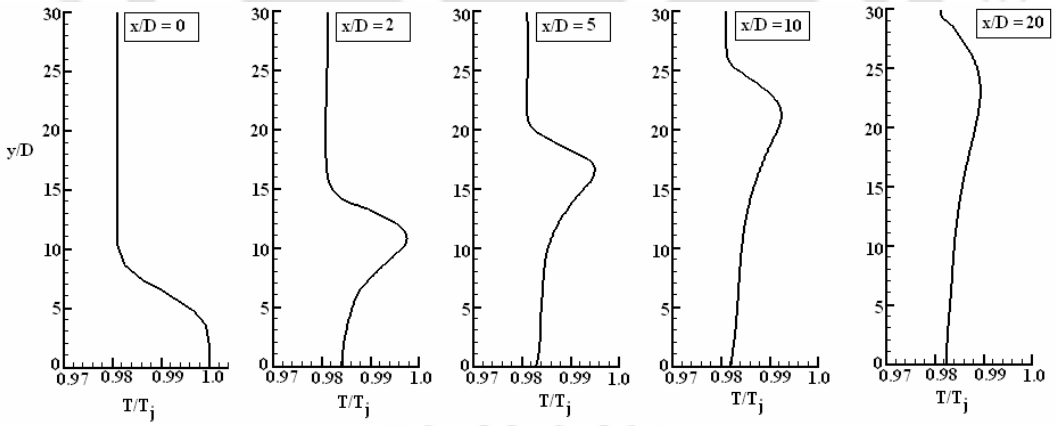

Fig. 5.68: Prediction of mean temperature at different down stream locations ($z/D = 0$) predicted by RST model for $R = 6$.

At the spanwise plane $z/D = 3$, the temperature profiles are almost similar to the profiles at the jet centre plane ($z/D = 0$) due to non-mixing and small interaction of the jet stream with the crossflow stream at this plane. The temperature distributions at the other two spanwise planes are significantly different from those at the first two planes ($z/D = 0$ and 3). At the plane $z/D = 5$, the vertical height of the peak temperature is reduced and the value of the peak temperature is also reduced for to a particular *x/D*

position. Moreover a temperature gradient is observed near the wall where the wall-jet layer is formed. The reduced values of the temperatures are observed due to high mixing of the hot jet fluid with the crossflow fluid along the jet edge.

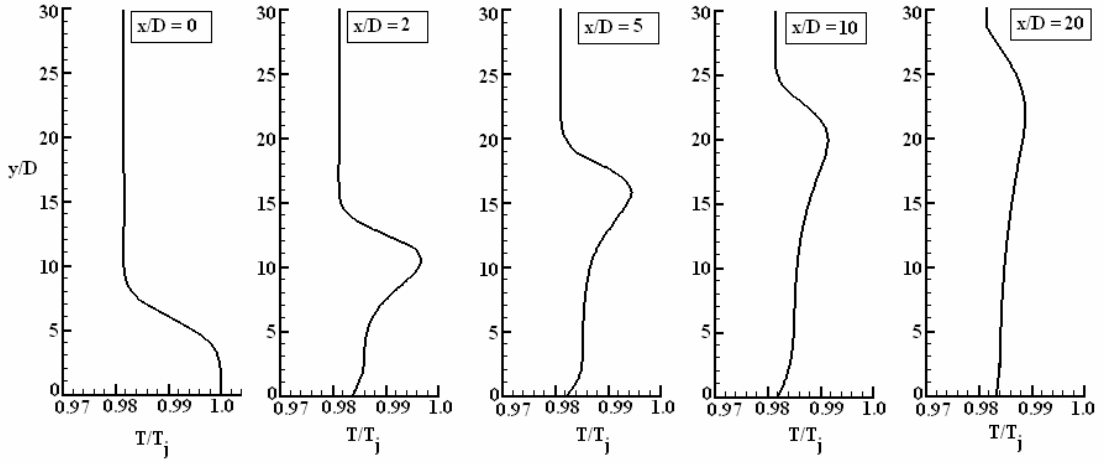

Fig. 5.69: Prediction of the mean temperature at different downstream locations (*z/D* = 3) predicted by RST model for *R* = 6.

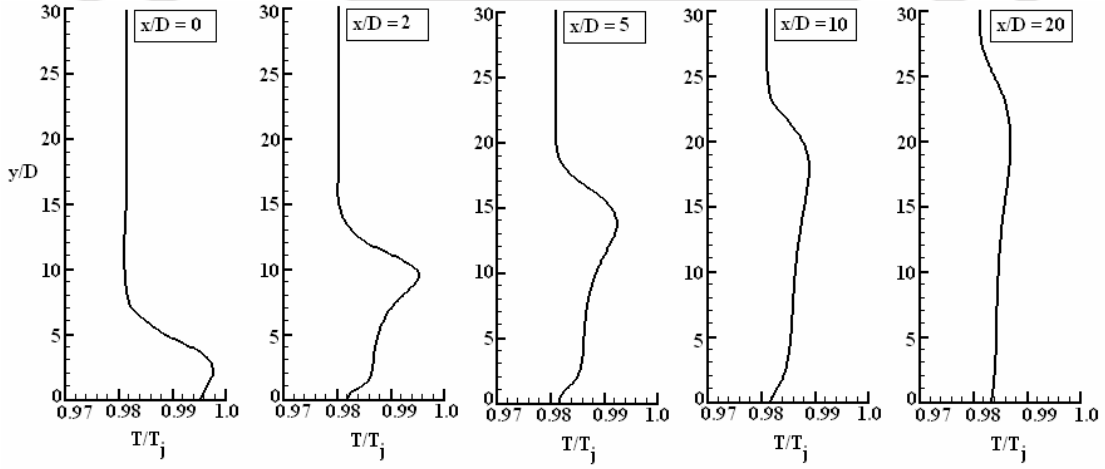

Fig. 5.70: Prediction of the mean temperature at different downstream locations (*z/D* = 5) predicted by RST model for *R* = 6.

The last spanwise plane considered is at *z/D* = 6. At this plane the value of the temperature near the bottom wall at the jet exit region (*x/D* = 0) is observed to be smaller, compared to that at the other spanwise planes (*z/D* = 0, 3 and 5). However the temperature distribution at other downstream locations shows an almost similar trend as at the plane *z/D* = 5. From the temperature profiles at all spanwise planes it can be concluded that the decay or dilution of the temperature along spanwise direction is small compared to the corresponding decay in the cross-stream direction.

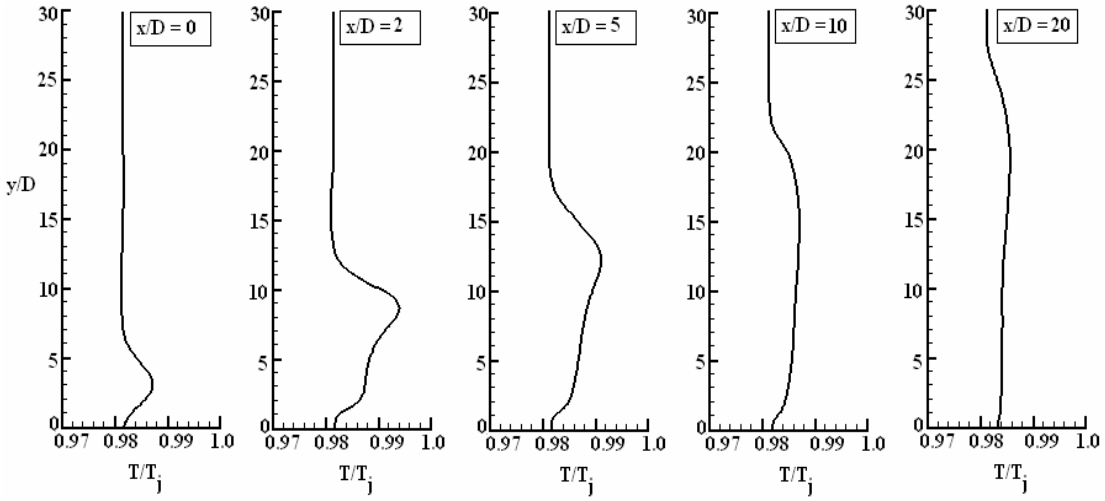

Fig. 5.71: Prediction of the mean temperature at different downstream locations (*z/D* = 6) predicted by RST model for *R* = 6.

In case of velocity ratio *R* = 9 the temperature profile shows similar behaviour (Figs. 5.72 to 5.75) as in the case of *R* = 6. In this case the peak values of temperature occurs at the higher vertical position compared to the case with *R* = 6. This is due to a higher trajectory and penetration of the jet. In this case also the temperature distributions are different at upper and lower halves. Moreover the profiles are different at different spanwise planes. The spread of the temperature profiles are slightly less at the outer spanwise planes (*z/D* = 5 and 6) compared to the inner spanwise planes (*z/D* = 0 and 3). Since the jet is comparatively stronger so appreciable temperature peak values are obtained even at the far downstream positions at two outer spanwise planes (*z/D* = 5 and 6), which was not observed in the case of *R* = 6.

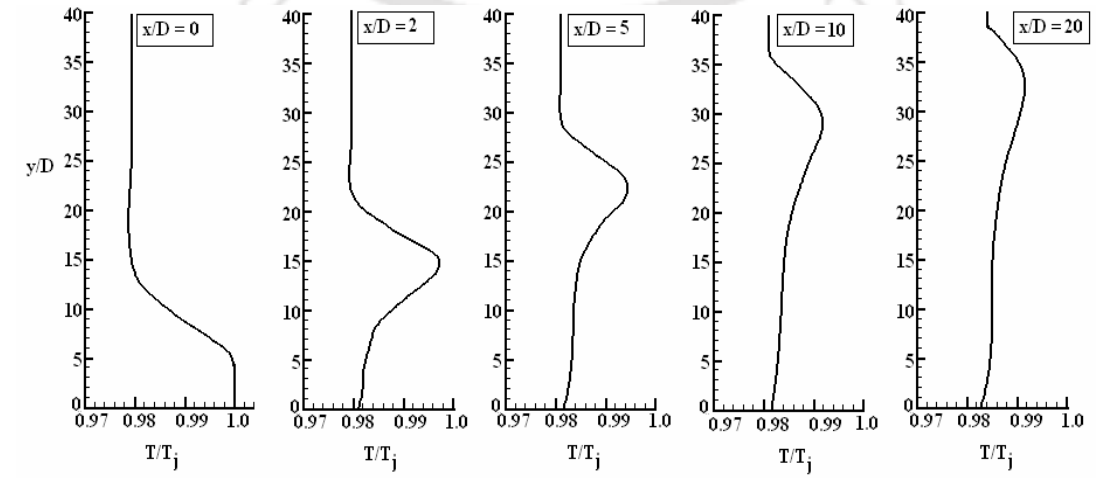

Fig. 5.72: Prediction of the mean temperature at different downstream locations (*z/D* = 0) predicted by RST model for *R* = 9.

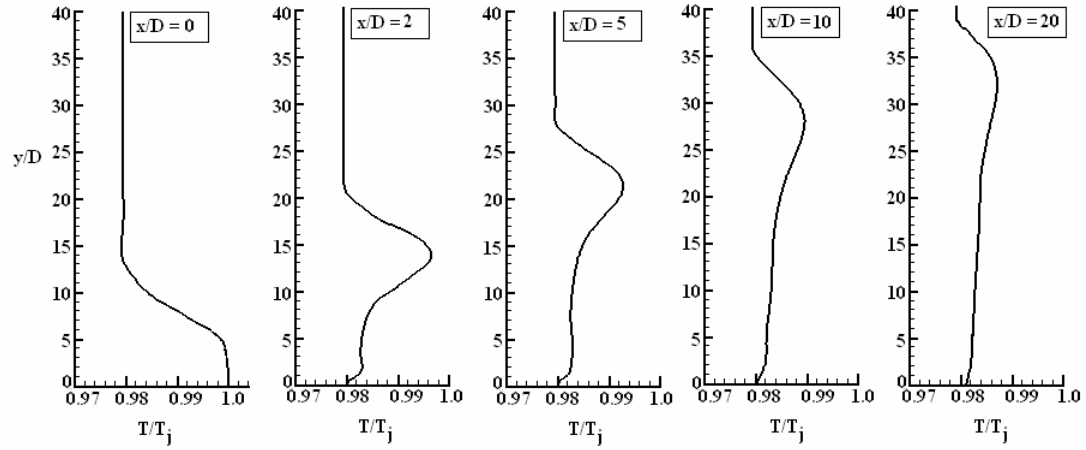

Fig. 5.73: Prediction of the mean temperature at different downstream locations (*z/D* = 3) predicted by RST model for *R* = 9.

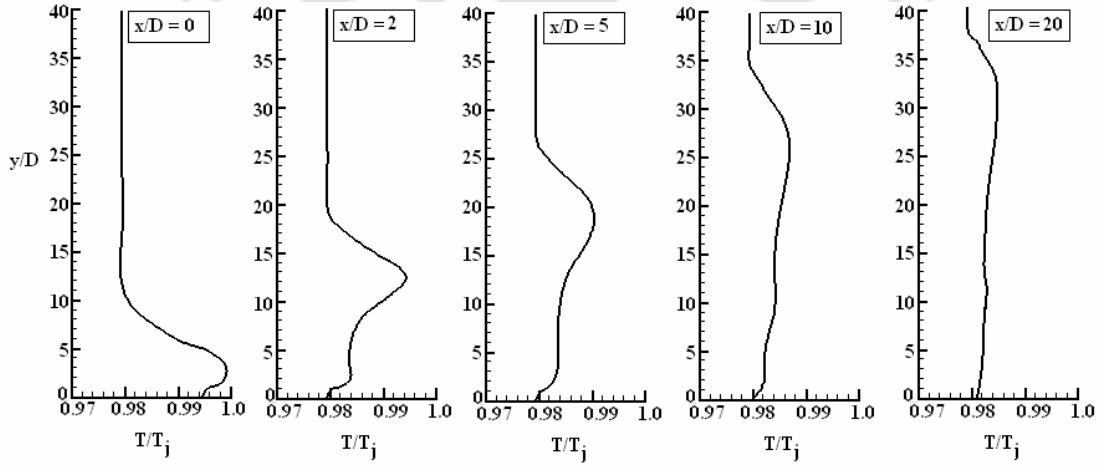

Fig. 5.74: Prediction of the mean temperature at different down stream locations (*z/D* = 5) predicted by RST model for *R* = 9.

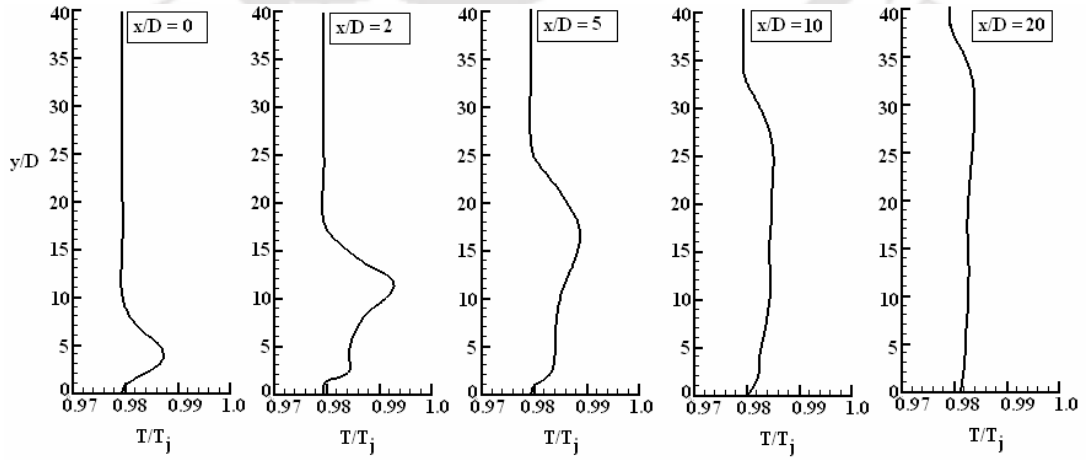

Fig. 5.75: Prediction of the mean temperature at different downstream locations (*z/D* = 6) predicted by RST model for *R* = 9.

Iso-contours of the mean temperature at three different spanwise planes (z/D = 0, 5 and 6) for R = 6 are presented in Fig. 5.76. The temperature contour shows shapes somewhat similar to the well known Gaussian distribution. The mean temperature variations of the heated free jet are small (Sherif and Pletcher, 1991). Therefore all the temperature fluctuations in the crossflow jet may result from the mixing and the interaction between the jet and crossflow. At the upper part of the jet, the distribution of the contour is dense, thus indicating that the mixing between the jet and the crossflow is rather active. In contrast, a relatively sparse contours are developed widely at the inner part of the jet. This originates from a low-velocity reverse flow region, which may promote the process of thermal spread at the inner part of the jet. The spread of the mean temperature is affected by the mean velocity field at different spanwise locations. At the edge and outside of the slot, the spread of the temperature is less compared to that at the centre, which is similar to the case of the mean velocity field distribution.

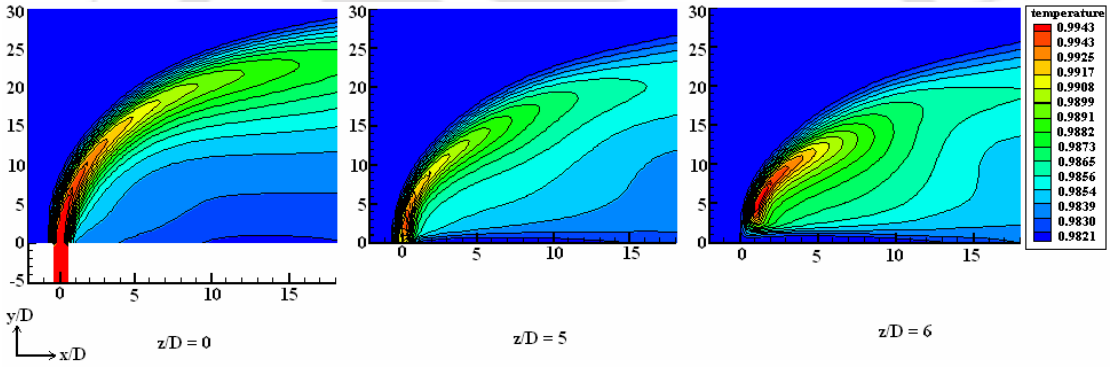

Fig. 5.76: Mean temperature contours at three different spanwise (x-y) planes predicted by RST model for R = 6, z/D = 0, 5 and 6.

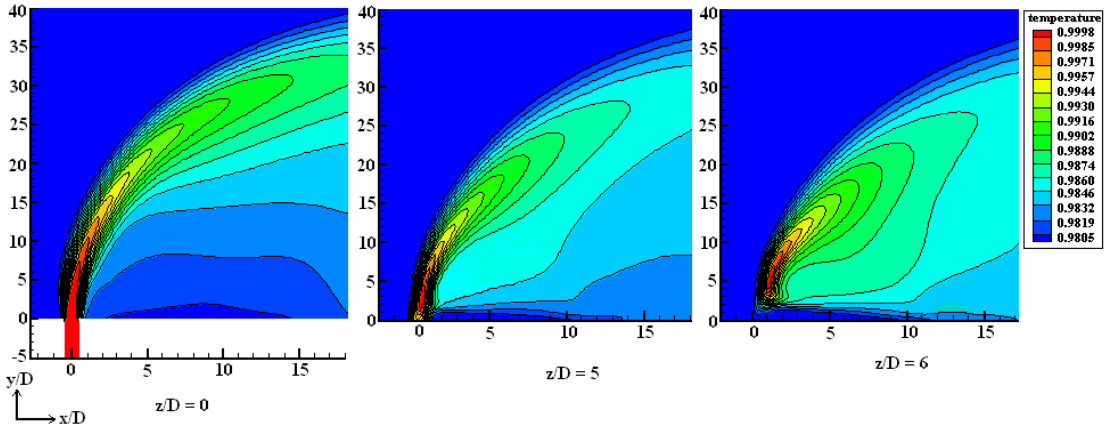

Fig. 5.77: Mean temperature contours at three different spanwise (x-y) planes predicted by RST model for R = 9, z/D = 0, 5 and 6.

In case of R = 9 the jet is relatively stronger and therefore the spread of the temperature or the penetration of the temperature occurs up to a higher position than that in the case of R = 6 (Fig. 5.77). The temperature distribution follows the mean velocity distribution in this case also.

Fig. 5.78 shows the mean temperature contours at various y–z planes at different downstream locations for the velocity ratio R = 6. The spread of the high temperature jet core due to the interaction of the jet with the crossflow can be understood from these plots. The high temperature jet fluid enters from the jet slot and after interaction with the crossflow this zone moves upward along with the down wash by the crossflow. It is observed that at the upper part of the jet, the distribution of the contour is dense whereas a quite coarse and relatively wide temperature distribution at the inner part of the jet occurs. The shape of the temperature distribution is more or less circular immediately downstream of the slot and it becomes kidney shaped further downstream. It is observed that the CRVP dynamics controls the temperature distribution. At all locations the shape is observed to be symmetric about the central vertical plane (z/D = 0).

In case of velocity ratio R = 9 the y-z plane mean temperature contours (Fig. 5.79) show a similar trend as in the case of R = 6, but far downstream the contours show some differences. At x/D = 10, the isotherm pattern near the bottom corners show some dissimilarity with those for R = 6.

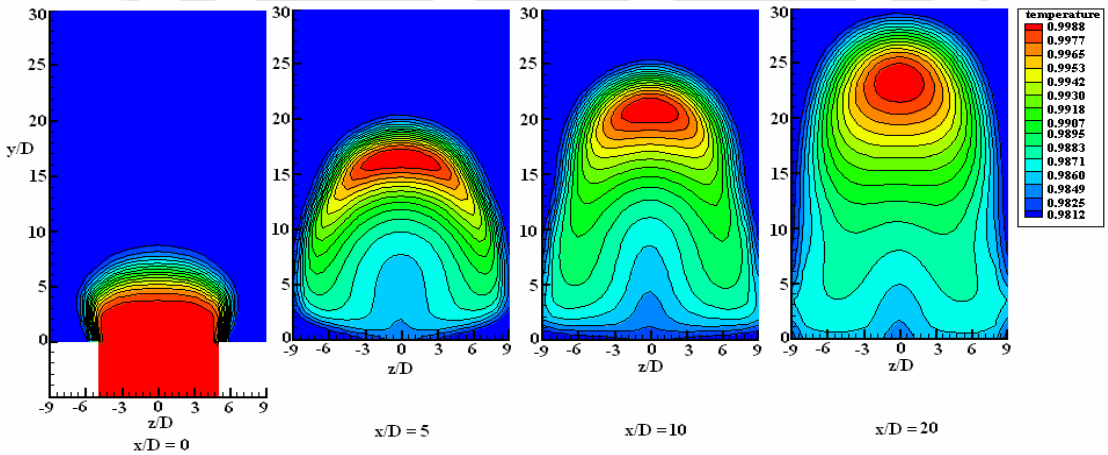

Fig. 5.78: Mean temperature contours at various y-z planes predicted by RST model for R = 6, x/D = 0, 5, 10 and 20.

At the position x/D = 20, sharp variations in temperatures are confined only to the upper part of the flow field and variations in the bottom part and near the wall are small. This also occurs due to the position of the CRVP at the upper part of the flow

field at that location which we have already discussed in the *y-z* plane velocity vector plot (Fig. 5.60).

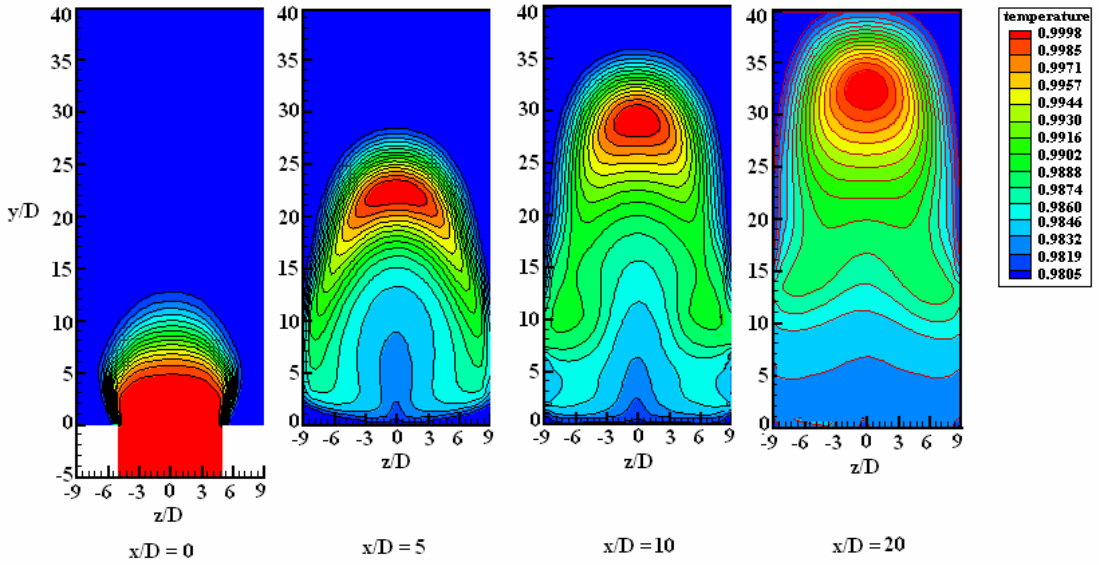

Fig. 5.79: Mean temperature contours at various *y-z* planes predicted by RST model for $R = 9$, $x/D = 0$, 5, 10 and 20.

The mean temperature contours are presented in Fig. 5.80 for three heights (y/D = 1, 5, 10) in the *x–z* planes for the velocity ratio $R = 6$. It is observed that as the height increases, the maximum of temperature moves downstream from the jet and the temperature gets distributed over a larger region.

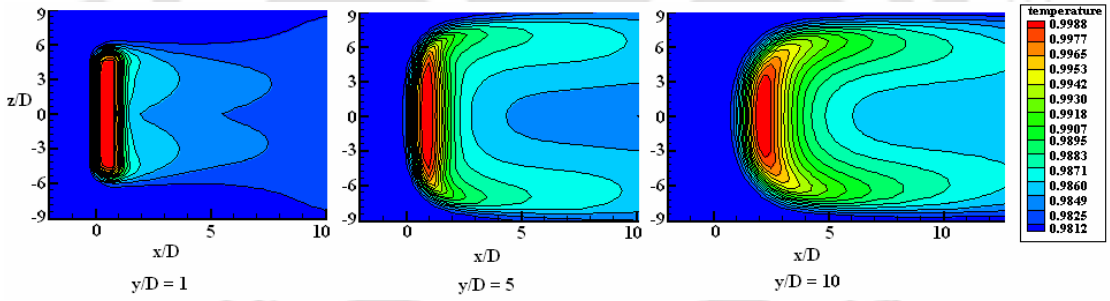

Fig. 5.80: Mean temperature contours at various *x-z* planes at different *y/D* locations predicted by RST model for $R = 6$.

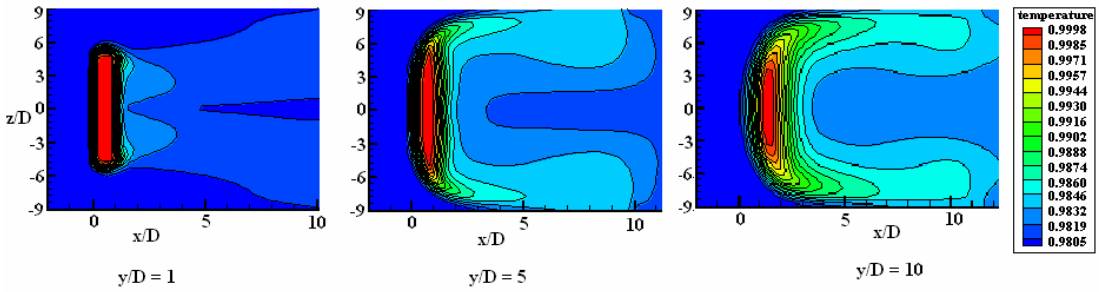

Fig. 5.81: Mean temperature contours at various *x-z* planes at different *y/D* locations predicted by RST model for $R = 9$.

Dispersion of the temperature is influenced by the pair of DSSN vortices formed in the *x*–*z* plane. The temperature distribution at different planes observed in the present work is similar to that reported by Shi et al. (2003) and Said et al. (2003). In case of velocity ratio $R = 9$ also the DSSN vortices control the temperature distribution, which is shown in Fig. 5.81.

5.4.5 Comparison with Measurements

In this section a comparison of the predictions by RST model and the standard *k*-*ε* model (Chapter 4) is made with the experimental data of Ramaprian and Haniu (1983) and Haniu and Ramaprian (1989). The results are presented in the *s*-*n* coordinate system.

A comparison of the normalized *s*-component profiles of the mean velocity (u_s/v_j) in the jet central vertical plane ($z/D = 0$) at four different downstream locations (s/D = 4.94, 9.68, 18.86 and 28.12) for the velocity ratio $R = 6$ with the experimental data is shown in Figs. 5.82 and 5.83. The RST model slightly over predicts in the upper part of the jet but it predicts accurately in the lower part of the jet. The standard *k*-*ε* model predicts the upper part ($n/D < 0$) of the jet quite well but over predicts in the lower part of the jet. The RST model predicts the jet peak value better than that by the standard *k*-*ε* model and it can be concluded that the overall performance of the RST model is slightly better than that of the standard *k*-*ε* model.

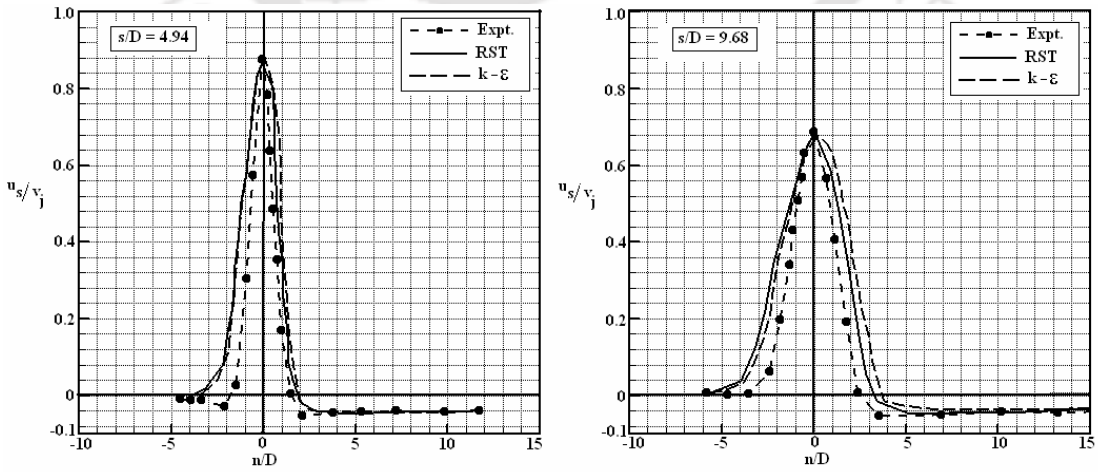

Fig. 5.82: Comparison of mean streamwise velocity at jet central plane ($z/D = 0$) for $R = 6$, s/D = 4.94 and 9.68.

In case of velocity ratio R = 9 (Figs. 5.84 and 5.85), a comparison of both the models show the same trends as in the case of R = 6. In this case also the RST model over predicts in the upper part and predicts better in the bottom part of the jet.

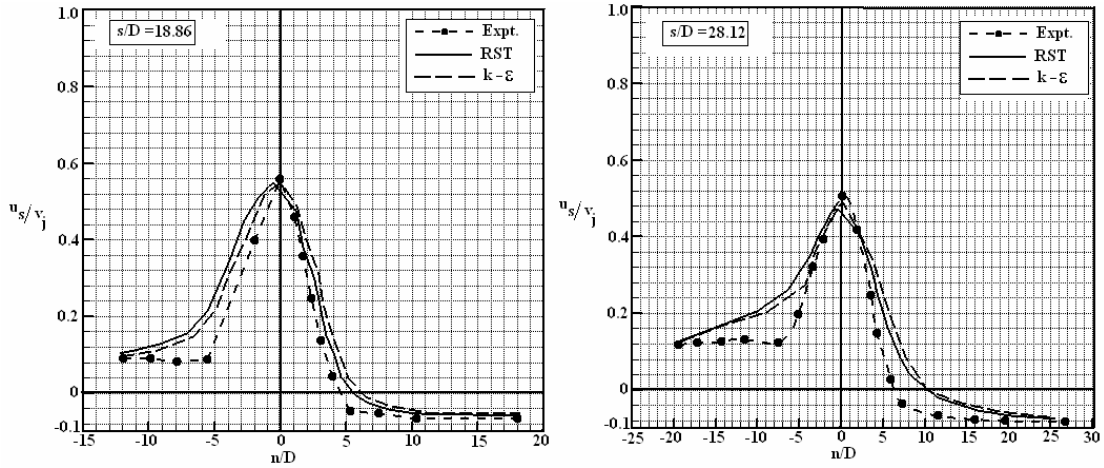

Fig. 5.83: Comparison of mean streamwise velocity at jet central plane (z/D = 0) for R = 6, s/D = 18.86 and 28.12.

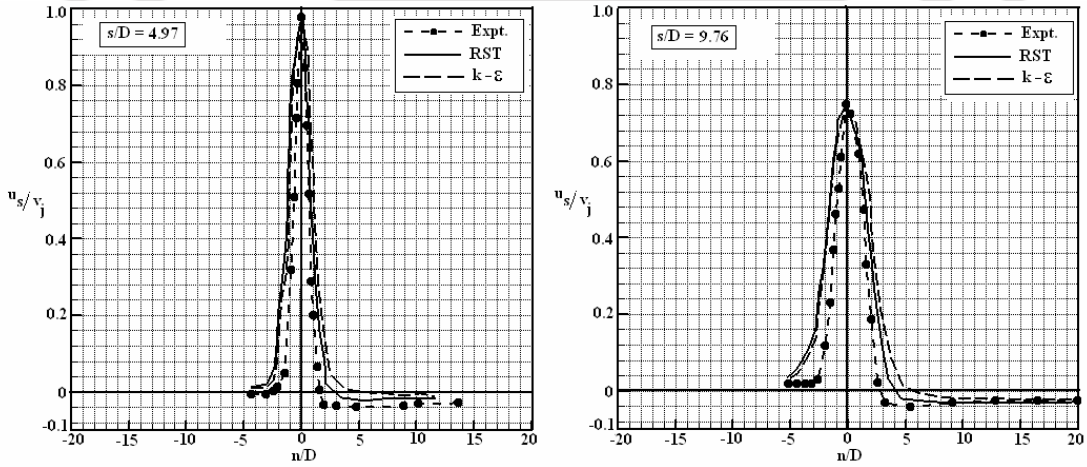

Fig. 5.84: Comparison of mean streamwise velocity at jet central plane (z/D = 0) for R = 9, s/D = 4.97 and 9.76.

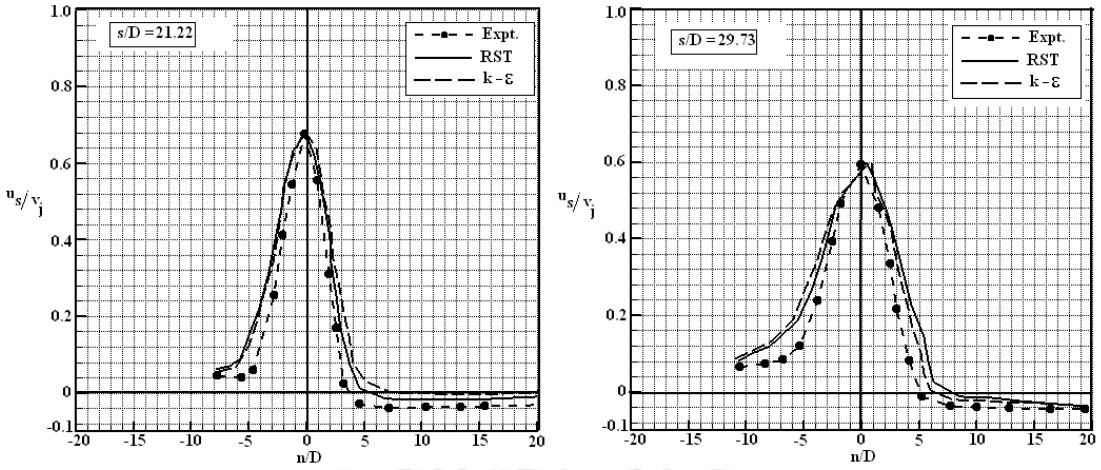

Fig. 5.85: Comparison of mean streamwise velocity at jet central plane ($z/D = 0$) for $R = 9$, $s/D = 21.22$ and 29.73.

Figs. 5.86 and 5.87 show a comparison of the normalized n-component velocity profiles (v_n/v_j) in the jet central vertical plane ($z/D = 0$) at four downstream locations with the experimental data for the velocity ratio $R = 6$. The predictions agree well with the experimental data, both quantitatively and qualitatively. The RST model shows a comparatively better agreement with the experimental data than the standard k-ε model.

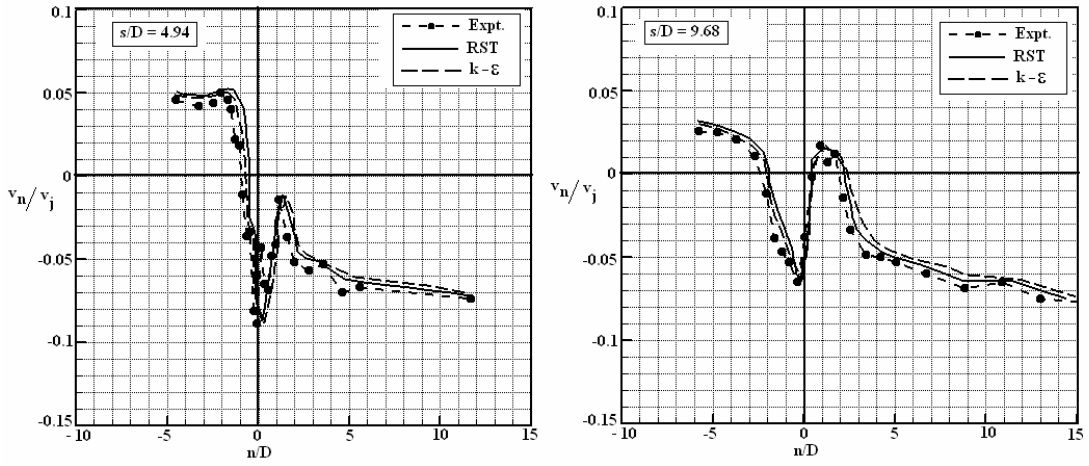

Fig. 5.86: Comparison of mean normal component velocity at jet central plane ($z/D = 0$) for $R = 6$, $s/D = 4.94$ and 9.68.

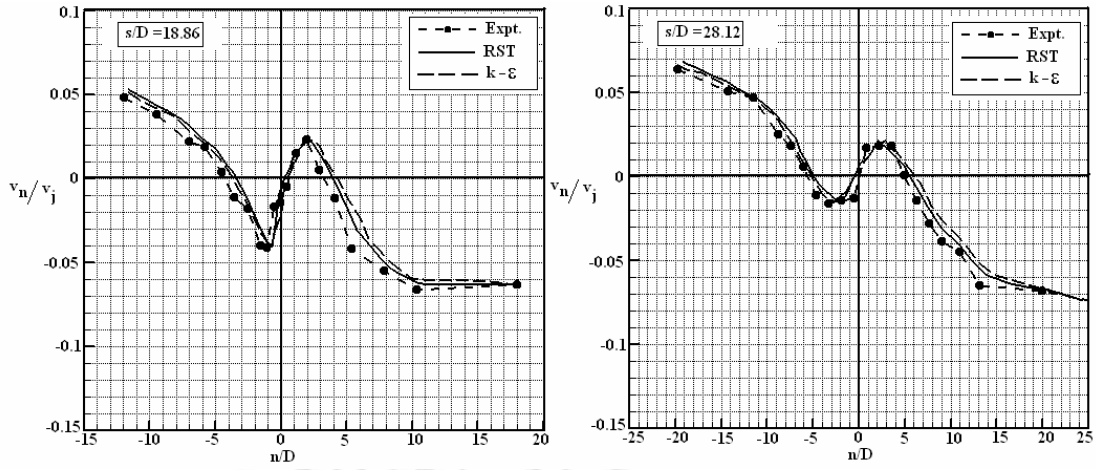

Fig. 5.87: Comparison of mean normal component velocity at jet central plane ($z/D = 0$) for $R = 6$, $s/D = 18.86$ and 28.12.

Comparisons of the normalized n-component profiles of the mean velocity (v_n/v_j) in the jet central vertical plane ($z/D = 0$) at four downstream locations ($s/D = 4.97$, 9.76, 21.22 and 29.73) with the experimental data for the velocity ratio $R = 9$ are presented in Figs. 5.88 and 5.89. Both the models show the same trend as in the case of the velocity ratio $R = 6$. The mean flow comparison indicates that the RST model slightly over predicts in the upper part of the jet but the agreement between the predictions and measurements is better in the lower part of the jet.

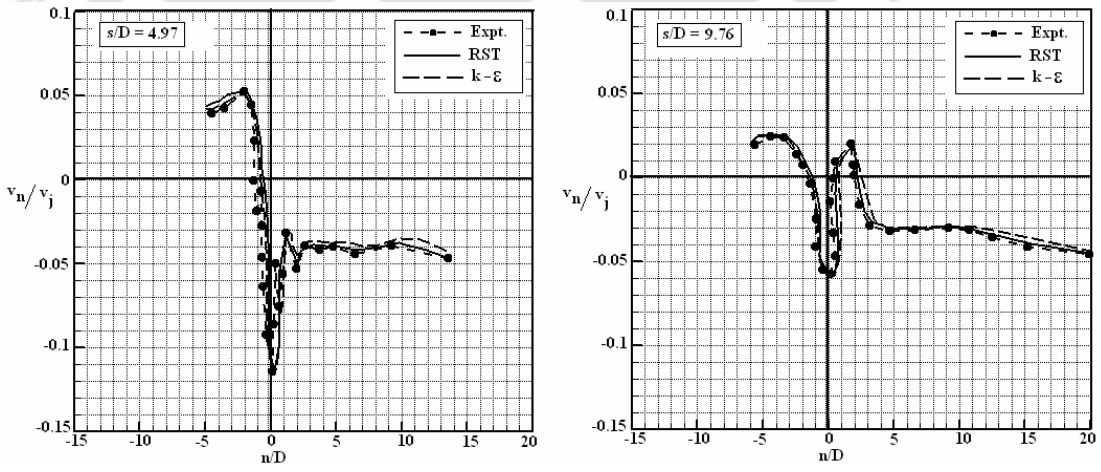

Fig. 5.88: Comparison of mean normal component velocity at jet central plane ($z/D = 0$) for $R = 9$, $s/D = 4.97$ and 9.76.

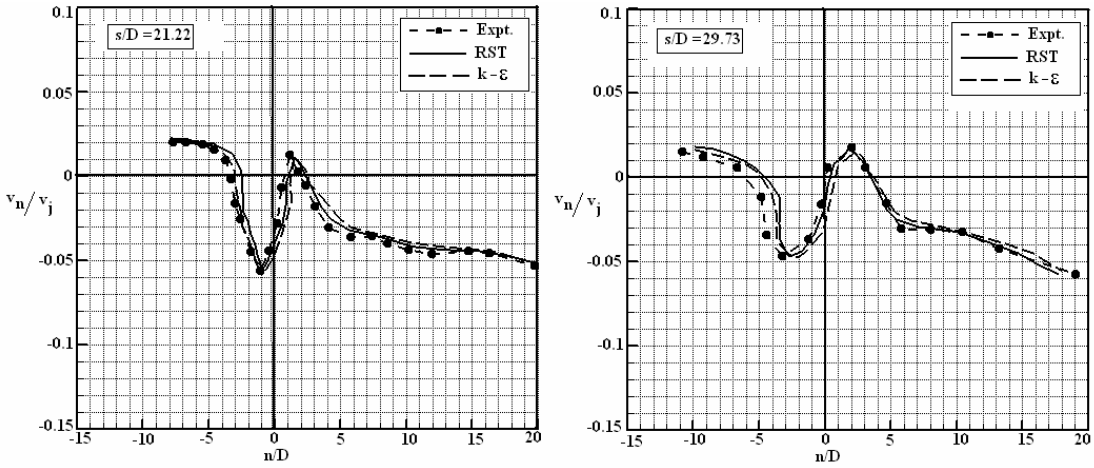

Fig. 5.89: Comparison of mean normal component velocity at jet central plane ($z/D = 0$) for $R = 9$, $s/D = 21.22$ and 29.73.

A comparison of the predicted normalized excess temperature profile ($\Delta T/\Delta T_j$), where $\Delta T = T - T_a$ and $\Delta T_j = T_j - T_a$, by the RST model with the experimental data in the jet central vertical plane ($z/D = 0$) at four downstream positions for the velocity ratio $R = 6$ is shown in Figs. 5.90 and 5.91. The RST model over predicts the temperature field. The performance of the model is better in the near-field region compared to the far-field. In the case of velocity ratio $R = 9$, the RST model shows the same behaviour but it over predicts more at the far downstream location ($s/D = 29.73$).

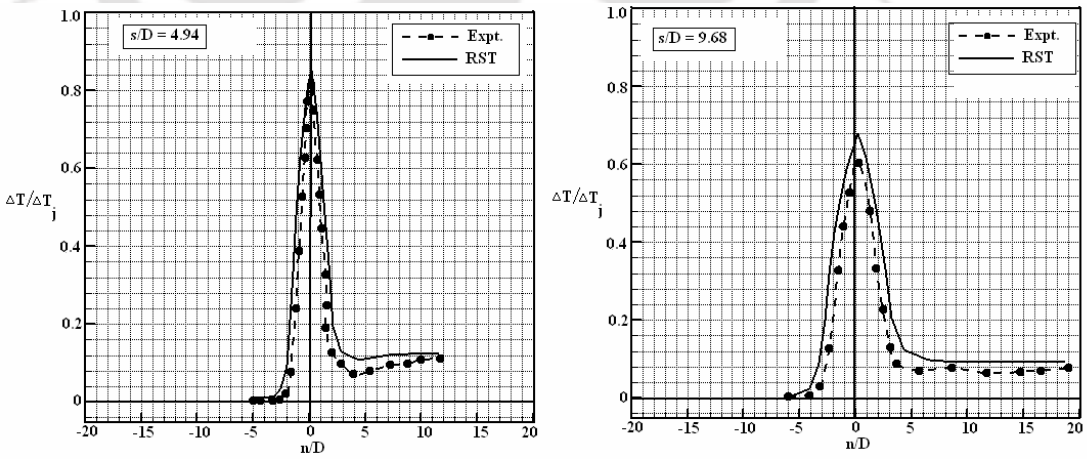

Fig. 5.90: Comparison of excess temperature at jet central plane ($z/D = 0$) for $R = 6$, $s/D = 4.94$ and 9.68.

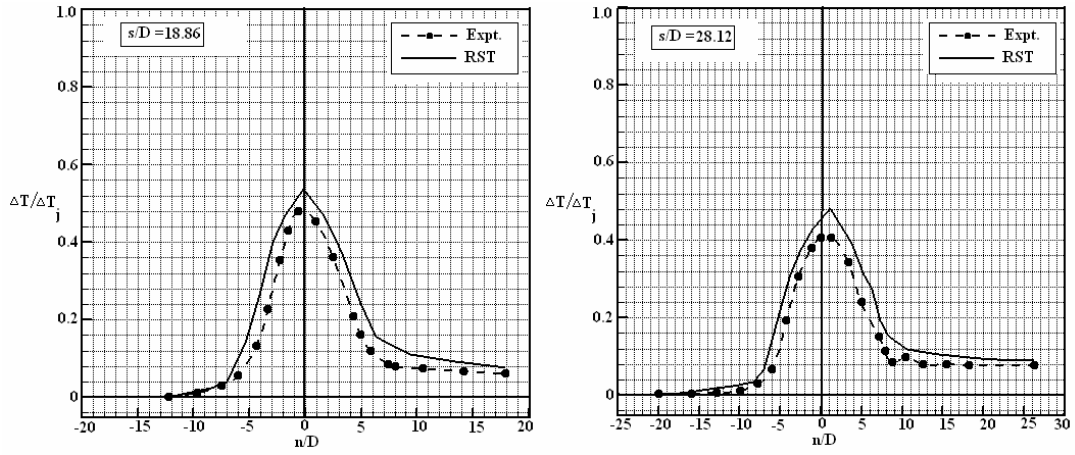

Fig. 5.91: Comparison of excess temperature at jet central plane ($z/D = 0$) for $R = 6$, $s/D = 18.86$ and 28.12.

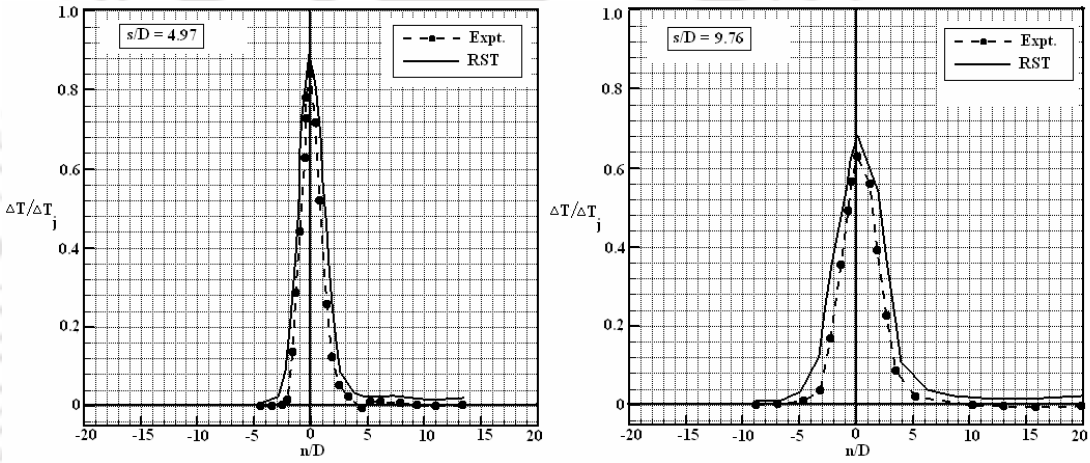

Fig. 5.92: Comparison of excess temperature at jet central plane ($z/D = 0$) for $R = 9$, $s/D = 4.97$ and 9.76.

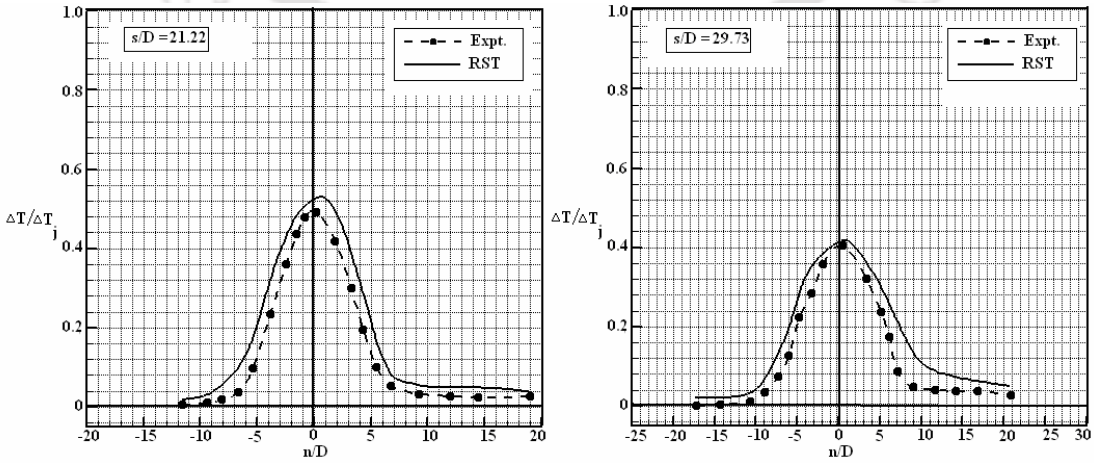

Fig. 5.93: Comparison of excess temperature at jet central plane ($z/D = 0$) for $R = 9$, $s/D = 21.22$ and 29.73.

Comparisons of the turbulence shear stress profiles in the jet central vertical planes at four downstream positions are shown in Figs. 5.94 and 5.95 for the velocity ratio R = 6 and in Figs. 5.96 and 5.97 for the velocity ratio R = 9. The large peak values observed in the experimental data and the present predictions are due to the high values of velocity gradient in the near jet-axis region. The standard k-ε model slightly over predicts the shear stresses especially in the inner half of the jet, where the flow faces reverse flow, whereas the predictions by the RST model agree better with the experimental results. Moreover, the predictions of the positive and negative peak values of the stresses by RST model match well with the experimental data.

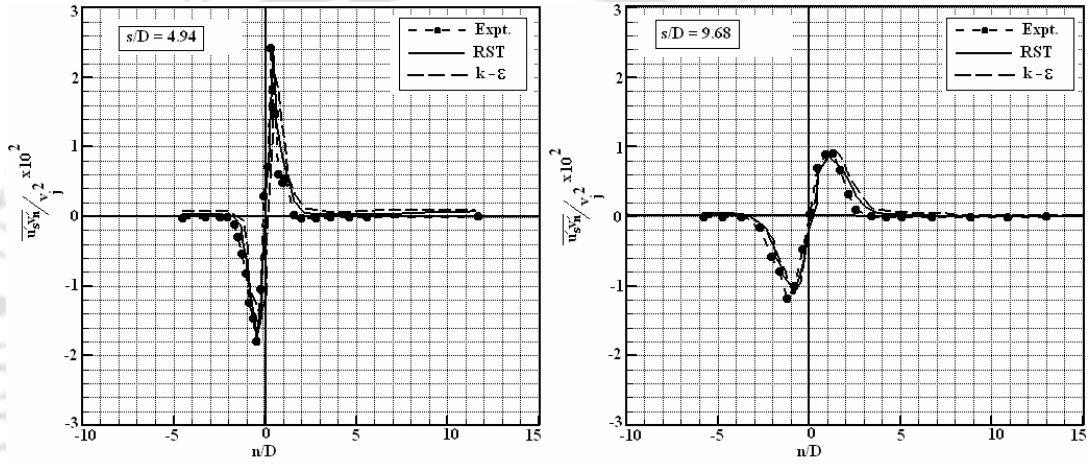

Fig. 5.94: Comparison of turbulence shear stress at jet central plane (z/D = 0) for R = 6, s/D = 4.94 and 9.68.

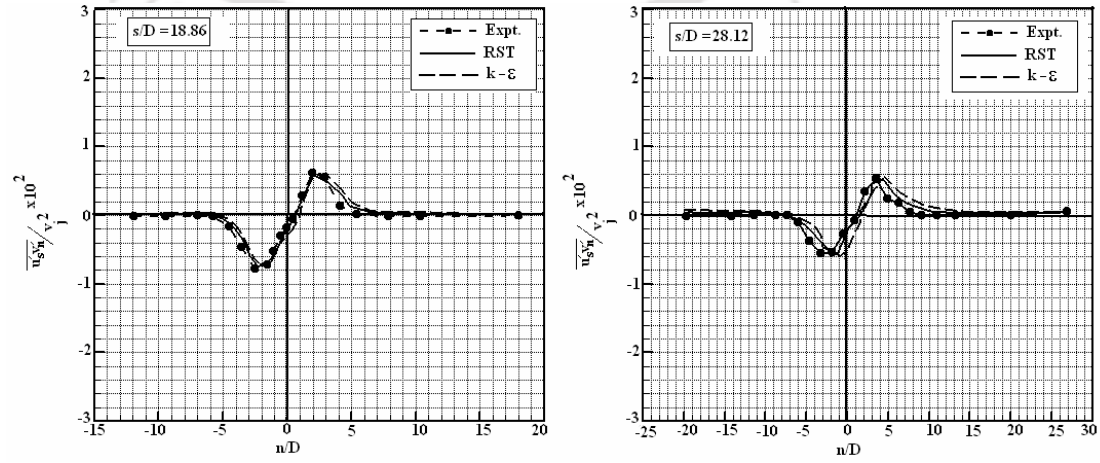

Fig. 5.95 Comparison of turbulence shear stress at jet central plane (z/D = 0) for R = 6, s/D = 18.86 and 28.12.

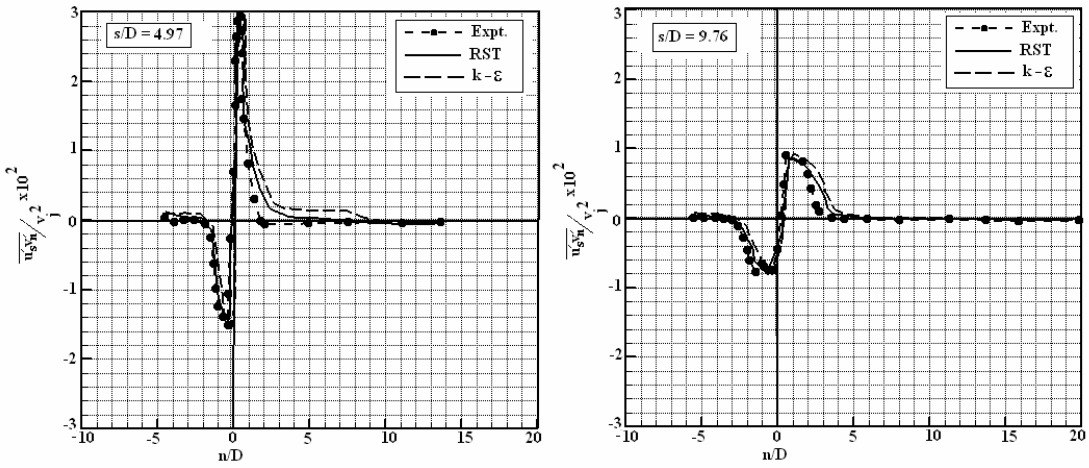

Fig. 5.96 Comparison of turbulence shear stress at jet central plane ($z/D = 0$) for $R = 9$, $s/D = 4.97$ and 9.76.

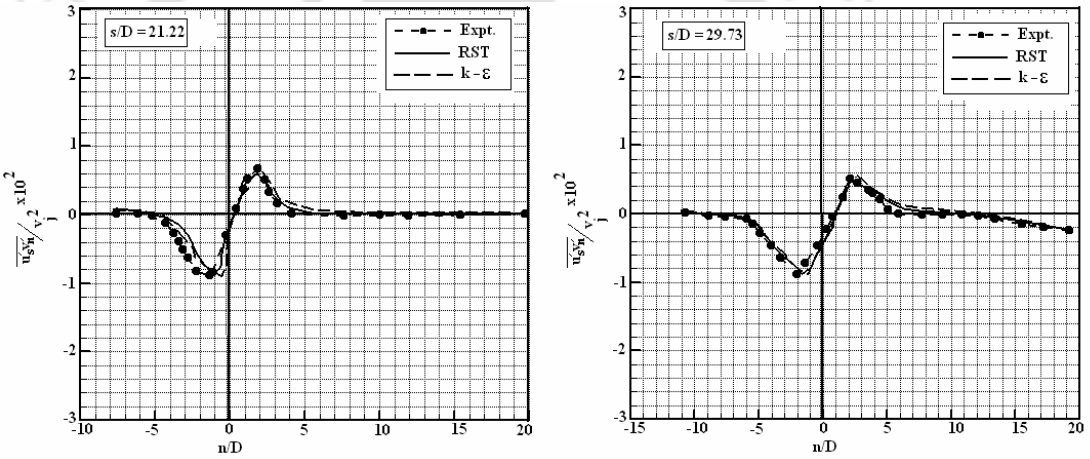

Fig. 5.97: Comparison of turbulence shear stress at jet central plane ($z/D = 0$) for $R = 9$, $s/D = 21.22$ and 29.73.

5.4.6 Comparisons of all models

In Chapter 3 we have presented the computational results of 2D flow fields using the standard k–ε model and streamline curvature modification to the standard k–ε model. Similarly the predictions of 3D flow field using the standard k–ε model and RST model are presented in Chapters 4 and 5, respectively. To make an assessment of all the predictions, we have compared all the predictions with the experimental data of Ramaprian and Haniu (1983) and Haniu and Ramaprian (1989) in this section. The streamline curvature model is shown in abbreviated form as Curv. in all the figures.

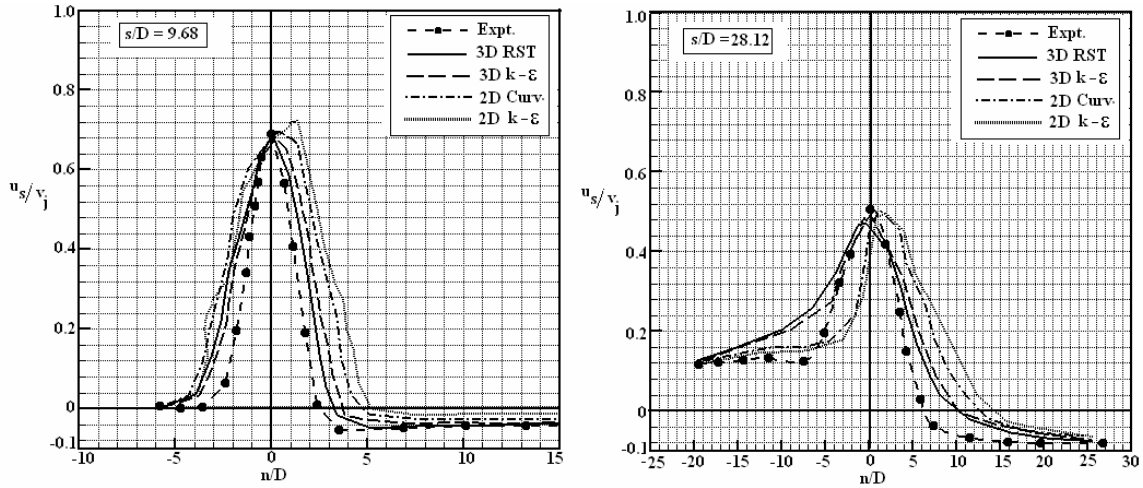

Fig. 5.98: Comparison of mean streamwise velocity at jet central plane (z/D = 0) for R = 6, s/D = 9.68 and 28.12.

A comparison of the normalized streamwise component of the mean velocity (u_s/v_j) at the jet central vertical plane (z/D = 0) with the experimental data at two different downstream locations (s/D = 9.68 and 28.12) for the velocity ratio R = 6 is shown in Fig. 5.98. As expected the 2D predictions of standard k–ε model show poorest agreement where as the RST model shows best agreement with the experimental data.

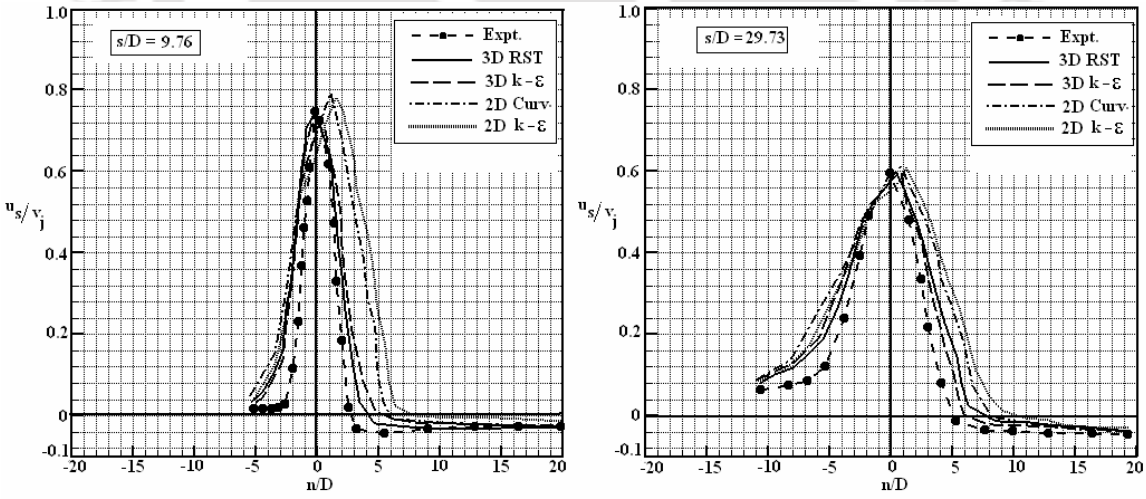

Fig. 5.99: Comparison of mean streamwise velocity at jet central plane (z/D = 0) for R = 9, s/D = 9.76 and 29.73

Fig. 5.99 shows the comparison of the normalized streamwise component of the mean velocity (u_s/v_j) at the jet central vertical plane (z/D = 0) at two different

downstream locations (s/D = 9.76 and 29.73) with the experimental data for the velocity ratio R = 9. In this case also similar observation is made in case of R = 6. In both cases the 2D predictions show a higher spread of the jet especially in the inner part of the jet and the position of the peak value is not matching with either the experimental or with the 3D predictions.

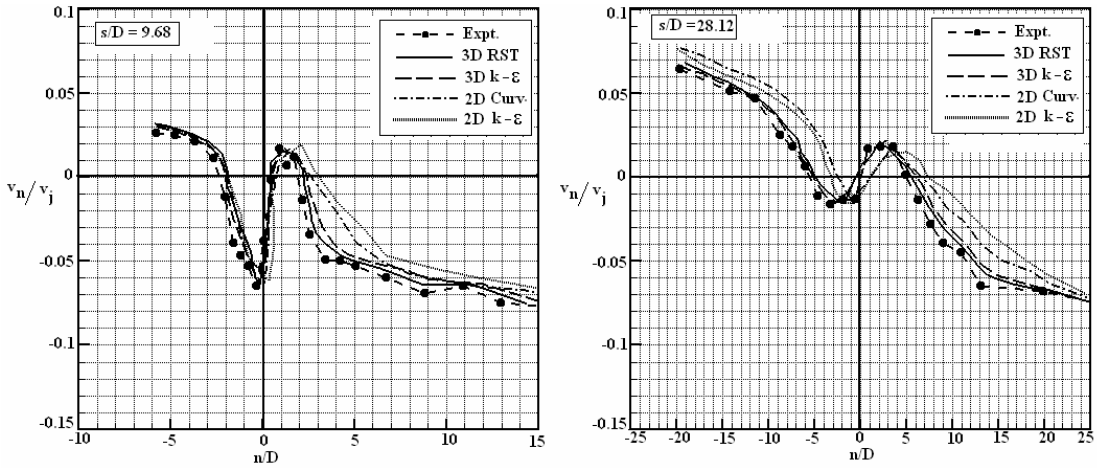

Fig. 5.100: Comparison of mean normal component velocity at jet central plane (z/D = 0) for R = 6, s/D = 9.68 and 28.12.

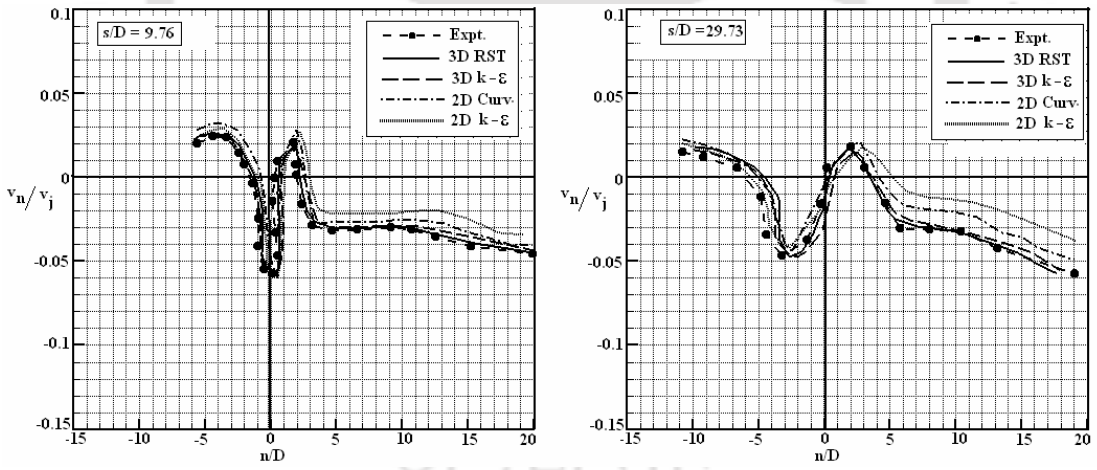

Fig. 5.101: Comparison of mean normal component velocity at jet central plane (z/D = 0) for R = 9, s/D = 9.76 and 29.73.

Comparisons of the normal component of the mean velocity (v_n/v_j) at the jet central plane (z/D = 0) is shown in Figs. 5.100 and 5.101 for R = 6 and 9 respectively. Due to unavailability of the entrainment and other secondary effects of the flow field, the 2D predictions show a higher spreading of the jet compared to the 3D predictions, thus producing poor agreement with the experimental data.

5.5 Conclusions

In this chapter the 3D flow field of a slightly heated rectangular jet discharged into a crossflow has been numerically investigated using the Reynolds stress transport (RST) model. The different terms of the Reynolds stress transport model are modelled based on the proposals in the literature that are suitable for the present flow configuration. The predicted flow properties by RST model and the standard k-ε model (described in Chapter 4) are compared with the experimental data. The predicted mean and turbulence properties such as velocity components and turbulence shear stress by both the models are shown to be in good agreement with the experimental data. The RST model shows some improvement especially in the reverse flow region but it does not show significant improvement compared to the standard k-ε model. The mean temperature distribution due to the strong convection effect of the jet is presented. The mean temperature field is governed by the mean velocity filed and the distribution of the temperature is controlled by the different vortices formed in the flow field. The temperature dispersions observed are consistent with similar results reported in the literature. The RST model produces reasonable agreement of the predicted temperature with the experimental data. RST model is also seen to capture two secondary vortices near the bottom wall at far downstream locations. The standard k-ε model failed to capture these two vortices.

Chapter 6

Conclusions and Scope for Future Work

6.1 Conclusions

The objectives of the present work were to (a) provide more detailed information about the flow characteristics of a heated rectangular jet discharged into a narrow channel crossflow with relatively high jet to crossflow velocity ratio than those obtained experimentally by Ramaprian and Haniu (1983) and Haniu and Ramaprian (1989) and (b) to assess the performance of different turbulence models in predicting the behaviour of this flow configuration. The investigation is carried out first for the 2D flow field and subsequently for the 3D flow field. In the 2D investigation, the computations are carried out using the standard k-ε model and the streamline curvature modification to the k-ε model. The physical effects of the streamline curvature on the flow field are studied and improvements over the standard k-ε model are commented upon. In the 3D investigation of the flow field, the standard k-ε model and the RST model are used. Computational tools in the form of two FORTRAN 77 computer codes based on the SIMPLE algorithm, finite volume and staggered grid arrangement are developed. The first code tackles the 2D problem using the standard k-ε model and its streamline curvature modification. The other code tackles the 3D problem through the standard k-ε model. In addition a commercial code FLUENT 6.2 is used to compute the 3D heated jets in crossflow using the RST model. The various terms of the Reynolds stress transport equations that need modelling are modelled based on the proposals in the literature that are suitable for the present flow configuration. The computations are performed in the Cartesian coordinates and results are presented to facilitate a good understanding of different aspects of the flow including those in the near-wall region. The results are then converted into those for an s-n coordinate system for the purpose of comparison with the experimental data of Ramaprian and Haniu (1983) and Haniu and Ramaprian (1989). Based on the work carried out in this thesis, the following conclusions and observations can be made

.

1. The 2D investigation of the flow field provides reasonably good information of the flow characteristics in the jet central plane. However, from the subsequent work in this thesis it is seen that the flow is 3D in nature with a plane of symmetry in the central vertical plane. Therefore, in those situations where smaller computational time gets priority over flow details and accuracy, a 2D investigation is definitely worth undertaking, as the results obtained for the jet central vertical plane are physically realistic.
2. The streamline curvature modification to the k-ε model produces somewhat improved results in the inner part of the jet and produces better agreement with the experimental data than those produced by the standard k-ε model. The maximum local improvement in some of the results by the curvature modification model over the standard k-ε model is observed to be about 20%. Thus the inclusions of the streamline curvature effect in the standard k-ε model for a 2D investigation to predict the flow field of a jet in crossflow is justified.
3. The curvature modification model works better in the case of the jet with R = 6 than that with R = 9 because of higher streamline curvature of the flow field in the former. Thus low values of the jet to crossflow velocity ratio, which entail higher curvature, are likely to find favour with the curvature modification model.
4. A look at the flow configuration suggests that the central vertical plane is likely to be a plane of symmetry. 3D computations carried out with both the standard k-ε model and RST model demonstrate that it is indeed so. This fact lends credibility to the computations using both the models suggesting that the other results are also physically meaningful. From this observation it may be concluded that for further studies, the computational time can be saved by considering only half of the flow field with symmetry boundary conditions.
5. In the case of 3D investigation the standard k-ε model performs well in reproducing many physical features that are similar to the results reported in the literature. The model also produces reasonably good agreement with the experimental data of Ramaprian and Haniu (1983) and Haniu and Ramaprian (1989).

6. The velocity ratio is found to affect the flow features such as the trajectory and the lateral spread of the jet and the low velocity region downstream of the jet. The turbulence properties such as the turbulence kinetic energy and shear stress are also affected by the value of the velocity ratio.
7. The formations of different types of vortices in the flow field are discussed. The present predictions capture well the steady structures of the wake vortices and counter-rotating vortex pair (CRVP). However, the structure of the horse-shoe vortices is captured weakly. The length scales of these vortices are significantly greater than those of eddies containing the turbulence energy and are therefore considered to be associated with the mean flow rather than the turbulence flow field. The velocity ratio is seen to affect the shape and sizes of these vortices. A high value of the velocity ratio is associated with the reduced size of the wake vortices and the reverse flow region downstream of the jet slot.
8. The RST model is used to predict the 3D flow field of a slightly heated jet in crossflow. The effect of the buoyancy in the flow field is negligible due to a small temperature difference so that the temperature is treated as a passive scalar and a good agreement with the experiments demonstrates the validity of this assumption.
9. The RST model shows some improvement in the predictions compared to the standard k-ε model especially in the reverse flow region. It also captures two secondary vortices at the bottom corners far downstream, whereas the standard k-ε model fails to do so. However it does not show significant overall improvement over the standard k-ε model.
10. The mean temperature field in the case of the heated jet appears to be closely linked to the mean velocity field and the distribution of the temperature is controlled by the different vortices formed in the flow field. The temperature dispersion observed in the present investigation is consistent with the similar results reported in the literature. The overall thermal characteristics obtained with the model are in reasonably good agreement with the experimental data reported in the literature.
11. The flow details in the main domain obviously result from the interaction between the jet ejected from the jet duct at the bottom wall and the cross-

stream. However, it is interesting to note that the flow in jet duct itself gets affected as a result of this interaction and the origin of the CRVP can be traced back to the jet duct itself. Needless to say, in the absence of the cross-stream, there will be no such vortical flow structures in the jet duct.

12. The present investigation establishes the three-dimensionality of the flow field. This is in some contrast to the observation of Ramaprian and Haniu (1983) and Haniu and Ramaprian (1989) who perhaps did not feel it necessary to carry out a detailed 3D experimental investigation. The results in the present work brings to light not only the various features in the jet-shear layer but also some interesting aspects of the flow in the neighbourhood including two hitherto unreported secondary vortices. Thus besides closely reproducing the experimental results of Ramaprian and Haniu (1983) and Haniu and Ramaprian (1989), the present investigation also provides a deeper insight into various features of this complex flow field that are absent in their reports. This suggests that a more detailed and careful 3D experimental investigation is perhaps in order to have a comprehensive picture of this complex and interesting flow field.
13. There are several factors that influenced the original aim of this work. First question that came to our mind was how good is a 2D numerical investigation at the central vertical plane? How does these results compare with the experimental investigations? Another question was: is it possible to obtain meaningful 3D details of the flow field even though there are no experimental results to compare them with? To find an answer to the second question a 3D code had been carefully developed and validated to ensure that when used to compute unknown situations, the results will enjoy some scientific prestige. To eliminate the possibility of the deficiency of a model (standard k-ε) which may fail to resolve some of the flow features another more sophisticated model (RST model) incorporated in the commercial code FLUENT was used. As the results of both the models do not contradict each other and agree to a great extent, the results produced may be considered to be physically meaningful. Thus it can be said that both of our original aims have been fulfilled to a large extent during the course of this work.

6.2 Scope for Future Work

The present study opens some interesting possibilities for further investigations. Some recommendations for future work are presented here.

1. To examine the accuracy and physical validity of the present numerical results a careful series of experiments can be carried out. The experimental facilities should contain more accurate flow measuring techniques such as the particle image velocimetry (PIV) than those used by Ramaprian and Haniu (1983) and Haniu and Ramaprian (1989). The measurement should be made across all the spanwise planes and should study different vortical structures in the flow field.
2. The present study can be extended to investigate the effects of various factors such as increasing or decreasing the jet slot size and its aspect ratio, varying the sidewall distances and for smaller velocity ratios such as R = 0.5, 1, 2, etc. These parametric studies may lead to the formation of functional equations relating those parameters with the jet and crossflow behaviour such as the jet trajectory, temperature trajectory, etc.
3. Further studies with the present problem can be made by incorporating different orientations to the jet slot as performed by Zhang (2000). The problem can be investigated by injecting the jet at different angles to the vertical axis. Moreover the investigation can also be performed for different skew angles of the crossflow stream.
4. Finally the present flow configuration can be investigated by considering an unsteady flow field. The study can be performed either by using unsteady RANS (URANS) model or by using more advanced turbulence models such as LES or DNS. These models can give an unsteady picture of the flow field which would be interesting phenomena to be observed and important for many practical implications.

Appendix

Transformation of Variables

Measured Mean Variable

In the present work the predicted values of the mean velocity components of turbulent rectangular jets in crossflow along the *x*- and *y*- directions are compared with the experimental data of Ramaprian and Haniu (1983) and Haniu and Ramaprian (1989). They have reported the experimental observations of turbulent plane jets in crossflow with $R = 6$ and 9 in both tabular and graphical forms in the *s*-*n* coordinate system (*s*- denotes the streamwise direction and *n*- normal to it, Fig. 3.1). For a certain value of *R* the experimental data is reported for various *s/D* locations corresponding to different *n/D* values together with the inclination (θ) of the jet trajectory with the *x*-axis.

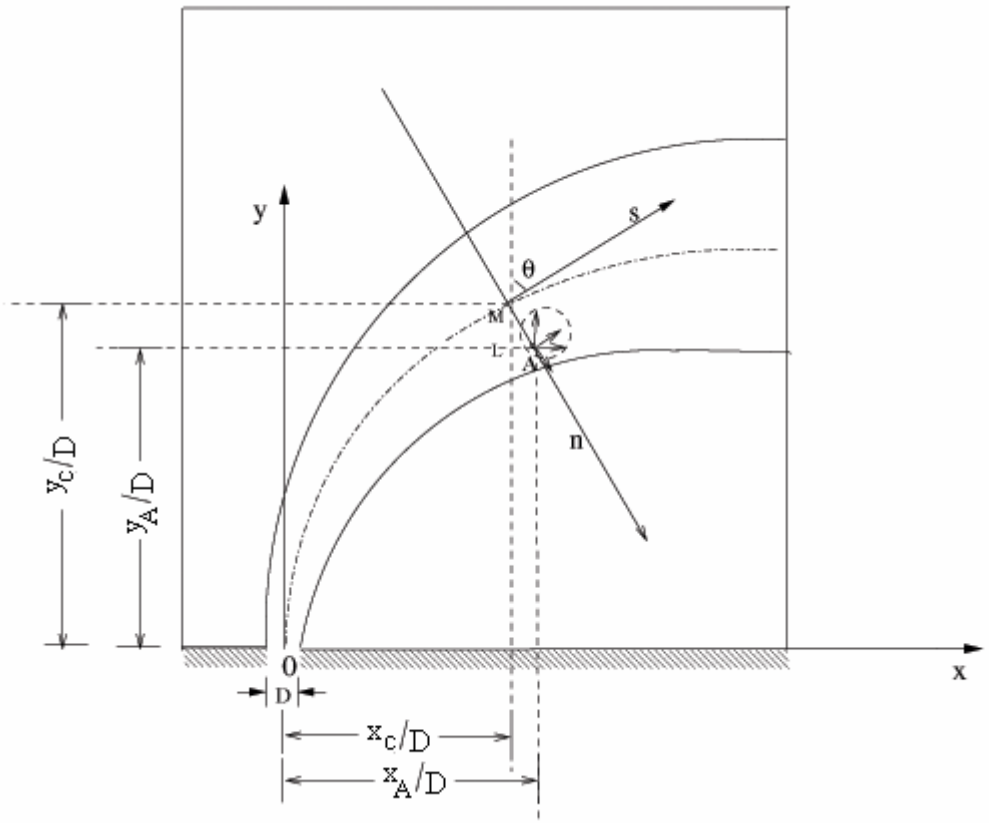

Fig. A.1: *x*-*y* and *s*-*n* coordinate systems in the domain of turbulent rectangular jet in crossflow.

The *x*- and *y*-coordinates of a point along the streamwise direction in the s-*n* coordinate system (*s/D, 0*), denoted by x_c/D and y_c/D, are also provided by Ramaprian and Haniu (1983) (Fig.A.1). It should be noted that the location of the maximum velocity and the direction of the tangent to the jet trajectory at any *s/D* location was obtained graphically by Ramaprian and Haniu (1983) from their mean flow data.

.

One can calculate the *x*- and *y*- components of the mean velocity, *u* and *v* respectively, at any given point A on the *n*- axis for a certain `*s*' location from the values of $u_s$ and $v_n$ and inclination of the jet trajectory ($\theta$). The point `A' shown in Fig. A.1, is encircled and the encircled area is shown enlarged in Fig. A.2. The following relations are used for the calculation:

$$u = u_s \sin\theta + v_n \cos\theta \qquad \text{(A.1)}$$

$$v = u_s \cos\theta - v_n \sin\theta \qquad \text{(A.2)}$$

where u_s and v_n are the measured mean velocity components along the *s*- and *n*-coordinates, respectively. In a similar way the measured *rms* values of the velocity fluctuations can be calculated in the rectangular coordinate system.

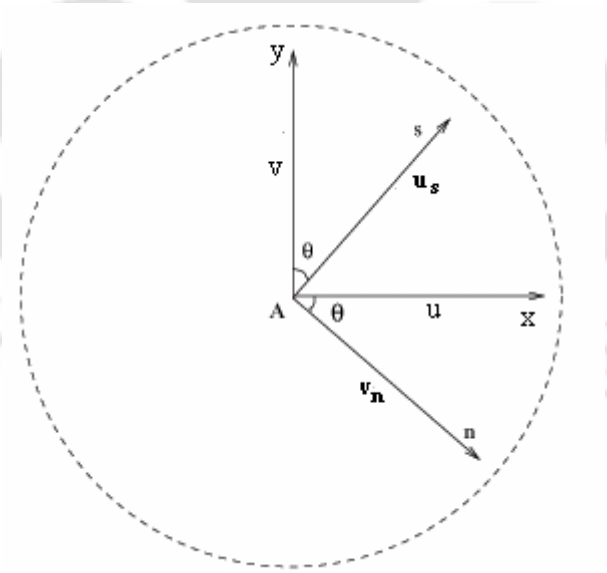

Fig. A.2: Enlarged view of the encircled region of `A'

Calculation of *x-y* Coordinates of A

The location of any point `A' on the *n*-axis corresponding to a certain *s/D* location can be calculated using the following relations:

$$x_A / D = x_c / D + (n / D)\cos\theta \qquad \text{(A.3)}$$

$$y_A / D = y_c / D - (n / D)\sin\theta \qquad \text{(A.4)}$$

Thus one can find the corresponding x and y coordinates of any point whose s-n coordinates are given.

References

1 Abhari, R.S., Guenette, G.R., Epstein, A.H., and Giles, M. B. 1991, *Comparison of time-resolved turbine rotor blade heat transfer measurements and numerical calculations*, ASME Paper No. 91-GT-268.

2 Abramovich G.N. 1963, *The theory of turbulent jets*, MIT press, Cambridge.

3 Acharya, S., Tyagi, M. and Hoda, A. 2001, *Flow and heat transfer predictions for film cooling, heat transfer in gas turbine systems*, Ann. N.Y. Acad. Sciences 934, 110 -125.

4 Ajersch, P., Ketler, S., Zhou, J.M., Gartshore, I. and Salcudean, M. 1997, *Multiple jets in cross-flow: measurements and numerical simulations,* ASME J. Turbomach. 119, 330-342.

5 Al-Sanea, S. 1992, *A numerical study of the flow and heat transfer characteristics of an impinging laminar slot jet including crossflow effects*, Int. J. Heat Mass Transfer 35, 2501–2513.

6 Alvarez, J., Jones, W.P. and Seoud, R., 1993, *Predictions of momentum and scalar fields in a jet in cross flow using first and second order turbulence closures*, In Computational and Experiment Assessment of Jets in Cross Flow, CP-534, AGARD.

7 Amer, A.A., Jubran, B.A. and Hamdan, M.A. 1992, *Comparison of different two-equation turbulence models for prediction of film cooling from two Rows of holes*, Numer. Heat Transfer A 21, 143-162.

8 Andreopoulos, J. 1982, *Measurements in a jet-pipe flow issuing perpendicularly into a cross stream*, ASME J. Fluids Engng. 104, 493–499.

9 Andreopoulos, J. and Rodi, W. 1984, *Experimental investigation of jets in a cross-flow,* J. Fluid Mech. 138, 93-127.

10 Andreopoulos, J. 1985, *On the structure of jets in a crossflow,* J. Fluid Mech. 157, 163- 197.

11 Atkinson, K.N., Khan, Z.A. and Whitelaw, J.H. 1982, *Experimental investigation of opposed jets discharging normally into a cross-stream*. J. Fluid Mech. 115, 493-504.

12 Baker, C.J. 1979, *The laminar horseshoe vortex*, J. Fluid Mech. 95, 347-367.

13 Baldauf, S., Schulz, A. and Wittig, S. 1999, *High resolution measurements of local effectiveness by discrete hole film cooling,* ASME Paper No. 99-GT-46.

14 Baldwin, B.S. and Lomax, H. 1978, *Thin layer approximation and algebraic model for separated turbulent flows*, AIAA Paper 78-0257.

15 Barata, J.M.M., Durao, D.F.G, Heitor, M.V. and McGuirk, J.J. 1991, *Impingement of single and twin turbulent jets through a crossflow*, AIAA J. 29, 595–602.

16 Barata, J.M.M. 1996, *Fountain flows produced by multiple impinging jets in a crossflow*, AIAA J. 34, 2523– 2530.

17 Bergeles, G., Gosman, A.D. and Launder, B.E. 1976, *The near-field character of a jet discharged normal to a main stream*, ASME J. Heat Transfer, 373–379.

18 Berhe, M.K. and Patankar, S.V. 1996, *A numerical study of discrete-hole film cooling*, ASME 96-WA/HT-8.

19 Berhe, M. K. and Patankar, S.V. 1999, Investigation of discrete-hole film cooling parameters using curved-plate models, ASME J. Turbomach. 121, 792-803.

20 Biswas, G. and Eswaran, V. (editors) 2002, *Turbulent Flows Fundamentals, Experiments and Modeling*, Narosa Publ. House, India.

21 Blanchard, J.N., Brunet, Y. and Merlen, A. 1999, *Influence of a counter rotating vortex pair on the stability of a jet in a cross flow: an experimental study by flow visualizations*, Exp. Fluids 26, 63-74.

22 Bouchez, J.P. and Goldstein, R.J. 1975, *Impingement cooling from a circular jet in a cross flow,* Int. J. Heat Mass Transfer 18, 719–730.

23 Bradshaw, P. 1969, *The effects of streamline curvature on turbulent flow* AGARDograph, no. 169.

24 Brittingham, R.A. and Leylek, J.H. 2000, *A detailed analysis of film-cooling physics: Part IV—compound-angle injection with shaped holes*, ASME J. Turbomach. 122, 133–145.

25 Broadwell, J.E. and Breidenthal, R.E. 1984, *Structure and mixing of a transverse jet in incompressible flow*, J. Fluid Mech. 148, 405–412.

26 Burd, S.W., Kaszeta, R.W. and Simon, T.W. 1996, *Measurements in film cooling flows: hole L/D and turbulence intensity effects*, ASME Paper No. 96-WA/HT-7.

27 Burd, S.W. and Simon, T.W. 1998, *Turbulence spectra and length scales measured in film coolant flows emerging from discrete holes*, ASME Paper No. 98-GT-190.

28 Callaghane, E. and Ruggerir, S. 1948, *Investigation of the penetration of an air jet directed perpendicularly to an air stream*, NACA Tech. Note, No. 1615.

29 Callaghane, E. and Ruggerir, S. 1951, *A general correlation of temperature profiles downstream of a heated-air jet directed perpendicularly to an air stream,* NACA Tech. Note, No. 2466.

30 Camussi, R., Guj, G. and Stella, A. 2002, *Experimental study of a jet in a crossflow at very low Reynolds number*, J. Fluid Mech. 545, 113-144.

31 Catalano, G.D., Chang, K.S. and Mathis, J.A. 1989, *Investigation of turbulent jets impingement in a confined crossflow*, AIAA J. 27, 1530-1535.

32 Cebeci, T. and Smith, A. M. O. 1974, *Analysis of turbulent boundary layers*, Academic Press, New York.

33 Chang, Y.R. and Chen, K.S. 1994, *Measurement of opposing heated line jets discharged at an angle to a confined crossflow*, Int. J. Heat Mass Transfer 37, 2935- 2946.

34 Chang, Y.R. and Chen, K.S. 1995, *Prediction of opposing turbulent line jets discharged laterally into a confined crossflow*, Int. J. Heat Mass Transfer 9, 1693-1703.

35 Chassing, P., George, J., Claria, A. and Sananes, F. 1974, *Physical characteristics of subsonic jets in a cross-stream,* J. Fluid Mech. 62, 41–64.

36 Chen, H.C. 1995, *Submarine Flows studied by second moment closure*, J. Fluid Mech. 121, 1136-1146.

37 Chen, K.S. and Hwang, J.Y. 1991, *Experimental study on the mixing of one and dual-line heated jets with a cold crossflow in a confined channel*, AIAA J. 293, 353-360.

38 Cheng, G.C. and Farokhi, S. 1992, *On turbulent flows dominated by curvature effects,* ASME J. Fluids Engng. 114, 52-57.

39 Chien, J.C., and Schetz, Y.A. 1975, *Numerical solution of the three-dimensional Navier-Stokes equations with applications to channel flows and a buoyant jet in a cross flow*, ASME J. Appl. Mech. 42, 575-579.

40 Chiu, S.H., Roth, K.R., Margason, R. J. and Tso, J. 1993, *A numerical investigation of a subsonic jet in a cross-flow,* AIAA Paper 93-0870, 1993.

41 Christopher, D., Seybert, J. and Evans, W. 2005, *PIV measurements of velocity of water in the presence of ice and comparison with calculated values,* Int. J. Heat Mass Transfer 48, 67-73.

42 Chuang, S.H., Chen, M.H., Lii, S.W. and Tai, F.M. 1992, *Numerical simulation of twin-jet impingement on a flat plate coupled with cross-flow*, Int. J. Numer. Methods Fluids 14, 459–475.

43 Claus, R.W. and Vanka, S.P. 1990, *Multigrid calculations of a jet in cross flow*, AIAA Paper No. 90-0444.

44 Coelho, S.L.V. and Hunt, J.C.R. 1989, *The dynamics of the near field of strong jets in crossflows,* J. Fluid Mech. 200, 95–120.

45 Cortelezzi, L and Karagozian, A.R. 2001, *On the formation of the counter-rotating vortex pair in transverse jets,* J. Fluid Mech. 446, 347–373.

46 Crabb, D., Duarao, D.F.G. and Whitelaw, J.H. 1981, *A round jet normal to a crossflow*, ASME J. Fluids Engng. 103, 142-153.

47 Cusano, D.M. and Plesniak, M.W. 1999, *Asymmetry in a confined rectangular jet in a crossflow*, Proc. Of Turbulence and Shear Flow Phenomena, Santa Barbara, CA, Paper No. 1-242.

48 Dahlstrom, S. 2003, *Large eddy simulation of the flow around a high lifts airfoil,* Ph.D. thesis, Chalmers University of Technology, Goteborg, Sweden.

49 Daly, B. J. and Harlow, F.H. 1970, *Transport equations in turbulence,* Phys. Fluids 13, 2634-2649.

50 Demuren, A.O. 1983, *Numerical calculations of steady three-dimensional turbulent jets in cross flow*, Comput. Meth. Appl. Mech. Engng. 37, 309-328.

51 Demuren, A.O. 1986, *Modeling turbulent jets in crossflow.* N. P. Cheremisinoff (ed.), Encyclopedia of Fluid Mech., Chap. 17, Vol. 2, Gulf Publishing Company, Houston, TX.

52 Demuren, D.K., Rodi, W. and Schonung, B. 1986, *Systematic study of film cooling with a three dimensional calculation procedure*, ASME J. Turbomach. 108, 124–130.

53 Demuren, A.O. 1993, *Characteristics of three-dimensional turbulent jets in crossflow*, Int. J. Engng. Sci. 31, 899-913.

54 Eiff, O.S., Kawall, J.G. and Keffer, J.F. 1995, *Lock-in vortices in the wake of an elevated round turbulent jet in a crossflow*, Exp. Fluids 19, 203-213.

55 Eiff, O.S. and Keffer, J.F. 1997, *On the structures in the near wake region of an elevated turbulent jet in a crossflow*, J. Fluid Mech. 333, 161-195.

56 Fan, L.N. 1967, *Turbulent buoyant jets into stratified or flowing ambient fluids,* Report-K-H-R-15, Keck Lab. Hydr. Water Res., Cal. Tech, CA, USA.

57 Fearn, R. and Weston, R. P. 1974, *Vorticity associated with a jet in a cross flow*, AIAA J. 12, 1666–1671.

58 Findlay, M.J., He, P., Salcudean, M. and Gartshore, I.S. 1996, *A row of streamwise inclined jets in crossflow: measurement and calculations,* ASME-96-GT-167.

59 FLUENT 6.2, Users Guide, 2005, Vol. 2, 10.1-10.82.

60 Fric, T.F. 1990, *Structure in the near field of the transverse jet,* Ph.D. Thesis, California Inst. Tech., Pasadena, CA, USA.

61 Fric, T.F. and Roshko, A. 1994, *Vortical structures in the wake of a transverse jet*, J. Fluid Mech. 279, 1-47.

62 Fu, S., Launder, B.E. and Leschziner, M.A. 1987, *Modeling strongly swirling recirculating jet flow with Reynolds-stress transport closures*, In Sixth Symposium on Turbulent Shear Flows, Toulouse, France.

63 Garg, V.K. and Gaugler, R.E. 1997a, *Effect of coolant temperature and mass flow on film cooling of turbine blade,* Int. J. Heat Mass Transfer 40, 435–445.

64 Garg, V.K. and Gaugler, R.E. 1997b, *Effect of velocity and temperature distribution at the hole exit on film cooling of turbine blades,* ASME J. of Turbomach. 119, 343-351.

65 Garg, V.K. 1999, *Heat transfer on a film-cooled rotating blade using different turbulence models,* Int. J. Heat Mass Transfer. 42, 789-802.

66 Garg, V. K. and Rigby, D. L. 1999, *Heat transfer on a film-cooled blade – effect of hole physics*, Int. J. Heat Fluid Flow 20, 10-25.

67 Garimella, S.V. and Schroeder, V.P. 2001, *Local heat transfer distributions in confined multiple air jet impingements,* ASME J. Electron. Packag. 123, 165–172.

68 Gibson, M.M. and Launder, B.E. 1978, *Ground effects on pressure fluctuations in the atmospheric boundary layer,* J. Fluid Mech. 86, 491-511.

69 Goldstein, R.J. and Behbahani, A.I. 1982, *Impingement of a circular jet with and without crossflow,* Int. J. Heat Mass Transfer 25, 1377–1382.

70 Gordier, R.L. 1969, *Studies on fluid jets discharging normally into moving liquid,* St. Anthony Hydraulics Lab, Uni. Minneapolis, Paper 28-B.

71 Gregoric, M., L.R. Davis and Bushnell, D.J. 1982, *An experimental investigation of merging buoyant jets in a crossflow,* ASME J. Heat Transfer 104, 236–240.

72 Grinstein, F., Gutmark, E. and Parr, T. 1995, *Near-field dynamics of subsonic, free square jets. A computational and experimental study*, Phys. Fluids 7, 1483–1497.

73 Gritsch, M., Schulz, A. and Wittig, S. 1997, *Adiabatic wall effectiveness measurements of film-cooling holes with expanded exits*, ASME Paper 97-GT-164.

74 Guo, X., Schro¨der, W. and Meinke, M. 2006, *Large-eddy simulations of film cooling flows*, Comp. Fluids 35, 587–606.

75 Hahn, S. and Choi, H. 1997, *Unsteady simulation of jets in a cross flow*, J. Comput. Phys. 134, 342-356.

76 Hale, C.A., Plesniak, M.W. and Ramadhyani, S. 2000, *Structural features and surface heat transfer associated with a row of short-hole jets in cross-flow*, Int. J. Heat Fluid Flow 21, 542-553.

77 Haniu, H and Ramaprian, B.R. 1989, *Studies on two-dimensional curved nonbuoyant jets in cross flow*, ASME J. Fluids Engng. 111, 78-86.

78 Hasselbrink, E. F and Mungal, M. G. 2001, *Transverse jets and jet flames. Part 1. Scaling laws for strong transverse jets*, J. Fluid Mech. 443, 1–25.

79 Haven, B.A. and Kurosaka, M. 1996, *The effect of hole geometry on lift-off behaviour of coolant jets*, AIAA-96-0618.

80 Haven, B.A. and Kurosaka, M. 1997, *Kidney and anti-kidney vortices in crossflow jets,* J. Fluid Mech. 352, 27-64.

81 Hinze. J.O. 1975, *Turbulence,* McGraw-Hill Publishing Co. 2nd edition, New York, USA.

82 Hoda, A., Acharya, S. and Tyagi, M. 2000, *Reynolds stress transport model predictions and large eddy simulations for film coolant jet in crossflow*, ASME-Intl. Gas Turbine Conference, Munich, Paper No 2000-GT-0249.

83 Hoda, A. and Acharya, S. 2000, *Predictions of a film coolant jet in crossflow with*

different turbulence models, ASME J. Turbomach. 122, 558-569.

84 Holdemann, J.D. and Walker, R.E.1977, *Mixing of a row of jets with a combined crossflow*, AIAA J. 15, 243–249.

85 Holdeman, J.D. and Srinivasan, R. 1984, *On modeling dilution jet flow fields*, NASA TM-83708, Cleveland.

86 Holdeman, J.D. 1993, *Mixing of multiple jets with a confined subsonic crossflow*, Energy Combus. Sci. 19, 31-70.

87 Holloway, A.G. L. and Tavoularis, S. 1992, *The effects of curvature on sheared turbulence,* J. Fluid Mech. 237, 569-603.

88 Humber, A.J., Grandmaison, E.W. and Pollard, A. 1993, *Mixing between a sharp-edged rectangular jet and transverse cross flow*, Int. J. Heat Mass Transfer 36, 4307-4316.

89 Hwang, R.R. and Chiang, T.P. 1995, *Numerical simulation of vertical forced plume in a crossflow of stably stratified fluid*, ASME J. Fluids Engng. 117, 696-705.

90 Hyams, D.G. and Leylek J.H. 2000, *A detailed analysis of film-cooling physics: Part III—streamwise injection with shaped holes*, ASME J. Turbomach. 122, 122–132.

91 Ince, N.Z. and Leschziner, M.A. 1990, *Calculation of single and multiple jets in crossflow with and without impingement using second-moment closure*, Engng. Turb. Mod. Exps. (Elsevier), 155-164.

92 Ince, N.Z. and Leschziner, M.A, 1993, *Computation of three-dimensional jets in cross-flow with and without impingement using Reynolds-stress transport closure,* AGARD Sym. Computational and Experimental Assessment of Jets in Crossflow, Paper 23.

93 Isaac, K.M. and Jakubowski, A.K. 1985, *Experimental study of the interaction of multiple jets and a crossflow,* AIAA J. 23, 1679–1683.

94 Jansson, L.S. and Davidson, L. 1996, *Numerical study of effusion cooling in a double-row discrete-hole configuration using a low-Re Reynolds stress transport model,* Engng. Turb. Mod. Exps. (Elsevier), 731-740.

95 Johnston, J.P., Mosier, B.P. and Khan, Z.U. 2002, *Vortex generating jets effects of jet-hole inlet geometry,* Int. J. Heat Fluid Flow 23, 744–749.

96 Jones, W.P. and Wille, M. 1996, *Large-eddy simulation of a plane jet in a cross-*

flow, Int. J. Heat Fluid Flow 17, 296-306.

97 Jordinson, R. 1956, *Flow in a jet directed normal to the wind*, British Aero. Res. Concil, R and M 3074.

98 Jovanovic M.B., de Lange, H.C. and van Steenhoven A.A. 2006, *Influence of hole imperfection on jet cross flow interaction*, Int. J. Heat Fluid Flow 27, 42–53.

99 Kaiser, A.S., Zamora, B. and Viedma A. 2004, *Correlation for Nusselt number in natural convection in vertical convergent channels at uniform wall temperature by a numerical investigation,* Int. J. Heat Fluid Flow 25, 671-682.

100 Kalita, K., Dewan, A. and Dass, A.K. 2002, *Prediction of turbulent plane jet in crossflow*, Numer. Heat Transfer A 41, 1-12.

101 Kamotani,Y. and Greber, I. 1971, *Experiments on turbulent jet in a crossflow,* NASA CR-72893.

102 Kamotani,Y. and Greber, I. 1972, *Experiments on turbulent jet in a crossflow*, AIAA J. 10, 1425–1429.

103 Kaplan, R.E. 1964, *The stability of laminar incompressible boundary-layers in the presence of compliant boundaries,* Technical report ASLR-TR-166-1, Aeroelastic and structures research lab., M.I.T., Cambridge.

104 Karagozian, A.R. Nguyen, T.T. and Kim, C.N. 1986, *Vortex modeling of single and multiple dilution jet mixing in a crossflow,* J. Prop. Power 2, 354–360.

105 Karagozian, A.R. 1986, *An analytical model for the vorticity associated with a transverse jet,* AIAA J. 24, 429-436.

106 Kassimatis, P.G., Bergeles, G.C., Jones, T.V. and Chew, J.W. 2000, *Numerical investigation of the aerodynamics of the near-slot film cooling,* Int. J. Numer. Methods Fluids 32, 97-117.

107 Kavsaoglu M.S., Schetz, J.A. and Jakubowski, A.K. 1989, *Rectangular jets in a crossflow*, J. Aircraft 26, 793-804.

108 Keffer, J. F. and Baines, W. D. 1963, *The round turbulent jet in a cross wind*, J. Fluid Mech. 15, 481–496.

109 Keimasi, R. and Rahni, T. 2001, *Numerical simulation of jets in a crossflow using different turbulence models,* AIAA J. 39, 2268-2277.

110 Kelso, R. M. and Smits, A. J. 1995, *Horseshoe vortex systems resulting from the interaction between a laminar boundary layer and a transverse jet,* Phys. Fluids 7, 153–158.

111 Kelso, R.M., Lim, T.T. and Perry, A.E. 1996, *An experimental study of round jets in crossflow,* J. Fluid Mech. 306, 111-144.

112 Kim, J., Moin, P. and Moser, R. 1987, *Turbulence statistics in fully developed channel flow at low Reynolds number*, J. Fluid Mech. 177, 133-166.

113 Kim, S.W. and Benson, T.J. 1993, *Fluid flow of a row of jets in crossflow -a numerical study*, AIAA J. 31, 806–811.

114 Kohli, A. and Bogard, D.G. 1995, *Adiabatic effectiveness, thermal fields, and velocity fields for film cooling with large angle injection*, ASME Paper No. 95-GT-219.

115 Kohli, A. and Thole, K.A. 1998, *Entrance effects on diffused film cooling holes,* ASME Paper No. 98-GT-402.

116 Kolar, V., Takao, H., Todoroki, T., Savory, E., Okamoto, S. and Toy, N. 2003, *Vorticity transport within twin jets in crossflow*, Exp. Therm. Fluid Sci. 27, 563–571.

117 Krothapalli, A., Lourenco, L. and Buchlin, J. M. 1990, *Separated flow upstream of a jet in a crossflow*, AIAA J. 28, 414–420.

118 Kuzo, D.M. 1995, *An experimental study of the turbulent transverse jet*, PhD thesis, California Institute of Technology, USA.

119 Laccarino, G. 2001, *Predictions of a turbulent separated flow using commercial CFD codes*, ASME J. Fluids Engng. 123, 819-828.

120 Lakehal, D., Theodoridis, G.S. and Rodi, W. 1998, *Computation of film cooling of a flat plate by lateral injection from a row of holes,* Int. J. Heat Fluid Flow 19, 418-430.

121 Lam, C.K.G. and Bremhorst, K.A. 1981, *Modified form of the k-ε Model for Predicting Wall Turbulence*, ASME J. Fluids Engng.103, 456-460.

122 Launder B.E. and Spalding D.B. 1972, *Lectures in mathematical models of turbulence,* Academic Press, London.

123 Launder, B.E. and Spalding, D.B. 1974, *The numerical prediction of turbulent flow,* Comp. Methods Appl. Mech. Engng. 3, 269-289.

124 Launder, B.E. 1989a, *Second-moment closure and its use in modeling turbulent industrial flows*, Int. J. Numer. Methods Fluids 9, 963-985.

125 Launder, B.E. 1989b, *Second-moment closure: present and future*, Int. J. Heat Fluid Flow 10, 282-300.

126 Lemmon, C. A., Kohli, A. and Thole, K. A. 1999, *Formation of counter-rotating vortices in film-cooling flows*, ASME Paper No. 99-GT-161.

127 Leschziner, M.A. and Rodi, W. 1981, *Calculation of annular and twin parallel jets using various descretization schemes and turbulence-model variations*, ASME J. Fluids Engng. 103, 352-360.

128 Leylek, J.H. and Zerkle, R.D. 1994, *Discrete-jet- film cooling: A comparison of computational results with the experiemnets*, ASME J. Turbomach. 113, 358-368.

129 Lien, F.S. and Leschziner, M.A. 1994, *Assessment of turbulent transport models including non-linear RNG eddy-viscosity formulation and second moment closure*, Comp. Fluids 23, 983-1004.

130 Lim, T.T., Kelso, R.M. and Perry, A.E. 1992, *A study of a round jet in cross-flow at different velocity ratios*, Proc. 11th Australian Fluid Mech. Conf. University of Tasmania, Hobart, Australia.

131 Lim, T.T, New, T.H. and Luo, S.C. 2001, *On the development of large-scale structures of a jet normal to a cross flow,* Phys. Fluids 13, 770–775.

132 Liscinsky, D.S., True, B. and Holdman, J.D. 1996, *Crossflow mixing of noncircular jets,* J. Prop. Power 12, 225-230.

133 Majander, P. and Siikonen, T. 2006, *Large-eddy simulation of a round jet in a cross-flow*, Int. J. Heat Fluid Flow 27, 402–415.

134 Makihata, T. and Miyai, Y. 1979, *Trajectories of single and double jets injected into a crossflow of arbitrary velocity distribution*, ASME J. Fluids Engng. 101, 217–223.

135 Margason, R.J. 1993, *Fifty years of jet in cross-flow research*, AGARD - CP 534.

136 McGovern, K.T. and Leylek, J.H. 2000, *A detailed analysis of film-cooling physics: Part II—compound-angle injection with cylindrical holes*, ASME J. Turbomach. 122, 113–21.

137 Mcmahon, H. M., Hestert, D.D. and Palfery, J.G. 1971, *Vortex shedding from a turbulent jet in a cross-wind,* J. Fluid Mech. 48, 73-80.

138 Metzger, D.E. and Korstad, R.J. 1972, *Effects of crossflow on impingement heat transfer*, ASME J. Engng. Power 94, 35–42.

139 Morton, B.R. and Ibbetson, A. 1996, *Jets deflected in a crossflow,* Exp. Therm. Fluid Sci. 12, 112–133.

140 Moser, D., Robert, D. and Moin, P. 1986, *The effects of curvature in wall-*

bounded turbulent flows, J. Fluid Mech. 175, 479-510.

141 Moussa, Z.M., Trischka, W.J. and Eskinazi, S. 1977, *The near field of the mixing of a round jet in cross-stream,* J. Fluid Mech. 80, 49–80.

142 Muppidi, S. and Mahesh, K. 2005, *Study of trajectories of jets in crossflow using direct numerical simulations*, J. Fluid. Mech. 530, 81–100.

143 Muppidi, S. and Mahesh, K. 2007, *Direct numerical simulation of round turbulent jets in crossflow,* J. Fluid Mech. 574, 59-84.

144 Nakabe, K., Suzuki, K., Inaoka, K., Higashio, A., Acton, J.S. and Chen, W. 1998, *Generation of longitudinal vortices in internal flows with an inclined impinging jet and enhancement of target plate heat transfer*, Int. J. Heat Fluid Flow 19, 573–581.

145 Narayanan, S., Barooah, P. and Cohen, J. M. 2003, *Dynamics and control of an isolated jet in crossflow*, AIAA J. 41, 2316-2330.

146 New T.H, Lim, T.T. and Luo, S.C. 2003, *Elliptic jets in cross-flow*, J. Fluid Mech. 494, 119–140.

147 New T.H, Lim T.T. and Luo, S.C. 2004, *A flow field study of an elliptic jet in cross-flow using DPIV technique*, Exp. Fluids 36, 604–618.

148 Niederhaus, C. E., Champagne, F. H. and Jacobs, J. W. 1997, *Scalar transport in a swirling transverse jet,* AIAA J. 35, 1697–1704.

149 Nishiyama, H., Ota, T., Hamada, M. and Takahashi, Y. 1993, *Temperature fluctuations in a slightly heated slot jet issuing into a crossflow*, Exp. Therm. Fluid Sci. 6, 252-262.

150 Patankar, S.V., Basu, D.K. and Alpay, S.A. 1977, *Prediction of three-dimensional velocity field of a deflected turbulent jet*, ASME J. Fluids Engng. 99, 758-762.

151 Patankar, S.V. 1980, *Numerical heat transfer and fluid flow,* Hemisphere Publishing Corporation, Washington, New York, London.

152 Patel, M.K. and Markatos, N.C. 1986, *An evaluation of eight discretisation schemes for two-dimensional convection-diffusion equation*, Int. J. Numer. Methods Fluids 6, 129-154.

153 Pathak, M., Dewan, A. and Dass, A.K. 2005, *An assessment of streamline curvature effects on the mixing region of a turbulent plane jet in crossflow,* App. Math. Modeling 29, 711-725.

154 Pathak, M., Dewan A. and Dass, A.K. 2006, *Computational prediction of a slightly heated turbulent rectangular jet discharged into a narrow channel cross-flow using two different turbulence models,* Int. J. Heat Mass Transfer 49, 3914-3928.

155 Pathak, M., Dewan A. and Dass, A.K., 2007, *Effect of streamline curvature on flow field of a turbulent plane jet in cross flow*, Mech. Res. Comm. 34, 241-248.

156 Peterson, S.D, and Plesniak, M.W. 2002, *Short-hole jet-in-crossflow velocity field and its relationship to film-cooling performance*, Exp. Fluids 33,889–898.

157 Peterson, S.D. and Plesniak, M.W. 2004, *Evolution of jets emanating from short holes into crossflow*, J. Fluid Mech. 503, 57–91.

158 Pietrzyk, J.R., Bogard, D.G. and Crawford, M.E. 1988, *Hydrodynamic measurements of jets in crossflow for gas turbine film cooling applications*, ASME Paper No. 88-GT-194.

159 Pietrzyk, J.R., Bogard, D.G. and Crawford, M.E. 1989, *Hydrodynamic measurements of jets in crossflow for gas turbine film cooling applications*. ASME J. Turbomach. 111, 139-145.

160 Piquet, J. 1999, *Turbulent flows: models and Physics*, Spring Verlag, Berlin.

161 Platten, J.L. and Keffer, J.F. 1968, *Entrainment in deflected axi-symmetric jets at various angles to the stream,* Technical Report UTME, TP-6808, University of Toronto, Canada.

162 Plesniak, M.W. and Cusano, D.M. 2005, *Scalar mixing in a confined rectangular jet in crossflow,* J. Fluid Mech. 524, 1-45.

163 Pratte, B. D. and Baines, W. D. 1967, *Profiles of the round turbulent jet in a cross flow*. J. Hydraul. Div., ASCE 92, 53–64.

164 Rajaratnam, N. and Gangadharaiah T. 1981, *Scales for circular jets in cross flow*, ASCE J. Hydraul. Div, HY4, 107:487-500.

165 Ramaprian, B.R. and Haniu. H. 1983, *Turbulence measurement in plane jets and plumes in cross flow*. Technical Report No. 266, IIHR, University of Iowa, Iowa City, IA, USA.

166 Reynolds, O. 1895, *On the dynamical theory of incompressible viscous fluids and the determination of the criterion*, Ph. Trans. Royal Soc. London, Series A, 186:123.

167 Rivero, A., Ferre J.A. and Giral,. F. 2001, *Organized motions in a jet in crossflow*

J. Fluid Mech. 444, 117–149.

168 Rodi, W. 1976, *A new algebraic relation for calculating the Reynolds stresses*, Zeitschrift fur Angewandte Mathematik and Mechanik, 56, T219-T221.

169 Rudman M. 1996, *Simulation of the near field of a jet in a cross flow*, Exp. Therm. Fluid Sci. 12, 134-141.

170 Ruggeri R.S., Callaghan, E.E., Bowden, D.T. 1950, *Penetration of air jets issuing from circular, square, and elliptical orifices directed perpendicularly to an air stream*, NACA Tech. Note no-2019.

171 Ruggeri, R.S. 1952, *General correlation of temperature profiles downstream of a heated air jet directed at various angles to an air stream*, NACA Tech. Note, no. 2855.

172 Saad, N.R., Mujumdar, A.S., Messeh, W.A. and Douglas, W.J.M. 1980, *Local heat transfer characteristics for staggered arrays of circular impinging jets with cross-flow of spent air*, ASME paper No. 80-TH-23, 105–112.

173 Said, N.M., Mhiri, H., Golli, S.E., Palec, G.L. and Bournot, P. 2003, *Three-dimensional numerical calculations of jet in an external cross flow: application to pollutant dispersion,* ASME J. Heat Transfer 125, 510-522.

174 Said, N.M., Mhiri, H., Golli, S.E., Palec, G.L. and Bournot, P. 2005, *Experimental and numerical analysis of pollutant dispersion from chimney*, Atmos. Environ. 39, 1727-1738.

175 San, J.Y. and Lai, M.D. 2001, *Optimum jet-to-jet spacing of heat transfer for staggered arrays of impinging air jets*, Int. J. Heat Mass Transfer 44, 3997–4007.

176 Sarkar, S. and Balakrishnan, L. 1990, *Application of a Reynolds-stress transport model to the compressible shear layer*, ICASE, Report No. 90-18, NASA CR 182002.

177 Sarkar, S. and Bose, T.K. 1995, *Comparison of different turbulence models for prediction of slot-film cooling: flow and temperature field*. Numer. Heat Transfer B 28, 217-238.

178 Sau, A., Hwang, R.R., Sheu, T.W. and Yang, W.C**.** 2003**,** *Interaction of trailing vortices in the wake of a wall-mounted rectangular cylinder,* Phys. Rev. E 68, 056303-15.

179 Sau, A., Sheu, T.W.H., Hwang, R.R. and Yang, W.C. 2004, *Three-dimensional simulation of square jets in cross-flow*, Phys. Rev. E 69, 066302-1-066302-20.

180 Savory, E. and Toy, N. 1991, *Real-time video analysis of twin jets in a crossflow,* ASME J. Fluids Engng. 113, 68–72.

181 Schlichting, H. and Andew, In. Z. 1933, *Math. Mech*. 13, 260-263.

182 Schluter, J. and Schonfeld, T. 2000*, LES of jets in cross flow and its application to a gas turbine burner*, Flow Turb. Comb. 65, 177–203.

183 Seal, C.V., Smith, C.R., Akin, O. and Rockwell, D. 1995, *Quantitative characteristics of a laminar, unsteady necklace vortex System in a rectangular block-flat plate juncture,* J. Fluid Mech. 286, 117-135.

184 Sen, B., Schmidt, D.L. and Bogard, D.G., 1994, *Film cooling with compound angle holes: heat transfer,* ASME Paper No. 94-GT-311.

185 Shan, J.W. and Dimotakis, P.E. 2001, *Turbulent mixing in transverse jets*, GALCIT FM: 2001.006.

186 Shan, J.W. and Dimotakis, P.E. 2006, *Reynolds-number effects and anisotropy in transverse-jet mixing,* J. Fluid Mech. 566, 47–96.

187 Shang, J.S., McMaster, D.L., Scaggs, N. and Buck, M. 1989, *Interaction of jet in hypersonic cross stream*, AIAA J. 27, 323-329.

188 Sharma, C. and Acharya, S. 1998, *Direct numerical simulation of a coolant jet in a periodic crossflow*, NASA/CR-1998-208674.

189 Sherif, S.A. and Pletcher, R. H. 1990, *The physical and thermal characteristics of the subsonic jet in a cross stream- a review*, Mixed Convection Environment Flows 152, 83-94.

190 Sherif, S.A. and Pletcher, R.H. 1991, *Jet-wake thermal characteristics of heated turbulent jets in crossflow*, J. Thermophysics 5, 181-191.

191 Sherif, S.A. and Pletcher, R.H. 1998, *Measurements of the thermal characteristics of a cooled jet discharged into a heated cross-flowing water stream*, Int. Comm. Heat Mass Transfer 25, 455-469.

192 Shi, Y., Ray, M.B. and Mujumdar, A.S. 2003, *Numerical study on the effect of cross-flow on turbulent flow and heat transfer characteristics under normal and oblique semi-confined impinging slots jets*, Drying Tech. 21, 1923-1939.

193 Sinha, A.K., Bogard, D.G. and Crawford, M.E. 1991, *Film-cooling effectiveness downstream of a single row of holes with variable density ratio*, ASME J. Turbomach. 113, 442-449.

194 Sivadas, V., Pani, B.S., Bütefisch, K.A. and Meier G.E.A. 1997, *Flow*

visualisation studies on growth of area of deflected jets. Exp. Fluids 23, 105–112.

195 Smith, S. H., Lozano, A., Mungal, M. G. and Hanson, R. K. 1993, *Scalar mixing in the subsonic jet in a crossflow*, AGARD CP-534.

196 Smith, S. H. and Mungal, M. G. 1998, *Mixing structure and scaling of the jet in crossflow*, J. Fluid Mech. 357, 83–122.

197 Spalart P.R. and Allmaras S.R. 1992, *A one–equation turbulence model for aerodynamic flows*, AIAA Paper No 92–0439.

198 Sparrow, E.M., Goldstein, R.J. and Rouf, M.A. 1975, *Effect of nozzle-surface separation distance on impingement heat transfer for a jet in a crossflow*, ASME J. Heat Transfer 97, 528–533.

199 Speziale, C.G., Sarkar, S. and Gataski, T.B. 1991, *Modelling the pressure-strain correction of turbulence: an invariant dynamical systems approach*, J. Fluid Mech. 227, 245-272.

200 Su, L. K. and Mungal, M. G. 2004, *Simultaneous measurement of scalar and velocity field evolution in turbulent crossflowing jets*. J. Fluid Mech. 513, 1–45.

201 Sykes, R.I., Lewellen, W.S. and Parker, S.F. 1986, *On the vorticity dynamics of turbulent jet in crossflow,* J. Fluid Mech. 168, 393-413.

202 Thole, K.A., Gritsch, M., Schulz, A. and Wittig, S. 1997, *Effect of a crossflow at the entrance to a film-cooling hole,* ASME J. Fluids Engng. 119, 533-540.

203 Thomas, A. S. W. 1987, *The unsteady characteristics of laminar juncture flow,* Phys. Fluids 30, 283- 285.

204 Versteeg, H.K. and Malalasekera, W. 1996, *An Introduction to Computational fluid dynamics the finite volume method*, Logman, Malaysia.

205 Vijayan, P. and Balaj, C. 2004, *Turbulent forced convection in a parallel plate channel with natural convection on the outside*, Int. Comm. Heat Mass Transfer, 31, 1027-1036.

206 Vincenti, I., Guj, G., Camussi, R. and Giulietti, E. 2003, *PIV study for the analysis of planar jets in crossflow at low Reynolds number*, ATTI 11th Convegno Nazionale AIVELA, Ancona, December 2-3.

207 Walters, D.K. and Leylek, J.H. 1997, *A Systematic computational methodology applied to a three-dimensional film-cooling flow field*, ASME J. Turbomach. 119, 777-785.

208 Walters, D.K. and Leylek J.H. 2000, *A detailed analysis of film-cooling physics:*

Part I—streamwise injection with cylindrical holes, ASME J. Turbomach. 122, 102–112.

209 Wark, C.E. and Foss, J.F. 1988, *Thermal measurement for jets in disturbed and undisturbed crosswind conditions,* AIAA J. 26, 901-902.

210 Wegner, B., Huai, Y. and Sadiki, A. 2004, *Comparative study of turbulent mixing in jet in cross-flow configuration using les*, Int. J. Heat Fluid Flow 25, 767–775.

211 Weston, R.P. and Thames, F.C. 1979, *Properties of aspect-ratio-4.0 rectangular jets in subsonic crossflow,* J. Aircraft 16, 701-707.

212 Wilcox. D.C. 1998, *Turbulence Modeling for CFD*, DCW Industries, Inc., La Canada, California, USA.

213 Wille, M. 1997, *Large eddy simulation of jets in cross flows*, Ph.D. thesis. Imperial College of Science, Technology and Medicine, Department of Chemical Engineering, London, UK.

214 Wittig, S., Schulz, A., Gritsch, M. and Thole, K.A. 1996, *Transonic film cooling investigations: effects of hole shapes and orientations*, ASME Paper No. 96-GT-222.

215 Wu J.M., Vakili A.D. and Yu F.M. 1988, *Investigation of the interacting flow of nonsymmetric jets in crossflow,* AIAA J. 26, 940-947.

216 Yang, Y.T. and Wang, Y.X. 2005, *Three-dimensional numerical simulation of an inclined jet with cross-flow*, Int. J. Heat Mass Transfer 48, 4019–4027.

217 Yuan, L. L. and Street, R. L. 1998, *Trajectory and entrainment of a round jet in crossflow*. Phys. Fluids 10, 2323–2335.

218 Yuan, L.L., Street, R.L. and Ferziger, J.H. 1999, *Large eddy simulations of a round jet in crossflow*, J. Fluid Mech. 379, 71-104.

220 Zaman, K. B. M. Q. and Foss, J. K. 1997, *The effect of vortex generators on a jet in a cross-flow,* Phys. Fluids 9, 106–114.

221 Zhang, X. 2000, *An inclined rectangular jet in a turbulent boundary layer-vortex flow*, Exp. Fluids 28, 344-354.

222 Zhao, B., Vanka, S.P. and Thomas, B.G. 2004, *Numerical study of flow and heat transfer in a molten flux layer,* Int. J. Heat Fluid Flow 26, 105-118.